The Decaheme Cytochrome MtrC as a Platform for Modular Biohybrid Photocatalysis

Samuel E. H. Piper

PhD Thesis, June 2021

University of East Anglia
School of Chemistry
Norwich
United Kingdom

Abstract

The development of technologies to store solar energy as fuel is a highly active field. So-called solar fuels have the potential to revolutionise humanity's energy infrastructure and reduce our reliance on fossil fuels. Of particular interest is the use of living cells, typically bacteria, as catalysts for the production of such fuels due to their ability to repair and replicate themselves autonomously. Photocatalytic production of fuels (e.g. hydrogen) by bacteria requires a supply of electrons which must cross from light absorbers in the extracellular environment to enzymatic catalysts inside the cells. Most bacterial membranes are insulating however some specialised "electrogenic" bacteria readily transfer electrons across their membranes to support anaerobic growth. Such bacteria, in particular *Shewanella oneidensis* MR-1, can use porin:cytochrome complexes such as the MtrCAB complex as membrane-spanning molecular wires which could be adapted to provide the cell with photogenerated electrons.

The work presented in this thesis aimed to develop liposomal nanoreactors which use a photosensitised MtrCAB complex to transfer electrons across lipid bilayers to support catalysis by an encapsulated nitrous oxide reductase enzyme. This goal was pursued by first considering each component of the intended system, from the assembly and photochemistry of a photosensitised MtrCAB complex, to the requirements and encapsulation of the enzyme catalyst. Ultimately, the nanoreactors developed and produced were able to couple extraliposomal photochemistry to intraliposomal enzyme activity, a feat which to our knowledge has not been previously achieved. These nanoreactors serve as a proof-of-principle for the use of MtrCAB as a means of providing living cells with photogenerated electrons for the production of solar fuels.

Acknowledgements

My first and greatest thanks must go to my supervisor Prof. Julea Butt, whose guidance and support I count myself privileged to have received. This thesis would not exist without her careful management. Her kindness and immense capacity for understanding have meant the past four (and a bit) years have been thoroughly enjoyable. She has been the best supervisor anyone could have asked for.

I must also extend my thanks to my secondary supervisors Drs. Tom Clarke and Aram Saeed. Their experience has underpinned many of the findings presented here and their insights have always been helpful.

I thank Drs. Jessica van Wonderen, Simone Payne and Marcus Edwards, who trained me in many of the techniques I have used, and who I count as dear friends. Their support over my time at UEA has been invaluable and I don't know what I would have done without them. Thanks also go to the wider community of Lab 2.30, whose companionship and comradery have made bad days bearable and good days all the more exciting. I wish all of them the best of luck in their future careers.

My friends in Biology and Chemistry have always been there to support me and help put struggles into perspective. One such friend deserves a special mention. Sarah Woodhouse was my housemate and my closest friend. She brought light, joy and a lot of noise into my life, without her my time in Norwich would undoubtedly have been poorer. She deserves all the good things in the world, and I wish her every success.

My sincere thanks go to our collaborators who have guided and supported aspects of my project. To Dr. Carla Casadevall and Prof. Erwin Reisner at the University of Cambridge, I thank you for your photochemical insights and for supplying the photosensitisers that enabled this work to be possible. To Drs. Anna Stikane and Huijie Zhang and Prof. Lars Jeuken and the University of Leeds, I thank you for helping to develop the methods used to form the liposomes that were the goal of this project. I also thank Dr. Anne Martel and the staff of the Institut Laue-Langevin for their support and experimental guidance in collecting Neutron scattering data.

This project was made possible through the financial support of the BBSRC NRP DTP programme. My thanks go to the DTP team for their coordination of training and other opportunities.

Finally I thank my family for their continued support and encouragement and for their enthusiastic attempts to understand my "magic bubbles"; to my Mum Jo, who can weather any storm, who has held all us together through difficult times, and whose love and compassion are an inspiration to me; to my Dad Tony, who I sometimes suspect to

be more excited for my graduation than I am; to my Brother Alfie, who I have disagreed with many times, I hope we continue our recent efforts to learn to understand and respect each other's differences, I know we will be better people for it; to my Sister Rachel, just starting out on her academic journey, whose charming combination of youthful optimism and mature intellect will, I have no doubt, set her on the path towards a bright future; and to the members of my close family who were there to see me start this journey, but who aren't here to see it end. I wish I were able to share this moment with my Grandad, whose name I proudly carry, and who I hope I have made proud.

Table of Contents

Abbrevations and symbols

For buffer compositions see Table 2.1.1.

%	Percentage
% (v/v)	percentage by volume per volume
% (w/v)	percentage by weight per volume
% (w/w)	percentage by weight per weight
°C	degrees Celsius
$\Delta A_{X\ nm}$	Change in absorbance at X nm
$\varepsilon_{X\ nm}$	extinction coefficient at X nm
η	Buffer viscosity
λ	wavelength
µg	microgram
µL	microlitre
µM	micromolar
µMol	micromole
µs	microsecond
µV	microvolt
$\bar{\upsilon}$	partial specific volume
ρ	density
τ	lifetime
Φ	quantum yield
ω	angular velocity
≈	approximately equal to
Å	Angstrom
A_{Bp}	Benzophenone-alanine
ATP	Adenosine triphosphate
a.u.	Arbitrary units
AUC	Analytical ultracentrifugation
$A_{X\ nm}$	Absorbance at X nm
BCS	Bathocuproinedisulfonic acid
BSA	Bovine serum albumin
CA	Cardiolipin
Ca[FeFe]	[FeFe] hydrogenase from *Clostridium acetobutylicum*
CB	Conduction band
cm	Centimeter
CQD	Carbon quantum dot

CR	Charge recombination
CS	Charge separation
CSS	Charge separated state
CT	Charge trapping
Cys	Cysteine
Da	Dalton
dH_2O	Milli-Q water
DLS	Dynamic light scattering
D_{max}	Maximum dimension
dmg	Dimethylglyoxime
DMSO	Dimethylsulfoxide
DNA	Deoxynucleic acid
DT	Sodium dithionite
E	Energy
e^-	Electron
E. coli	*Escherichia coli*
EDTA	Ethylenediiminetetraacetic acid
ETC	Electron transport chain
eq.	Equivalents
eV	Electron volt
f	Frictional coefficient
FAD	Flavin adenine dinucleotide
F_b	Buoyant force
F_d	Ferredoxin
F_f	Frictional force
F_{FNO2}	4-fluoro-3-nitrophenylalanine
Fld	Flavodoxin
fm	Femtometer
FMN	Flavin mononucleotide
FNR	Ferredoxin-NADP-reductase
F_s	Sedimenting force
g	Gram
g	Earth's gravitational force
GC	Gas chromatography
g-CDs	Graphitic carbon dots
GFP	Green fluorescent protein
GJ	Gigajoule
GM	Gentamycin

g-N-CDs	Graphitic nitrogen-doped carbon dots
h	Hour
H_{cc}	Dimensionless Henry solubility
H_{cp}	Henry's law coefficient
HEPES	(4-(2-hydroxyethyl)-1-piperazineethanesulfonic acid)
His	Histidine
HS	Headspace
hv	Photon
ILL	Institute Laue-Langevin
IR	Infrared
ISC	Intersystem crossing
K	Kelvin
k	rate constant
k_B	Boltzman constant
K_d	Dissociation constant
kDa	Kilodalton
kg	Kilogram
KM	Kanamycin
K_M	Michaelis-Menten constant
k_{obs}	Observed rate constant
kW	Kilowatt
L	Litre
LB	Luria Broth
LC-MS	Liquid chromatography-mass spectrometry
LDAO	Lauryldimethylamine oxide
LED	Light emitting diode
LHC	Light harvesting complex
L-pyr	4-pyridine-oxazolophenanthroline
M	Molar
m	Meter
M. thermoacetica	*Moorella thermoacetica*
MES	2-(N-morpholino)ethanesulfonic acid
Met	Methionine
mg	Milligram
min	Minute
MJ	Megajoule
mL	Millilitre
MLCT	Metal to ligand charge transfer

MM	Minimal media
mM	Millimolar
MR-1	*Shewanella oneidensis* MR-1
ms	Millisecond
mS	Millisiemens
mV	Millivolt
MV	Methyl viologen (general)
MV^{+}	Methyl viologen (singly reduced)
MV^{0}	Methyl viologen (doubly reduced)
MV^{2+}	Methyl viologen (oxidised)
MW	Molecular weight
MWCO	Molecular weight cut-off
MΩ	Megaohm
N	Normality
N_A	Avogadro's constant
NADH	Nicotinamide adenine dinucleotide
NADPH	Nicotinamide adenine dinucleotide phosphate
ND	Neutral density
ng	Nanogram
[NiFeSe]	[NiFeSe] hydrogenase from *Desulfomicrobium baculatum*
nm	Nanometer
nmol	Nanomole
NosZ	Nitrous oxide reductase
OEC	Oxygen evolving centre
OG	Octyl glucoside
OQ	oxidative quenching
p	Pressure
Pa	Pascal
PCR	Polymerase chain reaction
PE	Phosphatidylethanolamine
PG	Phosphatidylglycerol
phen	1,10-phenanthroline
PL	Photoluminescence
PLE	Polar lipid extract
pM	Picomolar
pMol	Picomole
ppm	Parts per million
PS	Photosensitiser

ps	Picosecond
PSI	Photosystem I
psi	Pounds per square inch
PSII	Photosystem II
Q	Momentum transfer
r	Radius
R	Gas constant
RB5	Reactive Black 5
R_g	Radius of gyration
RMS	Root mean square deviation
RMSD	Root mean square distance
RPM	Revolutions per minute
RQ	Reductive quenching
RR120	Reactive Red 120
RuA-I	$[Ru(bpy)_2(5\text{-iodoacetamido-1,10-phenanthroline})]^{2+}$
RuMe-Br	$[Ru(bpy)_2(4\text{-}CH_2Br\text{-}4'\text{-}CH_3\text{-bpy})]^{2+}$
RuN	$[Ru(bpy)_2(5\text{-amino-1,10-phenanthroline})]^{2+}$
RuP	$[Ru(bpy)_2(4,4'\text{-}(PO_3H_2)_2bpy]^{2+}$
s	Second / Sedimentation coefficient
SANS	Small-angle neutron scattering
SAS	Small-angle scattering
SAXS	Small-angle X-ray scattering
SDS-PAGE	Sodium dodecyl sulfate–polyacrylamide gel electrophoresis
SDM	Side directed mutagenesis
SE	Sedimentation equilibrium
SEA	Sacrificial electron acceptor
SED	Sacrificial electron donor
SHE	Standard hydrogen electrode
STC	Small tetraheme cytochrome from *Shewanella oneidensis* MR-1
SV	Sedimentation velocity
T	Temperature
TAS	Transient absorbance spectroscopy
TCEP	Tricarboxyethylphosphine
TEA	Triethylamine
TEOA	Triethanolamine
TiO_2	Titanium oxide
TMBD	3,3',5,5'-Tetramethylbenzidine
TOF	Turnover frequency

TON	Turnover number
Tris:HCl	Tris(hydroxymethyl)aminomethane hydrochloride
TRPL	Time-resolved photoluminescence
TX100	Triton X-100
u	Velocity of a sedimenting species
uAA	Unnatural amino acid
UV	Ultraviolet
UV-Vis	Ultraviolet-visible
V	Volt
VB	Valence band
V_{max}	Maximum enzyme rate
vs	Versus
VSTES	Vishniac and Santer trace-elements solution
WLP	Wood-Ljungdahl pathway
WT	Wild type
YFP	Yellow fluorescent protein

CHAPTER 1

INTRODUCTION

Chapter 1 - Introduction

1.1 - Solar fuels synthesis to solve the global energy crisis

One of the major issues facing humanity today is our ever-increasing demand for energy. From the industrial revolution until relatively recently this demand has been met almost entirely by using fossil fuels (coal, oil and natural gas) (Figure 1.1.1).[1] These materials were cheap and abundant, could be transported easily and burnt to release their energy as heat. Modern society was built on the use of these fuels to power infrastructure and produce electricity. Of course, as we know now, fossil fuels are non-renewable and release greenhouse gases upon combustion that are the main contributor to the present climate crisis. Changing weather patterns and rising sea levels are set to change the planet as we know it. In the coming decades humanity will experience disrupted food supplies, diminished access to fresh water and the displacement of billions of people from areas that are no longer habitable.

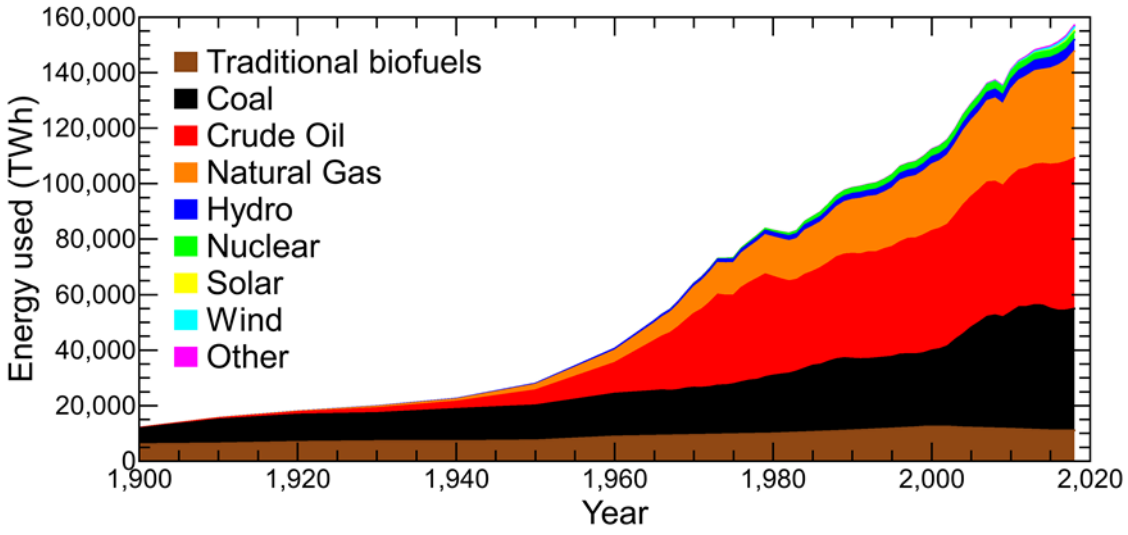

Figure 1.1.1 Global primary energy consumption over time since 1900[1] (Traditional biofuels = wood, charcoal etc.);

Finding a renewable source of energy to completely replace fossil fuels is not simple. Renewable electricity, sourced from wind, hydro, solar etc., has been steadily increasing as a share of the global energy market (Figure 1.1.1).[1] These sources, however, are reliant on specific climatic conditions such as time of day or wind speed. Storage of electricity to meet demand when supply is low is challenging; batteries cannot yet meet the needs of most developed countries and are typically too heavy to be used in some transport sectors such as air-travel. A fossil fuel replacement would ideally also be a fuel, meaning a chemical species with high energy-density that can be stored and transported

without a decrease in potency. The energy required to produce such fuels should derive from a renewable source, the greatest of which is sunlight. Fuels produced in this way are termed “solar fuels” and a selection of these are presented in Table 1.1.1.

Table 1.1.1 Energy density and thermodynamic reduction potentials of various solar fuels.

Solar fuel	Energy density[2] (MJ kg^{-1})	Standard reduction potential[3] (V vs Standard Hydrogen Electrode (SHE), pH 7)
Hydrogen	120	-0.42 $2H^+ + 2e^- \rightarrow H_2$
Carbon monoxide	10.1	-0.53 $CO_2 + 2H^+ + 2e^- \rightarrow CO + H_2O$
Methane	50	-0.24 $CO_2 + 8H^+ + 8e^- \rightarrow CH_4 + 2H_2O$
Methanol	19.9	-0.38 $CO_2 + 6H^+ + 6e^- \rightarrow CH_3OH + H_2O$
Formic acid	5.3	-0.61 $CO_2 + 2H^+ + 2e^- \rightarrow HCO_2H$

In addition to being a source of energy, fossil fuels are intimately tied to the chemicals industry. The vast majority of pharmaceuticals, plastics and all manner of other products are derived from hydrocarbons found in oil and require energy intensive processing to produce. Finding a replacement source for these organic materials will involve fixing carbon dioxide (CO_2) from the atmosphere, either directly or by using biomass derived from plants which are naturally able to use sunlight to fix CO_2 as part of photosynthesis (see Section 1.3). Natural photosynthesis has been used as inspiration for synthetic solar fuels synthesis. Components of the photosynthetic machinery have also been co-opted to create biohybrid photocatalytic systems due to their outstanding photochemical properties.

Recent decades have seen the development of vast quantities of systems capable of solar fuels synthesis.[4–8] Approaches range from using fully synthetic systems to purely biological, living organisms via hybrid materials which incorporate natural and synthetic components. Broadly, this work can be divided into heterogeneous (photoanodes/cathodes etc.) and homogeneous (molecular assemblies) systems. The two fields require quite different considerations at many levels including light absorption, charge transport and catalysis. The systems under study in this work better align with the homogeneous field, therefore only such systems will be discussed in the following sections.

1.2 - Properties of a photocatalytic system

A typical photocatalytic system for solar fuels synthesis must contain at least three core components (Fig. 1.2.1): a photosensitiser capable of absorbing visible light and converting this energy to a reducing equivalent/electron; a catalyst capable of accepting electrons from the photosensitiser and carrying out the desired reaction, and a source of electrons to replenish the photosensitiser. There are countless possible choices for each of these components and equally diverse options for assembling them. Here, only systems where the photosensitiser and catalyst are linked will be considered.

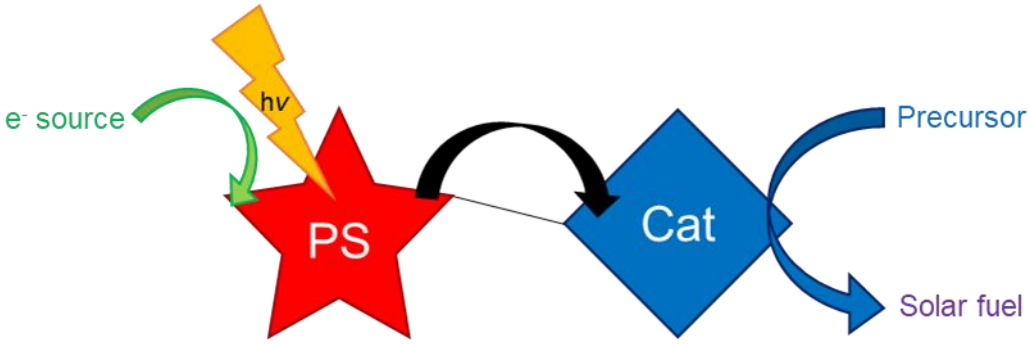

Figure 1.2.1 Generalised schematic of a solar fuels synthesis system including an electron source (Green), and a photosensitiser (PS - Red) linked to a catalyst (Cat – Blue), irradiation shown by yellow lightning bolt.

The role of the photosensitiser is to capture the energy of sunlight and convert it to chemical energy. Photons of a suitable wavelength are first absorbed, and the energy is used to excite an electron from a lower energy ground state to an excited state where the energy is converted into a more negative reduction potential. This, by definition, also creates a “hole” with a more positive reduction potential. Excited states are inherently thermodynamically unstable and in the absence of any other species the excited electron and hole will recombine, releasing the absorbed energy either as vibrational energy/heat or as a photon, termed photoluminescence (PL) (Fig. 1.2.2 - Left).

PL is a general term covering both fluorescence and phosphorescence. Fluorescence occurs in systems where the excited and ground states both have the same spin-state (i.e. both singlet states), meaning that the decay from the excited state back to the ground state is spin-allowed. The lifetime of fluorescent excited states is typically short, on the order of tens of nanoseconds.[9] Phosphorescence, on the other hand, occurs in species where intersystem crossing (ISC) leads to a change in the spin-state of the excited state (i.e. singlet to triplet, Fig. 1.2.2 - Left). The decay back to the ground state therefore becomes spin-forbidden leading to excited state lifetimes from tens of microseconds or longer.[9] For this reason, phosphorescent species typically make better photosensitisers as the excited state persists for a longer time.

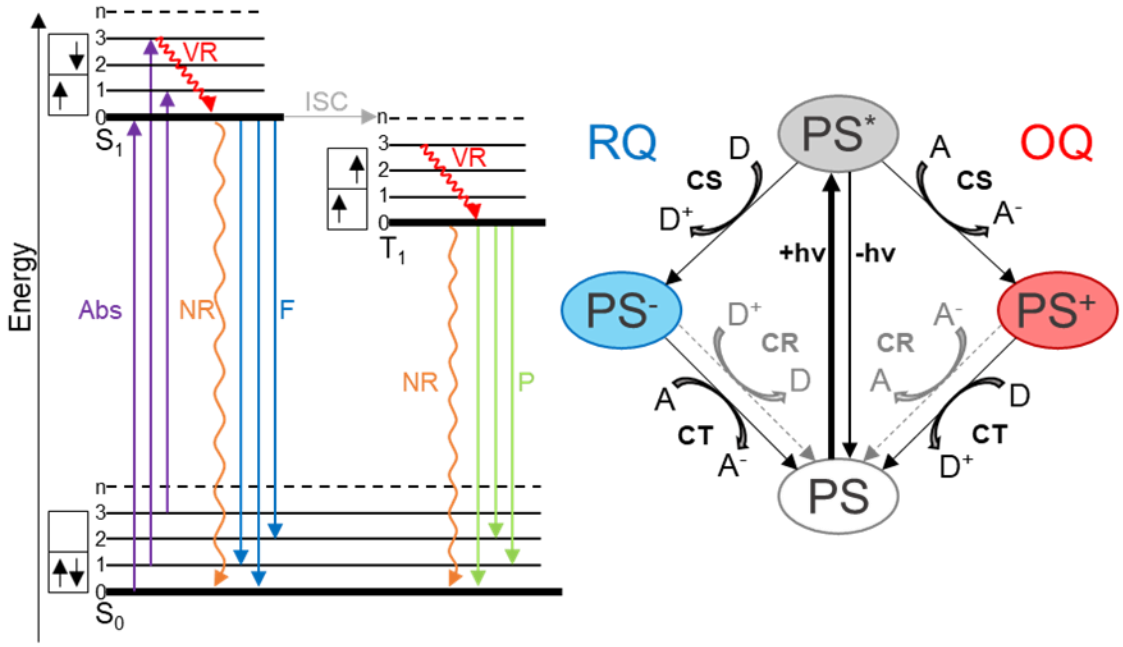

Figure 1.2.2 Left) Jablonski diagram describing the possible fates of a chromophore after absorbance of a photon. Energy levels are represented by solid lines with the thicker lines being the vibrational ground states of each electronic state (S – singlet, T – triplet) and thinner lines being the vibrational excited states within those electronic states. Spin states of the electrons are shown. Transitions between states are shown as arrows: Absorbance of a photon (Abs – Purple), Fluorescence (F – Blue), Phosphorescence (P - Green), Non-radiative decay (NR – wavy orange), Vibrational relaxation (VR – Red wavy), Intersystem crossing (ISC – Grey). **Right)** Quenching pathways for a photosensitiser (PS) after absorbance of a photon to reach the excited state PS*. Oxidative quenching (OQ) involves charge separation (CS) with an electron acceptor (A) generating PS^+ which can then either oxidise an electron donor (D) in a process termed charge trapping (CT) or undergo charge recombination with A^- (CR) reforming PS and A. Reductive quenching (RQ) involves CS with D to form PS^- followed by either CT with A or CR with D^-.

If an appropriate redox active molecule is close enough to the excited photosensitiser the excited state can be quenched by electron transfer. As noted above, upon excitation photosensitisers become both more potent reductants and oxidants due to the low-potential electron and high-potential hole respectively. The excited state can therefore be quenched in two ways, either by transfer of the electron to an acceptor (oxidative quenching) or by a donor filling the hole (reductive quenching) (Fig. 1.2.2 - Right). These processes create a charge separated state (CSS) where the electron-hole pair has been separated in space. The electron-hole pair will still seek to recombine and release their energy but, by separating the charges, charge recombination is slowed.

Extending the lifetime of the CSS is important as the only way to terminate the electron relays, and permanently capture the absorbed energy, is by coupling to an irreversible redox reaction (charge trapping). This step of the photocatalytic system is usually bimolecular, involving a sacrificial electron donor (SED)[10], and typically occurs on timescales far slower than intramolecular primary electron transfer events. The further

the charges can be separated, by sequential electron transfers to mediating redox centres, the slower charge recombination becomes[11–16], and charge trapping becomes more likely; this strategy is employed very well by natural photosystems (see Section 1.3). Solar fuels synthesis typically requires a minimum of two electrons (Table 1.1.1) whereas most photosensitisers produce electrons one at a time. Coupling of single-electron photochemistry to multi-electron catalysis is aided by mediating redox centres which may store electrons until enough are accumulated.[17,18]

This extension of the CSS lifetime, however, can come at a cost. Each thermodynamically favourable electron transfer uses some of the energy imparted by the absorbed photon and therefore lowers the energy available for catalytic work. It is therefore important when designing electron relays for photocatalysis to carefully tune the reduction potentials such that the CSS is long lived enough to be useful, but without losing too much energy that it can no longer drive the desired reaction.

The ideal electron source is water as it is abundant, cheap and produces oxygen upon oxidation. Water oxidation catalysts are, however, rare and the oxygen produced may deactivate or destroy hydrogen producing catalysts.[19–21] Instead, most researchers utilise sacrificial electron donors (SEDs) as the terminal reductant for their systems. These small molecules, often tertiary amines or sulfur compounds, can be oxidised with relative ease after which they rapidly convert to inert materials to prevent back-reactivity.[10]

After considering the prospects and pitfalls of photochemistry, Lubner et al. set out five attributes of a photocatalytic system[22]:

1) Efficient generation of primary CSS:
   Each photon absorbed should lead to the generation of an electron-hole pair

2) Long lived CSS:
   Terminal oxidation/reduction of the electron relays should be faster or at least competitive with charge recombination

3) Minimum energy wasted stabilising the CSS:
   The CSS should be stabilised by thermodynamically favourable electron transfers but only to enable terminal charge trapping to be competitive with charge recombination. Further extension is wasteful.

4) An antenna like system of energy harvesters should be established:
   By establishing a network of chromophores that can transfer energy to the photosensitiser the effective rate of photon absorbance is increased. Also of note is that very few chromophores can effectively absorb wavelengths of light from across the solar spectrum. By combining different chromophores with varied absorbance profiles into an antenna system, the spectral range of a photocatalytic module can be widened.

5) Robust or self-repairing system:
   Photochemistry involves high-energy chemical species and even small imbalances in electron or energy transfers can lead to problems including photosensitiser inactivation, disruption to the electron relays and potentially irreversible activity loss. An ideal system should either: be so well designed that these problems hardly ever occur or be capable of self-repair.

In the following sections these attributes will be used to evaluate both natural, artificial and biohybrid photocatalytic systems of different kinds.

1.3 - Natural photosynthesis

Photosynthesis describes the process carried out by plants and some prokaryotes whereby the energy of light is captured and converted to chemical energy for storage and further use. This energy can then be used to fix CO_2 (and in some cases N_2) to biomass, creating the foundations of the world's food chains. Photosynthetic organisms from across the tree of life use a variety of mechanisms to collect and store light-energy but the overall principal steps are generally the same: collect light using pigments and effectively transport this energy to a reaction centre; use the energy to generate an electron-hole pair; effectively separate these charges across an insulating interface such as a biological membrane; capture the energy of the resulting redox gradient in chemical bonds; use this captured energy for cellular processes including self-repair.

These steps reflect the 5 attributes of a photocatalytic module[22] as discussed previously and natural photosystems are widely regarded as the benchmark for photocatalysis, having evolved over billions of years to be able to support all life on our planet. Natural photosynthetic machinery will be explored to exemplify the properties of efficient photocatalytic units.

Natural photosystems can be grouped into two main types based on the energy carrier they are designed to generate, ATP or NAD(P)H. Cyanobacteria, algae and green plants

carry out oxygenic photosynthesis in their thylakoid membranes which contain two types of photosystem (Fig. 1.3.1). Photosystem II (PSII) truly changed the face of this planet as it is this protein complex that oxidises water, generating protons, electrons and dioxygen. PSII is the only protein known to be able to perform this reaction and does so using a unique Mn_4O_4Ca cluster capable of storing the four oxidising equivalents required.[23]

Electrons obtained from water oxidation are energised by the reaction centre of PSII, a pair of chlorophyll molecules termed the special pair or P680, and subsequently transferred down a chain of cofactors, exquisitely placed and with carefully tuned reduction potentials, with the effect that the final CSS ($Mn^+Q_B^-$) is formed with millisecond kinetics and with a quantum yield of 90%.[24] Electrons are transferred on by membrane-soluble redox shuttles and used by cyt b_6f to pump protons into the thylakoid lumen. This proton gradient is used by ATP synthase to generate ATP. The electrons are then transferred, via plastocyanin, to Photosystem I (PSI) which also possesses a special pair of chlorophylls, termed P700. The electrons are excited again and shuttled through a second chain of cofactors, reaching the final iron-sulfur (Fe-S) cluster F_B in under a millisecond and with near unity quantum yield. From there the electrons, still retaining around 60% of the energy obtained at P700,[25] are transferred, via ferredoxin, to Ferredoxin-$NADP^+$ reductase (FNR) and used to reduce $NADP^+$ to NADPH. Together these photosystems form the Z-scheme of oxygenic photosynthesis (Fig. 1.3.1).

In addition to the reaction centre chlorophylls which perform the initial charge separation steps, PSI and PSII are associated with light harvesting complexes (LHCs) which are large protein complexes containing many pigment molecules including chlorophyll-a, chlorophyll-b and carotenoids.[26] The LHCs act as antennas, absorbing light over a wider area and funnelling the energy to the reaction centres, thereby increasing the effective photon flux at the special pair. These pigments also widen the photosynthetic action spectrum, increasing the wavelengths of light that can be used for photosynthesis (Fig. 1.3.2).

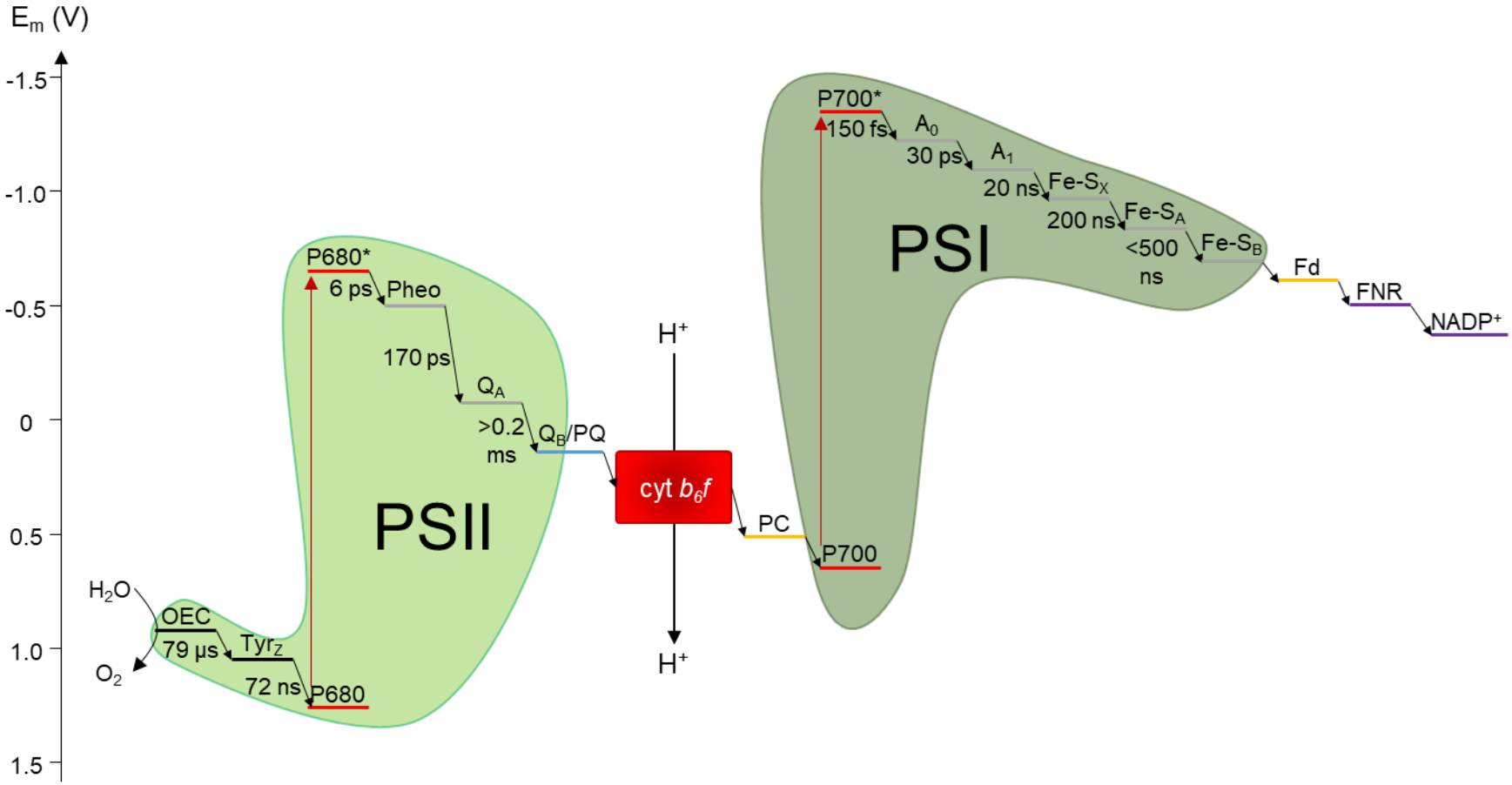

Figure 1.3.1 Photoelectrochemistry and kinetics of oxygenic photosynthesis. OEC – Oxygen evolving centre, Tyr_Z – D_1 Y160, P680 – PSII reaction centre, Pheo – pheophytin, Q – Plastoquinones, PQ – plastoquinol, PC – Plastocyanin, P700 – reaction centre of PSI, A – Phylloquinones, Fe-S – Iron-sulfur clusters, Fd – ferredoxin, FNR – Ferredoxin-$NADP^+$-reductase, $NADP^+$ - Nicotinamide adenine dinucleotide phosphate. Scheme adapted from Rasmussen et al.[27] Kinetics of forward electron transfers given as lifetimes ($1/k$).[24,25,28,29]

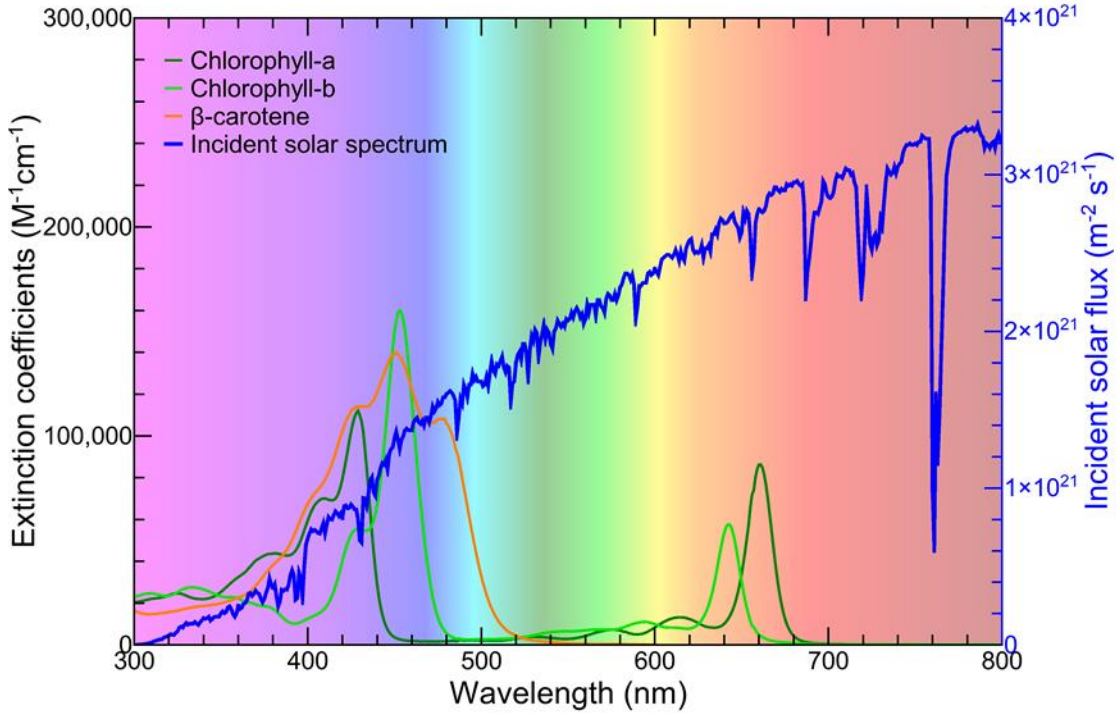

Figure 1.3.2 Extinction coefficient spectra of common photosynthetic pigments: chlorophyll-a (Dark green), chlorophyll-b (light green), β-carotene (orange)[30]; and the visible portion of the incident solar flux (Blue).[31]

Electron transfer in natural photosystems has had the benefit of billions of years of evolution to be perfected, resulting in unparalleled efficiency. The kinetics of the forward electron transfer steps in the electron transfer chains (ETCs) of PSI and PSI are typically orders of magnitude faster than the reverse steps, leading to near unity production of the CSSs with long (0.1 s) lifetimes.[25] The trade-off for these long-lived CSSs is that some of the energy given to the electrons upon excitation is lost, however enough remains at the end of the ETC to create the cellular energy carriers ATP and NADPH.

These systems are not perfect. Photoinhibition can cause significant efficiency losses. This typically occurs due to imbalances in electron flow through a photosystem which can lead to over-reduction or over-oxidation of chromophores etc. Such species can become inactive, or worse go on to cause damage to other components.[32–34]

Whilst the photochemistry of the Z-scheme is highly efficient, the overall efficiency of photosynthesis is low. One of the largest losses of energy is the roughly 55% of solar radiation reaching the surface of the earth that is unable to be absorbed by the LHCs (Fig. 1.3.2). In addition, the reaction centres of PSII and PSI only use photons with specific wavelengths (680 and 700 nm respectively) to perform charge separation. Energy is lost as heat during downconversion of higher energy photons. Another significant loss is to carbohydrate synthesis. The minimum energy required to create the

NADPH and ATP to assimilate one mole of glucose from CO_2 (5.2 GJ) is far greater than the energy obtained upon respiration of the glucose (2.9 GJ). The overall efficiency of conversion of incident solar energy to biomass for common crop plants such as maize and sugar cane, is around 5%.[35]

Despite these losses, the photosynthetic machinery of nature represents the best photocatalytic system we are aware of and fulfils each of the 5 attributes of a photocatalytic module posed by Lubner et al.[22]

1) Efficient charge separation:
   Primary CSSs in PSII and PSI are formed with quantum unity in picosecond timeframes

2) Long lived CSS:
   Final CSSs are formed with near quantum unity and have lifetimes of tens of milliseconds

3) Minimal energy expended to stabilise CSS:
   Some energy is lost through the ETCs of PSI and PSII, however the reduction potential of the final Fe-S cluster of PSI is sufficiently low (≈-700 mV)[27] to support almost any biologically relevant redox reaction or solar fuel synthesis (Table 1.1.1).

4) Antenna system for maximal effective photon flux:
   LHCs in thylakoid membranes absorb light between 400 and 700 nm and efficiently transfer this energy to the reaction centres. The presence of a variety of pigments increases spectral coverage and resistance to photodamage.

5) Robust or self-repairing:
   The photosynthetic machinery of PSI and particularly PSII are prone to light-induced damage and constant repairs and replacements are required in order to keep the system operational. Being a part of a living cell makes this possible, however it reduces the overall efficiency of photosynthesis somewhat.

These properties allow plants to capture enough energy to support the food chains of almost all life on earth. However, when looking to meet humanity's energy and materials demands natural photosynthesis by plants does not provide a perfect solution for many reasons:

Most plants require fresh water and soil in order to grow, meaning they take up space and resources that could otherwise be used to grow food to support the growing human population.

Common food plants (corn, sugar cane etc.) can be converted to biofuels which, while effectively carbon neutral, are typically grown using fertilisers which have many deleterious environmental consequences such as production of greenhouse gases, soil degradation and waterway contamination.[36]

The photosynthetic action spectrum covers less than 45% of the available solar radiation received at the Earth's surface, efforts to widen the absorption cross section of LHCs are ongoing.[37]

The products of photosynthesis are primarily geared towards supporting the life of the organism, not being useful to humans. Large quantities of cellulose and other chemically resistant biopolymers are produced. These cannot be easily broken down and are useful only for combustion after drying.

Plants typically have large polyploid genomes making genetic manipulation challenging, synthetic biology using plants therefore poses many difficulties.

Plants can be susceptible to disease and changing climatic conditions, making them a less secure prospect.

Some plants with unique properties have shown promise for biofuel production, one of the most successful being Giant Miscanthus (*Miscanthus x giganteus*). This crop has been shown to: increase soil organic carbon over its lifetime; require no nitrogen based fertiliser and minimal herbicide application; produce fewer greenhouse gases upon combustion than fossil fuels; have one of the highest water-use efficiencies of any crop; and contribute to flood prevention by improving soil structure.[36] Miscanthus can also be used as a building material and its pulp can be moulded into biodegradable items (plates, utensils cups etc.).[38]

Other photosynthetic organisms such as cyanobacteria may also hold promise. These bacteria, the ancestors of chloroplasts, can also carry out oxygenic photosynthesis and do not require arable land in order to be grown. Many can adapt to grow in salt-water,[39] meaning seawater could be used as growth medium, further reducing demand on agricultural resources. Desert environments are already being used to house large cyanobacterial farms.[40] Cyanobacteria have relatively small genomes and are more genetically tractable than plants. They do not, however, have the biosynthetic pathways for production of biofuels such as ethanol or butanol meaning synthetic biology is required to add these.[41] Hydrogen production is also difficult with cyanobacteria due to

the oxygen produced by the OEC of PSII. Many hydrogenase enzymes are notoriously oxygen sensitive and can be irreversibly inactivated upon exposure to small quantities of oxygen.

In summary, natural photosynthesis holds some promise for supplying humanity's demand for energy and raw materials, however, there exist major limitations in bringing these techniques to fruition and to market. Cyanobacteria may hold the answer to productivity without impinging on agricultural land but there is still much work to be done optimising these organisms for effective and economical operation.

1.4 - Artificial photosynthetic systems

Designs for homogeneous artificial photosynthetic synthetic systems typically take a modular approach; chemical species, selected for their desirable properties, are brought together in defined compositions to facilitate photochemistry. The three essential components of any photocatalytic system for solar-fuels synthesis (a photosensitiser, redox catalyst and source of electrons) can be assembled in a variety of ways. These methods can be broadly defined as:

Direct attachment – photosensitiser and catalyst are covalently attached but the intermediary material is simply structural and does not have a functional role in photocatalysis;

Mediated assembly – Photosensitiser and catalyst are covalently or electrostatically assembled with an intermediate that serves both a structural and functional role by accepting electrons from the photosensitiser and delivering them to the catalyst.

Hydrogen is the most common solar fuel target for artificial systems, in part for its high energy density but also its simplicity. In this section we will consider only systems which are designed to produce hydrogen.

1.4.1 - Direct attachment of photosensitisers and catalysts

Some of the most commonly used photosensitisers are analogues of Tris(bipyridine)ruthenium ($[Ru(bpy)_3]^{2+}$), used widely due to their: long-lived Metal-to-Ligand Charge Transfer (MLCT) excited states, absorbance in the visible region of the spectrum ($\lambda_{max} \approx 450$ nm), and large driving force for redox chemistry ($Ru^{II*/III} \approx -0.8$ V vs. SHE).[42,43] Ru-diimine complexes have been covalently bound to redox catalysts such as cobaloximes,[44] creating molecular dyads capable of hydrogen production. The third

component of the system (the electron source) is usually a SED such as a tertiary amine (ethylenediaminetetraacetic acid (EDTA), triethylamine (TEA), triethanolamine (TEOA)) or ascorbate.

Ru-diimine-cobaloxime dyads were first prepared by Fihri et al. by substituting one of the cobaloxime's axial water ligands for $[Ru(bpy)_2(L\text{-}pyr)]^{2+}$ (L-pyr=4-pyridine-oxazolophenanthroline) to form $Ru(bpy)_2(L\text{-}Pyr)\text{-}CoBF_2$ (Fig. 1.4.1).[45] Photochemical hydrogen production was performed in acetone with TEA as a SED and Triethylammonium as a proton source. A maximal turnover frequency (TOF) (moles of H_2 produced (mole of catalyst)$^{-1}$) of 16 h^{-1} was found for $Ru(bpy)_2Py\text{-}CoBF_2$ with a turnover number (TON) (moles of H_2 produced (mole of catalyst)$^{-1}$) of 103 after 15h. Under these conditions a mixture of $[Ru(bpy)_3]^{2+}$ and the free cobaloxime produced only traces of hydrogen, suggesting the linkage of the two units was vital for photocatalysis.

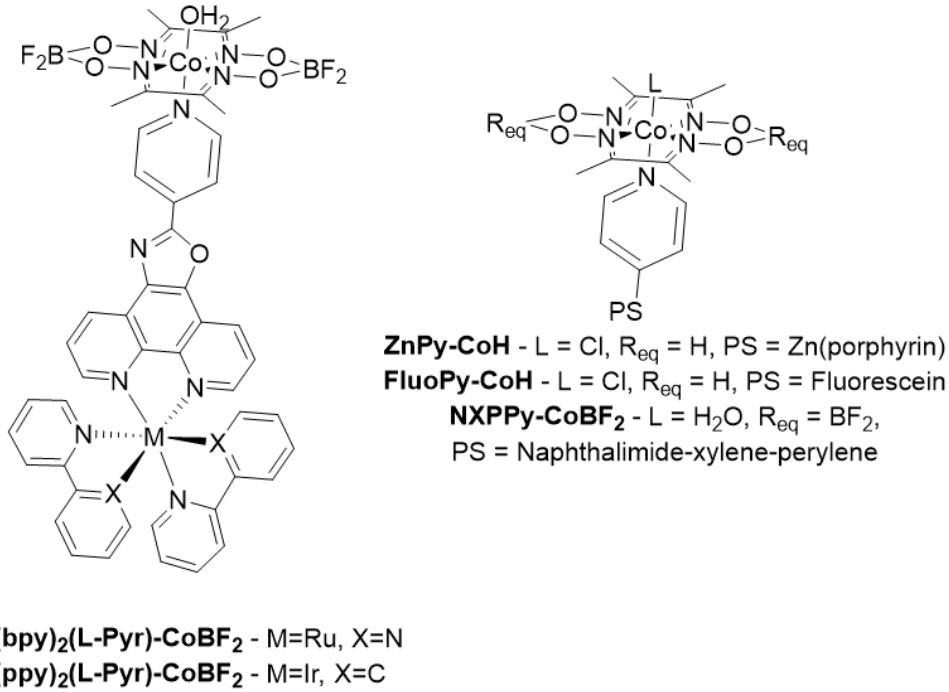

Figure 1.4.1 Structures of directly linked photosensitiser-cobaloxime dyads. Charges have been excluded for simplicity.

Further experiments on these systems have varied the metal and ligand set of the photosensitiser[46,47] and the composition of the link between the photosensitiser and the catalyst (Fig. 1.4.1).[48] Maximal activity was found with an iridium photosensitiser dyad ($Ir(ppy)_2(L\text{-}Pyr)\text{-}CoBF_2$).[46] It was later revealed, however, that charge-transfer induced dissociation of the photosensitiser and catalyst was prevalent due to the labile pyridine-cobalt bond.[49] This effect was also observed when using photosensitisers such as metalloporphyrins (ZnPy-CoH),[50] fluorescein (FluoPy-CoH),[51] and perylene ($NXPPy\text{-}CoBF_2$)[52] with similar axial pyridine linkages (Fig. 1.4.1). The equatorial glyoximate (dmg)

ligands of cobaloxime have also shown to be susceptible to dissociation during photocatalytic turnover and may be prone to hydrogenation leading to inactivation of the catalyst.[51]

Learning from these design flaws, new photosensitiser-cobaloxime dyads have been prepared with adapted designs which have added stability against ligand dissociation whilst retaining a proton relay to maintain activity.[53–56] These improvements, however, cannot overcome the fundamental issues with using dyad photochemical systems, namely that the distance between photosensititser and catalyst is short, and there is a lack of extended electron relays. These properties led to rapid charge recombination, and difficulty coupling single-electron photochemistry to multi-electron chemistry redox catalysis. This leads to low yields for photocatalysis, such systems are now typically produced only for kinetic studies, not as prospective artificial photosynthetic systems. The introduction of redox active mediators may serve to extend the CSS and allow accumulation of multiple electrons.

1.4.2 - Assembly of photosensitisers and catalysts with redox active mediator

An electron mediator for photosensitiser-catalyst coupling should have the following qualities:

- Appropriate chemical moieties to support binding of both photosensitiser and catalyst in photochemically productive orientations,
- reduction potentials between those of the photosensitiser and the catalyst to ensure efficient electron extraction from the photosensitiser and onward transfer to the catalyst,
- capacity to store multiple electrons to assist in coupling of single-electron photosensitiser chemistry to multielectron redox catalysis.

Semiconductors have been explored as potential mediators; these materials have unique electronic structures, containing a “band gap” where there are no accessible energy bands. The energy levels above and below this gap are termed the conduction band (CB) and valence band (VB) respectively. Multiple electrons are able to migrate through the conduction band and, in this way, semiconductors may efficiently mediate electron transfer from photosensitsers to catalysts.

Phosphate groups are titaniaphilic, and are regularly used to tether species to the surface of semiconducting TiO_2 particles with greater stability than other nucleophilic groups

such as carboxylates.[57] Phosphonated $Ru(bpy)_3^{2+}$ (RuP) and proton reduction catalysts (cobaloximes and nickel-based DuBois catalysts) have been coassembled on TiO_2 particles to form RuP-TiO_2-catalyst triads (Fig. 1.4.2).[58–61] The CB of TiO_2 is well positioned to facilitate electron transfer from RuP to these catalysts and these systems were shown to be capable of proton reduction with the NiP system[61] boasting higher TOF and TON than the analogous cobalt systems.[60]

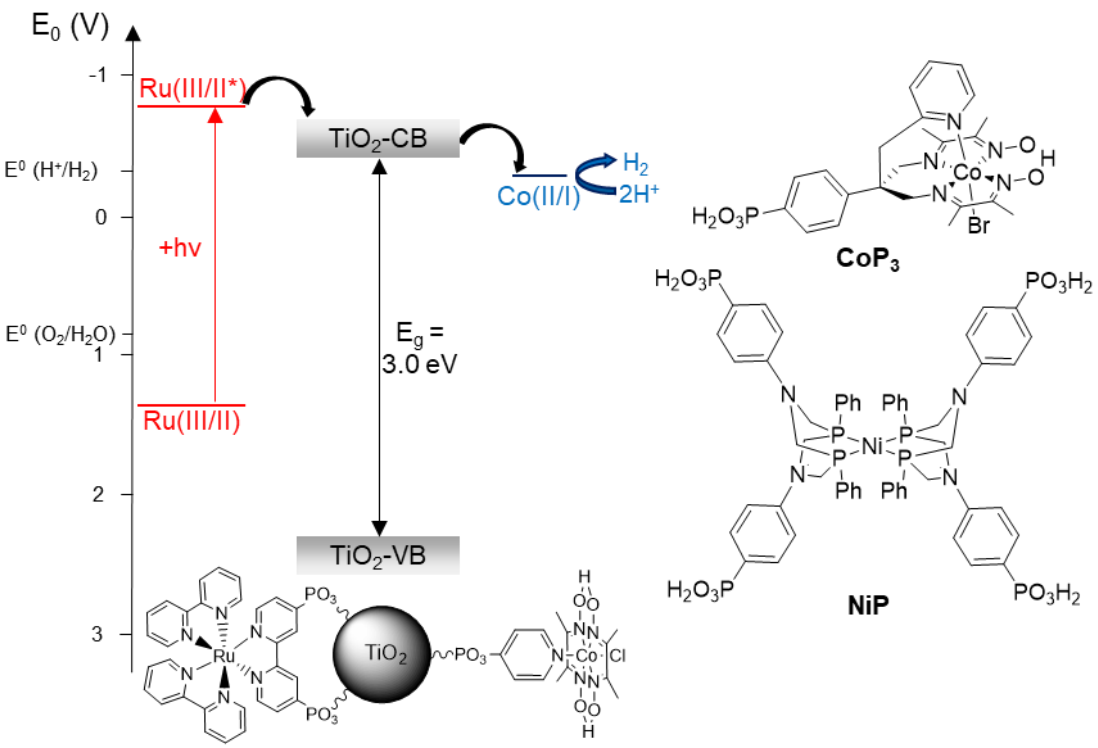

Figure 1.4.2 Left) Reduction potentials and structure of RuP-TiO_2-CoP_1.[58] Thermodynamic reduction potentials of proton reduction (-0.265 V vs SHE at pH 4.5) and water oxidation (963 mV vs SHE at pH 4.5) are also indicated; **Right**) Structures of CoP_3[60] and NiP[61]. Charges have been excluded for simplicity.

A side-by-side electrocatalytic comparison of NiP and CoP_1 revealed that the presence of 21% O_2 led to irreversible inhibition of NiP, attributed to oxidation of the phosphates to phosphine oxides. CoP_1 on the other hand was still around 22% active in the presence of O_2 with the main loss being due to competition between proton reduction and catalyst oxidation by O_2. Carbon monoxide (CO) has the opposite effect on these catalysts. NiP was mostly unaffected by the presence of CO whereas CoP_1 was completely inhibited. CoP_1 could, however, recover 100% of its electroactivity after purging with N_2 meaning this inhibition was reversible.[20] O_2 and CO are common gases in water splitting and syn-gas operations respectively, these results highlight that different catalysts may need to be used in different industrial scenarios.

Utilising specific covalent bond formation allows for more precise control over the interaction between components of a photocatalytic system than relying on non-specific electrostatic interactions. A particularly interesting medium for covalent photocatalyst assembly involves the use of proteins. Amino acid side chains provide many opportunities for specific attachment of photosensitisers and/or catalysts and their position and reactivity can be optimised for photocatalysis using molecular biology. Many proteins also contain redox active cofactors that can be used to: extend a CSS, transport electrons to a catalyst or act as an electron reservoir. Using proteins in this way could be viewed as a biohybrid technique, however as neither the photosensitiser nor the catalyst is biological these approaches are considered here to be biologically-mediated artificial photosynthesis.

Small redox-active proteins have been used to coassemble photosensitisers and proton reduction catalysts while participating in transfer and storage of electrons. Ferredoxin (Fd) from *Spinachia oleracea* is a 10.5 kDa protein which contains an Fe-S cluster. Soltau et al. used the native residues of Fd to bind a $[Ru(bpy)_3]^{2+}$ derivative and a cobaloxime catalyst. $[Ru(bpy)_2(4\text{-}CH_2Br\text{-}4'\text{-}CH_3\text{-}bpy)]^{2+}$ (RuMe-Br) is a widely used thiol reactive photosensitiser and was found to bind to Fd Cys18 with around 60% efficiency. Cobaloxime catalysts were found to covalently bind to RuMe-Fd via axial ligation from His90, producing RuMe-Fd-Co triads (Fig. 1.4.3 - Top) which produced hydrogen at rates greatly exceeding those previously discussed.[62,63]

RuMe and a hydrogen generating catalyst have also been assembled in a redox inactive protein; Flavodoxin (Fld) from *Synechococcus lividus* was partially unfolded to remove its flavin mononucleotide (FMN) cofactor. During the refolding process, the DuBois catalyst NiC was added and was incorporated into the protein's active site. RuMe was then covalently attached via Cys54, resulting in close positioning of the photosensitiser and catalyst. The RuMe-apoFld-NiC triad (Fig. 1.4.3 - Middle) was capable of light-driven proton reduction over a wide pH range. Notably, such catalysts have not previously been observed to function as proton reduction catalysts above pH 5. The FMN binding pocket of apoFld appears to stabilise the otherwise poorly water-soluble NiC and impart flexibility over a range of pH values from 3.5 to 12.[64]

Interprotein interactions have recently been used to create a more modular system. $CoBF_2$ was attached, non-specifically via histidine residues, to Ferredoxin-NADP-reductase (FNR) from *Anabaena* PCC 7119 and mixed with RuMe-labelled Fd as described previously (Fig. 1.4.3 – Bottom).[62] These two proteins are natural redox partners and terminate the Z-scheme of photosynthesis (Fig. 1.3.1). At a 1:4 ratio of $CoBF_2$:RuMe-Fd, these functionalised proteins evolved H_2 under irradiation. Interestingly, removal of either of the natural cofactors (Fe-S cluster/FAD) to generate

RuMe-apoFd or $CoBF_2$-apoFNR did not reduce the H_2 evolution activity; in fact, removal of both cofactors led to increased activity, suggesting that the natural cofactors were not involved in productive photocatalysis and were possibly causing non-productive side-chemistry.[65]

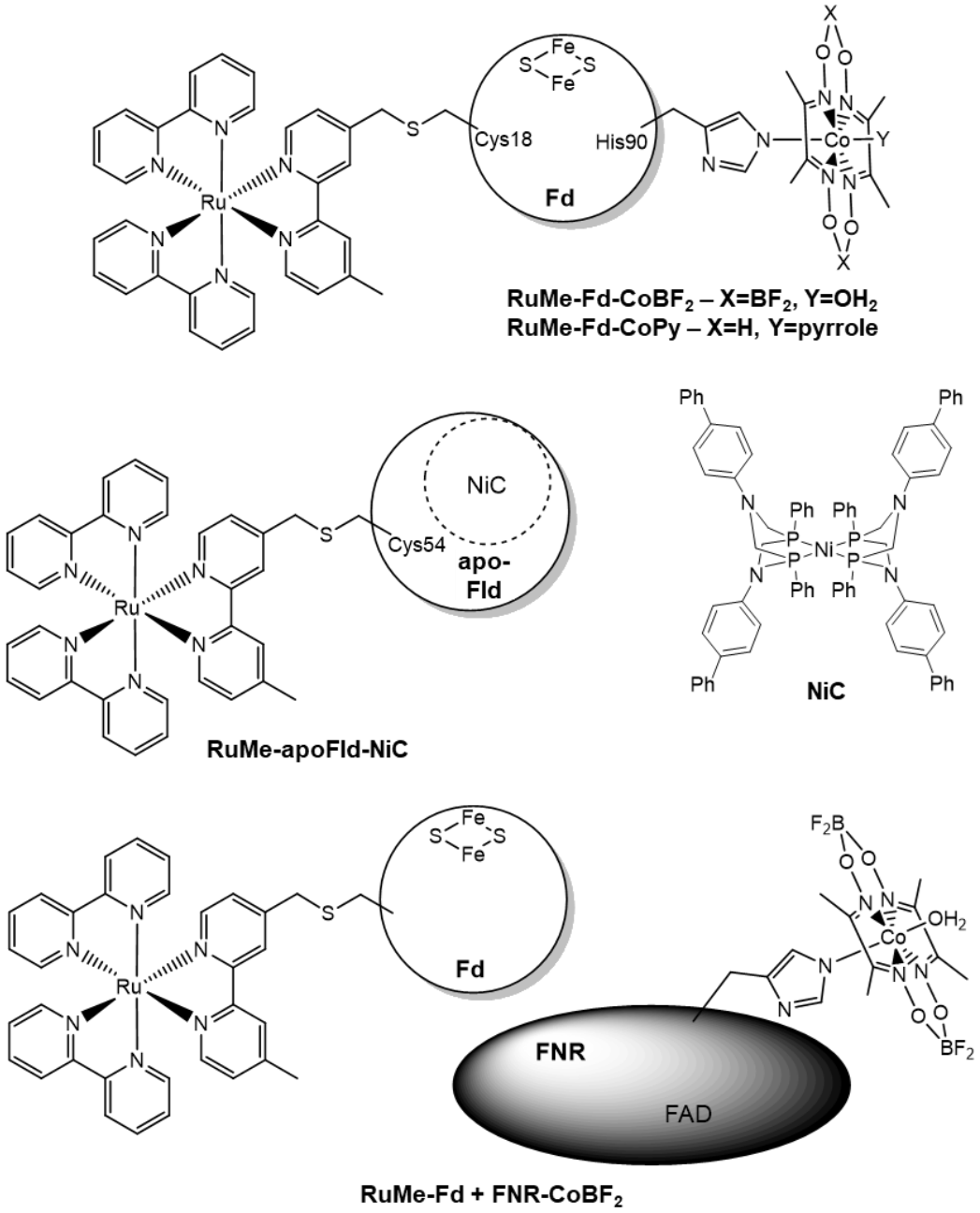

Figure 1.4.3 Biologically-supported artificial photosynthetic assemblies based on Fd (Top), apo-Fld (Middle) and a mixture of Fd and FNR (Bottom). Redox cofactors are shown where they are present, the FMN binding pocket of apo-Fld is shown as a dashed ring.[62–65] Charges have been excluded for simplicity

1.4.3 - Overview of artificial photosynthetic strategies

Interesting strategies have been used to link the functional components of artificial photosynthetic systems, from covalent attachment via the ligands of metal centres, to

electrostatic assembly on semiconductor surfaces, and to the use of specific amino acid residues in inert or redox-active protein scaffolds. In general, artificial photosynthetic assemblies are not able to match the efficiency of natural photosystems and their stability is poor leading to low TOFs and TONs. However, due to their overall structural simplicity (vs natural photosystems) detailed photochemical kinetic models have been obtained for some of these systems. This information helps to understand the parameters that affect the chemistry of the photosensitisers and catalysts and is valuable in the design of any photochemical setup. Evaluating these systems against Lubner's attributes of a photocatalytic module[22] we see that for the most part they do not measure up well.

1) Efficient charge separation

   Most of the systems described here use Ru-diimine based photosensitisers which have desirable photochemical properties including near unity formation of the first excited triplet state and long excited state lifetimes. This is advantageous for forming primary CSSs.

2) Long lived CSS

   Many of the systems discussed here do not have long-lived CSSs, the lack of extended electron relays in the structures prevent the distancing of the electron-hole pair and thus non-productive charge recombination is rapid.

3) Minimum energy expended to stabilise CSS

   The lack of extended electron relays in these systems means that minimal energy is wasted stabilising any CSSs. The typical hydrogen evolution catalysts used in these systems are based on cobaloxime and DuBois-type catalysts. The low overpotentials for proton reduction of these catalysts[49] means that incorporation of an electron relay into future systems would be feasible from a thermodynamic perspective.

4) Antenna system for maximal effective photon flux

   These systems generally do not have an antenna system in place. One could argue that the attachment of multiple units of RuP to a TiO_2 particle resembles an antenna however these photosensitisers would have identical absorption spectra and cover a limited portion of the incident solar spectrum.

5) Robust or self-repairing

   Artificial photosynthetic systems are typically limited in their ability to self-repair. Some cobaloxime based systems have been shown to regain activity upon addition of fresh dmg ligand[51] however damage to the photosensitiser portions of the system are usually irreparable. They also have relatively short lifetimes and are not, therefore, robust.

Artificial photosynthetic systems teach us about the features of a good photocatalytic system. They can be adapted in infinite ways to create bespoke systems and their relatively simple photochemistry can be studied to reveal useful kinetic data. On the whole, however, the systems discussed here are not effective photocatalysts for proton reduction. Balancing the kinetics of light absorption, charge separation, catalysis and charge trapping is exceptionally difficult in a small molecule. Whilst mediating materials can improve this situation by extending the CSS, creating a rival to natural photosystems would likely require a series of different mediators, each with carefully tuned reduction potentials. In the following section we will review work that has sought to couple the artificial with the natural to create biohybrid systems that have benefits of both fields.

1.5 - Biohybrid photosynthesis

Both synthetic materials, designed by humans, and biological constructs, perfected by billions of years of evolution, have potential to contribute to solving the impending energy and materials crises. Each branch has their own advantages and shortcomings (Table 1.5.1). In this section we will consider the efforts made to bridge the gap between the two areas, utilising components from each that compensate for the other's weaknesses.

Table 1.5.1 Advantages and disadvantages of natural and artificial catalysts and photosensitisers.

Natural photosensitisers		**Artificial photosensitisers**	
Advantages	**Disadvantages**	**Advantages**	**Disadvantages**
Near-perfect photocycle kinetics	Limited end product diversity	Diverse range of products	Imbalanced photocycle kinetics
Relatively wide spectral range	Large and complex systems	Well-defined photochemistry	Usually narrow spectral range
Clean electron source (H_2O)	Full function requires living cell	Infinitely adaptable	Reliant on SEDs
Uses earth abundant elements	Land/Water requirements	Compatible with modular designs	Often rare/toxic components
Enzymes		**Synthetic Catalysts**	
Advantages	**Disadvantages**	**Advantages**	**Disadvantages**
Composed of earth abundant elements	Costly protein purification	Some can be easy to prepare	Often rare/toxic components
Some operate in mild conditions	Many are degraded *in vitro*	Usually stable when not in use	Some require extreme conditions
Often have very high activity	Irreversible inhibition	Some flexibility in reactivity	Irreversible inhibition

As in the previous section, the majority of these technologies are focussed on photocatalytic hydrogen evolution though some other reactions will be considered. A biohybrid photosynthetic system, as defined here, must feature either a biological photosensitiser or a biological catalyst. Cases will also be examined where both components are biological but have been assembled in a non-physiological manner (Fig. 1.5.1).

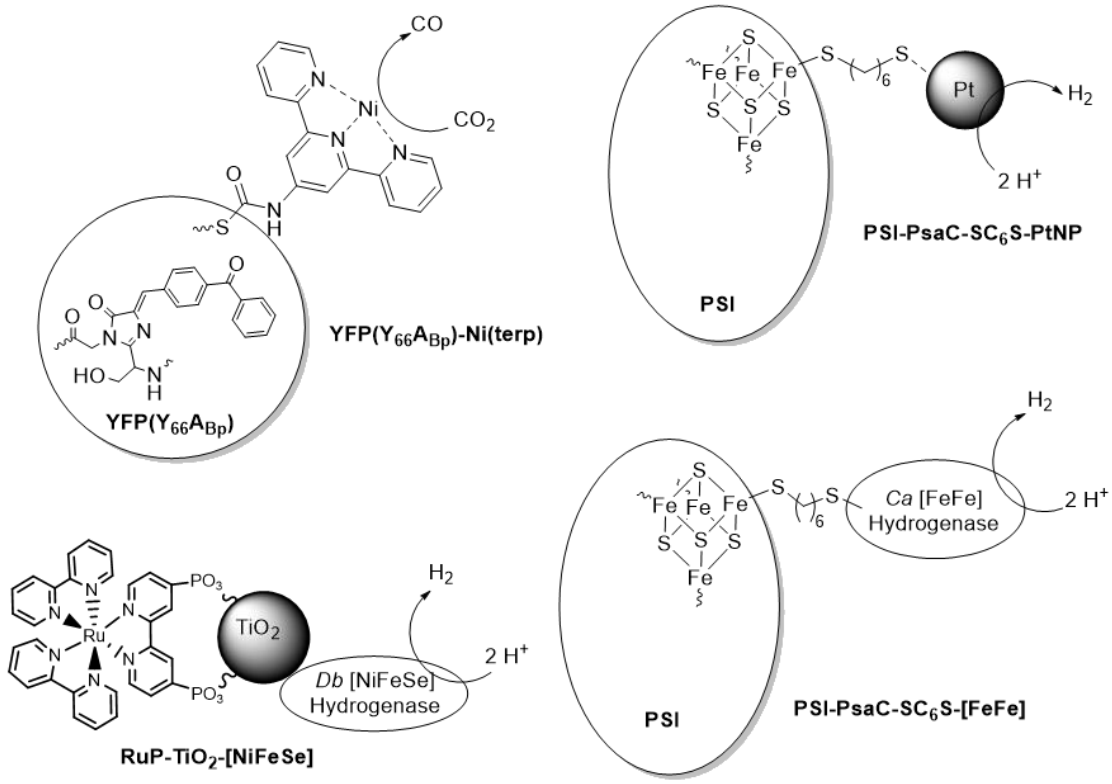

Figure 1.5.1 Examples of biohybrid photosynthetic systems. **Top Left)** Biological photosensitiser based on yellow fluorescent protein (YFP) linked to artificial nickel terpyridine catalyst by covalent attachment, YFP($Y_{66}A_{Bp}$) chromophore shown; **Top Right)** PSI photosensitiser linked to a platinum nanoparticle from the F_B cluster (shown) using a dithiol wire; **Bottom Left)** RuP-TiO_2 photosensitiser linked to the [NiFeSe] hydrogenase from *Desulfomicrobium baculatum* by electrostatic assembly; **Bottom Right)** PSI linked to the [FeFe] hydrogenase from *Clostridium acetobutylicum* from the F_B cluster (shown) using a dithiol wire. Electron sources are not shown. Charges have been excluded for simplicity.

1.5.1 - Biological photosensitisers + synthetic catalysts

Looking to biology we find what are probably the most efficient photosensitisers ever created: the LHCs and photosystems from photosynthetic membranes. As discussed previously these protein complexes are capable of absorbing large quantities of light and generating long-lived CSSs with quantum unity. Coupling of these CSSs to solar fuels synthesis is, however, not trivial. The acceptor side of both PSII and PSI have evolved to specifically pass electrons to native redox partner proteins which are, in turn designed to deliver electrons to specific enzymes such as FNR. Without careful system-design the natural pathways for electron flux tend to dominate *in vivo*, reducing rates of activity and

quantum yields for a desired product. Most studies to date have, therefore used purified proteins in an *in vitro* setting where they can be connected to appropriate catalysts. Some research groups have taken on the task of creating novel biological photosensitisers by adapting the well-studied chromophores related to green fluorescent protein (GFP).

1.5.1.1 - Photosynthetic photosystems + Pt nanoparticles

While water splitting is the ultimate goal for solar fuels synthesis, using PSII to achieve this is fraught with issues. PSII can only function when embedded in a thylakoid membrane which complicates its study and use. It is also prone to photoinhibition which cannot be repaired *in vitro*. PSI on the other hand, can be purified as a soluble photosensitiser, and well-established techniques have been developed for modification of many of its protein subunits and cofactors.

Utschig et al. demonstrated that preformed Pt nanoparticles with defined sizes and surface modifications could bind electrostatically to purified PSI.[66] The resulting biohybrids were good photocatalysts with TOF_{PSI} of 21000 h^{-1}. The nanoparticles were proposed to interact with PSI at the ferredoxin (Fd) binding pocket due to similar size (3 nm) and predominance of negative charges between the nanoparticles and Fd.

Numerous studies have since sought to gain finer control over Pt-nanoparticle positioning relative to PSI. Techniques have been developed to attach Pt-nanoparticles to specific cofactors of PSI, either the terminal F_B cluster[67–70] (Fig. 1.5.2 – Top & Middle) or though the A_{1A} quinone[71,72] (Fig. 1.5.2 - Bottom) with TOF_{PSI} of up to 278 h^{-1} being reported.[69] These results suggest that tethering the platinum nanoparticles in fact decreases the efficiency of the system. This could be due to poor kinetics of electron transfer to the nanoparticle and further research may allow these tethered systems to be improved.

Whilst these PSI-Pt nanoparticle systems have shown higher activities than seen previously for fully artificial systems, the use of noble-metals makes them prohibitive for large-scale applications. The heterogenous nature of the nanoparticle catalysts also makes detailed kinetic studies challenging. Use of molecular catalysts with earth-abundant metals is preferential. Such systems will now be considered.

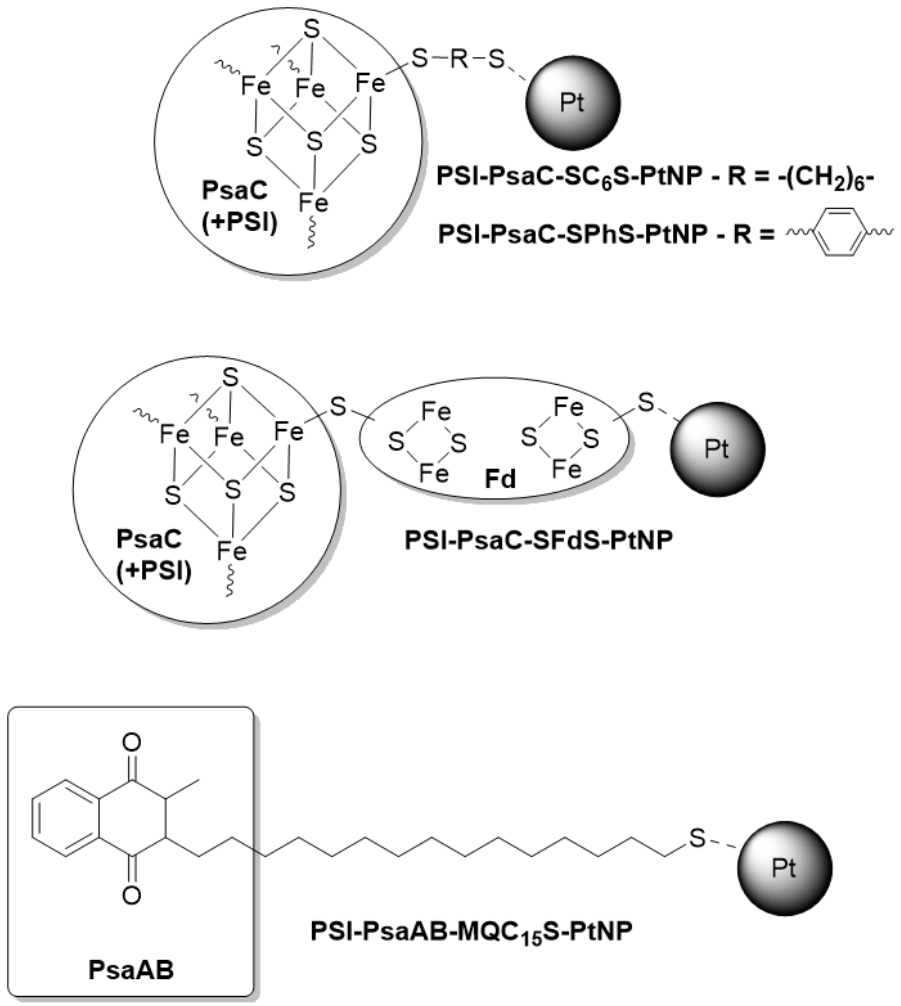

Figure 1.5.2 Strategies for directed covalent linkage of PSI and Pt nanoparticles. **Top)** Dithiol mediated attachment using the incomplete coordination sphere of F_B in $PsaC_{C13G,C33S}$[69]; **Middle)** *Clostridium pasteurianum* Fd ($S_{11}C$, $D_{40}C$, D_7S, $D_{36}S$) mediated attachment using the same principle[70]; **Bottom)** Alkylthiol-substituted naphthoquinone mediated attachment by replacement of the A_{1A} phylloquinone[72]

1.5.1.2 - Biological photosensitisers + molecular catalysts

A familiar set of catalysts have been studied in combination with photosynthetic machinery. Cobaloximes and DuBois-type nickel catalysts have been delivered to the reducing sites on PSI either by simple electrostatic interactions[73–75] or via interactions with native protein partners.[75] Other light-harvesting proteins have also been modified and converted into photocatalysts; proteins in the green fluorescent protein (GFP) family have been converted into more effective photosensitisers by expansion of the genetic code and linked to molecular catalysts for CO_2 reduction.[76–80]

Utschig et al. demonstrated that a cobaloxime could self-assemble with PSI to form a photocatalyst with H_2 evolution TOF_{PSI} of 10200 h^{-1}.[73] This construct degraded relatively quickly, after 90 minutes of irradiation the authors report that <10% of the original catalyst loading remained associated with PSI, highlighting one of the problems with using non-

covalently attached components. The DuBois-type catalyst NiC (see Fig. 1.4.3) was also found to self-assemble with purified PSI and H_2 and evolved with TOF_{PSI} of 2600 h^{-1} though with a longer lifetime than the analogous cobaloxime system.[75] This study also explored the interaction of PSI with the Fld-NiC hybrid discussed previously (Section 1.4.2, Fig. 1.4.3), with the aim of delivering NiC to the reducing end of PSI. This system had higher H_2 evolution rates than the free NiC system with TOF_{PSI} of 4500 h^{-1}, though with a similar lifetime of 3-4 h.[75]

Whilst it is an excellent photosensitiser, PSI from plants is a large protein complex formed of 13 protein subunits (PsaA-N) and binds over 120 cofactors of 4 different types.[81] Expression of the entire PSI complex in commonly used industrial organisms such as *E.coli* is not feasible and this restricts its use in large-scale operations. The far simpler biological chromophore Green fluorescent protein (GFP) from *Aequoria victoria* has been well established as an *in vivo* marker in organisms from across the tree of life.[82] It contains only 238 amino acids (versus the ≈2500 in PSI) and requires no cofactors, forming a chromophore intrinsically from its S_{65}-Y_{66}-G_{67} tripeptide.[83]

Site directed mutagenesis (SDM) has been used to modify the GFP chromophore and its surrounding environment, producing a wide library of fluorescent markers with absorption and emission profiles spanning the visible spectrum.[84] The development of unnatural amino acid (uAA) incorporation techniques[85–87] has expanded the photochemical possibilities of GFP-like proteins making them interesting candidates for biological photosensitisers.

The uAA 4-fluoro-3-nitrophenylalanine (F_{FNO2}) was incorporated into GFP and showed effective quenching of the GFP excited state with sub-ns electron transfer rates (k = 9×10^{10} s^{-1}). F_{FNO2} has a reduction potential of -310 mV meaning this construct could theoretically be used as a photosensitiser for hydrogen production if coupled with an appropriate catalyst.[79] uAAs have also been incorporated into the chromophore of GFP and related proteins to change the photochemistry at the core of the photosensitiser.[78] In a yellow fluorescent protein (YFP) variant, mutation of Y_{66} to benzophenone-alanine (A_{Bp}) produced a chromophore (Fig. 1.5.3) that, upon excitation, underwent ISC to a triplet state. This state could be reductively quenched by SEDs, producing a benzophenone radical with a lifetime >1 s and potential of <-1.14 V (vs SHE).[80]

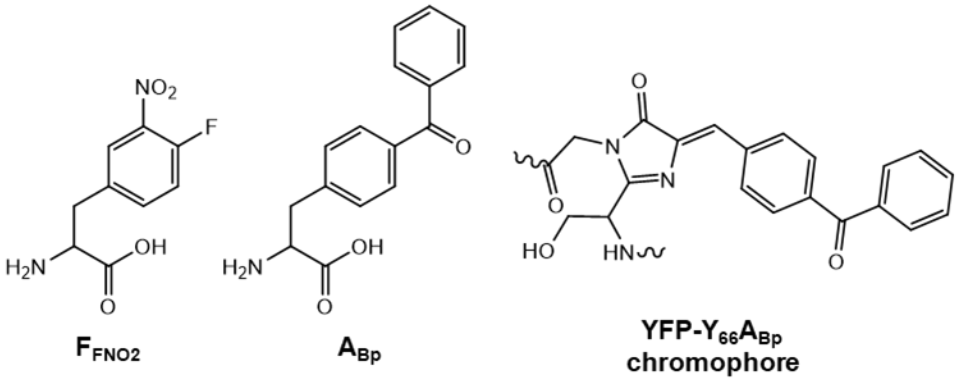

Figure 1.5.3 uAAs used to alter photochemistry of GFP and YFP.

Coupling of a Nickel terpyridine catalyst via a further mutation ($E_{95}C$), and introduction of tyrosines as proton relays ($V_{93}Y$, $T_{97}Y$), produced a photocatalytic system (Fig. 1.5.1 – Top Left) capable of light-induced reduction of CO_2 to CO with TOF $\approx$ 10 h^{-1} and a TON_{12h} of 75.[88] Adaptation of this system towards hydrogen production would be interesting to investigate. Molecular hydrogen catalysts could be covalently attached to the modified YFP or this protein could be linked to a hydrogenase enzyme, either by protein fusion or by an *in vitro* technique.

1.5.2 - Biological photosensitisers + non-native biological catalysts

The combination of biological photosensitisers and biological catalysts in non-natural ways presents the opportunity to couple the excellent photocycle kinetics of PSI and the high activity of hydrogenase enzymes. There are three types of strategy that have been employed to bring these proteins together: protein fusion, tethering via Fe-S cluster, and tethering via quinone sites. These will now be discussed further.

Protein fusion is achieved by combining the genes for two proteins such that they are transcribed and translated as a single polypeptide. Protein fusion has the advantage that the system should form *in vivo* without external intervention, though ensuring correct protein folding and cofactor insertion of the component proteins can be challenging. Hydrogenases have been fused to either the PsaE subunit of PSI[89] which is positioned near the terminal Fe-S clusters, or to Fd[90] which docks at this site to accept the electrons from PSI. The [NiFe] hydrogenase from *Ralstonia eutropha* was fused to the PsaE subunit from *Thermosynechococcus elongatus*. Purification from *R. eutropha* produced a PSI-Hydrogenase biohybrid with relatively poor hydrogen evolution activity (TOF_{chl} of 0.52 h^{-1}).[89] Fusion of the [FeFe] hydrogenase and Fd from *Chlamydomonas reinhardtii* produced a construct capable of producing hydrogen using either purified PSI or thylakoid membranes as photosensitisers with TOF_{chl} of up to 40 h^{-1} being reported.[90]

An alternative strategy is to tether a hydrogenase to a PSI cofactor. Techniques have been developed for preparing PSI with readily displaceable plastoquinones at the A_{1A} site.[71,72] Replacement of the plastoquinone with an alkyl-thiol-quinone allows for tethering of PSI to a hydrogenase via the open coordination site in *Clostridium acetobutylicum* [FeFe] hydrogenase$_{C97G}$.[91] The resulting biohybrid evolved hydrogen with a TOF_{chl} of 45 h^{-1}, only moderately improved over the fused proteins discussed above. This likely stems from the same issues that affected the A_{1A} tethered PSI-Pt-nanoparticle biohybrids discussed previously,[72] that electron transfer in PSI is geared towards reduction of the terminal Fe-S cluster. Attempts to extract electrons from earlier points in the ETC are typically unsuccessful.

The terminal Fe-S cluster of PSI has also been used as a tethering point. Using a dithiol wire, coordinatively-unsaturated Fe-S clusters of PSI and *Ca*[FeFe] hydrogenase can be brought together with a tunable distance.[92] The natural electron donor to PSI (cyt_{c6}) was then cross-linked to the acceptor side of PSI. The resulting biohybrid photocatalytic system (Fig. 1.5.4) had incredible activity and stability, able to evolve hydrogen with a TOF_{PSI} of 378000 h^{-1}.

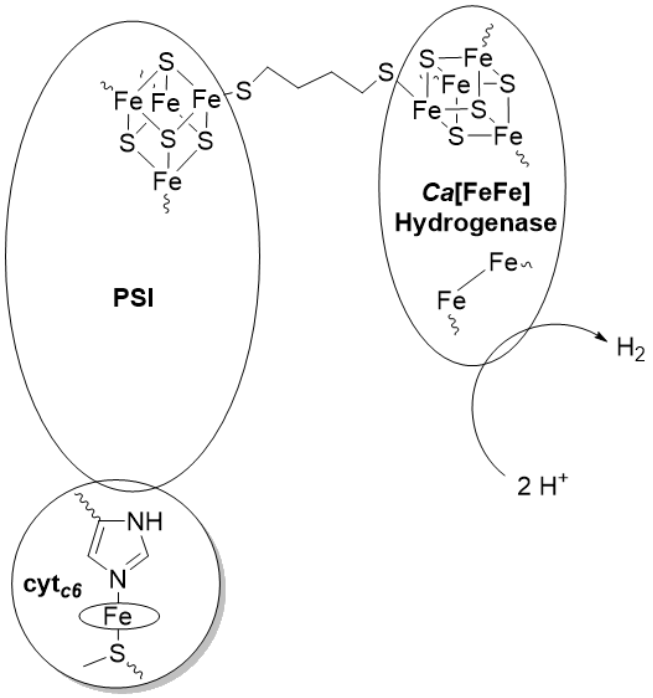

Figure 1.5.4 Schematic of the biohybrid formed from PSI (F_B cluster shown) and *Ca*[FeFe] hydrogenase (First Fe-S cluster and active site shown) with cyt_{c6} (Heme shown) cross-linked to the donor end of PSI.[93] Charges have been excluded for simplicity.

The construct seemed to suffer very minimal photodamage, being capable of producing hydrogen for 4h under irradiation with no loss in activity until the SED (ascorbate) ran

out. Hydrogen evolution could be restored by addition of fresh ascorbate and the construct was stable for at least 100 days stored anaerobically at room temperature.[93]

This system possesses the highest activity of any biohybrid photosynthetic system currently reported. It is, however, not without flaws these being that the system: cannot yet be assembled *in vivo*; is reliant on an exogenous dithiol wire to link the components; and is oxygen sensitive due to the *Ca*[FeFe] hydrogenase. Techniques are available to resolve some of these issues: the recently published Fd from *Clostridium pasteurianum* which was used previously to join PSI and a Pt nanoparticle (Fig. 1.5.2 - Middle)[70] could be used to replace the dithiol wire used here[93] creating a system that could be assembled by cyanobacteria; the use of a more oxygen tolerant hydrogenase such as the [NiFeSe] hydrogenase used by the Reisner group[94,95] may prove more robust which will be essential for integrating hydrogenase enzymes with water splitting systems.

Whilst the excellent kinetics of PSI make it an attractive choice for biohybrid systems, its large size and complexity restrict its use somewhat. Artificial photosensitisers, whilst possessing simpler and less efficient photochemistry, are more adaptable to the requirements of a particular system. Previously, systems composed of artificial photosensitisers and molecular catalysts have been discussed (Section 1.4); these typically suffered efficiency issues due to imbalanced kinetics and stability issues due to catalyst degradation. Interfacing artificial photosensitisers with more robust biological catalysts may, therefore prove promising. Such systems are discussed in the following section.

1.5.3 - Artificial photosensitisers + biological catalysts

Artificial photosensitisers offer defined, controllable, and comparatively simplified photochemistry over their biological counterparts. This, however, tends to come at the cost of overall photochemical efficiency due to limited spectral ranges and shorter CSS lifetimes. Nevertheless, biohybrid systems formed from enzymes and photosensitisers such as Ru-diimine complexes and semiconductor nanoparticles have been used to some success to drive solar fuels synthesis and other reductive transformations. Artificial photosensitisers have also been used to drive these reactions *in vivo* using whole, living cells; this strategy represents a move towards more sustainable self-replicating systems. As seen in the previous section, enzymes offer high activity under mild reaction conditions using earth-abundant elements, making them useful for biohybrid systems

1.5.3.1 - Direct attachment of ruthenium photosensitisers to enzymes

The simplest forms of photosensitiser-enzyme hybrids are those with a covalent link between the two components. Ru-diimine complexes are the most common class of photosensitiser to have been successfully integrated with enzymes for productive photocatalysis to date. Several chemical techniques are available for covalent bonding of Ru-diimine photosensitisers and proteins, many utilise cysteine residues due to their unique chemical properties and relative rarity in protein structures. Ru-diimine photosensitisers have been used to drive photocatalysis by nitrogenases, hydrogenases and cytochromes P450,[96–99] however only the first two will be discussed.

The nitrogenase enzyme catalyses the ATP-dependant 8-electron reduction of dinitrogen to ammonia. This reaction is vital for supporting global food chains and nitrogen-based fertilisers are widely used to supplement the natural supply of organic nitrogen in soils. The industrial source of ammonia for these fertilisers is the Haber-Bosch process which, in addition to being energy intensive, typically uses hydrogen derived from fossil fuels. Ammonia synthesis is estimated to account for 1% of global energy usage.[100] Nitrogenases on the other hand operate with high efficiency under ambient conditions, with the energy cost being supplied by ATP.[101,102]

Covalent attachment of a Ru-diimine photosensitiser to nitrogenase from *Azotobacter vinelandii* was achieved through site-directed introduction of cysteine residues and subsequent reaction with $Ru(bpy)_2$(5-iodoacetamido-1,10-phenanthroline)$^{2+}$ (RuA-I – Fig. 1.5.5). Attachment of RuA to L_{158}C-Nitrogenase produced a biohybrid capable of proton reduction to hydrogen, acetylene reduction to ethylene and reduction of cyanide to methane and ammonia although poor TOFs were obtained and the systems degraded rapidly.[103,104] Electron transfer in nitrogenases is thought to be closely coupled to ATP hydrolysis.[105] The systems described here are ATP-independent which may account for the slow electron supply to the active site.

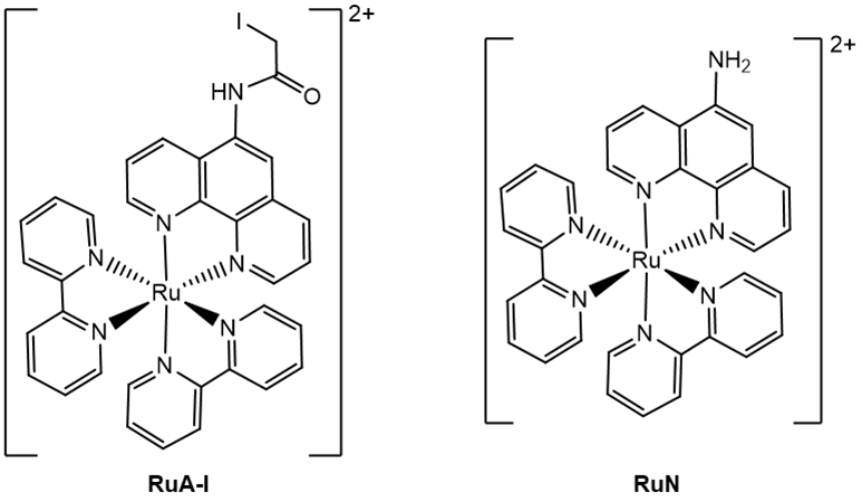

Figure 1.5.5 Structures of RuA and RuN.

To date only one study has been carried out on a directly photosensitised hydrogenase enzyme. $Ru(bpy)_2$(5-amino-1,10-phenanthroline)$^{2+}$ (RuN – Figure 1.5.5) was covalently attached to carboxylate residues on the surface of a [NiFe] hydrogenase from *Thiocapsa roseopersicina* using a coupling agent. Irradiation of this biohybrid in the presence of EDTA as a SED did not produce hydrogen. Given the non-specific placement of the RuN photosensitisers this is not overly surprising.

Addition of methyl viologen (MV) allowed the biohybrid construct to evolve hydrogen, presumably by mediating electron transfer from the RuN to the enzyme cofactors. This has been observed to occur in systems where Ru-diimine photosensitisers and hydrogenases are combined in solution.[106] Per-protein activity rates in the biohybrid system (121 nmol H_2 (mg hydrogenase)$^{-1}$ min^{-1}) were lower than for free enzyme with an excess of RuN (224 nmol H_2 (mg hydrogenase)$^{-1}$ min^{-1}) however the activity per-RuN was over an order of magnitude greater for the biohybrid (4481 vs 112 nmol H_2 (μM RuN)$^{-1}$ min^{-1}) possibly due to local concentration effects where the reduced MV ($MV^{\bullet+}$) concentration was greater around the hydrogenase than in bulk solution.[107]

These biohybrid systems have activities far below their maximum enzymatic rates which arises from non-optimised electron transfer kinetics between photosensitiser and active site. Imbalanced kinetics are likely also a contributing factor to degradation of the constructs as bottlenecks can cause the build-up of reactive intermediates which may degrade the protein structure or metal coordination sphere.

Attachment of photosensitisers to enzymes shows the same design flaws as the photosensitiser-catalyst dyads discussed in Section 1.4 and some of the same solutions have been used to try and optimise these systems. Semiconducting materials, as discussed previously in Section 1.4.2, can serve as an effective mediator between photosensitiser and enzyme, extending the CSS and acting as an electron reservoir.

1.5.3.2 - Electrostatic interactions of nanoparticles and enzymes

Nanoparticles have been explored as electrostatic mediators for assembly of synthetic photosensitisers and enzymes. Semiconducting nanoparticles such as TiO_2 have been explored due to their favourable electrical properties but also because some proteins have a natural affinity for the charged TiO_2 surface and will readily self-assemble. Photosensitiser nanoparticles such as cadmium chalcogenides (CdS, CdSe, CdTe) or carbon quantum dots (CQDs) have also been used to drive reductive chemistry, in these cases the nanoparticle acts as both the photosensitiser and a scaffold for photosystem assembly. [58–61,95]

The O_2 tolerant, titaniaphilic [NiFeSe] hydrogenase from *Desulfomicrobium baculatum* ([NiFeSe]),[108–111] has been interfaced with RuP-TiO_2 to form a RuP-TiO_2-[NiFeSe] biohybrid assembly (Fig. 1.5.6 - Middle).[95] This construct was capable of evolving hydrogen using light, with an initial $TOF_{[NiFeSe]}$ of up to 180000 h^{-1}, superior to any synthetic catalyst on a similar RuP-TiO_2 surface. The construct also had improved stability over its artificial counterparts, with minimal degradation after 4h and moderate O_2 tolerance.[94]

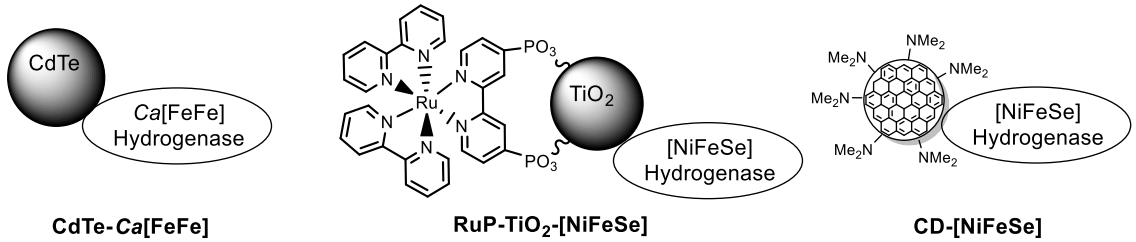

Figure 1.5.6 Schematics of biohybrid systems formed by electrostatic assembly of nanoparticle photosensitisers and hydrogenase enzymes

Cadmium chalcogenides are semiconductors with band gaps ranging from 2.3 eV for CdS to 1.4 eV for CdTe[112] giving them absorbances in the visible region of the electromagnetic spectrum. They therefore do not require sensitisation with a dye such as RuP. The CBs of Cadmium chalcogenides are equivalent or more negative than TiO_2 meaning they are thermodynamically capable of supporting solar fuels synthesis.

Water soluble CdTe nanoparticles were mixed *Ca*[FeFe] to form a CdTe-*Ca*[FeFe] biohybrid system (Fig. 1.5.6 – Left). The hydrogenase was proposed to interact with the nanoparticle via the positive patch of amino acids on the protein surface. This area is the docking site for Fd, the natural redox partner of the enzyme and thus the native site of electron uptake. When irradiated, this system evolved hydrogen with a $TOF_{Ca[FeFe]}$ of 90000 h^{-1} with a quantum yield of 1.8% under atmospheric light conditions. These constructs, however, suffered from poor stability, with hydrogen evolution typically ceasing after 30 minutes of irradiation.[113]

Great improvements were subsequently made when the CdTe nanoparticles were replaced by CdS nanorods which are better visible light absorbers, more photostable and have higher surface area. CdS_{NR}-*Ca*[FeFe] assemblies were found to be highly efficient hydrogen evolvers and could achieve $TOF_{Ca[FeFe]}$ of 3.4×10^6 h^{-1} under high light-intensity conditions which were still not saturating. This is an unprecedented rate for a system using an artificial photosensitiser. The assembly had a longer lifetime than its predecessor but still ceased activity after 5-6 hours with a final TON_{4h} of 1×10^6. This was attributed to oxidation of the CdS capping ligands.[114–117]

Carbon quantum dots (CQDs) represent a more recent advance in photosensitiser technology and are becoming more widely used due to their redox properties, low environmental impact and tunable size and surface chemistry.[118] Hutton et al.[119] prepared CQDs by thermal decomposition of citric acid, producing nanoparticles capped with carboxylate groups. These could not form a productive assembly with the [NiFeSe] hydrogenase discussed previously, likely due to mismatched surface charges. Modification of the CQD surface chemistry to give the CQDs a positive surface charge at pH 6 (confirmed by measurement of the particles' zeta-potential) enabled the formation of CQD-[NiFeSe] assemblies (Fig. 1.5.6 – Right) which evolved hydrogen with a $TOF_{[NiFeSe]}$ of 3900 h^{-1} and a TON_{48h} of 52000 under light-limiting conditions. Loss of activity was proposed to be due to degradation of the enzyme.

These systems include some of the highest efficiency photocatalytic systems currently reported. Proving that artificial photosensitisers can compete with natural photosystems in the right circumstances. The CdS nanorod-hydrogenase assembly, in particular, has outstanding rates of activity though is let down by its surface stability.[114,117] Degradation of photosensitisers and catalysts is a problem for creating photocatalytic systems with longevity. A target for some researchers is to have systems such as those described above operating in living cells which would be able to repair and replace damaged components. In the next section some studies on interfacing nanoparticle photosensitisers and living cells will be explored.

1.5.3.3 - Nanoparticle photosensitisers + whole-cell catalysts

Living cells, bacteria in particular, are attractive platforms for solar fuels production: they self-assemble, self-repair and reproduce under physiologically relevant conditions; they produce highly active catalysts (enzymes) from earth abundant elements; and many can be tuned with some precision through genetic manipulation. Many bacteria are also able to synthesise photosensitiser nanoparticles themselves as part of a detoxification system. Upon exposure to low concentrations of cysteine and toxic cadmium salts, some bacteria produce CdS nanoparticles to precipitate and thus remediate the cadmium.[120] Biosynthesis of photosensitiser nanoparticles has been used to create biohybrid constructs capable of light-driven redox chemistry using a variety of bacteria and other industrially relevant microbes. Quantification of activity is difficult in such systems as cell numbers or masses in a reaction chamber are often not known and vary widely between research groups. These studies will therefore be evaluated more qualitatively.

The first example of nanoparticle-bacteria assembly this used the acetogenic bacterium *Moorella thermoacetica* (*M. thermoacetica*) which is naturally capable of reducing CO_2

to acetic acid via the Wood-Ljungdahl pathway (WLP).[121] In this study cysteine was used both as a sulfide source to create CdS, using cysteine desulfydrase proteins, and also as a biocompatible SED (Fig. 1.5.7 – Left).[122] This treatment allowed *M. thermoacetica* to effectively become an autotroph, producing biomass in the absence of any other respiratory metabolite. Cells without CdS nanoparticles lost all viability after 1 day of irradiation, whereas cells with the nanoparticles retained 100% viability after 3 days of irradiation though viability dropped after that point. Transfer of electrons from cysteine to acetic acid was found to have a yield of over 90%, and the construct had a quantum yield (photons to electrons) of 52% under low light intensity conditions (8.3×10^{-11} Moles of photons cm^{-2} s^{-1}). This biohybrid could be used to create a system capable of both producing valuable products and self-replicating through biomass accumulation, though long-term cell viability may need to be improved.

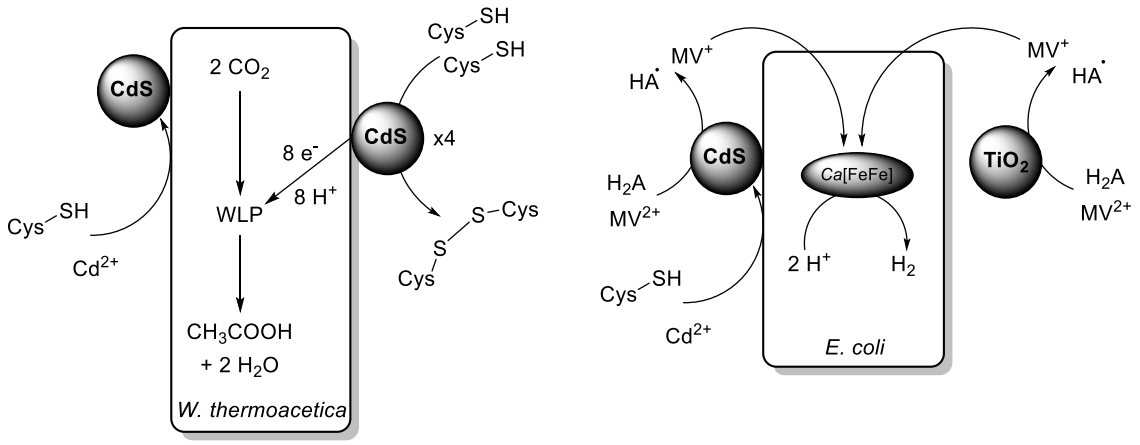

Figure 1.5.7 Examples of Whole-cell biohybrid photosynthesis with semiconductor-based photosensitisers. **Left)** powering the WLP in *M. thermoacetica* using CdS nanoparticles biosynthesised from cysteine and $Cd(NO_3)_2$[122]; **Right)** Engineered *E. coli* expressing the *Ca*[FeFe] hydrogenase is supplied with electrons from TiO_2[123] or biosynthesised CdS nanoparticles via MV, ascorbic acid (H_2A) is used as the SED.[124]

This system was further improved by addition of TiO_2 nanoparticles doped with manganese phthalocyanine as a water oxidation photocatalyst. This enabled the coupling of water oxidation to cystine reduction, regenerating the SED cysteine. The addition of these nanoparticles to the *M. thermoacetica*-CdS system described above led to enhanced photoproduction of acetic acid with a photochemical architecture reminiscent of the Z-scheme (Fig. 1.3.1). Whilst this system represents a long-term goal for artificial photosynthesis, CO_2 reduction coupled to water oxidation, the production of O_2 in this system caused a number of issues including spontaneous oxidation of cysteine back to cystine, oxidative damage to the CdS nanoparticle, and possibly oxygen induced cell death of the strictly anaerobic *M. thermoacetica*.[125]

This work has inspired the creation of numerous photocatalytic systems using different bacteria and different photosensitiser nanoparticles, some biosynthesised and others added exogenously. CO_2 fixation via the WLP has been driven in *M. thermoacetica* by preformed nanoclusters of gold and glutathione[126] and by organic semiconductors adhered to the cell membrane.[127]

More industrially-relevant bacteria have also been photosensitised with semiconductor nanoparticles. *E. coli* expressing the [FeFe] hydrogenase from *C. acetobutylicum* has been interfaced with TiO_2 nanoparticles[123] or, alternatively, was able to biosynthesise CdS nanoparticles (Fig. 1.5.7 – Right).[124] These constructs were found to be capable of light-driven hydrogen evolution, however activity was largely dependent on the presence of the membrane permeable mediator MV.[123,124] MV has been used as a transmembrane redox mediator for numerous purposes, however evidence suggests that cell viability decreases rapidly in the presence of reduced MV.[128] Photosensitiser-semiconductors have also been used with the photosynthetic bacteria *Rhodopseudomonas palustris* to enhance biomass accumulation[129] and with a strain of *Saccharomyces cerevisiae* to drive production of a valuable precursor molecule.[130]

Whole-cell photocatalysis with semiconductor nanoparticles represents an exciting new frontier in synthetic biology and solar fuels synthesis. Most of the nanoparticles described here are derived from toxic and costly elements, however the emerging field of CQDs may solve some of the problems associated with these materials. One of the key achievements is that the photosensitiser can be outside of the cell and still drive internal chemistry, though the mechanism for transmembrane electron transfer in these systems is not known. One of the inspirations for the work presented in this thesis is to apply this concept to organisms with dedicated transmembrane electron conduits which may provide significant improvements.

1.5.4 - Overview of Biohybrid photosynthetic systems

Artificial photosensitisers are capable of supporting reductive chemistry using enzymatic catalysts both *in vitro* and *in vivo*. Evaluating the constructs against Lubner's attributes of a photocatalytic module[22] we see some areas where these systems excel but in others they suffer the same drawbacks as the fully artificial systems.

1) Efficient generation of primary CSS

   All the photosensitisers discussed here, both natural and artificial, generate primary CSS with good efficiency. They absorb light in the visible region which

makes them good choices for practical photochemistry though some have narrow spectral coverage.

2) Long lived CSS

   Achieving CSSs of comparable length to natural photosystems (>50ms) is a challenge. With the exception of some special cases, the artificial systems described above do not possess CSSs on this timescale, and instead rely on charge trapping by SEDs to push electrons through the system. Charge recombination is likely a significant factor in the low quantum yields observed for these systems. Systems that use PSI have an advantage in this area.

3) Minimum energy wasted stabilising a CSS

   Most of the systems containing artificial photosensitisers lack extended ETCs and therefore the vast majority energy harvested by the dye or semiconductor is available for work. Though some energy is used to extend the CSS in natural photosystems (Fig. 1.3.1) there is typically more than enough to drive reactions of interest (Table 1.1.1).

4) An antenna like system of energy harvesters should be established

   The LHCs of natural photosystems act to absorb light and funnel it to the reaction centres, a comparable system using artificial photosensitisers has not yet been coupled to a solar fuels catalyst. RuP-TiO_2 could be considered an antenna-like system as the multiple RuP units funnel electrons into the CB of TiO_2. Such a system, however, may quickly become light-saturated due to the identical absorption spectrum of all RuP units. An effective antenna system should incorporate subunits that absorb across the visible spectrum.

5) Robust or self-repairing system

   Most of the *in vitro* systems described above have lifetimes of a few hours at most though some, particularly those featuring natural photosystems, were observed to have excellent activity over much longer time frames.[93] Activity loss was typically attributed to photosensitiser decay, enzyme inhibition/damage or degradation of the photosensitiser-enzyme interface. The *in vivo* whole cell systems have longer lifetimes, on the order of days, however even these succumb to photoinduced damage eventually. Mismatched electron transfer kinetics is the likely culprit for the majority of the damage. It is clear from studies of natural photosynthesis that bottlenecks in photocatalytic process can lead to significant problems therefore efficient electron throughput will be a key design feature of any effective biohybrid photocatalytic construct.

Biohybrid photosynthetic strategies have shown promise to revolutionise the field of solar fuels synthesis. The careful and considered integration of highly efficient natural photosensitisers and catalysts with the flexible, modular, defined nature of their artificial

counterparts has presented many opportunities for development. Of particular interest is the integration of artificial photosensitisers with living cells which hold great promise for creating self-replicating/self-repairing systems.

1.6 - Outline of this thesis

In the previous sections, examples of biohybrid photosynthetic systems have been discussed. In these systems, biological and artifical components are interfaced, making use of the benefits of both and covering for weaknesses (Table 1.5.1). Of particular interest is the finding that when coupled to hydrogenases, artificial photosensitiser nanoparticles (Section 1.5.3.2) can come close to matching the yields obtained by analogous PSI-based systems (Section 1.5.2). Natural photosystems are challenging to interface with non-native redox partners in a whole-cell context. Artificial photosensitisers have been demonstrated to interact with cells from a variety of species, and some can even be biosynthesised *in vivo* (Section 1.5.3.3). Electrons can be generated extracellularly by nanoparticles on the cell surface however it is not yet clear how these electrons access the cell interior where the enzyme catalysts are situated.

An ideal bacterial species for photocatalysis would have a well-characterised mechanism for electron transfer across their outer membrane. Many such species have been discovered and are generally termed “electroactive bacteria” with *Shewanella oneidensis* MR-1 (MR-1) having been studied in detail. MR-1 uses a protein complex named MtrCAB to transport respiratory electrons across the outer membrane (Fig. 1.6.1 - Top). This complex is also able to transfer electrons in the reverse direction which could be used to drive redox chemistry by the cell’s enzymes. Using MtrCAB to couple an extracellular photosensitiser to the catalytic machinery of MR-1 (Fig. 1.6.1 - Middle) is one of the long-term goals of our research group. This thesis will present studies that provide proof-of-principle for the development of such systems by using the MtrCAB complex to enable light-driven transmembrane electron transfer to an enzyme encapsulated in a liposome (Fig. 1.6.1 - Bottom). This liposome is an example of a nanoreactor, a compartmentalised chemical system on a nanoscale.

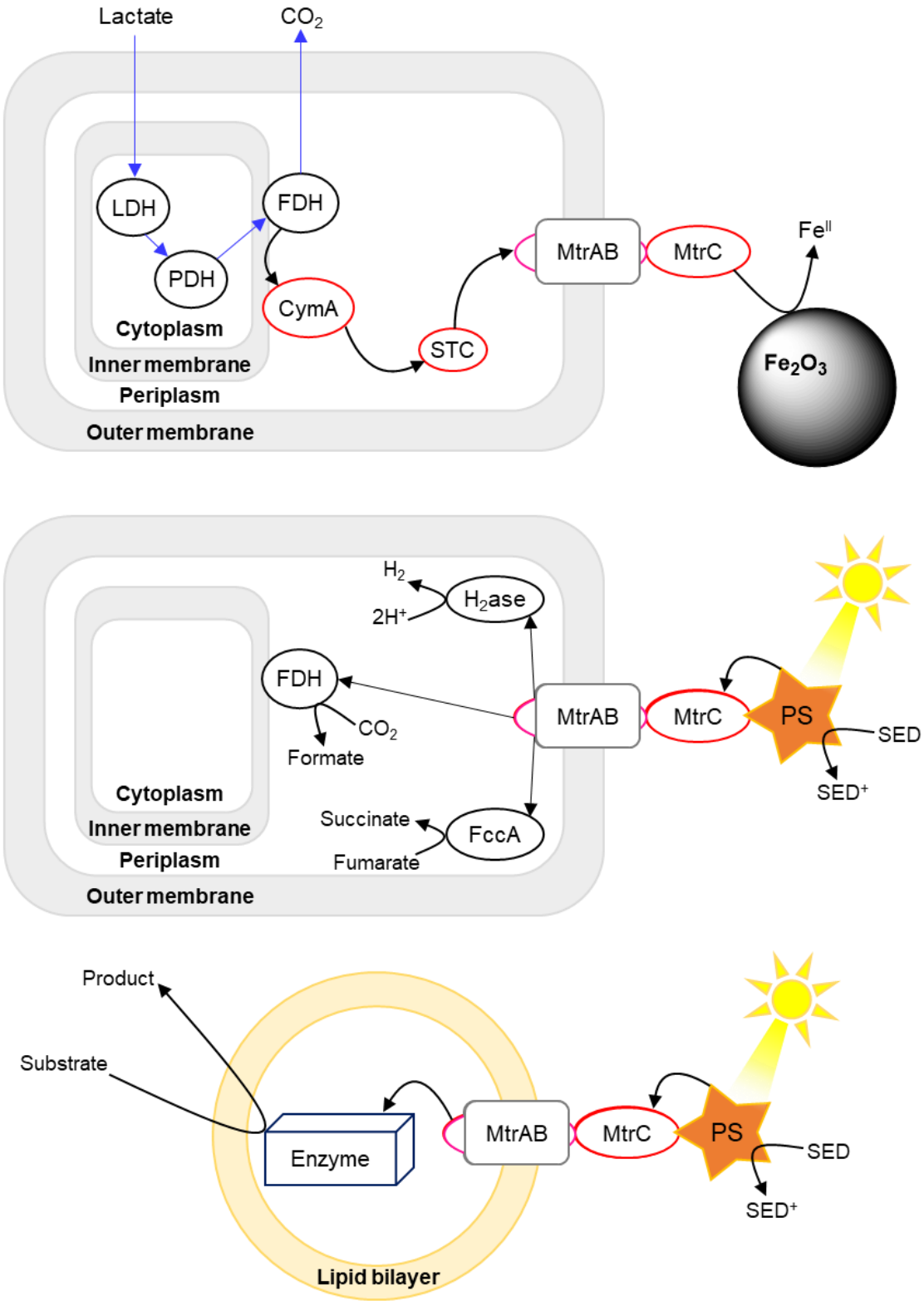

Figure 1.6.1 Top) Role of MtrCAB in extracellular reduction of iron oxides by MR-1 using electrons derived from oxidation of lactate; proteins involved are Lactate dehydrogenase (LDH), pyruvate dehydrogenase (PDH), formate dehydrogenase (FDH), CymA, small tetraheme cytochrome (STC) and the MtrCAB complex; electron flow shown as black arrows, lactate metabolism shown as blue arrows. **Middle)** Proposed system for whole-cell photocatalysis by MR-1 using an extracellular photosensitiser (PS) attached to MtrCAB. Intracellular redox chemistry includes hydrogen production by hydrogenases (H_2ase), fumarate reduction by fumarate dehydrogenase (FccA), and CO_2 reduction by FDH.[128] **Bottom)** Simplified schematic for a proof-of-principle nanoreactor using photosensitised MtrCAB to drive transmembrane electron transfer to an encapsulated redox enzyme.

The MtrCAB complex contains three proteins which form a chain of *c*-type hemes that crosses the outer membrane. MtrB and MtrA form a porin-cytochrome complex that imbeds in the membrane. MtrC is exported from MR-1 and binds to MtrAB on the cell surface. MtrC is the terminus of a chain of redox centres leading to the cell's enzymes; it therefore presents a target for photosensitisation. Previous work has established that the photosensitiser RuMe-Br (see Sections 1.4.2 & 2.3.1) can form a covalent bond to introduced cysteine residues in STC[131,132] and MtrC (J. van Wonderen et al. - in preparation) to produce RuMe-MtrC. In Chapter 3 of this work, the photoreduction of RuMe-MtrC using EDTA as a SED is explored, and a photochemical kinetic model for this process is presented. It will be demonstrated that MtrC acts as an electron reservoir for photogenerated electrons which enables multi-electron redox chemistry.

At present, RuMe-MtrC can only be produced from purified MtrC. MtrCAB complexes cannot yet be photosensitised *in vivo* or *in vitro*. The assembly of RuMe-MtrC with MtrAB is therefore of vital importance to producing a photosensitised transmembrane electron conduit. The ability of MtrC to form a complex with MtrAB that structurally and, more importantly, functionally resembles the WT MtrCAB complex will be evaluated in Chapter 4 using a number of different biophysical techniques. The photoreduction of RuMe-MtrCAB will also be investigated.

Subsequent chapters in this thesis consider assembly of MtrCAB within liposomes that act as light-driven nanoreactors using external photosensitisers and encapsulated redox enzymes. The enzyme selected for encapsulation is nitrous oxide reductase (NosZ) from *Paracoccus denitrificans*. This enzyme catalyses the 2-electron reduction of nitrous oxide (N_2O) to dinitrogen which, in nature, terminates the denitrification pathway. This enzyme was selected for a number of reasons: firstly both N_2O and N_2 are gases which, when dissolved in aqueous solution, can freely diffuse through biological membranes minimising the need for additional importers and exporters in the system; secondly, N_2O is a potent greenhouse gas and ozone depletor which has rising atmospheric concentrations[133]; thirdly, a procedure for purifying NosZ using a Strep-II has been developed by collaborators at UEA which allows for simplified preparation of pure enzyme. Chapter 5 will discuss the activity of this enzyme and the different redox partners that can be used to supply it with electrons. These will be considered with a view to effectively encapsulating NosZ and a redox partner in liposomes with MtrCAB incorporated in the liposome membrane.

In Chapter 6, results describing the formation and operation of nanoreactors formed from RuMe-MtrCAB, NosZ and redox partners will be presented. It will be demonstrated that the RuMe-MtrCAB complex, produced by photosensitisation of MtrC and reconstitution with MtrAB, is able to transport photochemically generated electrons across a lipid

bilayer. They can then be transported to NosZ, allowing for enzyme catalysis (Fig. 1.6.2). These findings provide evidence that a similar system, assembled in MR-1 (Fig. 1.6.1 - Middle) could be used to carry out artificial photosynthesis and produce solar fuels.

A final chapter places the key findings of this work into the broader context of biohybrid photosynthesis and explores future avenues of research that could build on this work.

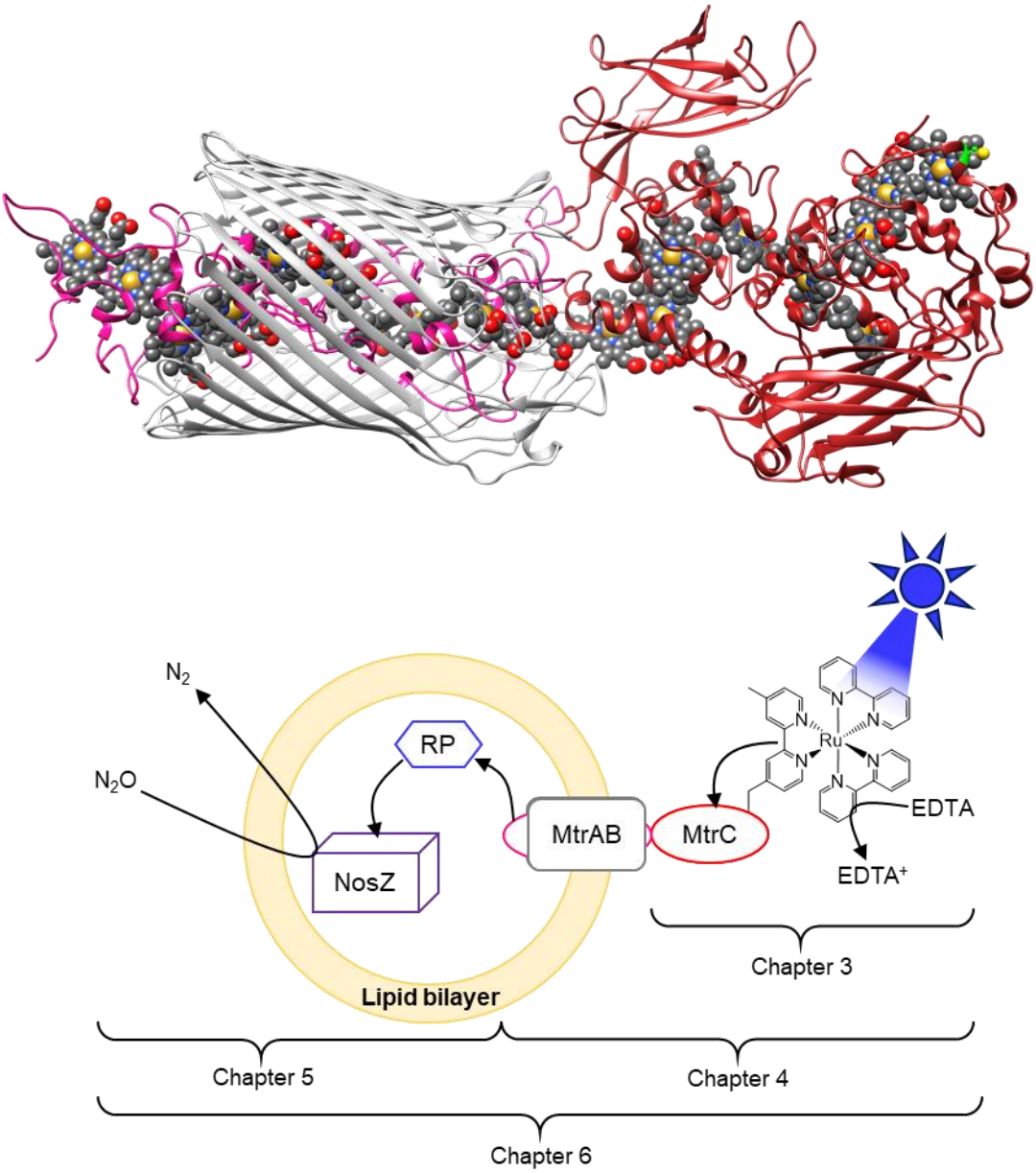

Figure 1.6.2 Top) Homology model of MtrCAB from MR-1, kindly provided by Dr. Marcus Edwards, based on structure of MtrCAB from *Shewanella baltica* (6R2Q)[134]; MtrA (Pink), MtrB (Grey) and MtrC (Red) are shown as ribbon structures and hemes are shown as spheres, coloured by heteroatom. MtrC contains the $Y_{657}C$ mutation (Green with yellow sulfur) which is the binding site for RuMe. Structure rendered in Chimera software. **Bottom)** Schematic of nanoreactors developed in this thesis and the focus of each chapter. Electron flow indicated by black arrows. RuMe-MtrCAB is photoreduced by irradiation with blue light with EDTA as a SED leading to transmembrane electron transfer. Electrons are passed to a redox partner (RP) which shuttles them to the enzyme NosZ where they are used to reduce N_2O to N_2 which, as gases, are able to pass freely across the lipid membrane.

In summary the aims of this thesis can outlined as follows:

Explore and explain the photochemical properties of RuMe-MtrC and use this understanding to identify rate-limiting processes in the photoreduction of this protein using a SED.

Identify and characterise the complex between RuMe-MtrC and MtrAB using biophysical methods. This complex will be compared to the structure of WT MtrCAB to identify any significant global deviations in structure. The ability of photogenerated electrons to pass from RuMe-MtrC to MtrAB in this complex will also be explored.

The activity of the enzymatic cargo NosZ will be investigated over short and long time frames with both native and exogenous redox partners. The suitability of these redox partners for use in a liposome environment will also be evaluated.

RuMe-MtrCAB will be assessed for its transmembrane electron transfer capabilities using encapsulated redox dyes and both chemical and photochemical reductants. Further, this complex will be demonstrated to transfer such reducing equivalents to encapsulated NosZ enabling light-driven activity of this enzyme.

CHAPTER 2

MATERIALS & METHODS

Chapter 2 - Materials & Methods

2.1 - General Techniques

2.1.1 - Buffer preparation

Buffers and media were prepared in Milli-Q water (dH_2O) (18.2 MΩ cm). pH was measured using a Mettler Toledo MP220 pH meter and adjusted using NaOH or HCl as appropriate. Buffers used in this work are listed in Table 2.1.1 along with abbreviations and their typical use.

Table 2.1.1 Buffer abbreviations, compositions, and typical uses

Buffer abbreviation	Composition	Typical use
HN	20 mM HEPES, 50 mM NaCl, pH 7.8	Mtr(C)AB purification
HNF	20 mM HEPES, 100 mM NaCl, 2.8 mM Fos-Choline-12, pH 7.8	Small Angle Neutron Scattering sample preparation
HNF1	20 mM HEPES, 1 M NaCl, 2.8 mM Fos-Choline-12, pH 7.8	Small Angle Neutron Scattering sample preparation
HNFD	20 mM HEPES, 100 mM NaCl, 2.8 mM Fos-Choline-12, pH 7.8, 13% D_2O	Small Angle Neutron Scattering data collection
HNTx	20 mM HEPES, 50 mM NaCl, 2% (v/v) Triton X-100, pH 7.8	Mtr(C)AB purification
HNTx1	20 mM HEPES, 1 M NaCl, 2% (v/v) Triton X-100, pH 7.8	Mtr(C)AB purification
T1	20 mM Tris:HCl, pH 7.5	RuMe labelling of MtrC
TK	50 mM Tris:HCl, 10 mM KCl, pH 8.5	Default buffer for protein and liposome handling
TKTx	50 mM Tris:HCl, 10 mM KCl, 0.2% (v/v) Triton X-100, pH 8.5	Membrane protein assays
10xTN	500 mM Tris:HCl, 1 M NaCl, pH 8.5	MtrC purification
TN	50 mM Tris:HCl, 100 mM NaCl, pH 8.5	MtrC purification
TN1	20 mM Tris:HCl, 1 M NaCl, pH 7.5	RuMe labelling of MtrC
TN2	100 mM Tris:HCl, 150 mM NaCl, pH 8	NosZ + PazSII purification
TNB1	50 mM Tris:HCl, 100 mM NaCl, 20 mM Biotin, pH 8.5	MtrC purification

TNB2	100 mM Tris:HCl, 150 mM NaCl, 20 mM Biotin, pH 8	NosZ + PazSII purification
TNTx	20 mM Tris:HCl, 50 mM NaCl, 2% (v/v) Triton X-100, pH 8.5	Mtr(C)AB purification
TNTx1	20 mM Tris:HCl, 1 M NaCl, 2% (v/v) Triton X-100, pH 8.5	Mtr(C)AB purification
PNL	50 mM H_2NaPO_4/HNa_2PO_4, 50 mM NaCl, 5 mM Lauryldimethylamine oxide, pH 7.5	Mtr(C)AB detergent exchange and gel filtration
PNL1	50 mM H_2NaPO_4/HNa_2PO_4, 1 M NaCl, 5 mM Lauryldimethylamine oxide, pH 7.5	Mtr(C)AB detergent exchange
PNTx	50 mM H_2NaPO_4/HNa_2PO_4, 50 mM NaCl, 0.1% (v/v) Triton X-100, pH 7.5	Analytical ultracentrifugation
Heme stain	250 mM Sodium acetate, pH 5	Heme staining gels

2.1.2 - Anaerobic sample handling

Much of the work presented here was carried out under anaerobic conditions. This was achieved by conducting experiments in degassed solutions inside anaerobic chambers. Two types of anaerobic chamber were used: A Belle Technology glove box, and a MBRAUN UNIlab Plus Glove Box Workstation. These machines have different features and designs however both achieve the same purpose and could be used interchangeably. The oxygen concentration in both boxes was maintained at <1 ppm as reported by internal O_2 sensors.

Buffers and other solutions were degassed before being introduced to the anaerobic chamber. Volumes >5 mL were first sparged by bubbling nitrogen into the sample to gradually remove any dissolved oxygen. Solutions were sparged for ≈ 15 mins per 100 mL of solution before sealing and transferring to an anaerobic chamber. Once under an anaerobic atmosphere the solution containers were opened and left stirring (typically overnight, using a magnetic stir plate to further remove any remaining traces of oxygen.

Where possible, small (<5 mL) solutions were prepared by introducing a pre-measured aliquot of pure solute in a sealed, sparged vial into the anaerobic chamber and adding the appropriate solvent (buffer or dH_2O) which had been degassed previously as above. This method was used to prepare anaerobic solutions of methyl viologen (Sigma), sodium dithionite (Sigma), octyl glucoside (Anatrace), Triton X-100 (Sigma), Reactive Red 120 (Sigma), Reactive Black 5 (Sigma), Amaranth (Sigma), calcium chloride, RuMe-Br (Hetcat Switzerland), potassium ferrioxalate (Alfa Aesar) and 1,10-phenanthroline (Sigma).

Protein solutions were degassed in small volumes (<100 µL) by purging with N_2 in the port of an anaerobic chamber for a minimum of 30 mins.

2.1.3 - Buffer exchange

Exchange of proteins into different buffers was carried out in two different ways depending on whether Triton X-100 (TX100) was present in either the original sample buffer or the target buffer. In the absence of TX100, Amicon Ultra 0.5 mL (Sigma) or Sartorius Vivaspin 20 mL (Fisher) centrifugal filters were used with Molecular weight cut-off (MWCO) selected for compatibility with the proteins being concentrated. Proteins were concentrated ≈ 10× and diluted back to their original volume in target buffer. This was repeated and after 3 cycles the buffer was deemed to have been exchanged. These centrifugal filters were also used to wash away small molecules from proteins and concentrate proteins.

TX100 has a large micelle size (≈100 kDa)[135] which means it cannot effectively be removed by centrifugal filter concentrators which typically have a maximum MWCO of 100 kDa. If such concentrators are used the TX100 concentrates with the protein and does not wash through with the filtrate. To exchange proteins from a buffer containing TX100 to a buffer without TX100, the sample was first loaded onto a 5 mL HiTrap Q FF column pre-equilibrated with the target buffer. The bound protein was then washed with the target buffer at 2.5 mL/min and $A_{280\ nm}$ was monitored. $A_{280\ nm}$ eventually levelled off at a low value indicating all TX100 had been removed from the column, this typically took 15-20 column volumes as detergent micelle exchange can be slow and TX100 can stick to plastics. The bound protein was then eluted in the target buffer with addition of a suitably high concentration of NaCl (usually 0.5 M). The concentration of NaCl was then lowered using centrifugal filters and the target buffer as described above.

2.1.4 - Media preparation

Three types of base media were used in this work for the growth of different species and strains of bacteria:

Luria Broth (LB) (Melford) was prepared according to instructions (25 g/L). pH was adjusted to 7.2 with concentrated HCl before being autoclaved to sterilise.

M72 media[136] was prepared using:

15 g/L Peptone from casein (Sigma)

5 g/L Papaic digest of soybean (Sigma)

5 g/L NaCl

pH was adjusted to 7.8 using 10 M NaOH and media was autoclaved to sterilise.

Before inoculation, the sterilised solution was supplemented with an electron and carbon source (lactate) and a terminal respiratory electron acceptor (fumarate) from a filter sterilised 10× stock:

200 mM DL-lactate (from 60% (w/w) solution) (Sigma)

200 mM Sodium fumarate

200 mM HEPES

pH adjusted to 7.8 with NaOH pellets and 10 M NaOH solution.

Minimal Media (MM) was prepared using

29 mM Na_2HPO_4

11 mM KH_2PO_4

10 mM NH_4Cl

30 mM sodium succinate

20 mM $NaNO_3$

pH was adjusted to 7.5 with 10 M NaOH and media was autoclaved to sterilise.

Before inoculation, $MgSO_4$ was added to a final concentration of 0.4 mM from a filter-sterilised 1 M stock along with 2 mL/L Vishniac and Santer Trace-elements solution (VSTES)[137]:

130 mM EDTA

7.64 mM $ZnSO_4$

25 mM $MnCl_2$

18.5 mM $FeSO_4$

0.89 mM $(NH_4)_6Mo_7O_{24}$

6.4 mM $CuSO_4$

6.72 mM $CoCl_2$

37.4 mM $CaCl_2$

pH adjusted to 6.6 and solution left open to air for a minimum of 1 month to oxidise and turn dark purple, then filter sterilised.

Additional reagents, e.g. antibiotics, trace metals and inducers, were added to the media as appropriate for each purification system. Stock solutions of 30 mg/mL kanamycin sulfate (KM) (Fisher), 20 mg/mL gentamycin sulfate (GM) (Formedium), and 0.5 M $CuSO_4$ were filter-sterilised and kept frozen at -20℃ until required. These stock solutions were then used by diluting 1000× or 500× into sterile media as appropriate. Inducers L-(+)-arabinose (Sigma) and Taurine (Melford) were added to growing cell cultures from freshly prepared, filter-sterilised 0.5 M stock solutions.

2.1.5 - Long-term storage of proteins and bacterial strains

Biological samples (proteins and bacterial cells) were stored at -80℃ to prevent degradation. Glycerol stocks were prepared of bacterial strains for long-term storage. The presence of glycerol prevents the formation of large ice crystals which might otherwise damage the cells. To 750 µL of 50% glycerol in dH_2O, autoclaved to sterilise, was added 750 µL of a stationary phase culture of bacteria, usually in LB. The resulting mixture was mixed and snap-frozen in liquid nitrogen then stored at -80℃. Proteins were prepared in an appropriate buffer, and similarly snap-frozen.

2.2 - Biochemical protein characterisation

2.2.1 - Protein gel electrophoresis

Sodium dodecyl sulfate–polyacrylamide gel electrophoresis (SDS-PAGE) analysis was routinely carried out using TruPAGE pre-cast gels (Sigma) with either 10% or 4-20% acrylamide. Samples were prepared using TruPAGE LDS Sample buffer and gels were run according to provided instructions. Gels were then washed thoroughly with dH_2O to prepare them for staining. Two types of staining procedure were carried out:

Coomassie staining was carried out to detect all proteins in the sample. Instant Blue stain was applied to the washed gels and the gels were agitated to ensure even staining. The

Coomassie dye present in the stain solution binds non-covalently to the charged groups of proteins, turning blue in the process.

Heme staining was carried out to detect only the *c*-type cytochromes in the sample. After thorough washing in dH_2O the gel was soaked for a minimum of 30 mins in dH_2O, this step was necessary to avoid gel shrinkage and distortion in the following steps. After the soaking and a second rinse, ≈20 mL 250 mM sodium acetate, pH 5 was added to the gel. This was followed by addition of 20 mg 3,3',5,5'-Tetramethylbenzidine (TMBD) (Sigma) dissolved in 20 mL methanol. To initiate the staining reaction, 200 µL H_2O_2 (30% w/w) (Sigma) was added. The presence of cytochromes in the gel catalyses the oxidation of TMBD to produce 3,3',5,5'-Tetramethylbenzidine diimine which has a strong blue colour and identifies the cytochromes on the gel. After sufficient staining had occurred the stain solution was removed, and the gel was rinsed with dH_2O.

Gels were imaged on a Syngene G:BOX Chemi XRQ imager.

2.2.2 - Liquid chromatography-mass spectrometry

Liquid chromatography-mass spectrometry (LC-MS) is a powerful analytical tool for quantification of the mass of proteins. LC-MS was carried out by Dr. Jessica van Wonderen with the assistance of the group of Prof. Nick Le Brun as reported previously.[132] To 20 µL of a ≈ 20 µM protein sample was added 180 µL 1% acetonitrile, 0.3% formic acid which denatured the protein, causing any non-covalently bound cofactors to dissociate. The sample was then loaded onto a ProSwift RP-1S column (4.6 × 50 mm, Thermo Scientific) on an Ultimate 3000 uHPLC system (Dionex,Leeds, UK). Material was eluted over a linear gradient from 2-100% acetonitrile, 0.1% formic acid. Positive mode electrospray ionisation mass spectrometry was carried out on the eluate in a Bruker microQTOF-QIII mass spectrometer.

2.2.3 - Bradford assay

This assay was used for quantification of copper-containing proteins (NosZ and Paz) where absorbance features derived from the cofactors are far weaker and less reliable than, for example, *c*-type cytochromes. Copper atoms also prevent the use of other protein assay techniques such as Biuret, Lowry or bicinchoninic acid assays which all use copper to quantify protein concentration.

To 750 µL Buffer was added 50 µL of sample and 200 µL of QuickStart Bradford 1 × Dye Reagent (BioRad). After 5 mins $A_{595\ nm}$ was recorded using a Jenway 7315

spectrophotometer. Buffer composition and pH can significantly affect the result of a Bradford assay which uses pH dependant Coomassie dyes, therefore Bradford assays were always carried out after exchange into 100 mM Tris:HCl, 150 mM NaCl, pH 8 buffer (TN2 Buffer). A standard curve was produced using bovine serum albumin (BSA) in TN2 Buffer which gave the following equation:

$$A_{595\ nm} = 1.465 \times [\text{protein}]\ (\text{mg/mL in original sample}) + 0.375$$

This assay was found to be suitable for protein concentrations from 0.05 to 0.2 mg mL^{-1}.

2.2.4 - BCS Copper assay

The complex of Cu^{I} and bathocuproinedisulfonic acid (BCS) has absorbance with $\varepsilon_{484\ nm}$ = 12250 M^{-1} cm^{-1}.[138] This can be used to spectrophotometrically detect and quantify copper concentrations. Proteins were first denatured in nitric acid to release all copper atoms into solution. Hydroxylamine was then added to reduce all Cu^{II} to Cu^{I} before BCS was added to create the chromophore.

Samples were mixed 1:1 with 33% nitric acid and incubated at 95℃ for 30 mins to fully denature the protein. Assay solutions were then prepared by combining:

200 µL protein-acid mixture

600 µL saturated sodium acetate solution

100 µL 100 mM hydroxylamine

100 µL 10 mM BCS

These solutions were allowed to develop for 30 mins before recording $A_{484\ nm}$ using a Jenway 7315 spectrophotometer. A standard curve was produced using $CuSO_4$ giving the following equation which is consistent with the reported extinction coefficient[138] for $[Cu(BCS)_2]^{3-}$:

$$A_{484\ nm} = 12000 \times [\text{Cu}]\ (\text{M in assay}) + 0.008$$

This assay was found to be suitable for samples with [Cu] from 20 to 200 µM (in original sample before addition of nitric acid) though it is likely also applicable to higher concentrations.

2.2.5 - Pyridine hemochromagen assay

The pyridine hemochromagen assay allows for determination of the heme extinction coefficients of a cytochrome which can vary according to heme ligation and protein environment. A UV-Vis spectrum is first obtained of the protein in its oxidised state, this sample is then denatured and pyridine is added to axially coordinate all the hemes in the sample, making them spectroscopically identical with a known extinction coefficient. The concentration of heme can therefore be determined and, based on the number of hemes per protein, the original protein concentration can be quantified and used to calculate the extinction coefficients of the intact protein. This can then be used to calculate the extinction coefficients of the hemes after reduction with sodium dithionite (DT).

Pyridine hemochromagen assays were carried out on MtrC, in TN Buffer, (data provided by Dr. van Wonderen) and on MtrAB, in 50 mM Tris, 10 mM KCl, 0.2% (v/v) TX100, pH 8.5 Buffer (TKTx Buffer), as described by Barr and Guo[139] using a Jasco V-650 spectrophotometer. The results are presented in Figure 2.3.1 and Table 2.3.1.

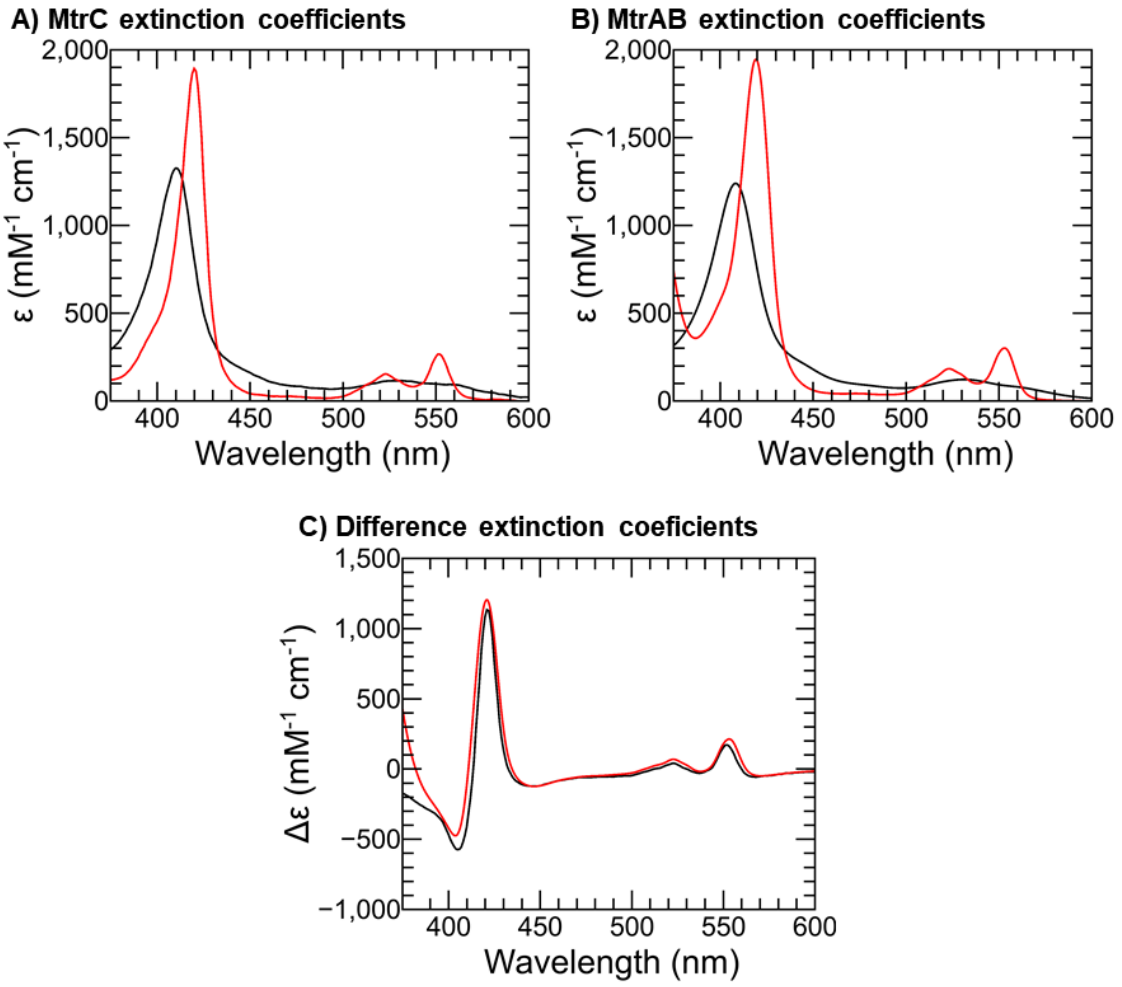

Figure 2.2.1 A&B) Extinction coefficient spectra determined by pyridine hemochromagen assay for MtrC (data provided by Dr. van Wonderen), and MtrAB in oxidised (Black) and reduced (Red) states; **C)** Reduced-oxidised difference spectra for MtrC (Black) and MtrAB (Red).

Table 2.2.1 Tabulated extinction coefficients for key spectral features of MtrC and MtrAB.

MtrC	Oxidised state		Reduced State		Red-Ox difference	
Peak descriptor	λ_{max} (nm)	ε (mM^{-1} cm^{-1})	λ_{max} (nm)	ε (mM^{-1} cm^{-1})	λ (nm)	Δε (mM^{-1} cm^{-1})
α peak	530	115	552	267	552	171
β peak			523	154	523	41
Soret (γ peak)	410	1326	420	1893	410	-413
					420	1084
MtrAB	Oxidised state		Reduced State		Red-Ox difference	
Peak descriptor	λ_{max} (nm)	ε (mM^{-1} cm^{-1})	λ_{max} (nm)	ε (mM^{-1} cm^{-1})	λ (nm)	Δε (mM^{-1} cm^{-1})
α peak	532	122	553	301	553	213
β peak			523	183	523	69
Soret (γ peak)	408	1238	419	1944	408	-320
					419	1136

2.3 - Protein Preparation

All chromatography was carried out at 4℃ using an Äkta Pure protein purification system (GE Healthcare). Centrifugation was carried out at room temperature, ultracentrifugation was carried out at 4℃. Progress of purifications were followed by colour of protein fractions and SDS-PAGE analysis (see Section 2.2.1). LC-MS was carried out by Dr van Wonderen (see Section 2.2.2). Purification procedures for RuMe-MtrC, MtrCAB, MtrAB and NosZ were developed by others and used with minor modifications. The purification procedure for PazSII was developed as part of this thesis drawing from previously reported strategies.[140,141]

2.3.1 - RuMe-MtrC

Replacement of the signal peptide of MtrC with that of MtrB leads to expression of soluble forms of MtrC which do not have a lipid anchor attached as in WT MtrCAB.[142] These soluble forms are secreted from MR-1 cells and can be purified from the spent media.

MtrC-Y_{657}C was purified from spent bacterial growth media using the method described in Lockwood et al.[143] with some small alterations. MR-1 containing a pBAD-TOPO plasmid encoding for MtrC with: the signal-peptide and N-terminal acylation site replaced with the signal peptide of MtrB, a C-terminal Strep-tag II, and a site directed mutation (MR1+pJvW001) was produced and kindly provided by Dr van Wonderen (in

preparation). Cells were grown from glycerol stocks in M72 media + additions + 30 μg/mL KM. Cultures were grown at 30℃ with shaking until $OD_{600\ nm}$ = 0.6 at which point 5 mM arabinose was added and shaking was stopped to create a microaerobic environment. Cultures were left to grow at 30℃ for a further 20 h.

Cells were pelleted by centrifugation at 4800 ×g for 30 mins (JLA 8.1000, 5000 RPM) and to each litre of supernatant was added 100 mL of 0.5 M Tris, 1 M NaCl, pH 8.5 (10xTN Buffer) and 200 μL biotin blocking solution (IBA Solutions for Life sciences). The resulting solution was checked to ensure the pH was above 8 and corrected with 0.5 M NaOH if required.

Spent media was first loaded onto a Strep-tactin XT Superflow high capacity column (IBA Solutions for Life Sciences) pre-equilibrated in 50 mM Tris, 100 mM NaCl, pH 8.5 Buffer (TN Buffer) at 2.5 mL/min. The bound protein was then washed with a minimum of 5 column volumes of TN Buffer. Protein was eluted with 2 column volumes of 50 mM Tris, 100 mM NaCl, 20 mM Biotin, pH 8.5 Buffer (TNB1 Buffer) at 2.5 mL/min. The column was then regenerated with 20 column volumes of 20 mM NaOH at 2.5 mL/min and re-equilibrated with TN Buffer. Typically, 1 L spent media contained enough protein to saturate the column's binding capacity therefore larger preparations were split into 1 L portions and multiple purification cycles were carried out. Eluted material was exchanged into TN Buffer using 30 kDa MWCO concentrators, snap-frozen and stored at -80℃. Yields of 10 mg L^{-1} were typically obtained.

SDS-PAGE analysis (Fig. 2.3.2 - Top) of the eluted material reveals a protein with the expected M_W of ≈ 70 kDa which was present in both Coomassie and Heme stained gels. LC-MS analysis of MtrC-Y_{657}C after treatment with 5 mM tricarboxyethylphosphine (TCEP) shows the protein has a mass of 76199 Da (Fig. 2.3.2 - Bottom) which is consistent with the predicted mass of this protein (76264 Da). The protein concentration was determined spectrophotometrically for the oxidised protein using $\varepsilon_{410\ nm}$ = 1326000 $M^{-1}\,cm^{-1}$ as determined by pyridine hemochromogen assay (see Section 2.2.5).

RuMe-MtrC was produced from MtrC-Y_{657}C using the method reported for labelling of STC and developed by Dr van Wonderen.[132] The reaction between MtrC-Y_{657}C and RuMe-Br proceeds by nucleophilic substitution as shown in Figure 2.3.1. MtrC-Y_{657}C was exchanged into 20 mM Tris:HCl, pH 7.5 Buffer (T1 Buffer) + 5 mM TCEP (Sigma) was added to cleave any disulfide bonds and generate the free thiol. After incubation for 40 mins at room temperature, TCEP was removed by exchange into T1 Buffer. A 2× excess of RuMe-Br was added from a 30 mM stock solution in dimethylsulfoxide (DMSO) (Sigma). The resulting solution was thoroughly wrapped in foil to prevent light-induced damage and gently mixed overnight at 4℃.

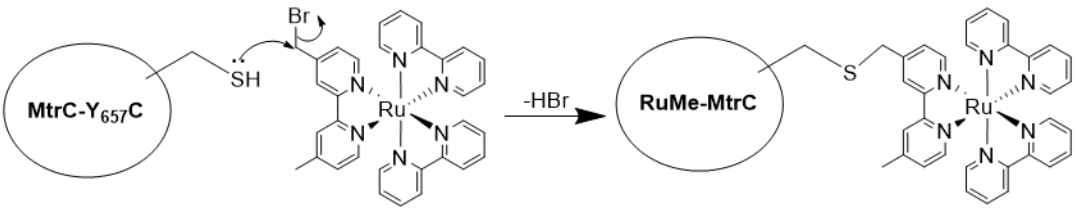

Figure 2.3.1 Mechanism of RuMe labelling of MtrC-Y_{657}C. Charges have been excluded for simplicity

To remove excess RuMe-Br the sample was loaded at 2 mL/min onto a 5 mL HiTrap Q FF column pre-equilibrated with T1 Buffer. The unreacted RuMe-Br did not bind to the column and was collected in the flow through. The bound protein was washed with 5 column volumes of T1 Buffer at 2 mL/min or until the $A_{280\ nm}$ had returned to baseline, confirming complete removal of RuMe-Br. Bound protein was eluted with a 10-50% gradient of T1 to 20 mM Tris:HCl, 1M NaCl, pH 7.5 (TN1 Buffer) over 20 column volumes at 2 mL/min. Eluted material was exchanged into TN Buffer and concentrated before being snap-frozen and stored at -80℃.

SDS-PAGE analysis of the eluted material reveals a protein with the same properties as MtrC-Y_{657}C (Fig. 2.3.2 - Top). Protein concentration was determined spectrophotometrically as above for MtrC-Y_{657}C. Labelling efficiency was determined by LC-MS (see Section 2.2.2) which can clearly resolve RuMe-MtrC from MtrC-Y_{657}C by an increase of ≈595 Da (Fig. 2.3.2 - Bottom). This procedure typically gave labelling efficiencies above 90% as judged by the ratio of labelled and unlabelled signals. LC-MS also confirms that only one RuMe is attached to MtrC as material with higher molecular weights is not identified.

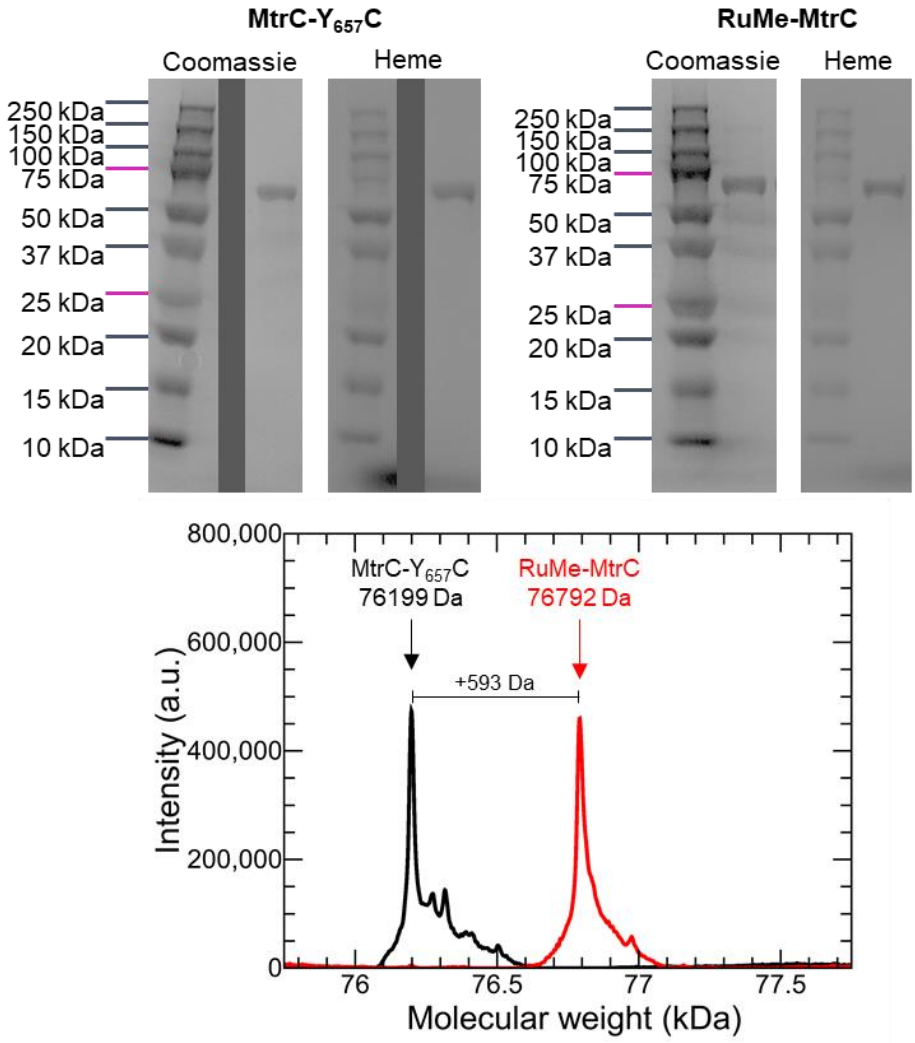

Figure 2.3.2 Top) SDS-PAGE analysis of indicated proteins with indicated staining procedures; **Bottom)** LCMS analysis of MtrC-Y_{657}C (Black) and RuMe-MtrC (Red).

2.3.2 - MtrCAB and MtrAB

MtrCAB and MtrAB were purified as described in Lockwood et. al.[143] with some minor modifications. MtrCAB was purified from MR-1 cells whereas MtrAB was purified from MR-1 *mtr*$^-$ (LS527) containing a pBAD-TOPO plasmid encoding MtrAB (pCL001). The cells were grown under different conditions but the protein purifications are identical.

For MtrCAB, MR-1 cells were grown from glycerol stocks in LB media with shaking to maintain an aerobic environment. For MtrAB, LS527+pCL001 cells were grown from glycerol stocks in M72 media + additions + 30 µg/mL kanamycin. These cultures were grown at 30℃ with shaking until $OD_{600\,nm}$ = 0.6 (approx. 2h in baffled flasks). At this point the cultures were induced with 5 mM arabinose and shaking was stopped to create a microaerobic environment. The cultures were grown at 30℃ for a further 20h.

Both strains were harvested by centrifugation at 4800 ×g for 30 mins (JLA 8.1000, 5000 RPM) and resuspended in 20 mL/L 20 mM HEPES, 50 mM NaCl, pH 7.8 buffer (HN Buffer). DNase1 (≈ 2 mg/L) (Sigma) and a SigmaFAST protease inhibitor cocktail tablet (Sigma) were added. After stirring for 30 mins cells were lysed by two passes through a French pressure cell at a pressure of 16,000 psi. Cell lysate was centrifuged at 5000 RPM in benchtop centrifuge for 30 mins to remove debris and intact cells. The supernatant was then centrifuged at 138000 ×g for 1h 40 mins (Type 45 Ti, 42000 RPM) to pellet membrane associated material.

This pellet was resuspended in 15 mL/L Buffer HN and stirred for 30 mins at 4℃ after which time sodium lauroyl sarcosinate (Sigma), dissolved in a minimal volume of HN Buffer, was added to a concentration of 1% (w/v). This detergent selectively solublises the inner membrane[144] however the outer membrane may also be solubilised if it is exposed to high concentrations of the detergent or if it is left for long time periods. For these reasons the detergent solution was added dropwise over 10 mins while stirring to avoid pockets of high detergent concentration and left stirring for no longer than 45 mins. Some Mtr protein is lost during this step.

The suspension was then centrifuged again at 138000 ×g for 1h 40 mins (Type 45 Ti, 42000 RPM) to pellet the still insoluble outer membrane fraction. The pellet was homogenised in 20 mL/L HN Buffer, TX100 was added to 5% (v/v) and this was stirred overnight at 4℃ to solublise the remaining material. The resulting suspension was centrifuged at 138000 ×g for 1h (Type 45 Ti, 42000 RPM) to remove any small amounts of unsolublised material.

The supernatant was loaded at 5 mL/min onto a Q-Seph column pre-equilibrated with 20 mM HEPES, 50 mM NaCl, 2% (v/v) TX100, pH 7.8 (HNTx Buffer). The bound protein was washed with 2 column volumes of HNTx Buffer at 5 mL/min. The protein was eluted using a 0-50% gradient of 20 mM HEPES, 1M NaCl, 2% (v/v) TX100, pH 7.8 (HNTx1 Buffer) over 5 column volumes at 5 mL/min. Fractions containing Mtr proteins eluted over ≈1 column volume with a peak at 21 mS/cm.

Mtr protein containing fractions were diluted 3-fold into 20 mM Tris, 50 mM NaCl, 2% (v/v) TX100, pH 8.5 (TNTx Buffer) to reduce the salt concentration and loaded at 5 mL/min onto a pre-equilibrated DEAE column. The bound protein was washed with 2 column volumes of TNTx Buffer at 5 mL/min. The protein was eluted using a 0-50% gradient of 20 mM Tris, 1 M NaCl, 2% (v/v) TX100, pH 8.5 (TNTx1 Buffer) over 5 column volumes at 5 mL/min. Fractions containing Mtr proteins eluted over ≈1 column volume with a peak at 15 mS/cm.

Fractions containing Mtr proteins were exchanged into PNL Buffer (50 mM H_2NaPO_4/HNa_2PO_4, 50 mM NaCl, 5 mM Lauryldimethylamine oxide (LDAO) (Sigma), pH 7.5) as described in Section 2.1.3 and concentrated to <5 mL for gel filtration. The sample was eluted at 0.5 mL/min through a Superdex 200 26/60 column pre-equilibrated with PNL Buffer. Fractions containing Mtr(C)AB were concentrated to give a final protein stock which was prepared, snap-frozen and stored at -80℃.

SDS-PAGE analysis of MtrCAB with a Coomassie stain reveals proteins with M_W of ≈80, ≈75 and ≈30 kDa (Fig. 2.3.3). The latter two proteins also stain when using the heme stain procedure. These results are consistent with the presence of MtrB, and two heme-containing cytochromes MtrC and MtrA respectively. In addition, sometimes weaker staining bands were present in Heme-stained gels with M_W of ≈120 kDa and 150 kDa, these are attributed to MtrAB and MtrCAB that have not fully dissociated. SDS-PAGE Analysis of pure MtrAB shows similar banding but without the presence of the 75 or 150 kDa bands attributed to the presence of MtrC. Protein concentrations were determined spectrophotometrically using extinction coefficients determined for the oxidised proteins by the pyridine hemochromagen assay (see Section 2.2.5): $\varepsilon_{410\ nm}$ = 2660000 M^{-1} cm^{-1} for MtrCAB and $\varepsilon_{408\ nm}$ = 1238000 M^{-1} cm^{-1} for MtrAB.

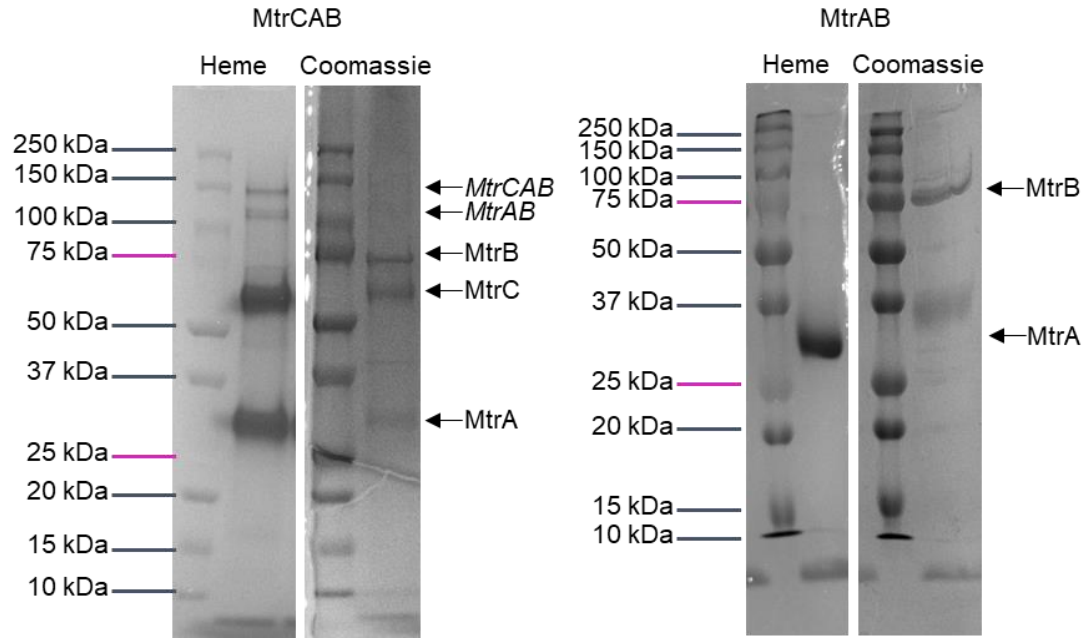

Figure 2.3.3 SDS-PAGE analysis of indicated proteins with indicated staining procedures

2.3.3 - NosZ

NosZ was purified from *Paracoccus denitrificans* strain PD1222+pMSL002 which encodes for NosZ with a C-terminal enterokinase cut site and Strep-tag II, kindly provided by Dr. Manuel Soriano Laguna.[145] This strain also produces genomic WT NosZ. Cells were grown from glycerol stocks in MM + 2 mL L^{-1} VSTES + 20 µg/mL Gentamycin (GM) in sealed flasks to create a microaerobic denitrifying environment. Cultures were grown at 30℃ until $OD_{600\,nm} \approx 0.6$ (approx. 6 h). At this time 10 mM taurine was added to induce overexpression and cultures were grown for a further 16 h at 30℃. Cells were harvested by centrifugation at 4800 ×g for 30 mins (JLA 8.1000, 5000 RPM) and resuspended in 20 mL/L 100 mM Tris:HCl, 150 mM NaCl, pH 8 Buffer (TN2 Buffer).

DNase 1 and a SigmaFAST protease inhibitor cocktail were added and the cells were lysed by 2 passes through a French pressure cell. The cell lysate was ultracentrifuged at 120000 ×g for 1h (Type 45 Ti, 40k RPM) to remove intact cells and membranes. Biotin blocking solution (10 µL per 100 mL) was added and the clarified lysate was loaded at 2.5 mL/min onto a Strep-tactin XT Superflow column pre-equilibrated with TN2 Buffer. Bound protein was washed with 10 column volumes of TN2 buffer at 2.5 mL/min and eluted in 2 column volumes of 100 mM Tris:HCl, 150 mM NaCl, 20 mM Biotin, pH 8 buffer (TNB2 buffer) at 2.5 mL/min. Eluted material was exchanged into TN2 Buffer using a 30 kDa MWCO centrifugal concentrator as described in Section 2.1.3.

SDS-PAGE analysis of the eluted material (Fig. 2.3.4 - Left) revealed a protein with M_W of ≈ 70 kDa, as expected for NosZ, and a second band at ≈ 140 kDa which is attributed to NosZ dimers. Protein concentration was determined by Bradford assay (see Section 2.2.3), and copper concentration was determined by BCS copper assay (see Section 2.2.4). Copper content was consistent with the protein containing ≈ 6 Cu per NosZ indicating the enzyme was fully loaded.

LC-MS revealed that the majority of the eluted material had a mass of 68106 Da (Fig. 2.3.4 - Right) which matches the predicted mass of the strep-tagged NosZ construct (68104 Da). A smaller peak at 66324 Da was also observed which matches the predicted mass of WT NosZ (66322 Da). It is hypothesised that this WT protein formed heterodimers *in vivo* with the Strep-tagged protein and was copurified. The two NosZ constructs are expected to have identical enzymatic properties therefore this WT material does not require any further consideration.

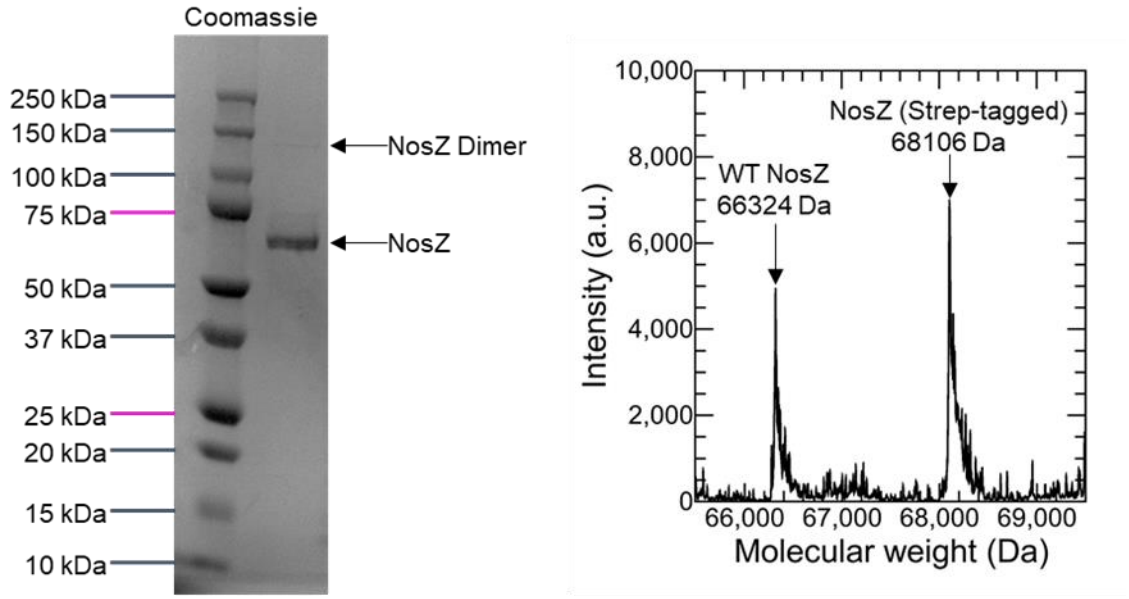

Figure 2.3.4 Left) SDS-PAGE analysis of purified NosZ, location of NosZ-dimer is indicated, the presence of this band is affected by protein loading and presence of reducing agents in the loading buffer; **Right)** LCMS analysis of purified NosZ with Strep-tagged and WT NosZ indicated.

2.3.4 - PazSII

Previously, Paz from *Paracoccus pantotrophus* had been purified in large quantities by heterologous over-expression in *E. coli* using a pET-24d based plasmid (pET-psaz).[140] The purification procedure for this protein involved obtaining a periplasmic extract, anion exchange, gel filtration and ammonium sulfate precipitation.[141] To simplify the purification for this work, a Strep-tag II was added to the C-terminus of the protein to produce PazSII which could be purified in one step.

The pET-psaz plasmid[140] was kindly provided by Dr Nick Watmough and was transformed into TOP10 chemically competent cells (Invitrogen) according to the instructions provided. These cells were plated onto LB-agar + 30 µg/mL KM and grown overnight at 37℃. Single colonies were picked and used to inoculate LB + 30 µg/mL KM which were grown for 24 h at 37℃. The plasmid was isolated using a GenElute Plasmid Miniprep kit (Sigma) according to provided instructions. The plasmid was sequenced using the T7 promoter forward primer (Table 2.2.1) which confirmed the sequence.

To install the Strep-II tag, polymerase chain reaction (PCR) primers PazSII-Fw and PazSII-Rv (Table 2.2.1) were designed to amplify pET-psaz outwards from the end of the gene and stop codon whilst adding half of the gene encoding for the Strep-tag II to either end of the plasmid. This technique has previously been used to add the Strep-tag II to STC[132] and MtrC (van Wonderen et al., in preparation). The PCR reaction was set up with 150 ng pET-psaz, 2.5 µM PazSII-Fw, 2.5 µM PazSII-Rv in 50 µL Phusion Flash

High-Fidelity PCR Master Mix (Thermo Scientific). PCR was run using a denaturing temperature of 98℃ (10 mins), an annealing temperature of 61℃ (30 s) and an extension temperature of 72℃ (6 mins). This cycle was repeated 35 times with an extension time of 10 mins on the final cycle.

Table 2.3.1 Primers used in this work. PazSII-Fw and PazSII-Rv are colour coded: part of Strep-tag II (Pink), spacer (Yellow), Paz stop codon (Cyan).

Primer name	Primer sequence (5'→3')	Primer purpose
PazSII-Fw	CCACAATTCGAGAAGTGACCGGGATCCGAATTCG	Addition of Strep-tag II to pET-psaz
PazSII-Rv	ATGAGACCAAGCGCTGTTGACCTGGGCCAGTTC	Addition of Strep-tag II to pET-psaz
T7 promoter forward primer	TAATACGACTCACTATAGGG	Sequencing of pET-psaz and pET-psazSII
T7 terminator primer	GCTAGTTATTGCTCAGCGG	Sequencing of pET-psaz and pET-psazSII

PCR product was cleaned up using GenElute PCR Clean up kit (Sigma) according to provided instructions. DNA was ligated to form a circular plasmid (pET-psazSII) using T4 DNA ligase (New England Biolabs) according to provided instructions. pET-psazSII was then transformed into *E. coli* XL1-Blue competent cells (Agilent) according to provided instructions (a misunderstanding led to this strain being used, the plasmid should have been transformed directly into *E. coli* BL21(DE3) cells). The transformed cells were plated onto LB-agar + 60 µg/mL KM and grown overnight at 37℃. Single colonies were picked and used to innoculate LB + 30 µg/mL KM which was then grown overnight at 37℃. pET-psazSII was then isolated by Miniprep (see above) and sequenced using the T7 promoter forward primer which confirmed the addition of the Strep-II tag.

pET-psazSII was then transformed into *E. coli* BL21(DE3) competent cells (Agilent) according to provided instructions. The transformed cells were plated onto LB-agar + 30 µg/mL KM and grown overnight 37℃. Single colonies were picked and used to innoculate LB + 30 µg/mL KM which was then grown overnight at 37℃. As a final check, pET-psazSII was isolated by Miniprep and sequenced using T7 terminator primer (Table

2.2.1) which confirmed the correct sequence. Glycerol stocks of the strain were prepared, snap-frozen and stored at -80°C.

Paz with a Strep-tag II (PazSII) was purified from *E.coli* BL21(DE3) + pET-psazSII. Cells were grown from glycerol stocks in LB + 30 µg/mL KM + 0.5 mM $CuSO_4$. Cultures were grown for 24h at 37°C with vigorous shaking to maintain an aerobic environment. Cells were pelleted by centrifugation at 5500 ×g (JLA 8.1000, 5500 RPM) and resuspended in 25 mL/L TN2 Buffer. DNase 1 and a SigmaFAST protease inhibitor cocktail tablet were added to the resuspended cells before lysis by two passes through a French pressure cell. Cell lysate was centrifuged at 185000 ×g (Ti45, 40000 RPM) for 30 mins to remove intact cells and membranes. To the clarified lysate was added 5 mM potassium ferricyanide and 5 mM $CuSO_4$ which caused the lysate to turn a dark blue colour, indicative of large quantities of PazSII.

The lysate was loaded at 2.5 mL/min onto a Streptactin XT Superflow column pre-equilibrated with TN2 Buffer. The column became rapidly saturated as evidenced by the resin turning a strong blue colour. The bound protein was washed with 5 column volumes TN2 Buffer before elution in 2 column volumes TNB2 Buffer. The column was then regenerated with 20 column volumes of 20 mM NaOH before re-equilibration and purification from more lysate. Multiple cycles of purification were carried out to isolate PazSII however, due to time constraints, less than half the PazSII was purified from the lysate. This prevents determination of an accurate yield, however a lower limit of 12 mg/L can be given. The eluted material was concentrated and exchanged into TN2 Buffer for further analyses.

SDS-PAGE analysis of the eluted material revealed a protein at 14-15 kDa, which is consistent with the predicted mass of PazSII (Fig. 2.3.5C). A band was also observed at ≈30 kDa however this was removed by the presence of β-mercaptoethanol in the loading buffer, this is consistent with the formation of PazSII dimers. LC-MS of PazSII showed a single peak at 14540 Da (Fig. 2.3.5B) which matches perfectly with the predicted mass of PazSII (14540 Da).

Bradford and copper assays (see Sections 2.2.3 & 2.2.4) were carried out and determined the protein and copper concentrations in the stock PazSII to be 1 mM and 1.1 mM respectively, indicating the protein was fully loaded. UV-Vis spectra of the purified material show characteristic broad features spanning the entire visible spectrum with maxima at 450 nm, 590 nm and 750 nm (Fig. 2.3.5A). Addition of DT led to loss of these features, consistent with reduction of Cu^{II} to Cu^{I}. The oxidised spectrum is consistent with the reported extinction coefficient of 1360 M^{-1} cm^{-1}.[140]

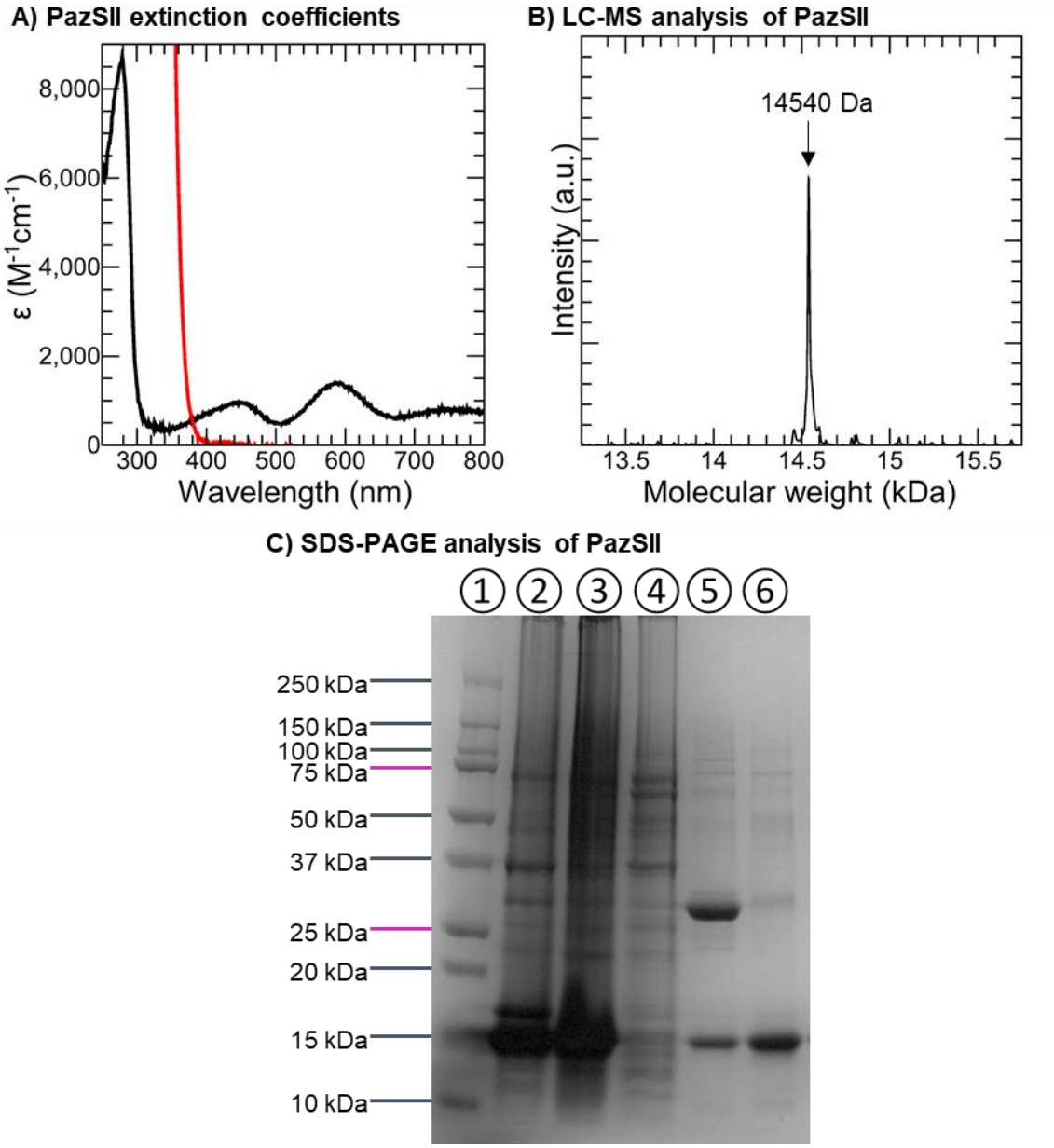

Figure 2.3.5 Characterisation of PazSII. **A)** Extinction coefficient spectra of PazSII in oxidised (Black) and reduced (Red) states, based on a 50 µM solution in TK Buffer, concentration quantified by Bradford Assay; **B)** Result of LCMS analysis of PazSII showing a single peak at 14540 Da; **C)** SDS-PAGE analysis of PazSII and of samples taken during the purification process by Coomassie stain, loading buffer contained 10% β-mercaptoethanol unless otherwise stated: ① Precision Plus Dual Colour, ② BL21(DE3) + pET-psazSII cells, ③ Clarified cell lysate, ④ Initial flow through from Streptactin XT Superflow column, ⑤ Eluted material (without β-mercaptoethanol), ⑥ Eluted material.

2.4 - Assays of NosZ activity

NosZ catalyses the two electron reduction of nitrous oxide (N_2O) to dinitrogen (N_2). The source of electrons for this reduction *in vitro* is usually DT however a redox active mediator must be used to effectively transfer electrons from DT to NosZ. This mediator can be an artificial redox active chemical such as MV, or a native redox partner such as Paz. These mediators have redox-dependant absorbances which can be used to spectroscopically quantify activity (Figs. 2.3.5A & 2.4.1). DT also has absorbance in the UV region with $\varepsilon_{315\ nm}$ = 8000 M^{-1} cm^{-1} which can also be used to monitor activity if DT is present in excess.[146] Alternatively, gas chromatography (GC) can be used to monitor the concentration of N_2O in the headspace above a solution. Both spectroscopic and chromatographic techniques were used in this work.

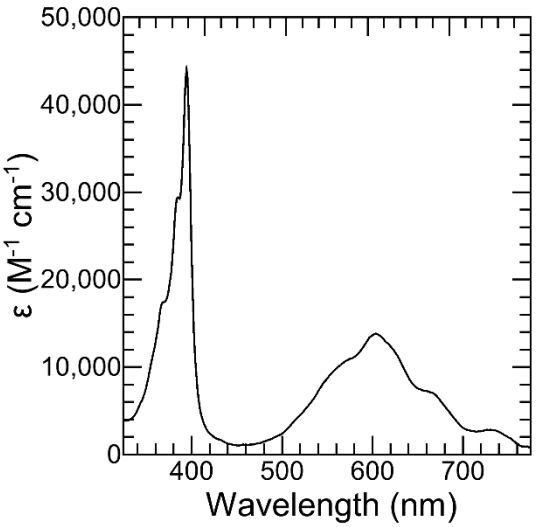

Figure 2.4.1 Extinction coefficient spectrum of MV•+

2.4.1 - Spectrophotometric determination of activity

Spectrophotometric assays utilising the absorbance of $MV^{\bullet+}$ (Fig. 2.4.1) were routinely used to quantify activity of NosZ. These were carried out in an anaerobic chamber using thoroughly degassed buffers. Disposable plastic cuvettes were commonly used for such assays and these were moved into the anaerobic chamber a minimum of 1 week before the assays to allow adsorbed oxygen to desorb.

A solution of N_2O in buffer was produced by first adding 5 mL anaerobic TK buffer to an 11 mL crimp-top vial and sealing the vial with a septum seal. The vial was then sparged with N_2O (CK Gas Products, 99%) for 5 minutes to saturate the solution, GC was used to determine the aqueous N_2O concentration which was typically 15 mM.

Solutions of blue $MV^{\bullet+}$ were produced by addition of 30 μM DT to a large excess of colourless MV^{2+} in anaerobic TK Buffer giving a $MV^{\bullet+}$ concentration of 60 μM ($A_{600\ nm}$ ≈0.8). Absorbance measurements were obtained using a Jenway 7315 spectrophotometer. From this point one of two methods was used depending on the need for enzyme activation.

Method 1 - NosZ was added to the solution of $MV^{\bullet+}$ and allowed to activate for 5 mins after which time N_2O was added to a final concentration of ≈750 μM. Addition of N_2O initiated oxidation of the $MV^{\bullet+}$ (decrease in $A_{600\ nm}$) which was followed over time.

Method 2 – N_2O was added to the $MV^{\bullet+}$ solution, and NosZ was added 30 s later. The addition of NosZ initiated oxidation of $MV^{\bullet+}$.

The rate of absorbance change at 600 nm was used to determine the enzyme turnover frequency (TOF) (moles of N_2O reduced per mole of NosZ s^{-1}) according to the following equation where $\varepsilon_{600\ nm}$ = 13700 M^{-1} cm^{-1} [147]:

$$TOF\ (s^{-1}) = \frac{-\frac{dA_{600\ nm}}{dt}}{\varepsilon_{600\ nm} \times 2 \times [NosZ]}$$

2.4.2 - Headspace [N_2O] quantification by GC

GC was used to quantify gaseous N_2O concentrations. Measurements were made on a Clarus 500 Gas Chromatograph with an Elite-Q Plot capillary column (30m × 0.53 mm) and an electron capture detector which is able to detect electrophilic species such as N_2O. The carrier gas was N_2 and 5% methane in argon was used as the make-up gas. Using a Hamilton SampleLock syringe, 50 μL of gas was manually injected and N_2O eluted from the column after 5 mins. The peak area then was integrated to give a signal.

A standard curve was produced using standard gases at 100, 1000, 5000 and 10000 ppm in N_2 (mol/mol) (Air Liquide creative oxygen) (Table 2.4.1 & Fig. 2.4.2). The volume occupied by a gas is directly proportional to its partial pressure, meaning ppm in mol/mol is equal to ppm in terms of volume. Assuming ideal gas behaviour, these concentrations in ppm can be converted to molar concentration using the ideal gas equation. From this standard curve the GC signal was found to relate to the N_2O concentration by the following equation:

$$GC\ Signal\ (\mu V\ s) = [N_2O]\ (\mu M) \times 193$$

Table 2.4.1 Conversion from ppm to concentration in μM for N_2O gas standards

ppm (mol/mol)	N_2O as proportion of volume	Moles of N_2O in 1 m^3	[N_2O] (μM)
100	0.0001	0.004	4
1000	0.001	0.04	40
5000	0.005	0.2	200
10000	0.01	0.4	400

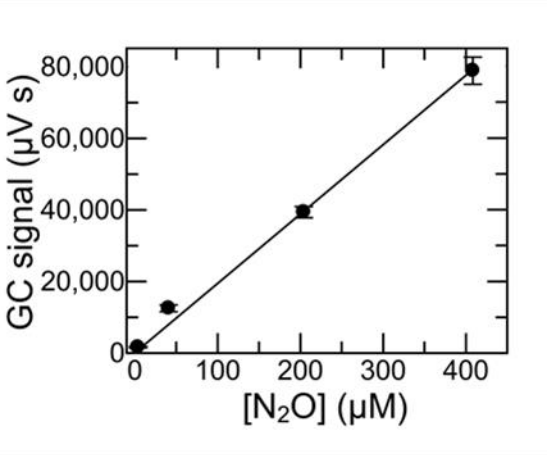

Figure 2.4.2 Standard curve of GC signal against [N_2O]. Data are the average of n≥3 measurements and error bars represent standard deviation. Line shows a linear fit to the data.

At equilibrium, the concentration of gas in a headspace can be related to the solution concentration using Henry's Law:

$$H^{cp} = \frac{[Gas]_{aq}}{p}$$

where H^{cp} is the Henry's law coefficient, $[Gas]_{aq}$ is the concentration of gas in the aqueous phase in mol m^{-3}, and p is the partial pressure of the gas in the headspace in Pa.

Henry's law can be adjusted to use different units; the dimensionless Henry solubility (H^{cc}) is especially useful as it directly relates the aqueous concentration to the headspace concentration ($[Gas]_{HS}$) in the same units:

$$H^{cc} = H^{cp} \times RT = \frac{[Gas]_{aq}}{[Gas]_{HS}}$$

where R is the gas constant and T is the temperature in K.

Under standard conditions (T = 298.15 K, 25℃) H^{cc} for N_2O is 0.595 meaning that, at equilibrium, the headspace concentration is 1.68× the aqueous concentration.[148] The overall distribution of N_2O in a sealed system is determined by the total moles of N_2O and the volumes of the aqueous phase and headspace according to the following equation:

$$\text{Total moles of } N_2O = (Volume_{HS} \times [N_2O]_{HS}) + (Volume_{aq} \times [N_2O]_{aq})$$

$$= [N_2O]_{aq} \times (Volume_{aq} + (1.68 \times Volume_{HS}))$$

GC was also used to detect activity of NosZ. To 3.9 mL TK Buffer + 1.25 mM MV in a sealed cuvette with a septum (total volume 5 mL) was added 100 µL N_2O stock solution (see above). This was allowed to equilibrate for a minimum of 1 h after which the headspace [N_2O] was measured using GC as above. And was found to be ≈500 µM with some variation between samples. To these solutions was added a known quantity of DT (quantified using $\varepsilon_{315\ nm}$ = 8000 M^{-1} cm^{-1})[149] producing blue $MV^{\bullet+}$. NosZ was added to a concentration $10^4\times$ less than the concentration of DT, this ensured the reactions completed in approximately the same time frame. When the $MV^{\bullet+}$ had been completely oxidised to colourless the system was allowed to equilibrate for 30 mins with occasional inversion. GC measurements were then made of the headspace.

Using Henry's law and other equations described above, the number of moles of N_2O that were consumed matched the number of moles of DT that were added (Table 2.4.2, Fig. 2.4.3). Unfortunately, GC has low data resolution with a realistic maximum of one data point every 10 mins. This, accompanied by issues regarding gas equilibration, makes it immensely challenging to quantify the enzyme TOF using GC. Detecting gross changes in [N_2O], however, is possible and these data suggest this technique is valid and reliable for detecting N_2O consumption by NosZ.

Table 2.4.2 Relationship between moles of DT added to reaction and amount of N_2O consumed.

Moles of DT added	ΔGC signal (µV s)	$\Delta[N_2O]_{HS}$ (µM)	ΔTotal µmol of N_2O
0	4800 ± 6760	24.9 ± 35.0	0.084 ±0.12
0.32	16600 ± 3600	86.0 ± 18.6	0.29 ± 0.063
0.5	35400 ± 6600	183 ± 34.2	0.62 ± 0.12
1	55700 ± 5950	289 ± 30.8	0.98 ± 0.10
1.4	79000 ± 4390	409 ± 22.8	1.4 ± 0.077

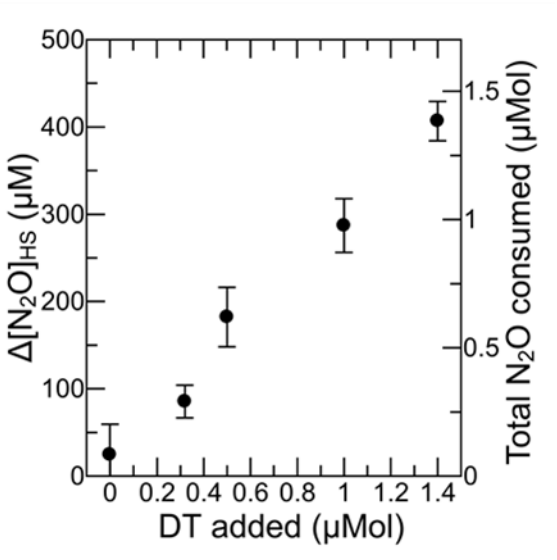

Figure 2.4.3 Plot of relationship between moles of DT added to reaction and amount of N_2O consumed. Data points are an average of n=3 GC measurements, error bars show standard deviation.

2.5 - Photochemistry

2.5.1 - Light sources

Two light sources were used in this work to irradiate samples and drive photochemistry. For excitation of the RuMe photosensitiser a Royal Blue mounted LED (light emitting diode) equipped with a collimator adapter (Thorlabs) was used. The spectral profile of this lamp is relatively narrow, with maximal emission at 450 nm which overlaps well with the metal to ligand charge transfer (MLCT) band of RuMe (Fig. 2.5.1 – Left). For excitation of graphitic carbon dots (g-CDs) and graphitic nitrogen-doped carbon dots (g-N-CDs), which have a broad absorption spectrum, a Krüss cold light source was used. This source emits throughout the visible region of the electromagnetic spectrum with minimal UV or IR emission (Fig. 2.5.1 – Right). This aided in preventing the irradiated sample from heating up or undergoing radiation induced damage.

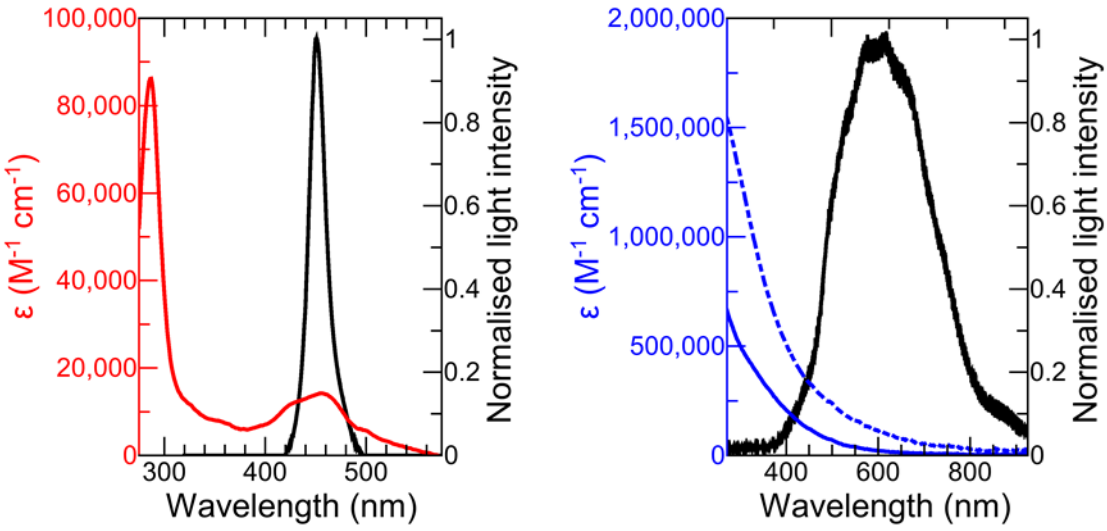

Figure 2.5.1 Spectral distributions of light source emissions and photosensitiser absorbances. **Left)** Normalised emission spectrum of Blue LED (provided by Thorlabs) (Black) and extinction coefficent spectrum of RuMeBr based on 10 μM solution (Red); **Right)** Normalised emission spectrum of Krüss cold light source (recorded by Dr. Sam Rowe using a HR2000CG-UV-NIR Ocean Optics fibre optic spectrometer) (Black) and extinction coefficient spectra of g-CDs (Blue-solid) and g-N-CDs (Blue-dashed) based on 10 μg/mL solutions and M_W of 33 and 21 kDa respectively.[150]

2.5.2 - Quantification of light intensity

Light intensity of the Krüss light source was quantified using an Amprobe Solar-100 solar power meter. On full power the irradiance at the sample was determined to be 2.5 kW m^{-2}. The Krüss light source has a power dial, measurements were also made at

"half power" and at minimum power; these irradiances were measured at 1.6 kW m^{-2} and 0.6 kW m^{-2} respectively.

As the Blue LED is effectively monochromatic, the validity of the light meter was not assured. Ferrioxalate actinometry was used to quantify the light intensity instead. Potassium ferrioxalate absorbs light below 500 nm (Fig. 2.5.2 - Left) and undergoes photolysis to form ferrous iron with a well-defined quantum yield (Φ). This ferrous iron can then be spectrophotometrically detected by complexation with 1,10-phenanthroline (phen) forming ferroin ($[Fe(phen)_3]^{2+}$) which has a characteristic λ_{max} at 511 nm ($\varepsilon_{511\ nm}$ = 11100 $M^{-1}\,cm^{-1}$) (Fig. 2.5.2 - Right).[151]

$$2\ K_3[Fe(C_2O_4)_3] + hv \rightarrow 2\ K_2[Fe(C_2O_4)_2] + K_2C_2O_4 + 2\ CO_2\ (\Phi_{450\ nm} = 1.01^{152})$$

$$K_2[Fe(C_2O_4)_2] + 3\ phen + 2\ H_2SO_4 \rightarrow [Fe(phen)_3]SO_4 + 2\ C_2O_4H_2 + K_2SO_4$$

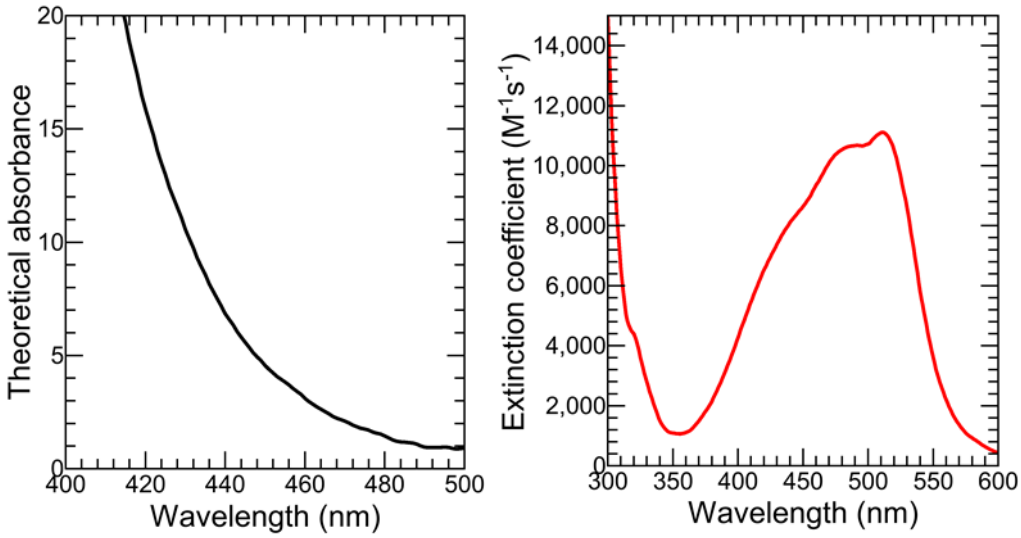

Figure 2.5.2 Left) Theoretical absorbance spectrum of a solution of 150 mM Potassium ferrioxalate, produced by scaling of a solution of 1.5 mM potassium ferrioxalate in 0.1 N H_2SO_4. **Right)** Extinction coefficient spectrum of ferroin based on a 90 μM solution generated by addition of 100 μM $FeSO_4$ to 270 μM 1,10-phenanthroline in 85 mM sodium acetate, 25 mM H_2SO_4.

Actinometry experiments were carried out in an anaerobic chamber based on the method reported by Pitre et al.[152]. A solution of 0.15 M Potassium ferrioxalate (Alfa Aesar) was prepared in anaerobic 0.1 N H_2SO_4. Care was taken to minimise light exposure and the solution was stored in a vial wrapped in black tape. A developing solution was prepared containing 1 mg mL^{-1} phen in anaerobic 1.7 M sodium acetate, 0.5 M H_2SO_4.

1 mL of the ferrioxalate solution was transferred to a cuvette and placed in a WPA Biowave II spectrophotometer to mirror photoreduction experiments (see Section 2.5.3). The solution was irradiated from above with the blue LED for set time intervals. After each irradiation the solution was mixed well and a 20 μL aliquot was removed and added

to a cuvette containing 50 µL developing solution and 930 µL anaerobic dH_2O. This solution was allowed to develop for a minimum of 10 mins before spectra were recorded using the same spectrophotometer.

The gradient of $A_{511\ nm}$ against irradiation time was and used to quantify the photon flux:

$$\text{photon flux}\left(\text{cm}^{-2}\text{s}^{-1}\right) = \frac{\frac{d[Fe^{II}]}{dt} \times N_A}{\Phi \times \text{sample area}} = \frac{\frac{dA_{511\ nm}}{dt} \times 50 \times 0.001\ \text{L} \times N_A}{\varepsilon_{511\ nm} \times \Phi \times 0.4\ \text{cm}^2}$$

where N_A is Avogadro's number and Φ is the quantum yield.

2.5.3 - Photoreduction of RuMe-MtrC

Standard photoreduction of RuMe-MtrC with EDTA was carried out in an anaerobic chamber (see Section 2.1.2) and the progress of reduction was quantified using a WPA Biowave II spectrophotometer. This spectrometer is open-topped which allowed for simultaneous irradiation and data collection. It also uses diode array optics meaning the sample is probed with white light and a full spectrum can be obtained simultaneously; this is highly useful for monitoring processes at multiple wavelengths such as during heme reduction. A downside, however, is that the probe light of the spectrophotometer contains 450 nm photons that can excite the RuMe photosensitiser. As a result of this, photoreduction rates were found to be affected by data collection frequency.

To remove this effect and obtain "clean" photoreduction traces the spectrophotometer was fitted with a 425-525 notch filter (Omega Optical) situated between the light source and the sample. This filter absorbs all light between 425 and 525 nm (Fig. 2.5.3) which minimises the excitation of RuMe by the spectrophotometer but also allows for spectroscopic monitoring of the Soret band (λ_{max} = 420 nm) and the α band (λ_{max} = 552 nm) which can be used to quantify reduced heme.

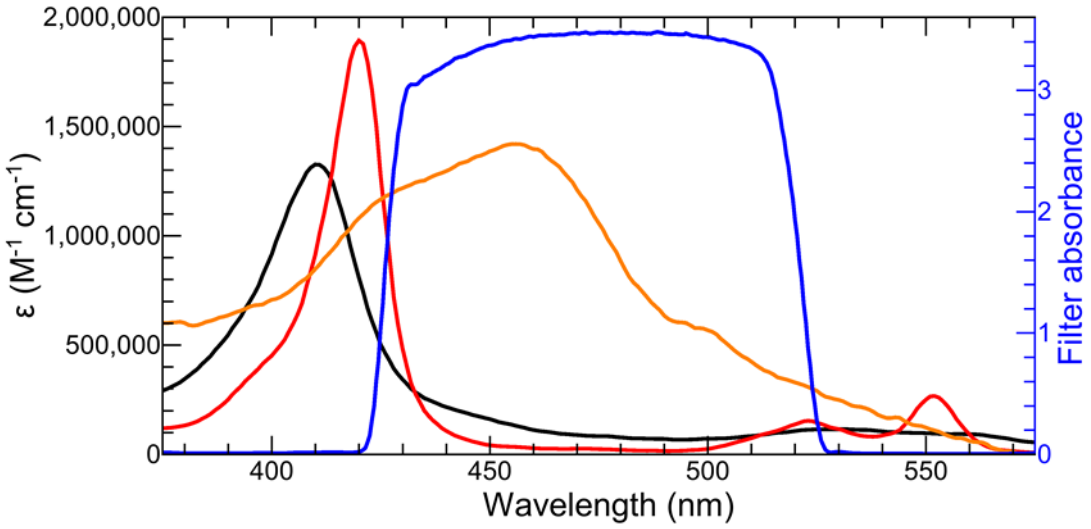

Figure 2.5.3 Extinction coefficient spectra of MtrC in oxidised (Black) and fully reduced (Red) states, and RuMe-Br (Orange) which has been scaled up 100× to be comparable to MtrC, shown in blue is an absorbance spectrum of the 425-525 notch filter obtained on a Jasco V-650 spectrophotometer.

Small aliquots (<100 µL) of concentrated RuMe-MtrC were purged with N_2 in the port of the anaerobic chamber for a minimum of 30 mins to degas them. The pH of 0.5 M EDTA solution (Fisher) was adjusted from 8 to 8.5 by addition of concentrated NaOH and degassed as described in Section 2.1.2. In a 1 cm pathlength semi-micro quartz cuvette, a 1 mL solution containing RuMe-MtrC (0.1 – 1 µM) and a desired concentration of EDTA in TK buffer was prepared. The cuvette was placed in the spectrophotometer and a t=0 spectrum was recorded.

The sample was then irradiated from above using the blue LED (whilst still in the spectrophotometer) and spectra were obtained after certain time intervals, starting out more frequently and then becoming less frequent as the reduction rate slowed down. After 1 h of irradiation the blue LED was switched off and an excess of DT was added to obtain a spectrum of the fully reduced protein.

The spectra obtained in this way were first buffer-subtracted, then each spectrum was zeroed at $A_{800\ nm}$ to account for baseline drift, finally spectra were corrected for dilution if necessary. Examples of processed spectra are shown in Figure 2.5.4 - Left. The redox state of the hemes was quantified using the difference in either $A_{420\ nm}$ (Soret maximum for reduced heme) or $A_{552\ nm}$ (α-band maximum for reduced heme). The wavelength used was dependent on the protein concentration; for [RuMe-MtrC] below 0.4 µM the Soret band was used beause the α-band was too weak for accurate determination; above 0.4 µM the α-band was typically used. Figure 2.5.4 - Right shows comparisons of analysis carried out at both wavelengths demonstrating that they give very similar results. The

proportion of hemes that are reduced at a given time was calculated using the following equation:

$$\text{Proportion of hemes reduced} = \frac{A_t - A_{t0}}{A_{DT} - A_{t0}}$$

where A_t is the absorbance (at either 420 or 552 nm) at time t, A_{t0} is the absorbance at t=0 and A_{DT} is the absorbance after addition of DT.

This equation assumes that each of the hemes in RuMe-MtrC has identical spectroscopic properties and thus contributes equally to the change in absorbance.

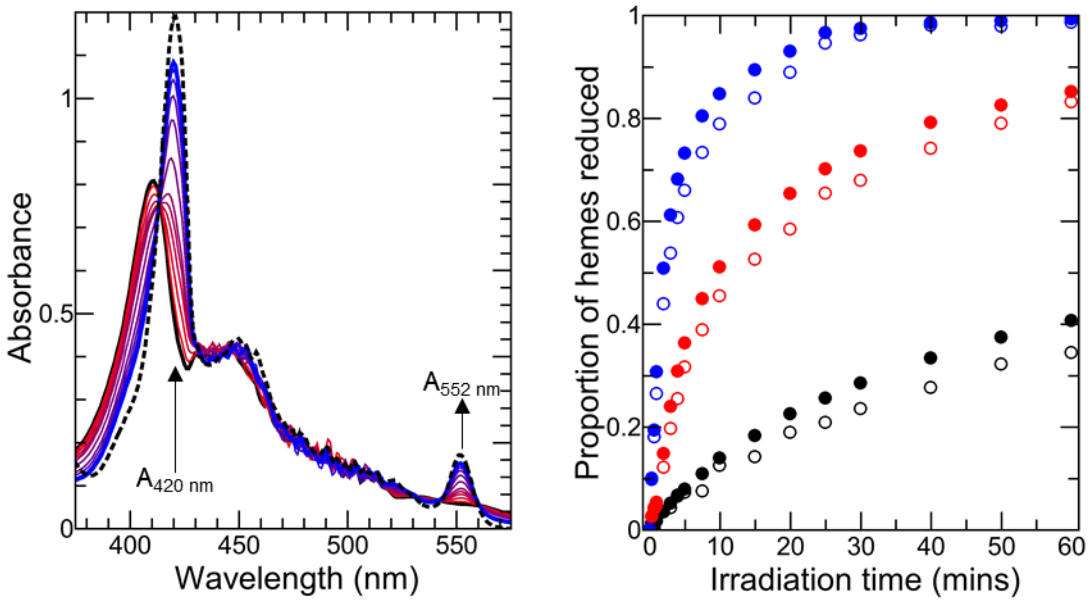

Figure 2.5.4 Left) example of spectra collected for photoreduction of 0.5 μM RuMe-MtrC in TK Buffer + 50 mM EDTA, including spectrum of oxidised protein (t=0) (solid black), spectra obtained over 1 h irradiation (Red-to-blue) and after addition of DT Dashed black), wavelengths of interest are indicated; **Right)** comparison of photoreduction timecourses for 0.5 μM RuMe-MtrC in TK Buffer + 5 (Black), 50 (Red) and 250 (Blue) mM EDTA, timecourses were generated using either $A_{420\ nm}$ (Filled) or $A_{552\ nm}$ (Hollow).

2.5.4 - Photoluminescence spectroscopy

Photoluminescence spectroscopy was used to study the decay of the RuMe excited state in RuMe-Br, RuMe-MtrC and RuMe-BSA. This analysis was performed on a Cary Eclipse fluorescence spectrophotometer. Samples were prepared anaerobically (see Section 2.1.2) in desired anaerobic buffers and sealed in photoluminescence cuvettes. Emission and excitation spectra were then obtained for the sample. The excitation slit width was 20 nm and the emission slit width was 10 nm. The detector voltage was set to medium. The inbuilt 550-1100 nm emission filter was used.

For emission spectra, the excitation wavelength was 460 nm and emission was measured from 500 to 850 nm.

For excitation spectra, the emission wavelength was 625 nm and excitation was measured from 300 to 520 nm.

2.6 - Biophysical characterisation techniques

2.6.1 - Analytical ultracentrifugation

2.6.1.1 - Principles of analytical ultracentrifugation

Analytical ultracentrifugation (AUC) is a powerful biophysical technique for studying macromolecules in solution. Using specialised rotors in a centrifuge with a spectroscopic attachment one can study the radial distribution of species in a centrifugal field. This is relatively simple for species with inherent absorbance but colourless species can also be studied by using interference spectroscopy. There are two main branches of AUC, sedimentation equilibrium (SE) and sedimentation velocity (SV). Both have been used in this work, though SE was used far more and will be described in more detail.

The forces acting on a species in a centrifugal field are:

The sedimenting force F_s imposed by the centrifuge:

$$F_s = \frac{M_W}{N_A} \omega^2 r$$

where M_W is the molecular weight of the species, N is Avogadro's constant, ω is the angular velocity in radians per second and r is the radius from the centre of rotation;

The opposing buoyant force (F_b) which describes the mass of solvent that must be displaced for the species to move:

$$F_b = \frac{M_W}{N_A} \bar{\upsilon} \rho \omega^2$$

where $\bar{\upsilon}$ is the volume of solvent in mL that each gram of species displaces, it is known as the partial specific volume and is around 0.72 for most proteins, and ρ is the density of the solvent;

And the frictional force F_f which describes the drag experienced as the species moves through the solvent:

$$F_f = fu$$

where f is the frictional coefficient which depends on how much the shape of the species deviates from a sphere and u is the velocity of the species moving through the solvent.

A species in a centrifugal field moves with constant velocity which, according to the second law of motion, means that the forces acting on the species must be balanced:

$$F_s - F_b - F_f = 0$$

The equations above can therefore be rearranged to give

$$\frac{M_W(1-\bar{\upsilon}\rho)}{N_A f} = \frac{u}{\omega^2 r} \equiv s$$

where s is the sedimentation coefficient

As the species sediments, a concentration gradient develops which resists sedimentation. As a result of these forces, a species in a conical centrifuge cell will, after sufficient time, reach a concentration equilibrium derived from a Boltzman distribution[153]:

$$c_r = c_{r_0} e^{\frac{M_W(1-\bar{\upsilon}\rho)\omega^2(r^2-r_0^2)}{2RT}}$$

where c_r is the concentration at a given radius r, and c_{r0} is the concentration at the meniscus (radius r_0).

Taking the derivative of the natural log of this equation gives:

$$\frac{d\ln(c_r)}{d(r^2-r_0^2)} = \frac{M_W(1-\bar{\upsilon}\rho)\omega^2}{2RT}$$

Which can be arranged to give

$$M_W = \frac{2RT}{(1-\bar{\upsilon}\rho)\omega^2} \times \frac{d\ln(c_r)}{d(r^2-r_0^2)}$$

The molecular weight of the species is therefore directly proportional to the gradient of a plot of $\ln(c_r)$ against radius of rotation at equilibrium. Interactions of species can also be detected as complexation will create a species with greater M_W which will sediment more strongly. SE is carried out using moderate centrifugation speeds and experiments can take days due to the time necessary to reach equilibrium.

SV, on the other hand, involves spinning samples at much greater speeds and observing the sedimentation process over time. Radial distributions of species are obtained over a few hours. These are then fitted to a series of Lamm equations which describe the sedimentation of species in a sector shaped cell as a function of the sedimentation coefficient.[154] Software exists to give estimates of the solutions to these equations and give a sedimentation coefficient distribution for a sample. SV is useful for many applications including detecting heterogeneity in a sample.

2.6.1.2 - Experimental setup and data analysis

Both SE and SV experiments were carried out using a Beckman Optima XL-1 Analytical Ultracentrifuge with an 8 cell Ti50 rotor. Protein samples were prepared in 50 mM H_2NaPO_4/HNa_2PO_4, 50 mM NaCl, 0.1% (v/v) TX100, pH 7.5 buffer (PNTx Buffer). All experiments were carried out at 20℃ and this temperature was maintained throughout.

For SE experiments:

100 µL of each sample was loaded into AUC cells and 120 µL of buffer was used as a reference. Samples were centrifuged at 8000 RPM for 24 h to reach the first equilibrium, at this time 10 radial scans of each cell (Fig. 2.6.1) were taken at an appropriate wavelength (absorbance between 0.4-0.8 at t=0). The centrifuge speed was then increased to 10000 RPM and left to equilibrate for 18 h after which time another 10 scans were taken. Finally, the centrifuge speed was increased to 12000 RPM for a further 18 h and 10 more scans were taken. As no systemic changes were observed through each set of 10 scans the system was confirmed to have reached equilibria.

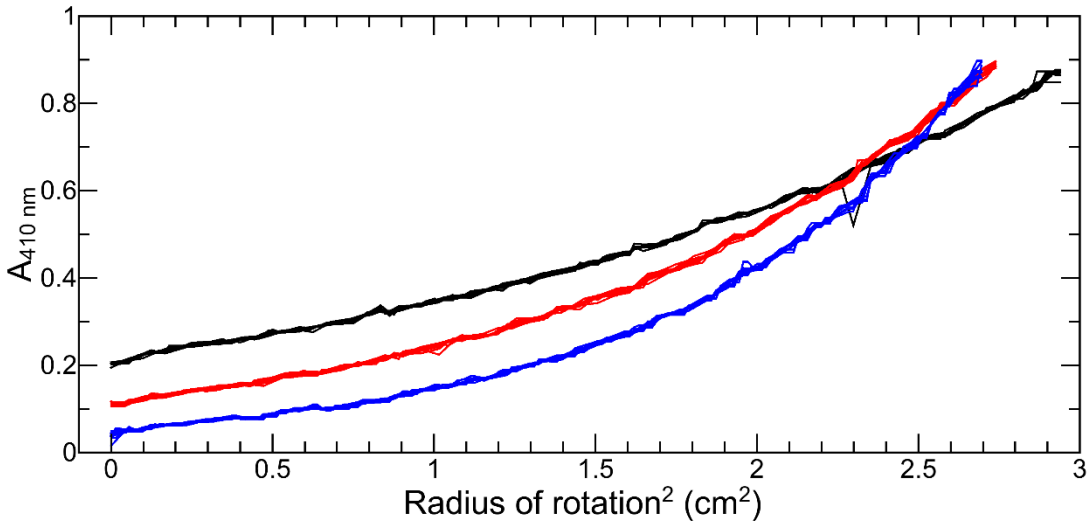

Figure 2.6.1 Example of complete data set obtained for 0.5 µM MtrAB. 10 scans are shown at each of three centrifuge speeds: 8k (Black), 10k (Red) and 12k (Blue) RPM.

Data analysis was performed using Ultrascan II software. $\bar{\upsilon}$ values were calculated from the protein sequence using the built-in tool and the buffer density was estimated to be 1.007 g/mL. Three clean scans from each speed were selected for the global fitting procedure, the fitting algorithm used was the modified Gauss-Newton.

Two caveats should be noted, firstly the contribution to $\bar{\upsilon}$ of the RuMe label or *c*-type hemes is unknown, for all samples the protein sequence alone was used to calculate the $\bar{\upsilon}$. Secondly, the detergent (TX100) is not considered during fitting. TX100 forms large micelles of ≈100 kDa however it has a $\bar{\upsilon}$ of 0.91 mL g^{-1}.[135] This value is close to the density of the buffer which minimises its effect on the sedimentation of the proteins.

For SV experiments:

380 µL of sample was loaded into AUC cells with 400 µL of buffer as a reference. Samples were centrifuged at 38000 RPM and radial scans were obtained continuously in a round-robin style; with three samples this resulted in intervals of ≈80 s between each scan for each sample. This was carried out over a 3 h period. Examples of such scans are shown in Figure 2.6.2 where the effect of centrifugation can be visualised.

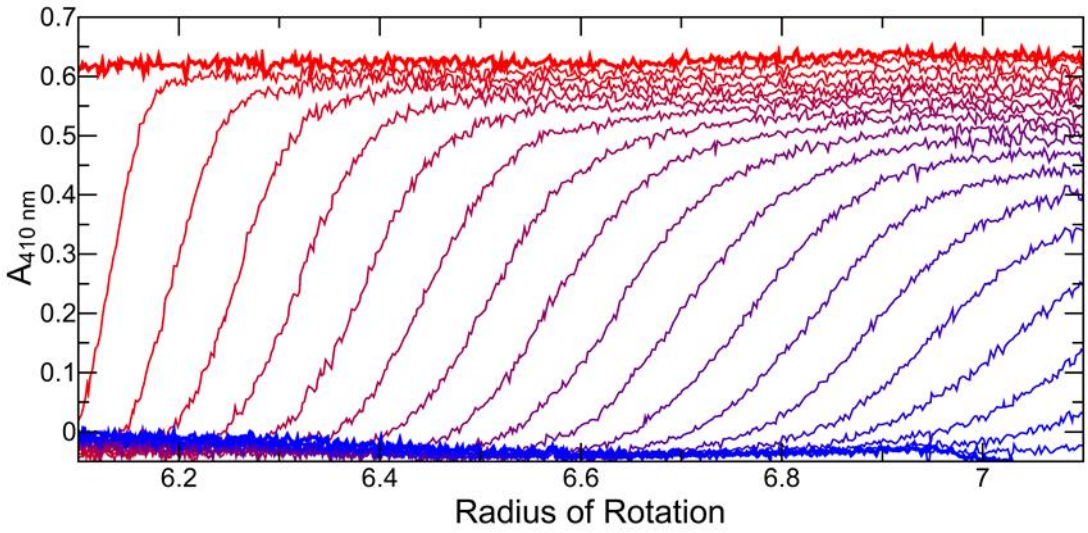

Figure 2.6.2 Examples of SV scans obtained for a 0.5 µM sample of RuMe-MtrCAB. Scans show radial concentration distribution before (Red) and during centrifugation at 38k RPM (Red-to-Blue).

Scans were analysed in Sedfit software[154] which uses the Lamm equation to determine a distribution of sedimentation coefficients for the sample. This was then converted to a M_W distribution using values of $\bar{\upsilon}$ and ρ from Ultrascan II.

2.6.2 - Small-angle neutron scattering

2.6.2.1 - Principles of small-angle neutron scattering

Small-angle scattering (SAS) techniques enables collection of structural information on species in solution, avoiding the need to produce crystals. Small-angle X-ray scattering (SAXS) is commonly used for the study of soluble proteins however the presence of detergent micelles, which scatter X-rays strongly, prohibits the use of SAXS for the study of membrane associated proteins.

Small-angle neutron scattering[155] (SANS), on the other hand, is very useful for studying proteins in detergent solution. This is due to the high contrast in scattering length between hydrogen (-3.74 fm) and deuterium (6.67 fm) nuclei.[156] The scattering of the buffer in which the species is dissolved is therefore hugely dependant on the H_2O:D_2O ratio. Due to their average molecular composition, different types of molecules (e.g. detergent vs. protein) have different scattering properties. By using a particular concentration of D_2O, some species in a mixture will produce scatter indiscriminate from that of the buffer; this allows the remaining components to be resolved with high contrast. This technique is known as contrast matching and uses D_2O concentrations known as match points. Match points for detergents and lipids are typically in the 5-20% D_2O range whereas for proteins ≈40% D_2O is required.[156]

Neutrons scatter due to elastic scattering off atomic nuclei in a species. When a collimated beam of in-phase neutrons interacts with a sample, each nuclei behaves as a source of spherical waves. Constructive interference between nuclei leads to scattering at a particular angle (2θ) which is related to the distance between the nuclei (d) and the wavelength of the neutrons (λ) (Fig. 2.6.3 - Left), from this angle we can derive the momentum transfer (Q) (Fig. 2.6.3 - Right). For a species in solution, the random orientation of the species gives a scattering pattern with radial symmetry. This is averaged to give a plot of scattering intensity (I) vs Q (Fig. 2.6.4A) which can be used to determine numerous structural properties of a species.

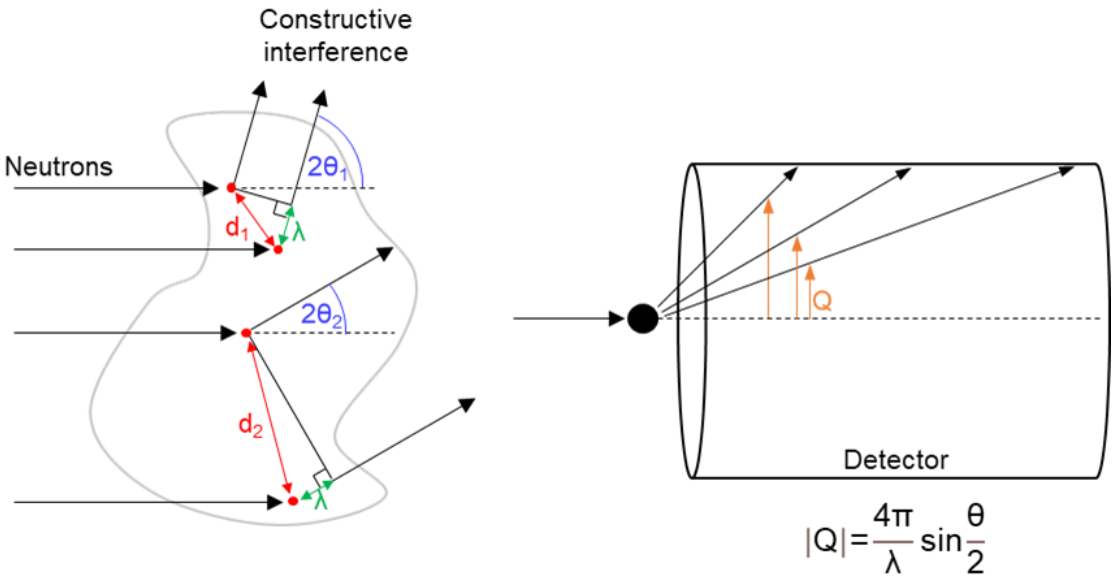

Figure 2.6.3 Principles of SANS. **Left)** Examples of neutron scattering deriving from constructive interference between two pairs of nuclei (red dots) with distances d_1 and d_2, these distances determine the angle (2θ) of the scattering; **Right)** example of how scattered neutrons emanating from a sample (Black circle) are detected in a tubular detector, size of the momentum transfer (Q) is shown by the length of the orange arrows, Q and θ are related by the given equation.

2.6.2.2 - Experimental setup and data collection

Samples of RuMe-MtrC:MtrAB and MtrC:MtrAB were prepared by reconstitution and gel filtration (see Section 4.2.1). Together with WT MtrCAB, these protein complexes were exchanged into 20 mM HEPES, 100 mM NaCl, 2.8 mM Fos-Choline-12, pH 7.8 Buffer (HNF Buffer) as described in Section 2.1.3. These samples were snap-frozen and transported to Institute Laue-Langevin (ILL) where experiments and data analysis were performed in collaboration with Dr Anne Martel (ILL) and Dr Marcus Edwards (UEA). On site these samples were dialysed against 20 mM HEPES, 100 mM NaCl, 2.8 mM Fos-Choline-12, 13% D_2O, pH 7.8 Buffer (HNFD Buffer) overnight at 4°C. Previous experiments had established 13% D_2O as the match point for Fos-choline 12.[157] This is in agreement with literature values.[158,159]

Samples were then prepared at two concentrations by dilution into the bulk dialysis buffer. For RuMe-MtrC:MtrAB and WT MtrCAB the concentrations were 6.3 and 3.1 mg/mL, for MtrC:MtrAB the concentrations were 11.9 and 4 mg/mL. Scattering data were obtained for each sample and the bulk dialysis buffer using the D22 instrument with detector distances of 1.4, 8 and 17.6 m and a neutron wavelength of 6 Å. Radial integration and subtraction of background scattering were carried out by Dr. Anne Martel on site at ILL. Scattering from the buffer was then subtracted to give the contribution from the protein (Fig. 2.6.4A). The scattering intensity after buffer subtraction was found to scale linearly with protein concentration meaning that concentration dependent affects

were not present (Fig. 2.6.4B). The data for the concentrated samples were taken forwards. The scattering curves at each detector distance have sufficient overlap to allow them to be confidently merged and baseline corrected using SANS and USANS Data Reduction and Analysis software in Igor Pro to form continuous scattering curves from Q = 0.005 to 0.55 $Å^{-1}$ (Fig. 2.6.4C). Further analyses are presented in Section 4.3.

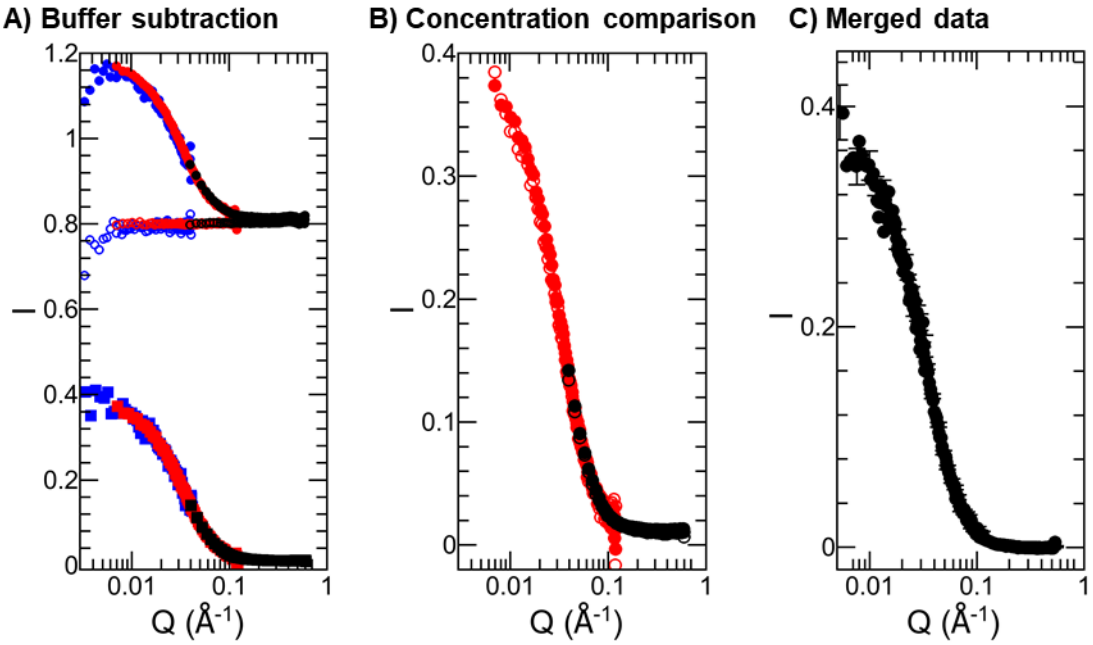

Figure 2.6.4 SANS initial data processing. **A)** Scattering data for 6.3 mg/mL RuMe-MtrC:MtrAB (Filled circles), buffer (Empty circles) and after subtracting buffer data from protein data (Squares), three detector distances shown in different colours, 1.4 m (Black), 8 m (Red), 17.6 m (Blue); **B)** Comparison of buffer-subtracted scattering data for 6.3 mg/mL (Filled) and 3.1 mg/mL (Empty) RuMe-MtrC:MtrAB after scaling up by a factor of 2.03, colour coding as in A; **C)** Final merged and baseline-corrected scattering curve for RuMe-MtrC:MtrAB.

2.7 - Liposome preparation and analyses

2.7.1 - Liposome nomenclature

Liposomes in this work are named according to their composition using this template:

Membrane protein:Lipid-[Cargo]

For example, liposomes with MtrCAB incorporated into a lipid bilayer composed of polar lipid extract (PLE) with Reactive Red 120 (RR120) as a cargo are named:

MtrCAB:PLE-[RR120]

And liposomes without any membrane proteins but with NosZ encapsulated using PLE are named:

PLE-[NosZ]

2.7.2 - Liposome preparation

Liposome formation, cargo encapsulation and membrane protein incorporation were carried out simultaneously by removal of detergent from a solution of lipid, cargo and membrane protein. Two methods were used to remove the detergent.

The first method is termed the Dilution method and was adapted from that reported in Stikane et al.[160] It was designed to be used for encapsulation of molecular cargos such as azo dyes. This method requires a large volume of prospective cargo at a relatively high concentration which makes it somewhat prohibitive for encapsulating valuable cargos such as enzymes.

The second method was developed as part of this thesis and uses Biobeads (macroporous, non-polar, polystyrene beads) to sequester detergent from a small volume of solublised lipid, cargo and membrane protein. This method is termed the Biobead-mediated detergent sequestration method. A smaller commitment of cargo is required and it has a higher encapsulation efficiency than the Dilution method. This method was designed for the encapsulation of valuable cargos such as enzymes.

Methods of liposome formation and washing are described below. All centrifugation carried out at 4℃.

2.7.2.1 - Dilution method of liposome preparation

This method was used to encapsulate azo dyes and was ultimately required to encapsulate enzymes as will be discussed in Section 6.4, the latter required slight variations to the initial part of the method.

Liposome formation:

To encapsulate azo dyes, 20 mg of PLE (Avanti Polar Lipids) was suspended in 750 µL TK Buffer + 10 mM RR120 or RB5 (both sourced from Sigma) and vortexed vigorously for 30 mins to fully suspend the lipid. To this was added 500 µL 250 mM Octyl glucoside (OG) (Anatrace) in TK buffer. This caused the solution to turn from cloudy to clear, indicating solubilisation of the lipid. Mtr protein (typically 100 µL, 25 µM) was then added (either MtrCAB, RuMe-MtrCAB or MtrAB) in PNL buffer. If the liposomes were being prepared without Mtr proteins an equivalent volume of PNL buffer was added for consistency. The lipid-protein solutions were left for 30 mins at 4℃ to allow for complete detergent exchange before being diluted to 50 mL in ice-cold TK Buffer + 10 mM Azo dye which produced a dilute suspension of liposomes.

To encapsulate NosZ, 20 mg PLE was suspended in 500 µL anaerobic TK buffer and vortexed vigorously for 30 mins to fully suspend the lipid. 250 µL of 500 mM OG was then added to solubilise the lipid followed by addition of PNL buffer ±Mtr proteins as above. DT and MV were then added to 500 µM and 100 µM respectively and finally fully activated NosZ (15 µM, 400 µL) was added. The solutions were then diluted to 50 mL in TK buffer + 100 µM MV + 500 µM DT which produced a dilute suspension of liposomes

Liposome washing:

Dilute suspensions were centrifuged at 205000 ×g (Type 45 Ti, 42k) for 1 h. The pellet was transferred to an anaerobic chamber and resuspended in 50 mL anaerobic TK buffer (+500 µM DT for NosZ liposomes) then centrifuged as before. The resulting pellet was resuspended in 750 µL anaerobic TK Buffer (+100 µM DT for NosZ liposomes) which yielded ≈1 mL stock liposome suspension. This suspension was centrifuged for 5 mins at 3000 RPM in a benchtop centrifuge to pellet any non-incorporated/aggregated material and then left standing in an anaerobic chamber for 16 h at room temperature to degas.

2.7.2.2 - Biobead-mediated detergent sequestration method of liposome preparation:

This method was developed for the encapsulation of cargos such as enzymes where the dilution method was deemed too wasteful. This method was, however, found to be impeded by the presence of some organics, namely $MV^{\bullet+}$.

Liposome formation:

20 mg PLE was suspended in 500 µL anaerobic TK buffer by vigorous vortex for 30 mins. 250 µL of 500 mM OG was added to solubilise the lipid followed by PNL buffer ±Mtr proteins as above. Cargo proteins (PazSII and NosZ) were then added along with 500 µM DT to maintain anaerobicity. To remove the detergent, a 50 mg aliquot of thoroughly degassed Biobeads (Bio-rad) were added and the sequestration was allowed to proceed for 30 mins with occasional inversion. The solution was then transferred to a fresh 50 mg aliquot of Biobeads for a further 30 mins, followed by two 30 min incubations with 100 mg Biobeads. At this point the solution was cloudy, indicating the presence of liposomes, and was diluted into 25 mL TK Buffer + 500 µM DT.

Liposome Washing:

The liposome suspension was centrifuged three times at 434000 ×g (Type 70 Ti, 65k RPM) for 30 mins with resuspension in 25 mL TK buffer + 500 μM DT. After the final centrifugation the pellet was resuspended in 750 μL TK Buffer + 100 μM DT yielding ≈1 mL liposome suspension. The suspension was centrifuged for 5 mins at 3000 RPM in a benchtop centrifuge to pellet any non-incorporated/aggregated material and then left standing in an anaerobic chamber for 16 h at room temperature to degas.

2.7.3 - Dynamic light scattering

Dynamic light scattering[161] (DLS) is a technique that can be used to quantify the size of particles in solution. All particles in solution undergo Brownian motion, where collision with solvent molecules causes them to migrate randomly through the solution. As a result, the scattering pattern from a collimated, polarised laser beam passing through a solution will vary in intensity over time. Because larger particles move more slowly than small particles the scattering intensity fluctuates more slowly for larger particles, however the amplitude of the signal is greater (Fig. 2.7.1 - Left). The fluctuating signal is converted to a correlation function by comparing the intensity of scattering at a particular point with the intensity at all other points. Because larger particles have slower fluctuations the correlation function decays more gradually (Fig. 2.7.1 - Right).

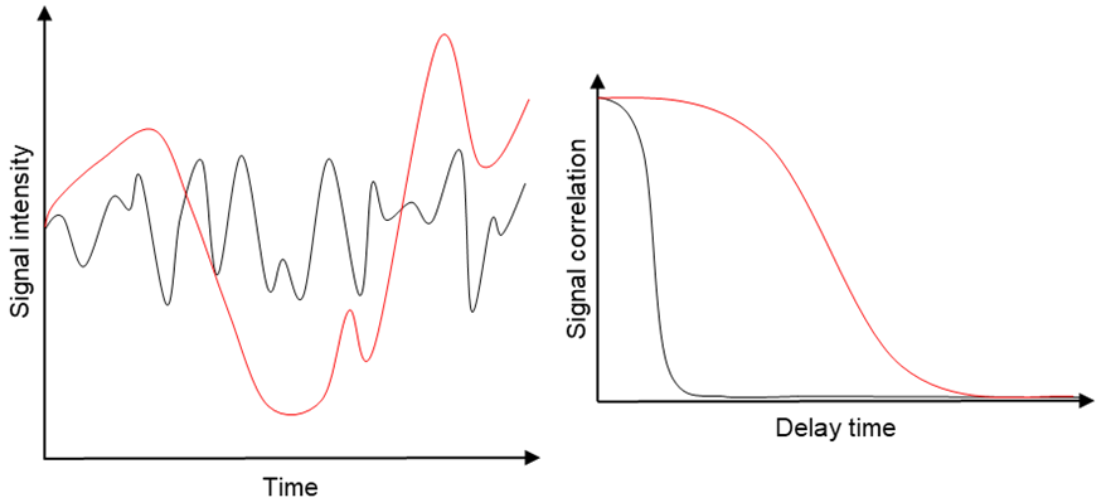

Figure 2.7.1 Principles of DLS. **Left)** theoretical examples of fluctuations in scattering signal intensity for a small particle (Black) and a large particle (Red); **Right)** Conversion of signal fluctuations to correlation functions.

The correlation function can be used to derive the diffusion coefficient (D), or range of diffusion coefficients, which is related to the particle size by the Stokes-Einstein equation:

$$D = \frac{k_B T}{6\pi\eta r}$$

where k_B is the Boltzman constant, T is temperature in kelvin, η is the solvent viscosity and r is the radius of the solute.

Dynamic light scattering (DLS) was used to measure the size distribution of liposomes after formation. Liposome stocks were diluted into 1 mL TK buffer (typically 50× dilution) and transferred to DTS1070 folded capillary cells (Malvern Panalytical). DLS measurements were carried out on a Zetasizer Nano (Malvern Panalytical) after equilibration for 2 mins at 25℃. Data analysis was automatically carried out in real time by Malvern software. The solvent viscosity was considered to be that of water.

2.7.4 - Estimating number of liposomes

Determining the concentration of nanoparticles in a solution is challenging, especially when a range of sizes are present. One method that can be used is Nanoparticle tracking analysis[162] however this was not available during this project. Estimates were made based on knowledge of the lipid formulation, the mass of lipid used and the size of the liposomes as determined by DLS (see Section 2.7.3).

The distribution of lipid types in PLE is provided by Avanti[163] (Table 2.7.1) along with average molecular weights provided for “pure” *E. coli* phosphatidylethanolamine[164] (PE), phosphatidylglycerol[165] (PG) and cardiolipin (CA)[166].

Table 2.7.1 Composition of PLE sourced from Avanti[163–166]

Component	Percentage by weight	Average molecular weight (Da)	Percentage by number
Phosphatidylethanolamines (PE)	67	719.3	71.3
Phosphatidylglycerols (PG)	23.2	761.1	23.4
Cardiolipin (CA)	9.8	1430.0	5.3

An average molecular weight for PLE can therefore be determined:

$$\frac{(71.3\times719.3\text{ Da})+(23.4\times761.1\text{ Da})+(5.3\times1430.0\text{ Da})}{100} = 766.7\text{ Da}$$

DLS of the liposomes prepared in this work reveal that most have a size distribution with a mean diameter of either ≈100 nm or ≈250 nm. The width of a phospholipid bilayer is ≈4 nm,[167] meaning the inner leaflets of these liposomes have diameters of ≈92 nm or ≈242 nm. Using these values and the formula for the surface area of a sphere ($4\pi r^2$) the total surface area of a liposome can be estimated:

$$\text{For 100 nm liposome: } 4\pi(50\text{ nm})^2 + 4\pi(46\text{ nm})^2 \approx 58000\text{ nm}^2$$

$$\text{For 250 nm liposome: } 4\pi(125\text{ nm})^2 + 4\pi(121\text{ nm})^2 \approx 380000\text{ nm}^2$$

The average footprint of a phospholipid is ≈0.7 nm^2.[167] This means the number of lipids required to form one liposome can be estimated:

$$\text{For 100 nm liposome: } \frac{58000\text{ nm}^2}{0.7\text{ nm}^2} = 82866$$

$$\text{For 250 nm liposome: } \frac{380000\text{ nm}^2}{0.7\text{ nm}^2} = 543000$$

Each liposome therefore has a M_W of :

$$\text{For 100 nm liposome: } 82866 \times 766.7\text{ Da} = 64\text{ MDa}$$

$$\text{For 250 nm liposome: } 543000 \times 766.7\text{ Da} = 417\text{ MDa}$$

These molecular weights can be used to calculate the total number of liposomes that can be prepared from 20 mg PLE.

$$\text{For 100 nm liposomes: } \frac{2\times10^{-2}\text{ g}}{6.4\times10^{7}\text{ g mol}^{-1}} \approx 300\text{ pMol} = 1.8\times10^{14}\text{ liposomes}$$

$$\text{For 250 nm liposomes: } \frac{2\times10^{-2}\text{ g}}{4.17\times10^{8}\text{ g mol}^{-1}} \approx 50\text{ pMol} = 2.9\times10^{13}\text{ liposomes}$$

After final resuspension in 1 mL, these liposome suspensions are therefore estimated at 300 and 50 nM respectively.

The total internal volume of the liposomes can be calculated using the formula for the volume of a sphere ($\frac{4}{3}\pi r^3$) and internal diameters of 92 nm or 242 nm:

$$\text{For 100 nm liposomes: } \frac{4}{3}\pi(46\text{ nm})^3 \times 1.8\times10^{14} = 7.3\times10^{19}\text{ nm}^3 = 73\ \mu\text{L}$$

$$\text{For 250 nm liposomes: } \frac{4}{3}\pi(121\text{ nm})^3 \times 2.9\times10^{13} = 2.1\times10^{20}\text{ nm}^3 = 210\ \mu\text{L}$$

CHAPTER 3

PHOTOCHEMISTRY OF RuMe-MtrC

Chapter 3 - Photochemistry of RuMe-MtrC

3.1 - The MtrCAB complex and RuMe-MtrC

A complex of MtrC, MtrA and MtrB, termed MtrCAB (Fig. 3.1.1 - Left),[168] has been identified as the main route for electrons to cross the outer membrane of *Shewanella* species. MtrC and MtrA each contain ten *c*-type hemes that form a conductive chain (Fig. 3.1.1 - Right) Whilst not being redox active itself, MtrB plays a vital role, acting as a porin and allowing the multiheme cytochromes to insert into the otherwise insulating outer membrane. Recent structural characterisation of MtrCAB from *Shewanella baltica* shows that MtrA inserts almost fully into the 28-strand β-barrel of MtrB, MtrC is found on the extracellular face of the complex and is oriented such that heme 5 of MtrC is within 14 Å of heme 10 of MtrA.[134] This complex allows electrons to pass from the periplasm of the bacterium to the extracellular environment and also has a role in catalysing the reduction of extracellular substrates.[168–170]

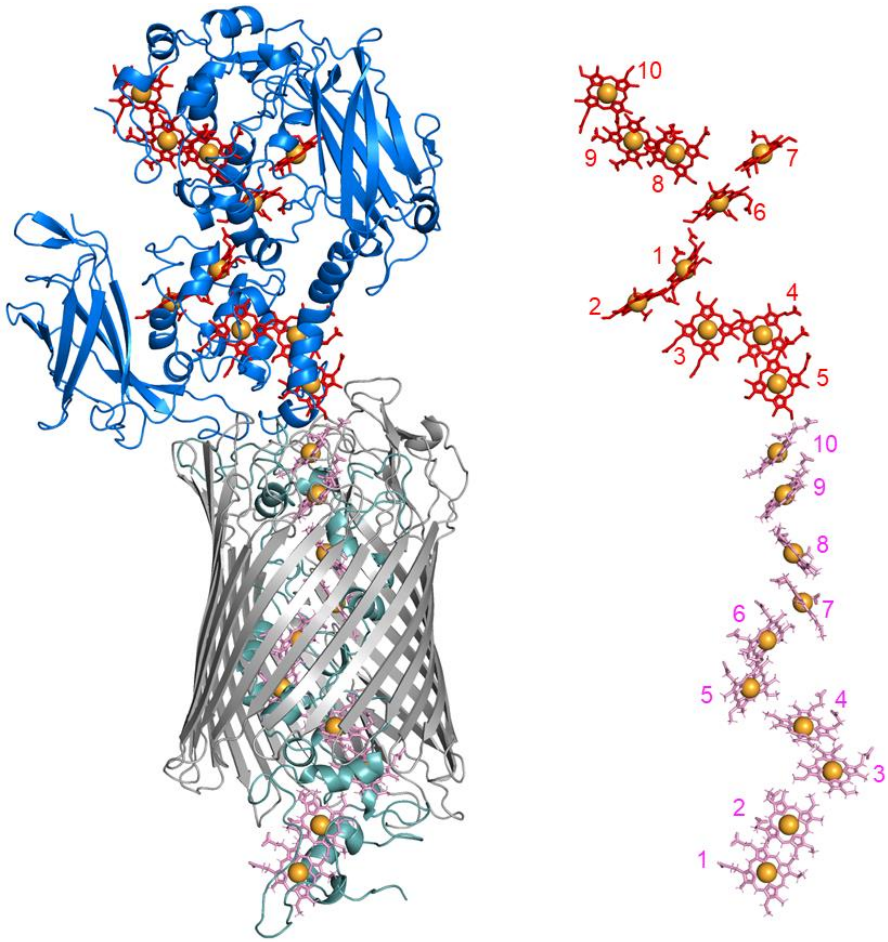

Figure 3.1.1 Left) Homology model of MtrCAB from MR-1 built from structure of MtrCAB from *S. baltica* (6R2Q)[134], MtrC (blue with red hemes), MtrA (teal with pink hemes) MtrB (grey), Iron atoms shown as bronze spheres; **Right)** Heme chain from homology model of MtrCAB with hemes numbered according to position in amino acid sequence. Models rendered in Chimera software.

The MtrCAB complex has been studied *in vitro* by numerous methods revealing much about its structural, biophysical and electronic properties. Those studies will be explored in more detail in Chapter 4, the focus of this chapter will be on the extracellular cytochrome MtrC. The ten hemes of MtrC have chemically identical His/His ligation which are challenging to distinguish spectroscopically, complicating the task of elucidating the properties of any specific heme. Redox windows for the ten hemes of MtrC have been reported from voltametric studies of protein adsorbed on electrodes and potentiometric titrations in solution. These reveal that the hemes of MtrC have reduction potentials between 0 and -400 mV (vs. SHE).[171,172]

Recent work in our lab has allowed MtrC to be purified, in quantities suitable for biochemical studies, as a water-soluble Strep-II tagged protein from an inducible plasmid in MR-1 (see Section 2.3.1).[143] The electrochemical properties of this MtrC construct have been examined by potentiometric titration and cyclic voltammetry and the hemes of MtrC are found to have a macroscopic reduction potential window ranging from +31 to -233 mV or -25 to -331 mV respectively. This construct is amenable to SDM, allowing for introduction of cysteines as photosensitiser binding sites (van Wonderen et al., in preparation). Use of the cysteine reactive photosensitiser RuMe-Br was pioneered by Millett and Durham[173–175] and has since been used to photosensitise cytochromes such as PpcA[176] and STC[131,132] as well as other proteins (see Section 1.4.2). Here, RuMe has been covalently attached to MtrC-Y_{657}C. In this construct the RuMe photosensitiser is positioned close to heme 10 of MtrC with a distance of ≈5 Å between the edge of RuMe to the edge of heme 10.

From previous studies of multiheme cytochromes labelled in this way[131,132,173–176] we would expect RuMe-MtrC to have a photocycle as depicted in Figure 3.1.3. Excitation of RuMe with ≈450 nm light (①) generates singlet $^{1}Ru^{II*}$-Fe^{III} which undergoes rapid (<ps) ISC to give the long-lived triplet state $^{3}Ru^{II*}$-Fe^{III}. The excited state $^{3}Ru^{II*}$-Fe^{III} may then return to the ground state by a non-luminescent pathway or by photoluminescence (②), releasing a photon at ≈620 nm. Alternatively, the excited state can undergo charge separation (CS - ③) leading to the CSS Ru^{III}-Fe^{II}. The CSS can then decay back to the ground state Ru^{II}-Fe^{III} by charge recombination (CR - ④), however if an appropriate SED is present the Ru^{III} can be reduced (⑤) giving Ru^{II}-Fe^{II}. This process of light-driven electron accumulation is termed photoreduction. Each of these electron transfer processes has an associated rate constant, some of which have also been investigated for other photosensitised cytochromes.[131,173–176]

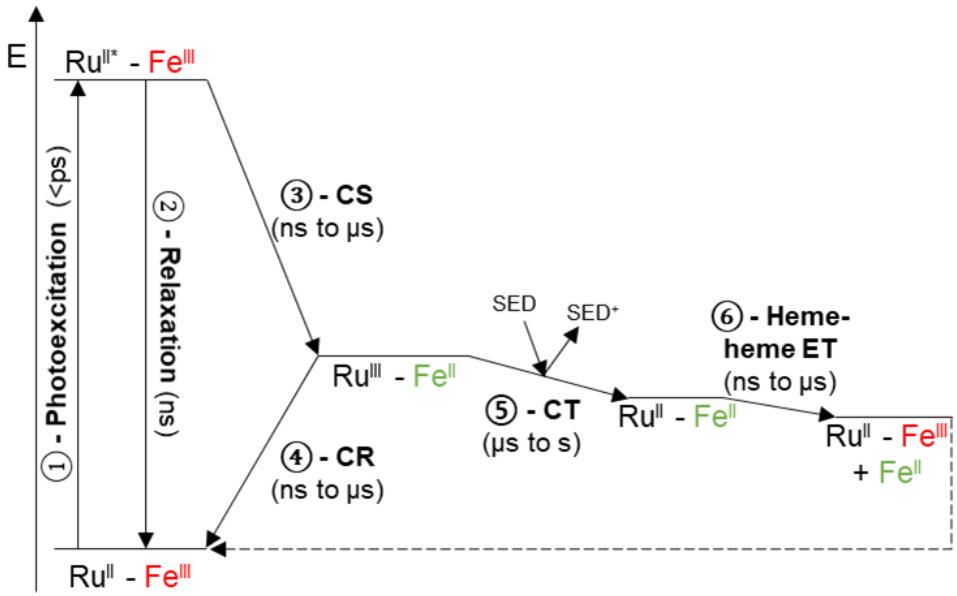

Figure 3.1.2 Proposed photocycle for RuMe-MtrC. For simplicity the spin states of RuMe are omitted and only the first heme of MtrC (Heme 10) is explicitly shown. After step ⑥-Heme-heme ET the system is considered to have effectively returned to the ground state (dashed arrow) and can undergo photoexcitation again. Approximate timescales of each process are also indicated. See Table 3.1.1 for (photo)reduction potentials for redox transitions in this photocycle.

Table 3.1.1 Reduction potentials for RuMe in ground and excited states[177], heme 10[178], and EDTA[10].

Redox transition	Reduction potential (mV vs SHE)
$Ru^{III/II}$	1270
$Ru^{III/II*}$	-870
$Ru^{II*/I}$	790
$Ru^{II/I}$	-1360
$Fe^{III/II}$ (heme 10)	≈ 0
$SED^{0/+}$ (EDTA)	814-1164

The aim of this chapter is to evaluate RuMe-MtrC as a component of a photocatalytic system. Firstly, this involved identifying the conditions under which RuMe-MtrC could be photoreduced (generate and accumulate electrons upon irradiation). The photochemistry of RuMe-MtrC was then explored to understand its photocycle under these conditions. The factors that limit the rate of photoreduction were investigated and the stability and longevity of electron production by RuMe-MtrC were determined using a redox dye as a colourimetric indicator of electron production. The findings from these studies were then used to create a kinetic model of photoreduction of RuMe-MtrC exploring the different rate-determining parameters that affect its photochemistry.

3.2 - Investigating the photochemistry of RuMe-MtrC

3.2.1 - Developing a method for photoreduction of MtrC

Photoreduction forms the first key component of the photocatalytic nanoreactor depicted in Figure 1.6.2. This process requires a source of electrons and the use of SEDs as electron sources for such systems has been described previously (Section 1.2). Here, potential SEDs were tested for their capacity to support cumulative photoreduction of RuMe-MtrC as indicated by optical changes characteristic of Fe^{III} to Fe^{II} heme during continuous irradiation by blue light. Chemicals were screened from different families of molecules reported to act as SEDs in other systems: tertiary amines, carboxylic acids and thiols.[10] Some common pH buffering components were also assessed for their ability to act as SEDs to facilitate the design of future experiments.

Fully oxidised RuMe-MtrC was diluted to ≈0.5 μM in anaerobic 50 mM NaH_2PO_4/Na_2HPO_4, 50 mM NaCl, pH 7.5 buffer (PN Buffer) supplemented with 50 or 100 mM SED also at pH 7.5. In the cases where buffer components were being investigated as potential SEDs PN Buffer was not used and a 50 mM buffer of appropriate pH was used instead (Table 3.2.1). Irradiation was supplied using a mounted LED with an emission maximum at 455 nm (see Section 2.5.1). Spectra were obtained over this time and the redox state of the hemes of RuMe-MtrC was quantified through changes in the absorbance at the Soret (420 nm) and/or α-band (552 nm) as described fully in Section 2.5.3.

In the absence of any SED (PN buffer only) no photoreduction was observed (Fig. 3.2.1A). Of the SEDs screened (Table 3.2.1), only EDTA was found to be suitable as an SED. EDTA was able to support photoreduction under irradiation conditions (Fig. 3.2.1B) with no reduction observed in the dark (Fig. 3.2.1E). Cysteine was also found to support light-driven reduction (Fig. 3.2.1C), however in control experiments without irradiation cysteine led to a slow reduction of RuMe-MtrC (Fig. 3.2.1D). This dark reaction precludes the use of cysteine in the detailed kinetic studies that are the goal of this chapter.

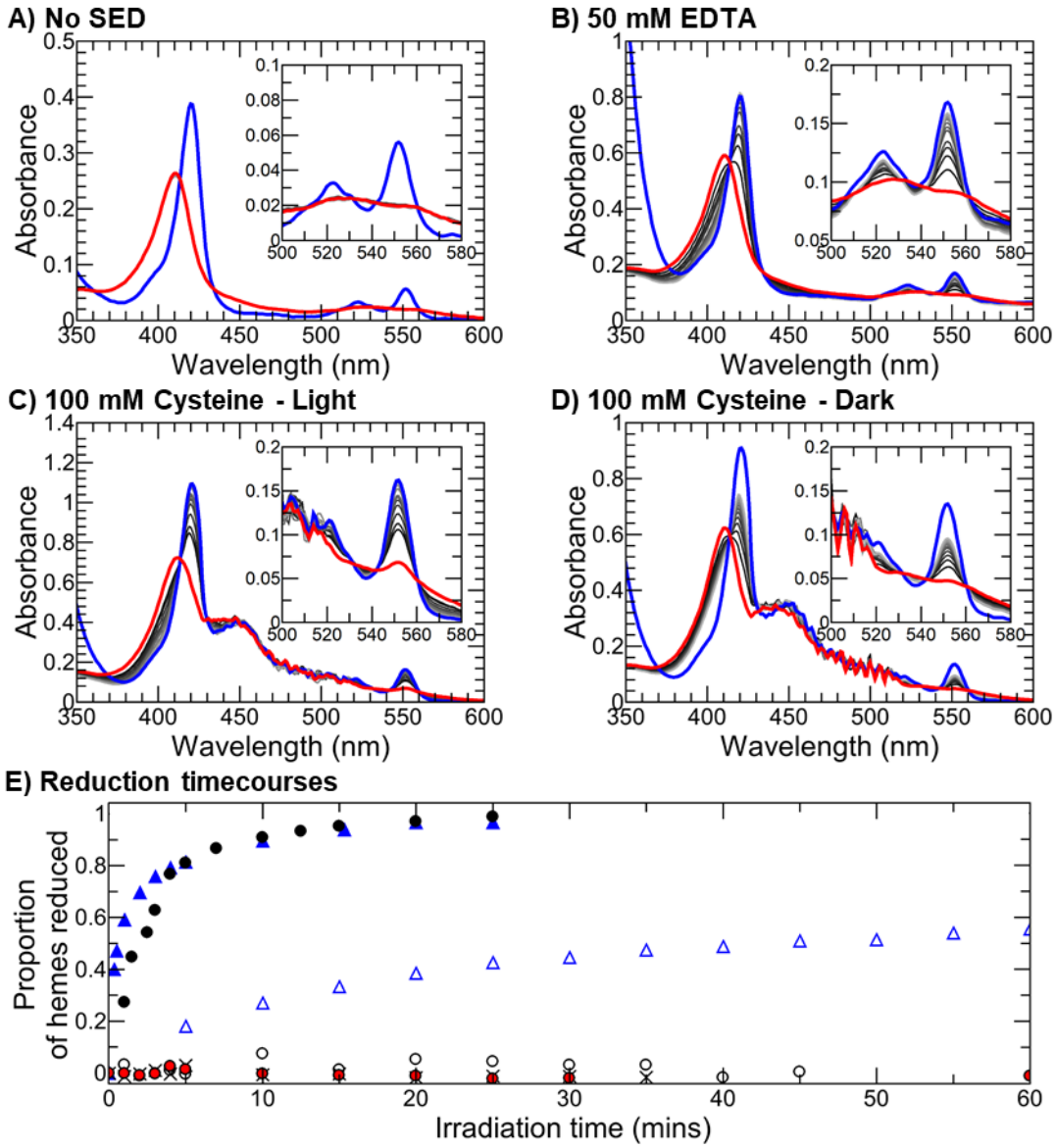

Figure 3.2.1 (Photo)reduction of RuMe-MtrC with different SEDs: **A-D)** Spectral changes upon treatment with the indicated conditions. Spectra at t=0 shown in red, Intermediate spectra obtained during irradiation shown in black-to-grey, spectra of DT reduced state shown in blue. Inserts show changes in the α-β region. Light source for A-C was Blue LED, no light source was used for D. **E)** Reduction timecourses derived from the change in absorbance at 552 nm between fully oxidised and DT reduced states during experiments under different SED conditions in anaerobic PN buffer: 100 mM Cysteine - Light (Blue filled triangles), 100 mM Cysteine - Dark (Blue empty triangles), 50 mM EDTA - Light (Black filled circles), 50 mM EDTA - Dark (Black empty circles), 50 mM EDTA + 100 mM $CaCl_2$ - Light (Red filled circles), No SED (Black crosses).

Many of the other SEDs tested here have been reported to act as SEDs for similar ruthenium complexes[47,58,62–65,94,179,180]; the reason they are not able to support photoreduction of RuMe-MtrC is not clear but is likely related to the kinetics of the RuMe-MtrC photocycle which will be explored later in this chapter.

As a result of the screening carried out here, EDTA was selected as the SED of choice for the studies in this thesis. EDTA is able to chelate a wide variety of cationic species and it is possible that it forms some sort of complex with RuMe which allows it to be oxidised more easily.[181] This is supported by the observation that if calcium was added to EDTA prior to the photoreduction experiment then EDTA was not able to support photoreduction of RuMe-MtrC (Fig. 3.2.1E). The EDTA:Calcium complex has a K_d of around 25 pM[182] which is orders of magnitude lower than the reported K_d for $Ru(bpy)_3^{2+}$:EDTA ion pairing (8.7 mM).[181] Like most SEDs, the oxidation of EDTA is complex, potentially involving numerous radical species and pH dependant degradation pathways (Fig. 3.2.2).[10,183] In addition, it is possible that each EDTA can yield up to four electrons (two from each amine). Further study of these pathways and mechanisms is, however, beyond the scope of this work.

Table 3.2.1 Results of SED compatibility screening

SED	Reaction conditions:	Results
EDTA	PN Buffer + 50 mM EDTA pH 7.5	Photoreduction observed. Full reduction in ≈ 30 mins
Cysteine	PN Buffer + 100 mM Cysteine (pH unknown)	Capable of reducing MtrC in the dark, faster reduction observed with irradiation
Ascorbate	PN Buffer + 100 mM ascorbate pH 7.5	Capable of reducing ≈18% of MtrC in the dark, no further reduction was observed upon irradiation
Oxalate	PN Buffer + 50 mM oxalate pH 7.5	Photoreduction not observed
Dimethylaminobenzoate	PN Buffer + 50 mM Dimethylaminobenzoate pH 7.5	Photoreduction not observed
Anisidine	PN Buffer + 50 mM Anisidine pH 7.5	Photoreduction not observed (May also lead to protein degradation – heme absorbance decreased over time)
TEOA	PN Buffer + 50 mM TEOA pH 7.5	Photoreduction not observed
HEPES	50 mM HEPES, 50 mM NaCl, pH 7.5	Photoreduction not observed
MES	50 mM MES, 50 mM NaCl, pH 6	Photoreduction not observed
Tris:HCl	50 mM Tris:HCl, 50 mM NaCl, pH 8.5	Photoreduction not observed

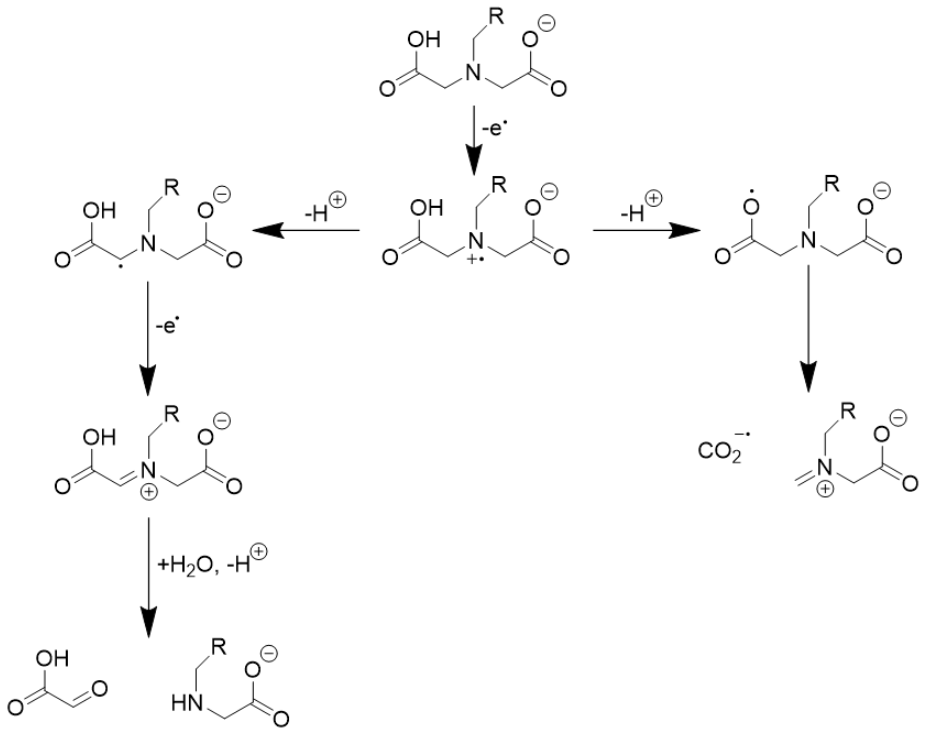

Figure 3.2.2 Possible degradation pathways of EDTA upon single-electron oxidation.[10,183] R=$CH_2N(CH_2COOH)(CH_2COONa)$.

3.2.2 - Probing the photocycle of RuMe-MtrC by photoluminescence spectroscopy

As discussed in Section 1.2, photochemical reactions may proceed via different mechanisms depending on the kinetic and thermodynamic properties of the different components. The first question that must be asked is what is the initial fate of the excited state (PS*)? In general, PS* may undergo any of 3 processes (see Fig. 1.2.2 - Right): relaxation to the ground state (either radiative or non-radiative), reductive quenching where an electron donor is used to generate PS^-, or oxidative quenching where an electron acceptor generates PS^+.

Based on the available redox transitions in the RuMe-MtrC system we would anticipate that Ru* would either relax to the ground state or be oxidatively quenched by a ferric heme as shown in Figure 3.1.3. The degree to which each of these pathways occurs in RuMe-MtrC can be determined by comparing the PL emission intensity of RuMe-MtrC to that of RuMe labelled Bovine Serum Albumin (RuMe-BSA) kindly prepared by Dr van Wonderen.[132] BSA does not contain any cofactors and is therefore not able to quench Ru* through electron transfer. The PL emission intensity from RuMe-BSA thus represents the maximum we can expect from these systems and any lowering of this intensity in RuMe-MtrC can be attributed to quenching by electron transfer.

PL experiments were carried out as described in Section 2.5.4 on anaerobic samples of 4 μM RuMe-MtrC and 1.4 μM RuMe-BSA (as determined by ε_{452} = 14600 M^{-1} cm^{-1}) in anaerobic TK Buffer. Excitation and emission spectra are shown in Figure 3.2.3A. The PL intensity of RuMe-MtrC is 2% of that of RuMe-BSA after normalising to the same concentration of RuMe. This indicates the presence of alternate decay pathways in RuMe-MtrC that outcompete PL; the most likely pathway being oxidative quenching by Heme 10 of MtrC. This is consistent with previously reported studies on RuMe-STC and RuMe-PpcA proteins which also undergo oxidative quenching[131,132,176].

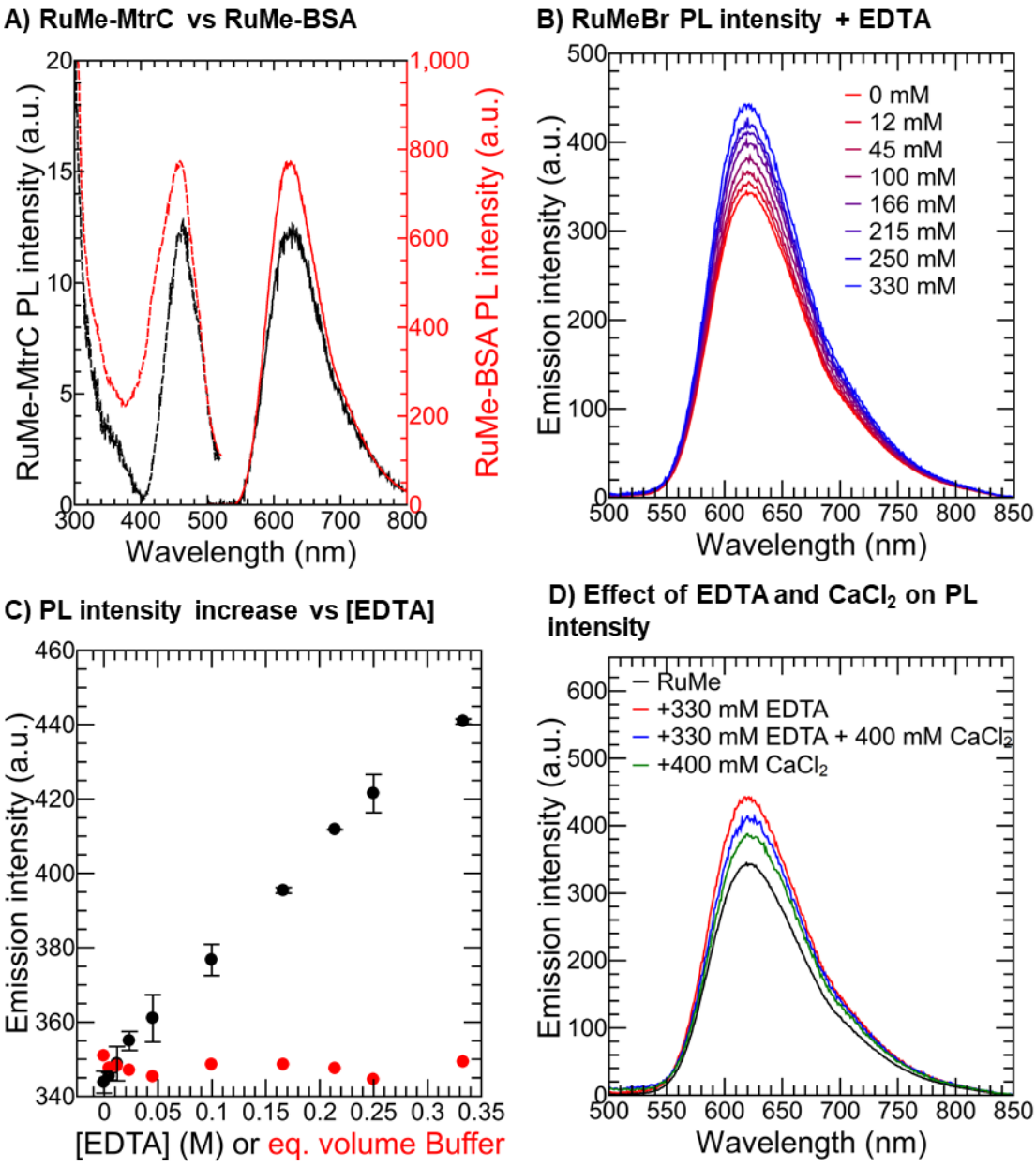

Figure 3.2.3 A) PL emission spectra of RuMe-MtrC (Black, left axis) and RuMe-BSA (Red, right axis) in anaerobic TK Buffer. Excitation spectra shown as dashed lines, emission spectra shown as solid lines. **B)** PL emission spectra of 2 μM RuMeBr in anaerobic TK Buffer (Red) with increasing [EDTA] (Red to Blue). **C)** Increase in PL intensity from B as a function of [EDTA] (Black), error bars show data range (n=2), PL intensity after addition of identical volume of buffer (Red) is also shown. **D)** PL emission spectra from: 2 μM RuMe-Br + indicated reagents.

It is also feasible that EDTA might be able to reductively quench Ru* given the highly oxidising potential of the $Ru^{II*/I}$ transition and the poorly defined potential for EDTA oxidation (Table 3.1.1). To test this, PL titration experiments were carried out with RuMe-Br and, intriguingly, EDTA was found to increase the PL intensity of RuMe-Br (Fig. 3.2.3B&C). This unusual behaviour could be explained by formation of a complex or ion pair between RuMe-Br and EDTA which stabilises the Ru* excited state such that it becomes more emissive. The addition of $CaCl_2$ at concentrations ≈equimolar with EDTA reversed this effect and the emission intensity returned to be comparable to the control experiment where only $CaCl_2$ was added (Fig. 3.2.3D). These findings provide further evidence for ion-pairing between RuMe and EDTA.[181] They also suggest that EDTA is not capable of acting as a reductive quencher for RuMe which greatly simplifies the photoreduction mechanism of RuMe-MtrC.

3.3 - Factors limiting the rate of RuMe-MtrC photoreduction

Photoreduction of RuMe-MtrC forms the foundation of the proposed photocatalytic systems whose formation is outlined in Section 1.6. Understanding of the factors that limit photoreduction of RuMe-MtrC is therefore of high importance. In contrast to conventional chemical reactions which typically have a single rate limiting step, photochemical processes can have multiple rate-limiting steps. Absorption of photons is often limiting in photochemical processes; this is an external limitation that determines the frequency at which the photocycle is initiated. An internal limitation is typically present which is more familiar and is usually the slowest step in the photocycle. The limiting factors affecting photoreduction of RuMe-MtrC were explored and the results are presented below.

3.3.1 - Internal rate-limiting step of RuMe-MtrC photoreduction

In the RuMe-MtrC photocycle the only step which involves more than one chemical species is the oxidation of the SED (Fig. 3.1.3, step ⑤). All the other steps are intramolecular processes with kinetic parameters inherent to RuMe-MtrC which cannot be readily altered. SED oxidation was, therefore, investigated by altering the concentration of EDTA in the photoreduction experiment.

Photoreduction experiments were carried out as described in Section 2.5.3 with varying concentrations of EDTA. Briefly, 0.5 μM RuMe-MtrC in TK buffer ± EDTA was irradiated with blue light and absorbance spectra were obtained at appropriate time points. After

60 mins of irradiation an excess of DT was then added to obtain a spectrum of the fully reduced protein. The absorbance at 552 nm was used to quantify the redox state of the hemes as described previously and the photoreduction timecourses are shown in Figure 3.3.1.

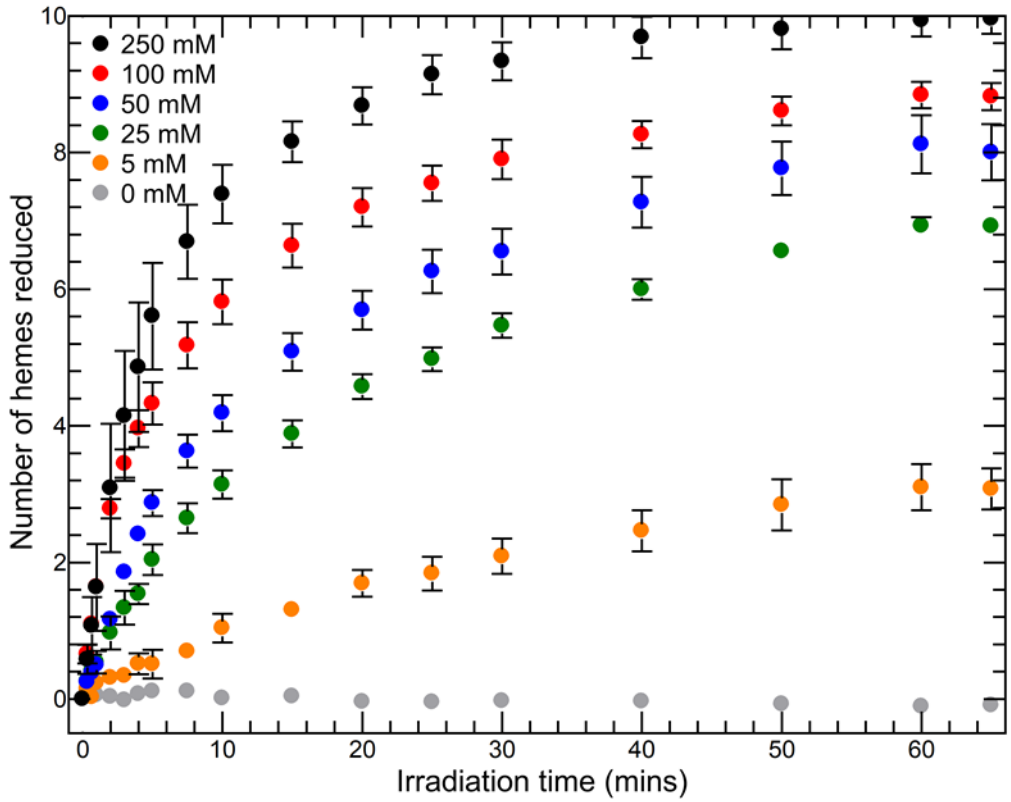

Figure 3.3.1 Photoreduction of 0.5 μM RuMe-MtrC with varying concentrations of EDTA. Number of hemes reduced was derived from $\Delta A_{552\ nm}$. Data shown are an average of n=3 experiments for 250 mM to 10 mM EDTA, and n=2 for 5 mM and 0 mM EDTA. Error bars represent the standard error. Samples in anaerobic TK Buffer + indicated concentration of EDTA.

The overall rate of photoreduction increased along with the concentration of EDTA suggesting that the reaction of the oxidised RuMe (Ru^{III}) with EDTA was rate limiting for productive photoreduction. It is also evident from this data that RuMe-MtrC does not accumulate electrons at a consistent rate, rather the rate of reduction at a given time appears to depend on both the EDTA concentration and the redox state of the hemes at that time. The rate of reduction is seen to decrease as the hemes become more reduced, the reasons for this will be explored mechanistically in Section 3.5.

3.3.2 - Determining whether light intensity is an external limiting factor for RuMe-MtrC photoreduction

Light intensity was investigated as an external limitation on RuMe-MtrC photoreduction. To quantify this, the output of the light source first had to be measured and converted to a photon flux. This was carried out using potassium ferrioxalate ($K_3[Fe(C_2O_4)_3]$) as a chemical actinometer as described in Section 2.5.2. Briefly, an anaerobic solution of potassium ferrioxalate was irradiated under conditions identical to the photoreduction experiments. Aliquots of this solution were periodically removed and developed in a phenanthroline solution. The absorbance of the developed solution was measured and $A_{511\ nm}$ was determined. Examples of the absorbance spectra obtained are shown in Figure 3.3.2 - Left and a plot of $A_{511\ nm}$ against irradiation time is shown in Figure 3.3.2 - Right. Photon flux was determined as described in Section 2.5.2.

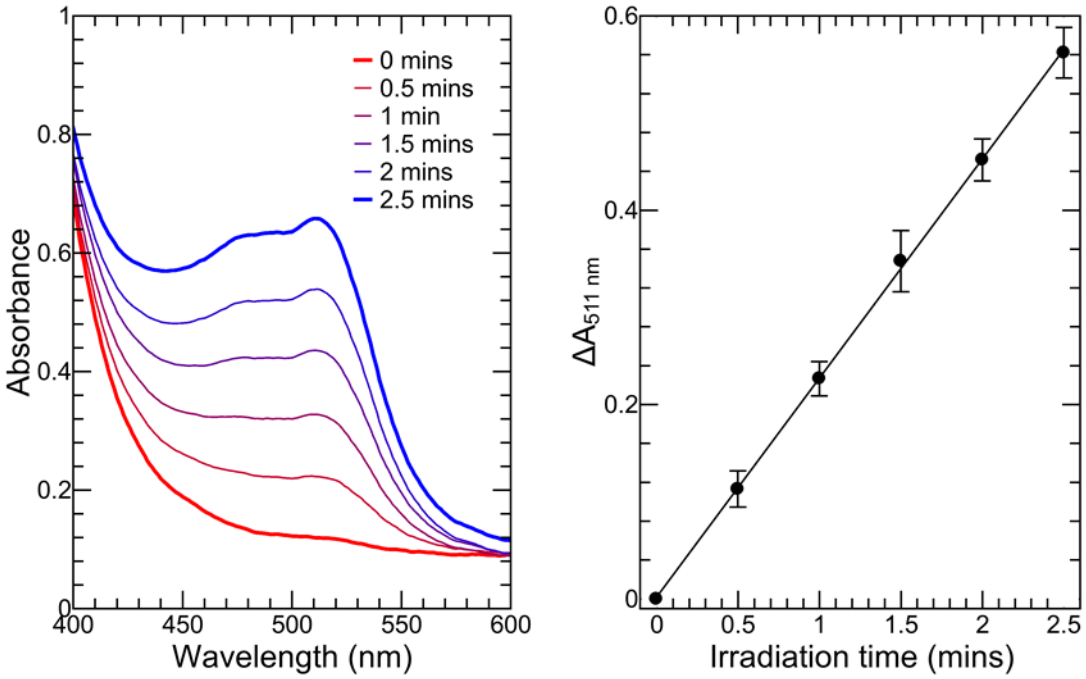

Figure 3.3.2 Left) Absorbance spectra reporting increasing ferroin concentration after development of an irradiated ferrioxalate solution. **Right)** Increase in $A_{511\ nm}$ after development of an irradiated ferrioxalate solution, data points are an average of n=3 data sets with error bars representing the standard deviation. A linear fit to these data is shown.

To determine the effect of light intensity on photoreduction of RuMe-MtrC, we required the means to adjust the light intensity in a controlled way. This was achieved by using neutral density (ND) filters. Actinometry was carried out as above with a selection of these filters (ND2, ND4 and ND8) installed on the LED light source. The results of these experiments are shown in Figure 3.3.3 - Right where it is seen that the filters decrease the rate of ferrioxalate photolysis. The absorbance properties of these filters were

examined by conventional absorbance spectroscopy (Fig. 3.3.3 - Left) and the transmission at 450 nm was determined. The findings are summarised in Table 3.3.1 where it can be seen that the calculated photon fluxes correlate well with the filters' transmission at 450 nm.

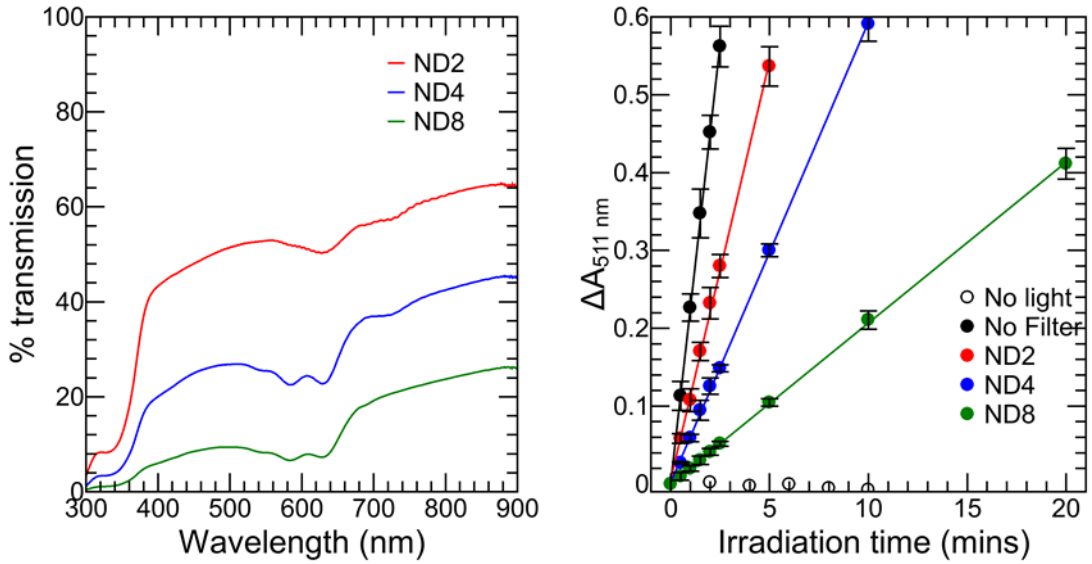

Figure 3.3.3 Left) %transmission of ND2, ND4 and ND8 filters measured by absorbance spectroscopy. **Right)** Increase in $A_{511\ nm}$ after development of an irradiated ferrioxalate solution using filters to restrict photon flux. Data points for irradiated samples are an average of n=3 data sets with error bars representing the standard deviation, for the non irradiated sample n=1.

Table 3.3.1 Calculations of photon flux from actinometry data and $\%trans_{450\ nm}$ obtained from spectra of the ND filters.

Filter	$\Delta A_{511\ nm}$ (s^{-1})	Photon flux ($cm^{-2}\ s^{-1}$)	$\%trans_{450\ nm}$	$\frac{\text{Photon flux } (cm^{-2}\ s^{-1})}{\%trans_{450\ nm}}$
None	0.0038	2.52×10^{16}	100	2.52×10^{16}
ND2	0.0018	1.23×10^{16}	48	2.55×10^{16}
ND4	0.00099	6.65×10^{15}	25	2.62×10^{16}
ND8	0.00035	2.32×10^{15}	8.5	2.73×10^{16}

Subsequently the rate of photon absorption per photosensitiser (k_{ex}) was determined using: the photon flux, the irradiated area of the sample, the photosensitiser's extinction coefficient (ε), the photosensitiser concentration (c), the sample pathlength (l), the sample volume (V), and Avogadro's number (N_A) according to the equation:

$$k_{ex}\ (s^{-1}) = \frac{\text{Rate of photon absorbance } (s^{-1})}{\text{Number of photosensitisers}} = \frac{\text{photon flux } (cm^{-2}\ s^{-1}) \times \text{Area } (cm^2) \times (1\text{-}10^{-\varepsilon cl})}{c \times V \times N_A}$$

The photon absorbance rates were calculated in this way for 1 mL of 0.5 μM solution of RuMe-MtrC with a path length of 2.5 cm and an area of 0.4 cm^2 and the results are given in Table 3.3.2.

Table 3.3.2 Calculated photon absorbance rates and k_{ex} for 1 mL of 0.5 μM RuMe-MtrC with different ND filters. l = 2.5 cm, $\varepsilon_{452\ nm}$ = 14600 M^{-1} cm^{-1}.

Filter	Rate of photon absorbance (s^{-1})	k_{ex} (s^{-1})
None	4.2×10^{14}	1.4
ND2	2.0×10^{14}	0.67
ND4	1.1×10^{14}	0.36
ND8	3.8×10^{13}	0.13

These values of k_{ex} represent the first-order rate constant for excitation of RuMe-MtrC (Fig. 3.1.3 - step ①). From reported values in the literature we would expect other steps in the photocycle, relaxation, CS, CR and interheme electron transfer (②,③,④,⑥), to have rate constants orders of magnitude larger than those determined for k_{ex}.[131,132,173–176] It is likely that photon absorbance is externally rate-limiting for RuMe-MtrC photoreduction.

To confirm this, the photoreduction of RuMe-MtrC was measured at different light intensities. Samples of 0.25 μM RuMe-MtrC were prepared in TK Buffer + 100 mM EDTA. The samples were first photoreduced to 25% reduced to ensure no oxygen was present in the sample which might impact the timecourses. From this point the samples were photoreduced with either the unobstructed light source or with a ND filter (ND2 or ND4) attenuating the light intensity. Absorbance measurements were taken over the course of 1 h irradiation (Fig. 3.3.4 - Left) and spectra of the final state after this time are shown in Figure 3.3.4 - Right along with the oxidised and fully reduced states.

This data shows clearly that light intensity has a significant impact on the photoreduction rate of RuMe-MtrC. When the ND2 and ND4 filters were installed on the light source the rate of electron accumulation was decreased and the state reached after 1 h was less reduced. The initial rate of photoreduction ($t \leq 10$ mins) under these conditions was found to correlate very well with the rate of photon absorbance calculated using ferrioxalate actinometry (Table 3.3.3). These data thus support the hypothesis that light intensity is a limiting factor for photoreduction of RuMe-MtrC, as expected from the small k_{ex} values.

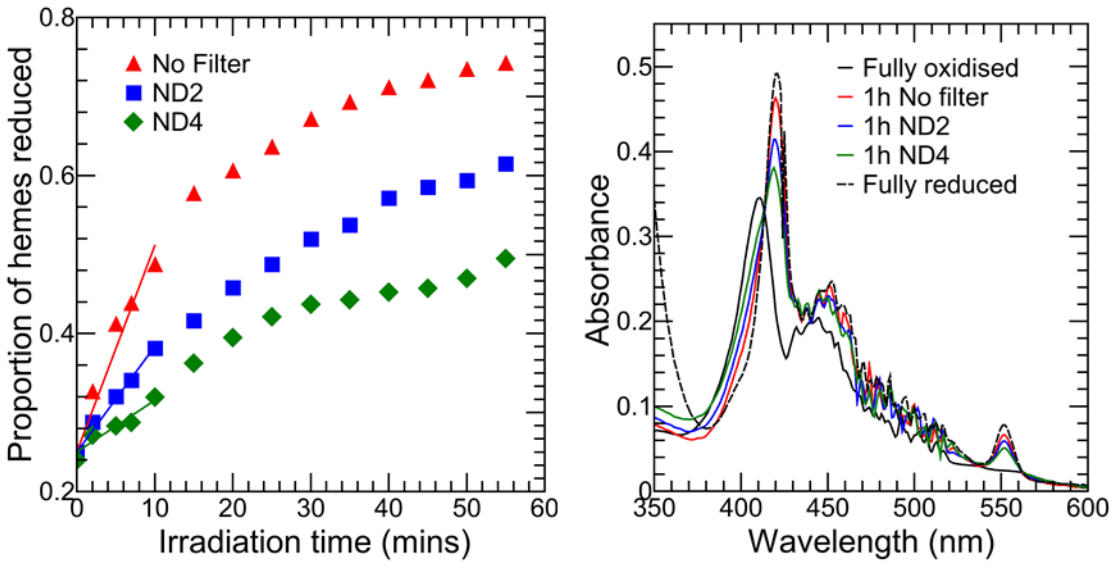

Figure 3.3.4 Photoreduction of 0.25 μM RuMe-MtrC ± ND filters in anaerobic TK Buffer + 100 mM EDTA. **Left)** Photoreduction timecourses for RuMe-MtrC without a filter (Red), with an ND2 filter (Blue) and ND4 filter (Green), proportion of hemes reduced was calculated using $A_{420\ nm}$, data points are the average of n=2 data sets, solid lines show linear fits to the data for t≤10 mins; **Right)** Spectra of the fully oxidised RuMe-MtrC (Black solid), fully reduced RuMe-MtrC (Black dashed) and of RuMe-MtrC after 1h irradiation with indicated filters.

Table 3.3.3 Correlation of initial photoreduction rate with k_{ex} with different ND filters.

Filter	k_{ex} (s^{-1})	Number of hemes reduced min^{-1}
None	1.4	0.261
ND2	0.67	0.134
ND4	0.36	0.065

3.3.3 - Limitation on accumulation of multiple electrons

Both light intensity and EDTA concentration are expected to remain effectively constant throughout the photoreduction timecourse. A third factor must therefore be implicated to explain why, under all conditions presented thus far, RuMe-MtrC photoreduction starts out relatively fast and then slows down as the timecourse progresses (Figs. 3.2.1, 3.3.1 & 3.3.4). This factor appears to be dependent on the redox state of RuMe-MtrC at any given time and a simple explanation can be proposed for its origin. As the hemes of RuMe-MtrC are reduced, the probability of heme 10 being reduced at any given time increases; if heme 10 is reduced it cannot accept an electron from Ru* and therefore the rate of RuMe-MtrC photoreduction decreases as a function of overall redox state. It could be argued that electron accumulation in RuMe-MtrC suffers from a built-in negative feedback loop.

Experimentally proving this hypothesis would be challenging. One possibility would be to study the PL intensity of RuMe-MtrC as a function of heme redox state. If the hypothesis were correct, we would expect the PL intensity to increase to the level of RuMe-BSA when all ten hemes are reduced. In practise this may be complicated by reductive quenching of Ru* by ferrous heme as has been reported for other photosensitised cytochromes.[176] The possibility of a reductive quenching pathway in RuMe-MtrC will be explored further in Section 3.5.

The factors limiting the rate of photoreduction of RuMe-MtrC and the ramifications of these factors are summarised as follows:

Externally limited by light intensity

Increasing the photon flux should cause a corresponding increase in photoreduction rate. The lamp used in these experiments can generate a photon flux of up to $\approx 2.5 \times 10^{16}$ photons cm^{-2} s^{-1}.

Internally limited by SED oxidation

The first option to overcome the limitation by SED oxidation would be, of course, to increase the [SED]. EDTA, however, has a maximum solubility of ≈0.5 M so the concentration cannot be increased much further beyond the data presented. A better solution would be to optimise the kinetics of the photocycle. The reaction of Ru^{III} with EDTA (Fig. 3.1.3 - step ⑤) is in competition with CR (Fig. 3.1.3 - step ④) therefore if CR could be slowed the photoreduction rate would be expected to increase. Work to this end is underway and will be discussed further in Chapter 7.

Overall redox state of the decaheme chain limits accumulation of multiple electrons

This factor has drastic implications on the full photoreduction of RuMe-MtrC, however in a functional photocatalytic unit the electrons produced by RuMe-MtrC would ideally be rapidly extracted and used by the catalyst. Prevention of a build-up of electrons, by having an electron sink available, should minimise this limiting factor. This will be investigated in the following section.

3.4 - Determining the photostability of RuMe-MtrC

As has been seen consistently across the literature reviewed in Chapter 1, photocatalytic systems are often subject to degradation on timescales of minutes to hours.[45,60,61,94,95,113,119,122] Such systems typically report both TOFs and TONs that describe the activity over short times and the lifetime of the system. In order to better compare RuMe-MtrC photoreduction against such literature it is necessary to determine the long-term photostability of RuMe-MtrC. To do this, a sacrificial electron acceptor (SEA) will be required; this species must be able to oxidise the hemes of MtrC and should ideally undergo an irreversible reaction such that the reduced species cannot interfere with the photochemistry. Oxidants like potassium ferricyanide can rapidly accept electrons from MtrC, however in doing so potassium ferrocyanide is generated which has the thermodynamic potential to reductively quench Ru* generating Ru^{I}. In addition, reduction of ferricyanide to ferrocyanide is a single electron process that can be carried out by RuMe-Br (Data not shown).

Azo dyes are characterised by their intense colouration and the presence of azo moieties (R-N=N-R') within their structure. These bonds contribute to the extended π-delocalisation within the dye structures which gives rise to their spectroscopic properties. Azo dyes make up 70% of the worlds synthetic commercial dyes[184] and are desirable for their structural diversity, photostability, and resistance to microbial damage. All of these factors, however, make azo dyes persistent environmental pollutants with toxic effects on some aquatic species.[185]

Biological remediation of azo dyes is an active research area and much of the literature is focussed on targeting the azo linkage as this is a common structural motif among all azo dyes.[186,187] In nature, several routes have been discovered for breaking the azo bond. Some enzymes, including dedicated azoreductases[188–191], are able to reduce azo bonds to a pair of amines, requiring a total of 4 electrons. Other enzymes such as laccases[192,193], peroxidases[194,195] and polyphenol oxidases[196] have also been shown to cleave azo bonds via oxidative processes however the products are more diverse owing to complex radical-based chemistry.[186]

Cleavage of these bonds typically results in decolourisation of the dye due to the loss of the extended π structure; it also breaks the structure of the dye into less biologically recalcitrant fragments. MR-1 has been studied for its ability to reduce azo dyes[197] and MtrC was found to have a key role in this azoreductase activity.[198]

A selection of azo dyes (Fig. 3.4.1) with different sizes and structural motifs were screened to investigate whether any might be a suitable SEA for RuMe-MtrC.

Approximately 0.5 µM RuMe-MtrC was mixed with ≈0.5 µM of the azo dyes and 100 mM EDTA in anaerobic TK Buffer. These samples were irradiated with blue light for 2h and spectra were obtained periodically to monitor the redox state of RuMe-MtrC and the bleaching of the dye (Fig. 3.4.2).

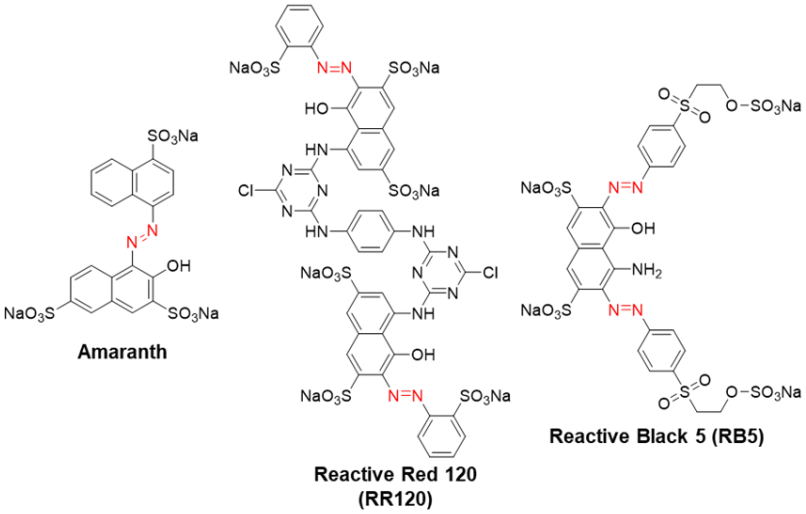

Figure 3.4.1 Structures of azo dyes used in this work with azo bonds indicated in red

Initial screenings revealed that only Reactive Black 5 (RB5) (Fig. 3.4.2C) ($\varepsilon_{600\ nm}$ = 23000 M^{-1} cm^{-1})[a] was able to effectively be reduced by RuMe-MtrC; bleaching of the dye was observed at 600 nm and the hemes of RuMe-MtrC remained mostly oxidised over the course of the experiment, as determined by minimal changes to $A_{420\ nm}$. These findings suggest a reductive route of azo bond cleavage producing the corresponding amines. RR120 and amaranth were reduced very slowly (Fig. 3.4.2A&B) and the hemes of RuMe-MtrC were observed to be mostly reduced throughout these experiments (Fig. 3.4.2E), indicating a deficiency in protein-to-dye electron transfer.

[a] Determined from 10 µM solution in TK buffer

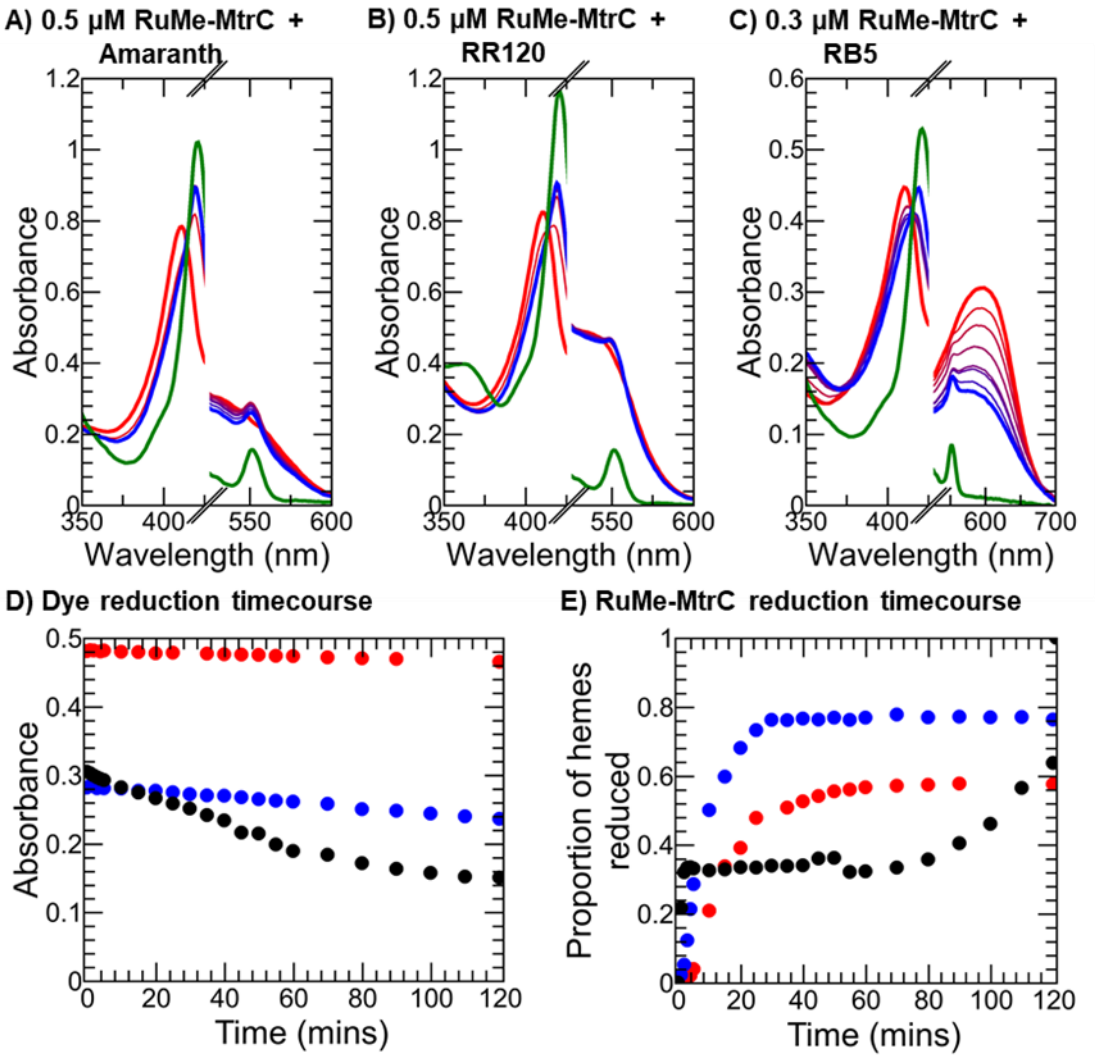

Figure 3.4.2 Photoreduction of 12.5 µM azo dyes by RuMe-MtrC. **A-C)** Spectra of indicated azo dye + RuMe-MtrC (Red) + 100 mM EDTA in TK Buffer, over 2h irradiation (Red to Blue), and after addition of DT (Green); **D)** Timecourses following reduction of azo dyes: Amaranth (Blue - $A_{529\ nm}$), RR120 (Red – $A_{539\ nm}$) and RB5 (Black – $A_{600\ nm}$); **E)** Timecourses of RuMe-MtrC redox state in presence of azo dyes, determined from $\Delta A_{420\ nm}$, colours as in D.

The reduction of RB5 appeared to be biphasic (Fig. 3.4.2D) with an initial fast phase followed by a slower phase, with a comparable rate to the other dyes. This observation may stem from the presence of a primary amine (instead of a hydroxyl) adjacent to one of the azo bonds in RB5 (Fig. 3.4.1). A hydroxyl group adjacent to an azo bond on an aromatic ring is well documented to undergo tautomerisation to give a hydrazone form (Fig. 3.4.3).[199] It is not well understood whether this makes the azo bond easier or harder to reduce, with conflicting findings being reported.[200,201] Given that RR120 and Amaranth have hydroxyl groups adjacent to both of their azo bonds this work suggests that a hydroxyl group makes the azo bond more difficult to reduce. Other remediation trials with RB5 have found similar biphasic kinetics.[200,201]

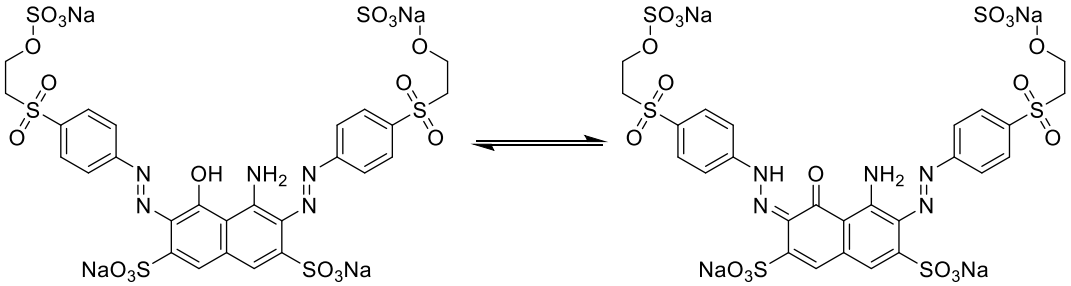

Figure 3.4.3 Tautomerisation of RB5

RB5 was selected as a SEA to assess the photostability of RuMe-MtrC. Increasing the initial concentration of RB5 led to an extended fast phase but gave the same overall trend (Fig. 3.4.4A). This suggests that the observed behaviour is not due to the protein degrading and is instead due to the non-equal nature of the two azo bonds in RB5. Only the initial "fast" phase will be considered in further kinetic analyses.

Increasing the concentration of EDTA to 250 mM led to an increase in the initial rate of RB5 reduction and higher concentrations of reduced heme throughout (Fig. 3.4.4B). Decreasing the EDTA concentration to 25 mM slowed down RB5 reduction and RuMe-MtrC remained at ≈22% reduced for the first 40 mins of the experiment. These results demonstrate that, as expected, the rate of reduction of RB5 is linked to the rate of electron production by RuMe-MtrC which depends on the EDTA concentration.

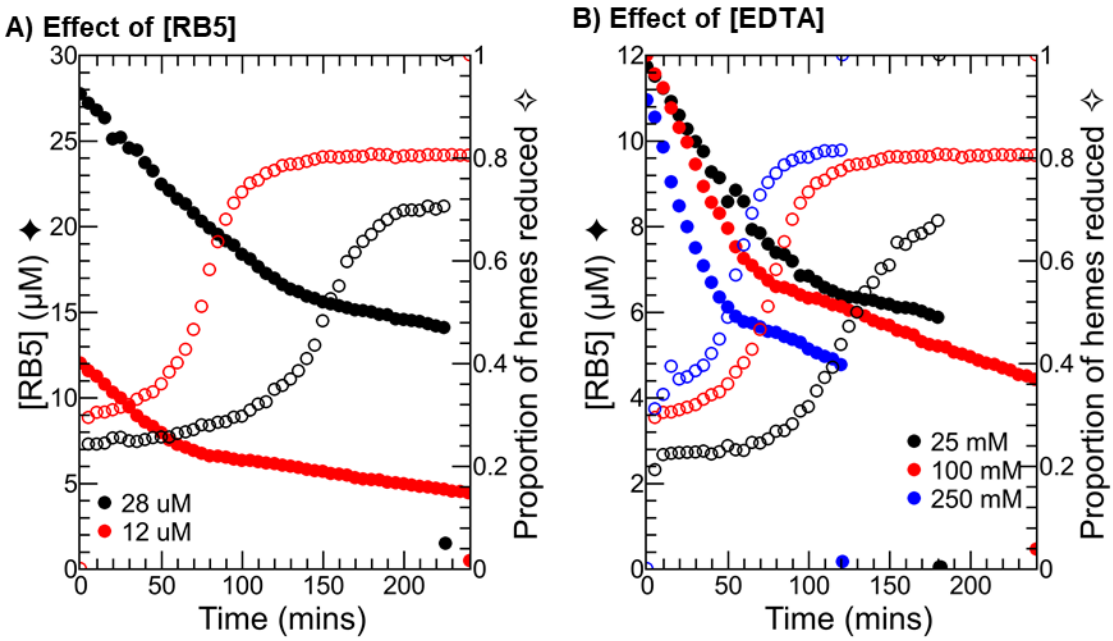

Figure 3.4.4 Effects of [RB5] (A) or [EDTA] (B) on photoreduction of RB5 by RuMe-MtrC. [RB5] (Solid) determined from $A_{600\ nm}$, Proportion of hemes reduced (Hollow) determined from $\Delta A_{420\ nm}$. [RuMe-MtrC] = 0.9 μM, for A) [EDTA] = 100 mM, for B) [RB5] = 12 μM. Samples in TK Buffer

To assess the longevity of this system and obtain a TON, 0.8 μM RuMe-MtrC was mixed with 100 μM RB5 and 100 mM EDTA then irradiated for 9 h with spectra taken periodically (Fig. 3.4.5).

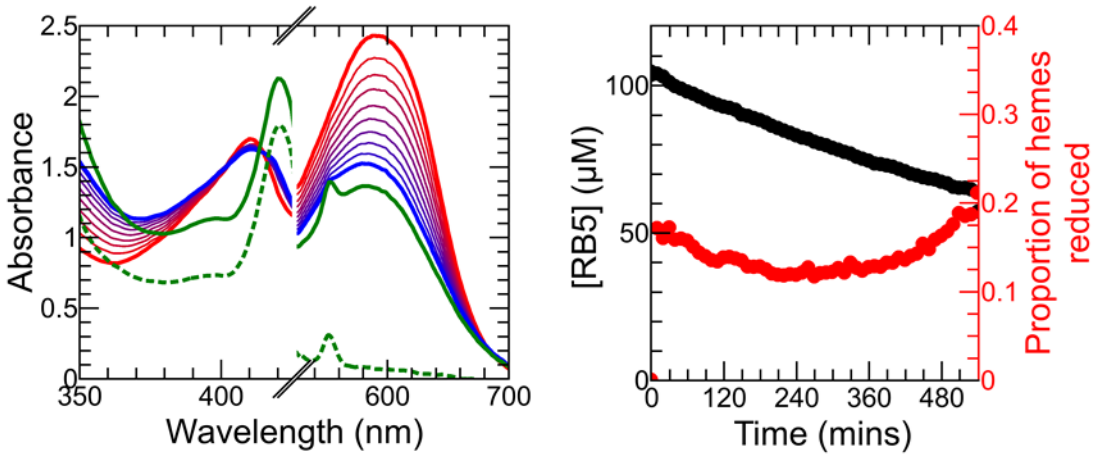

Figure 3.4.5 Determination of TON for photoreduction of RB5 by RuMe-MtrC. **Left)** Spectra obtained of 0.8 μM RuMe-MtrC + 100 μM RB5 + 100 mM EDTA in anaerobic TK Buffer (Red), during irradiation over 9h (Red to Blue), immediately after addition of DT (Green-solid), and after 30 mins (Green-dashed); Spectra recorded in 0.4 cm pathlength cuvette and scaled up 2.5×; **Right)** Timecourses of [RB5] (Black) determined from $A_{600\ nm}$ and proportion of hemes reduced (Red) determined from $\Delta A_{420\ nm}$.

The rate of electron production (TOF) by RuMe-MtrC decreased by 30% over this time period from 0.85 e^- min^{-1} to 0.6 e^- min^{-1} though this may also have been due to the decreasing concentration of RB5 in the solution. If fresh RB5 had been added the initial rate may have been able to be recovered. In total, the TON (electrons RuMe-$MtrC^{-1}$) was 400 in 9 h which is by no means high but greater values might be obtained if higher concentrations of RB5 or EDTA were used. The initial TOF obtained here (0.85 min^{-1}) is close to the initial rate of photoreduction for RuMe-MtrC with 100 mM EDTA (≈0.8 min^{-1}) (Fig. 3.3.1). This suggests that EDTA oxidation is rate limiting and, during the fast phase, RB5 reduction is not.

The inflexions in the level of hemes reduced over time may be caused by absorbance changes occurring beneath the heme Soret band. While RB5 does not absorb strongly at 420 nm it does have some absorbance in this area. This is evident from the difference between the spectra obtained immediately after DT addition and after 30 mins (Fig. 3.4.5 Left - solid vs dashed Green). Small decreases in A420 nm during photoreduction of RB5 could have caused the downward inflection observed in Figure 3.4.5 Right (t=0 to 120 min).

In the following section the photocycle will be kinetically modelled using results from the previous sections as source data. This modelling will allow for identification of areas for improvement to the RuMe-MtrC photochemistry.

3.5 - Modelling the photocycle of RuMe-MtrC

Ongoing studies, both in our group and with collaborators, have sought to determine the kinetic parameters defining electron transfers in photosensitised multiheme cytochromes. We are now in a position to bring these studies together and, along with the data presented in this chapter, create a kinetic model that describes the single and multielectron photochemistry of RuMe-MtrC. This model will use the data presented in Figure 3.3.1 as a basis for parameter fitting and will be based principally on the photocycle outlined in Figure 3.1.2. Experimental definition of most of the kinetic parameters is essential for creating a reliable kinetic model. All but one of the rate constants that describe RuMe-MtrC photoreduction have been be determined using actinometry (see Sections 2.5.2 and 3.3.2), time resolved photoluminescence (TRPL) or transient absorbance spectroscopy (TAS) (Table 3.5.1); these experiments are discussed in greater detail in Section 3.5.1. At present, a direct experimental observation of Ru^{III} oxidising EDTA is not available. This rate constant (k_{SED}) will be fitted to photoreduction timecourses at varying EDTA concentrations presented previously (Fig. 3.3.1)

Table 3.5.1 Rate constants determined by actinometry or time-resolved techniques

Step (as in Fig. 3.1.2)	Rate constant	Value (s^{-1})	Source
① - Excitation	k_{ex}	1.4	Ferrioxalate actinometry
② - Relaxation	k_{rlx}	2.2×10^6	TRPL
③ - CS	k_{CS}	1.1×10^8	TAS
④ - CR	k_{CR}	3.3×10^8	TAS
⑥ - Heme-Heme electron transfers	$k_{10,9}$	2.5×10^8	TAS
	$k_{9,10}$	1.4×10^7	TAS

3.5.1 - Determining the kinetics of the RuMe-MtrC photocycle

The rate constant for excitation, k_{ex}, was determined in Section 3.3.2 using potassium ferrioxalate actinometry to quantify the photon flux from the blue LED lamp used for photoreduction studies. Using this photon flux, and several other experimental parameters (see also Section 2.5.2) k_{ex} was determined to be 1.4 s^{-1}.

The rate at which Ru^{II*} returns to the ground state by PL and non-radiative decay, k_{rlx}, can be determined using TRPL. This technique measures the intensity of emission from a chromophore as a function of time following an excitation pulse. Work by Dr. van Wonderen has determined that RuMe-Br has an excited state lifetime of 462 ns giving k_{rlx} of $2.2 \times 10^6\ s^{-1}$. This value is generally consistent with literature values for Ru-diimine complexes which typically have lifetimes around 600 ns in water.[202]

Rates of charge separation, k_{CS}, and charge recombination, k_{CR}, were derived from TAS of RuMe-MtrC using procedures similar to those reported for analysis of STC.[131] Kinetic analysis and modelling by Dr. van Wonderen and the group of Prof. Blumberger has allowed for the single-electron photocycle of RuMe-MtrC to be fully defined (van Wonderen et al., in preparation).

Kinetic analysis of the TAS data reveals three kinetic contributions to charge separation in RuMe-MtrC (τ_{CS} = 0.2 ns, 9 ns and 192 ns) and three corresponding rates of charge recombination (τ_{CR} = 0.009 ns, 3 ns and 12 ns) making up 20%, 66% and 14% of the observed signal respectively. These contributions are expected to derive from different conformers of RuMe on the surface of MtrC as has been reported for the comparable STC system.[131] For simplicity, only the largest contributor will be considered for the model. This gives k_{CS} and k_{CR} values of $1.1 \times 10^8\ s^{-1}$ and $3.3 \times 10^8\ s^{-1}$ respectively.

This TAS analysis also gives values for heme 10↔9 electron transfer rates:

$k_{10,9}$ – $2.5 \times 10^8\ s^{-1}$

$k_{9,10}$ – $1.4 \times 10^7\ s^{-1}$

The remaining heme-heme transfer rates and k_{SED} are not able to be directly experimentally determined at this time.

3.5.2 - Designing a kinetic model of the RuMe-MtrC photocycle

Modelling of the RuMe-MtrC photocycle was carried out using the rate constants presented in Table 3.5.1 in Dynafit software[203] and the full scripts for each of the models presented here can be found in Appendix A3. The photocycle presented in Figure 3.1.2 is somewhat simplified as many of the mechanistic steps can, in reality, occur in a number of different orders; for example, electron transfer from heme 10 to heme 9 could easily occur before EDTA oxidation. In the model, such flexibility was built in by defining all possible interconversions between species (see Appendix A2).

The first strategy that was considered was to break down RuMe-MtrC into 11 separate components (RuMe and 10 individual hemes) and have them interact with each other in

appropriate mechanistic steps (Figure A1.1). This created a simple framework with only 23 microstates. Dynafit, however, will consider a mechanistic step of the form:

$$A + B \rightarrow C$$

to have a second-order rate constant and there is no apparent way to override this. Aside from SED oxidation, all the electron transfer steps considered in these models are intramolecular, first-order processes meaning that a model built using this framework would be invalid.

Alternatively, a framework could have been created that fully defined RuMe-MtrC using first-order kinetics with each of the 10 hemes of MtrC being able to be oxidised or reduced and the RuMe being either in ground state, excited state or oxidised. This model would require the definition of over 3000 microstates (Figure A1.2), each with many possible specific interconversions accounting for many thousands of lines of script. Clearly this approach was not feasible to produce or run and a compromise would have to be struck between the fully second-order and fully first-order frameworks.

Most of the electron transfer steps that are of interest for this study occur between the RuMe-label, heme 10 and heme 9. Thus, an initial kinetic model (Model 1) for the cumulative photoreduction considered a framework where these three components were treated as a single unit with 12 possible microstates (Fig. A1.3). The remaining hemes were allowed to exist as independent components although electrons were restricted to follow the heme architecture imposed by MtrC (i.e. heme 5 can interact with heme 4 but no other hemes). This compromise allowed the well-defined first-order processes of the photocycle to be coupled to the remaining heme pool whilst minimising the number of possible microstates that needed to be defined. The heme-heme transfer rates for hemes 8-1 were set to 1×10^{9} M^{-1} s^{-1}. This is likely an oversimplification of the system, as electrons do not pass between hemes at the same rate; however, the pseudo second-order nature of these steps in the model prevents the assignment of a meaningful value.

A simplified scheme of Model 1 is presented in Figure 3.5.1, for a full map of the possible interconversions in the RuMe-H10-H9 unit see Figure A2.1.

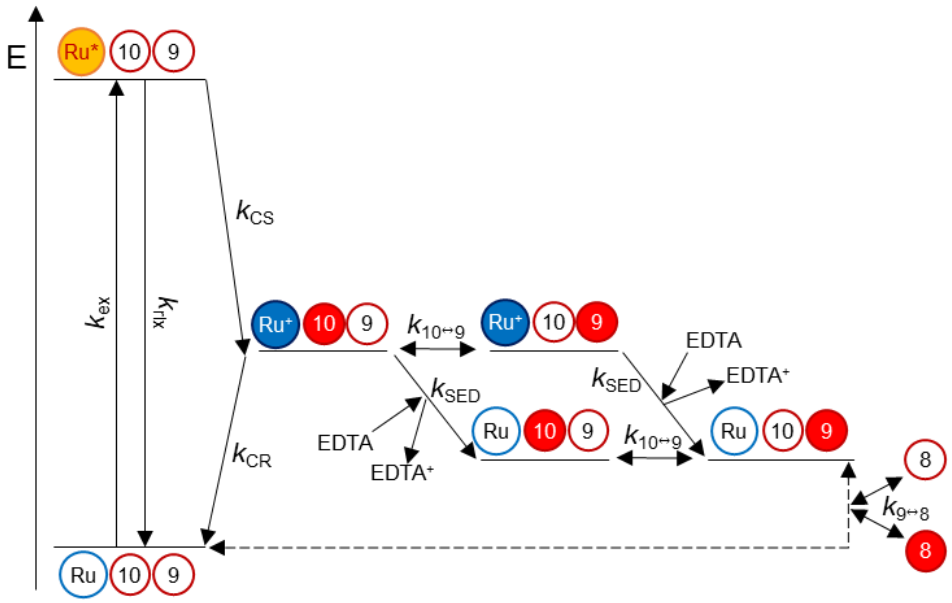

Figure 3.5.1 Simplified photocycle scheme for Model 1 showing first-order module and heme 8. RuMe shown in ground state (Ru), excied state (Ru^*) or oxidised state (Ru^+); hemes shown in oxidised (hollow) or reduced (red-filled) states.

Using Model 1 and the parameters in Table 3.5.1, the data presented in Figure 3.3.1 were fitted (Figure 3.5.2A) (root mean square deviation (RMS)[c] = 0.0052). This fitting determined a k_{SED} of 2.1 × 10^6 M^{-1} s^{-1}. Model 1 reproduced the key features of the measured data, however the fits undershot the data when the hemes were mostly oxidised and overshot when the hemes were mostly reduced, with a crossing point at around 50% ferrous heme. This is likely due to the multi-electron limiting factor discussed in Section 3.3.3. This suggests that another mechanism is in play that is slowing down photoreduction of RuMe-MtrC in the more reduced state leading to the determined value for k_{SED} being too low.

[c] RMS = $\sqrt{\frac{\sum_{i=1}^{N}((\text{Data at t=x})-(\text{model at t=x}))^2}{N}}$

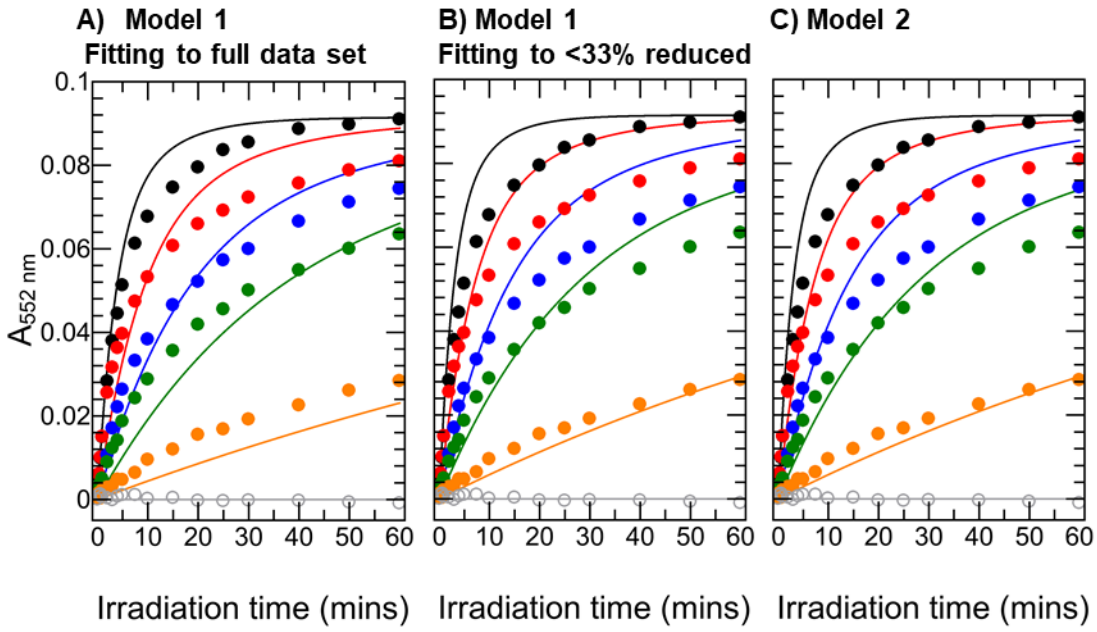

Figure 3.5.2 Outputs from kinetic modelling of RuMe-MtrC photoreduction using Models 1&2 and parameters in Table 3.5.1. EDTA concentrations: 250 mM (black), 100 mM (red), 50 mM (blue), 25 mM (green), 5 mM (orange), 0 mM (grey). Source data shown as circles, generated fits shown as solid lines.

The data was refitted using data points corresponding to RuMe-MtrC with <33% ferrous heme to find the k_{SED} before the photoreduction began to slow down. Modelling the data in this way (Fig. 3.5.2B) gave a slightly higher value for k_{SED} of 2.8×10^6 M^{-1} s^{-1} which, unsurprisingly, resulted in fits that better reflected the data below 40% ferrous heme but then overshot the data beyond this point (RMS = 0.0066).

The factor limiting electron accumulation when MtrC is more reduced could also be non-productive reductive quenching of Ru^{II*} by ferrous heme 10. This type of quenching has been observed previously for photosensitised cytochromes[43,176] A reductive quenching pathway was introduced to the model, adding onto Model 1 to form Model 2 with additional microstates (Fig. A1.4) and rate constants for the reductive quenching pathways termed $k_{CS'}$ and $k_{CR'}$.

Ideally, the kinetics of these alternative charge-separation and charge-recombination steps would be determined experimentally using TAS on fully reduced RuMe-MtrC as in Kokhan et al.,[176] however this was not available within the timeframe of this work. TRPL carried out by Dr. van Wonderen, however, was used to give $k_{CS'}$ of 1.4×10^7 s^{-1}. As with the oxidative quenching regime, TRPL tells us nothing about charge recombination and this parameter ($k_{CR'}$) was therefore fitted to the data. Figure 3.5.3 shows a simplified schematic of Model 2, a full map of possible interconversions is shown in Figure A2.2. The result of fitting the source data with Model 2 is shown in Figure 3.5.2C.

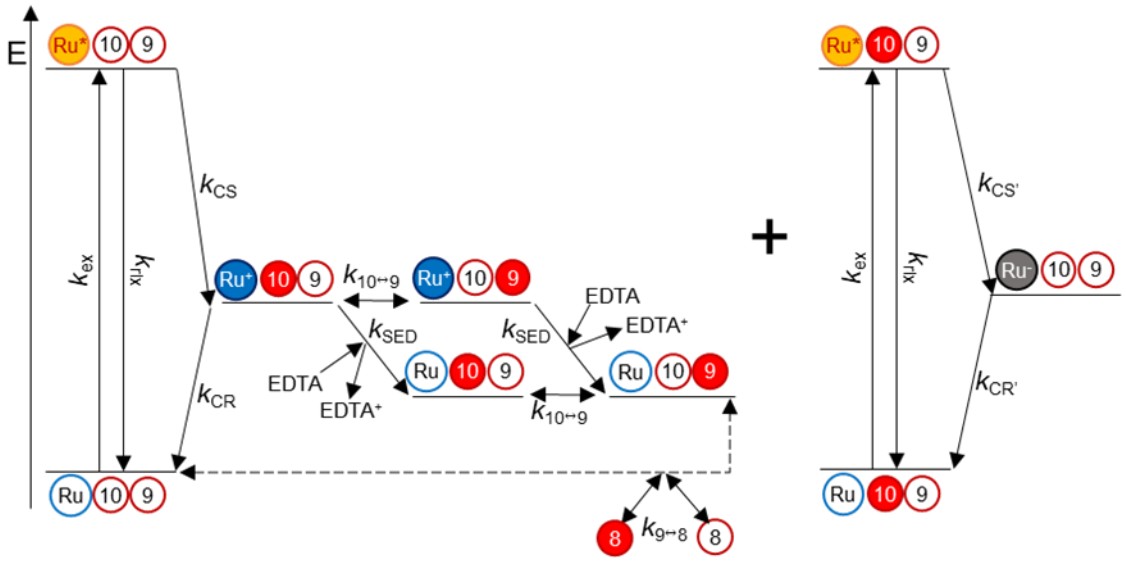

Figure 3.5.3 Simplified photocycle schemes for Model 2 showing first-order module and heme 8. RuMe shown in ground state (Ru), excied state (Ru^{*}), oxidised state (Ru^{+}) or reduced state (Ru^{-}); hemes shown in oxidised (hollow) or reduced (red-filled) states.

Fitting using Model 2 (RMS = 0.0066) appears to show no significant improvement over Model 1. This is likely due to the model's design; $k_{10,9}$ is over an order of magnitude greater than $k_{9,10}$ meaning that, in this model, heme 10 will rarely be reduced and therefore will rarely be able to reductively quench Ru^{II*}. The potential of heme 8 is predicted to be more negative than that of heme 10 and 9 and is expected to act as a hurdle for electron flow through MtrC (Fig. 3.5.4).[178,204] TAS analysis of RuMe-MtrC gave predicted values for $k_{9,8}$ (1.1 $\times 10^{8}$ s^{-1}) and $k_{8,9}$ (1.6 $\times 10^{9}$ s^{-1}) (van Wonderen et al., in preparation).

The decision was made to include heme 8 in the first-order unit of the model, producing Model 3 with 38 microstates (Fig. A1.5). Introduction of heme 8 added a bottleneck for electron flow to increase the probability of heme 10 being reduced at any time and thus slow down the photoreduction.

Fitting Model 3 to the experimental data (Fig. 3.5.5A) produced a better fit at all time points (RMS = 0.0028) than Models 1 and 2 and gave a k_{SED} of 6.7×10^{6} M^{-1} s^{-1}. A reductive quenching pathway was added to Model 3 to give Model 4 with 42 microstates (Fig. A1.6). This did have a small effect on the fits produced (Fig. 3.5.5B) however it is not clear whether this provided any overall improvement to the fit (RMS = 0.0028).

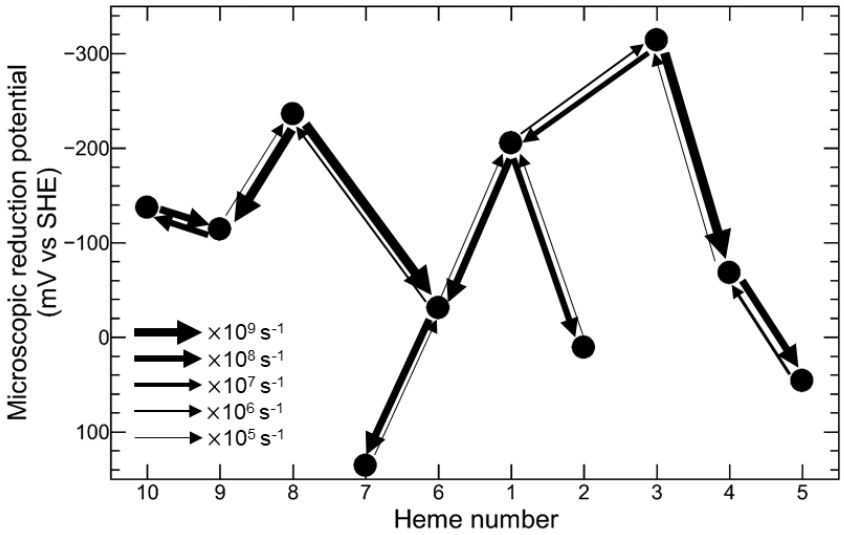

Figure 3.5.4 Microscopic reduction potentials and interheme electron transfer rates of MtrC.[204] Electron transfers shown as arrows with faster rates having thicker arrows.

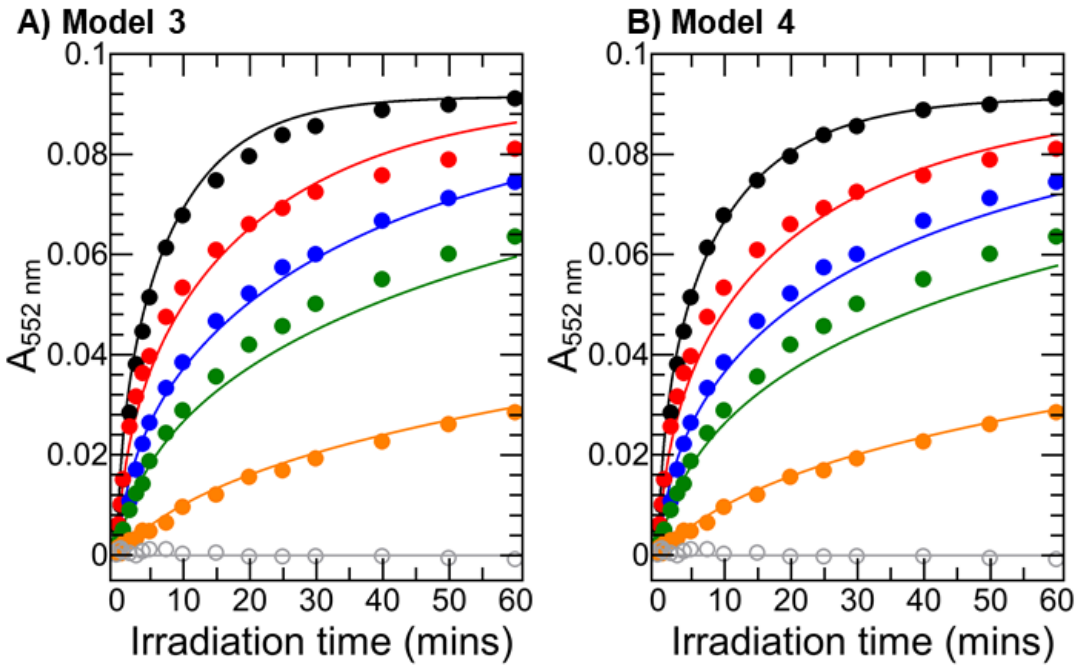

Figure 3.5.5 Outputs from kinetic modelling of RuMe-MtrC photoreduction using Models 3&4 and parameters in Table 3.5.1. EDTA concentrations: 250 mM (black), 100 mM (red), 50 mM (blue), 25 mM (green), 5 mM (orange), 0 mM (grey). Source data shown as circles, generated fits shown as solid lines.

An alternative reason that the photoreduction slows down as more of the hemes of MtrC become reduced could be that the microscopic reduction potentials of heme 10 may change as a function of overall number of reduced hemes. As calculated by Barrozo et al., the microscopic reduction potentials of MtrC in the singly-reduced and singly-oxidised states could be quite different (Fig. 3.5.6) and the lower potentials in the fully reduced state may slow down the rate of oxidative charge separation.[178] It is possible that these changes impact on the observed photoreduction timecourses.

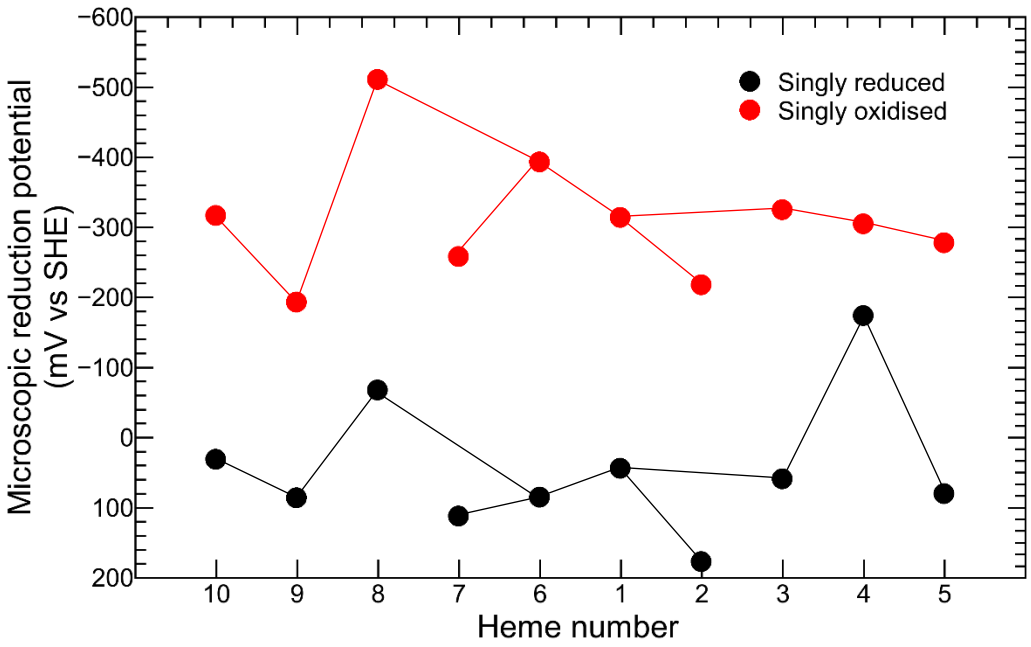

Figure 3.5.6 Microscopic reduction potentials for singly reduced (black) and singly oxidised (red) MtrC predicted by Barrozo et al.[178]

The models presented here (Model 3 in particular) present a useful platform for studying RuMe-MtrC under different conditions. The model should be able to be adapted to predict photoreduction timecourses for other RuMe-MtrC variants or even other RuMe-cytochrome conjugates provided the photocycle kinetics are known. The model also highlights areas where the photocycle of RuMe-MtrC could be optimised for more efficient photochemistry. This will be discussed further in Chapter 7.

3.6 - General discussion

This chapter has explored the photochemistry of RuMe-MtrC with the goal of using this biohybrid construct to capture light and produce electrons. RuMe-MtrC has been demonstrated to photoreduce upon irradiation in the presence of the SEDs EDTA and cysteine, and its photocycle has been examined using different techniques. The findings from these experiments have enabled the generation of a kinetic model for RuMe-MtrC that can reproduce the observed photoreduction behaviours with good agreement.

The wider aim of this work is to use RuMe-MtrC as the first subunit in a photocatalytic system. It is therefore prudent at this point to evaluate RuMe-MtrC against Lubner's attributes of a photocatalytic system[22] set out in Section 1.2:

1) Efficient charge separation

Ru-diimine complexes have favourable properties for generating CSSs due to efficient ISC to long-lived triplet excited states. This, together with close positioning of RuMe close to heme 10 of MtrC allows for efficient generation of the primary CSS. We see over 98% quenching of the inherent PL of RuMe upon attachment to MtrC and rates of charge separation in RuMe-MtrC have been shown to be between 1 and 2 orders of magnitude faster than the radiative/non-radiative decay pathways. These observations suggest that the primary CSS forms with near unity quantum yield.

2) Long lived CSS

The primary CSS of RuMe-MtrC does not, unfortunately, have a long lifetime. The close positioning of RuMe and heme 10 of MtrC means that in addition to fast charge separation the corresponding charge recombination is also rapid (Table 3.5.1). This gives little chance for the SED to be oxidised before the system returns to the ground state. The quantum yields for electron generation are thus quite poor with a maximum of 20% obtained for initial rate of photoreduction with 250 mM EDTA.

3) Minimum energy expended to stabilise CSS

The hemes of MtrC have reduction potentials spanning from around 0 to -400 mV, while these potentials can be altered to some extent by modifying the coordination environments, this has its limits. Fortunately, most solar fuels have thermodynamic potentials higher than the hemes of MtrC (see Table 1.1.1), as do many biological redox reactions which could be targeted in MR-1 (see Fig. 1.6.1). The energy lost generating the RuMe-MtrC CSS does not, therefore, preclude its use in a biohybrid photocatalytic module.

4) Antenna system for maximal effective photon flux

At present, only one photosensitiser is attached to each MtrC. An antenna system would be an excellent way to increase light absorption and, hopefully, rates of photoreduction. The staggered-cross arrangement of the hemes in MtrC could form the basis of an antenna system, with multiple photosensitisers attached to MtrC at the termini of these branches. Ideally, the photosensitisers attached to MtrC would have different absorbance profiles spanning the visible region such that they do not compete with one another for the available sunlight. Options to achieve this will be explored further in Chapter 7.

5) Robust or self-repairing

MtrC is a relatively stable protein and it has been demonstrated that RuMe-MtrC has excellent photostability, being able to continuously reduce RB5 over 9h with minimal decrease in rate. RuMe-MtrC could therefore be considered to be robust if not self-repairing. If applied to whole-cell photocatalysis, MtrC could be replenished by the host cell but these new proteins would likely need to be photosensitised *in situ*. The development of biocompatible labelling strategies and photosensitisers is therefore of great importance and will be considered further in Chapter 7.

The ability of RuMe-MtrC to undergo photoreduction is a promising start for the development of the nanoreactor (Fig. 1.6.2) and the whole-cell photocatalytic systems (Fig. 1.6.1) described in Section 1.6. During photocatalytic azo dye reduction by RuMe-MtrC it is hypothesised that the hemes of MtrC act in a similar manner to the conduction bands of doped semiconductors[58–61,95] by storing accumulating electrons for subsequent multielectron chemistry. RuMe-Br alone was not found to be able to reduce RB5 (data not shown) highlighting the important role of the hemes as an electron reservoir.

At present, the rate of electron production or TOF by RuMe-MtrC is relatively low, at $\approx$1 min^{-1} with 100 mM EDTA as a SED. Nevertheless, until more optimised variants are produced, RuMe-MtrC is sufficiently photoactive to continue developing proof-of-principle nanoreactors. RuMe-MtrC, as a relatively large, soluble protein, cannot transport electrons across a membrane. Formation of a RuMe-MtrC:MtrAB will be essential for moving the electron generated by RuMe-MtrC to the inside of a liposome. Formation of such complexes will be explored in the next chapter.

CHAPTER 4

BIOPHYSICAL CHARACTERISATION OF RECONSTITUTED MtrC:MtrAB COMPLEXES

Chapter 4 - Biophysical characterisation of reconstituted MtrC:MtrAB complexes

4.1 - Structure of MtrCAB

The MtrCAB complex forms part of the Mtr pathway in MR-1. It spans the outer membrane of the bacterium and allows electrons to cross from the periplasm to extracellular acceptors (Fig. 1.6.1). The structure of MtrCAB from *Shewanella baltica* (*S. baltica*) was resolved recently by X-ray crystallography.[134] The structure of this protein complex was solved to 2.7 Å resolution and showed that MtrC is oriented with domain II in close contact with MtrAB and a distance of less than 14 Å between heme 5 of MtrC and heme 10 of MtrA. There is high sequence similarity between the protein sequences of *S. baltica* and MR-1 allowing for a homology model to be created for MtrCAB from MR-1 (Fig. 1.6.2). This structure is of great value for understanding the transmembrane electron transport properties of MtrCAB. Alongside these structural studies, analysis of the electronic properties of MtrCAB and its isolated components have revealed that both MtrA and MtrC have a similar range of reduction potentials with both proteins being redox active between 0 and -400 mV (v.s. SHE).[171,172]

In the nanoreactor described in Figure 1.6.2, RuMe-MtrCAB provides a conduit for photogenerated electrons to cross the liposome membrane. However, at present we are not able to directly purify MtrCAB with SDMs and therefore the RuMe photosensitiser cannot be attached. In order to construct a light-driven electron conduit we can instead consider whether RuMe-MtrC will combine spontaneously with MtrAB complexes to form the desired constructs. Evidence that supports the *in vitro* complexation of MtrC and MtrAB, including some of the data presented here, has been reported previously.[143,171] Native PAGE and analytical ultracentrifugation (AUC) were used to demonstrate the 1:1 complexation of MtrAB with soluble forms of MtrC. An understanding of this complex and its properties is thus of importance in designing our desired nanoreactors.

The aim of this chapter is to establish whether or not RuMe-MtrC and MtrAB form a RuMe-MtrC:MtrAB complex that structurally and functionally resembles WT MtrCAB. Various biophysical techniques were used to address this aim and the photoreduction of the resulting complex was assessed as a foundation for demonstrating light-driven transmembrane electron transfer.

4.2 - Assembly of MtrC:MtrAB complexes

4.2.1 - Establishing evidence for interaction of RuMe-MtrC and MtrAB

While RuMe-MtrC has been demonstrated to photoreduce in the presence of EDTA it will need to be reconstituted with MtrAB in order to act as part of a transmembrane electron conduit. A number of techniques were used to determine whether these proteins would form a complex and what the nature of this reconstituted complex might be. To provide initial evidence for an interaction between RuMe-MtrC and MtrAB, analytical gel filtration was used. A Superose 6 Increase 10/300 GL (GE Healthcare) column was pre-equilibrated with 50 mM NaH_2PO_4/Na_2HPO_4, 50 mM NaCl, 5 mM LDAO, pH 7.5 buffer (PNL Buffer) at 0.25 mL/min. Experimental samples of RuMe-MtrC, MtrAB and a 2:3 mixture of RuMe-MtrC and MtrAB were prepared and eluted from the column with a flow rate of 0.25 mL/min. Chromatograms from these experiments are shown in Figure 4.2.1 and absorbance ratio analysis is described in Table 4.2.1. SDS-PAGE analysis of the eluted fractions shows bands for the expected proteins (Fig. 4.2.1).

Table 4.2.1 Wavelength analysis[d] from analytical gel filtration of RuMe-MtrC and MtrAB using a Superose 6 Increase 10/300 GL column. Absorbance readings obtained using Äkta Pure multiwavelength chromatograph.

Sample	Elution volume (mL)	$A_{410\,nm}/A_{280\,nm}$
RuMe-MtrC	17.8	5.83
MtrAB	17.2	3.69
RuMe-MtrC + MtrAB	17.2	3.64
	16	4.82
Predicted for RuMe-MtrC:MtrAB	-	4.76

[d] Predicted absorbance ratio for RuMe-MtrC:MtrAB obtained by averaging ratios of RuMe-MtrC and MtrAB.

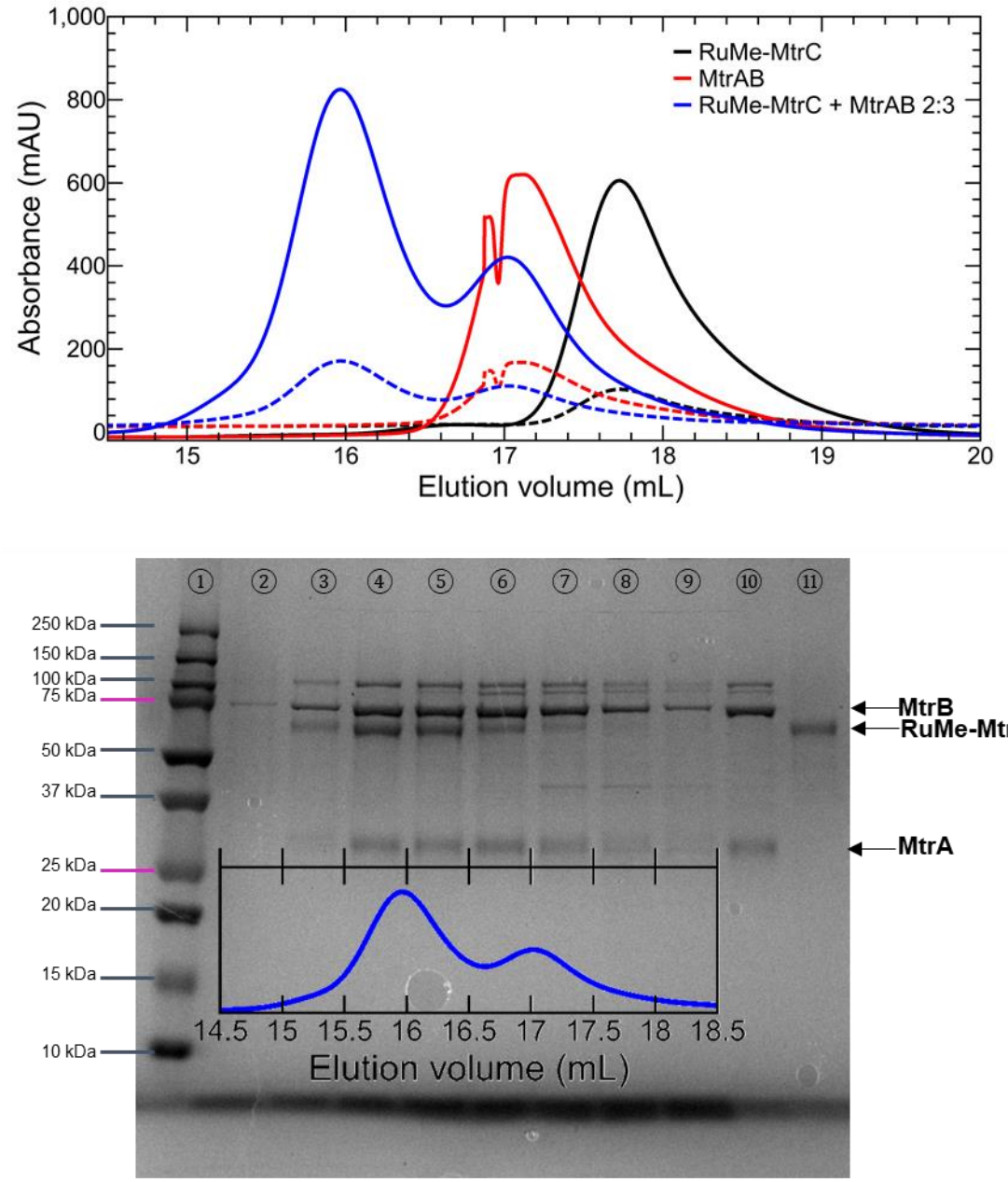

Figure 4.2.1 Top) Gel filtration chromatograms for samples of 40 µM RuMe-MtrC (Black), 40 µM MtrAB (Red) and a mixture of 32 µM RuMe-MtrC and 48 µM MtrAB (blue) in PNL Buffer, solid lines show absorbance at 410 nm, dashed lines show absorbance at 280 nm; **Bottom)** SDS-PAGE analysis of eluted fractions from gel filtration of a mixture of RuMe-MtrC + MtrAB (2:3), gel is Coomassie stained: ① - Precision Plus Dual colour with molecular weights indicated, ②-⑨ - Eluted fractions corresponding to superimposed chromatogram showing absorbance at 410 nm against elution volume, ⑩ - MtrAB, ⑪ - RuMe-MtrC.

RuMe-MtrC elutes with maximal concentration at 17.8 mL whereas MtrAB elutes earlier, with maximal concentration at 17.2 mL which is explained by the larger size of MtrAB (≈114 kDa vs ≈ 77 kDa). When these two proteins are combined at a 2:3 ratio of RuMe-MtrC to MtrAB a species elutes at 16 mL suggesting that a complex forms when RuMe-MtrC is combined with MtrAB and its higher molecular weight and size results in it eluting

earlier from the gel filtration column. This suggestion is backed up by the wavelength ratio analysis (Table 4.2.1) which finds that this putative complex has an $A_{410\ nm}/A_{280\ nm}$ ratio very similar to that predicted for a 1:1 RuMe-MtrC:MtrAB complex. Also significant is that when RuMe-MtrC and MtrAB are mixed there is no feature at 17.8 mL in the chromatogram, indicating that all the RuMe-MtrC present has formed a complex with MtrAB.

SDS-PAGE analysis of fractions eluted from the mixture of RuMe-MtrC and MtrAB is also supportive of complex formation in this sample. Bands corresponding to RuMe-MtrC, MtrA and MtrB are apparent in the fractions proposed to contain the complex (15.5-16.5 mL, lanes ④+⑤). The band for RuMe-MtrC fades through the later fractions and is not evident in the fraction containing material eluted at 17.8 mL (lane ⑧). As has been discussed in Section 2.3.2, higher molecular weight bands are often present when working with Mtr proteins which correspond to the masses of MtrAB, and in some cases MtrCAB, which may not have fully dissociated. Bands corresponding to MtrAB are evident here above the bands for MtrB.

The putative RuMe-MtrC:MtrAB peak and the peak from MtrAB are difficult to resolve from one another as evidenced by the presence of RuMe-MtrC (and therefore putative RuMe-MtrC:MtrAB) in SDS-PAGE analysis from lane ③ to lane ⑦. Elution rates were slowed to attempt to gain better resolution by reducing turbulence however no improvement was observed (data not shown). As a result, when purifying the proposed reconstituted complex only eluate ≤16.5 mL was considered to be pure putative RuMe-MtrC:MtrAB.

In these experiments LDAO was used as a detergent instead of the more commonly used detergent TX100 as the micelle size of TX100 is similar to the size of the proteins being studied[135] and therefore may have hindered their progress through the column matrix; LDAO micelles are smaller and less likely to interfere with protein elution (≤21.5 kDa).[205–207] In addition, TX100 has a strong absorbance at 280 nm which would have complicated the absorbance ratio analysis presented in Table 4.2.1.

These experiments give us initial confidence that the MtrC:MtrAB assembly can be reconstituted. They also serve as a means to purify the reconstituted complex for further experiments that will be described later. Gel filtration, however, has limitations for determining the accurate molecular weight of proteins and complexes, particularly for membrane proteins where detergent micelles may have an effect on protein migration through the column matrix. Running protein standards on the column to produce a standard curve could have provided more evidence that the putative complex was eluting in the appropriate position, however the presence of detergents may have invalidated

any results. Given these limitations, additional techniques were required to gain a more analytical insight into the nature of the reconstituted complex.

4.2.2 - Sedimentation analysis of the reconstituted RuMe-MtrC:MtrAB complex

The technique and theory of AUC has been described previously in Section 2.6.1. This sensitive and powerful technique allows the molecular weight of macromolecules in solution to be determined. In these experiments TX100 is used as a detergent (see below). This is because TX100 micelles have a partial specific volume ($\bar{v}$) of 0.91 mL g^{-1} which means they have a similar density to the buffer and therefore are largely unaffected by the centrifugal forces used here[135] allowing the proteins to be studied without detergent influence.

Sedimentation equilibrium (SE) experiments were carried out as described in Section 2.6.1.2. Briefly, protein samples were prepared in 50 mM NaH_2PO_4/Na_2HPO_4, 50 mM NaCl, 0.1 % (v/v) TX100, pH 7.5 Buffer (PNTx Buffer) and loaded into AUC cells using PNTx Buffer as the reference. The samples were then centrifuged until equilibrium was reached at 8000, 10000 and 12000 RPM. At each equilibrium, absorbance vs radius of rotation scans of the samples were obtained at 410 nm. An example of a full data set can be found in Figure 2.6.1. Data was analysed and fitted to a 1-component model using Ultrascan II software with $\bar{v}$ values derived from the protein amino acid sequences and a buffer density estimated as 1.007 g/mL.

In addition to RuMe-MtrC, MtrC and MtrAB, a further protein was tested in this way. OmcA is another outer-membrane decaheme cytochrome from MR-1. The *omcA* gene appears in the *mtr* operon and X-ray crystal structures show a similar global structure to MtrC[208] however it is not encoded alongside an MtrAB homologue and has not previously been observed to interact with MtrAB.[143] It is included here as a control to determine the specificity of any interactions observed.

One way to present and interpret SE data is to plot the natural log of the absorbance against the radius of rotation squared. For an ideal 1-component system this will generate a straight line with a gradient proportional to the protein mass and the rotation speed. Figure 4.2.2 presents results from SE analysis of MtrC, RuMe-MtrC, MtrAB and OmcA plotted in this way. Parameters relevant to these analyses are presented in Table 4.2.2 where it is seen the masses derived for these proteins are within 7% of the masses predicted from sequence analysis. These results confirm that, as expected, MtrC,

RuMe-MtrC and OmcA behave as monomers in solution at this concentration and that MtrA and MtrB behave as a strongly associated heterodimer.

The percentage mass difference for RuMe-MtrC is larger than MtrAB and MtrC; this may be due to the unknown contribution of the RuMe label to the $\bar{v}$ of the protein. The derived mass for OmcA, which has no such label, is lower than the mass calculated from its sequence. Which may be rationalised by differential cleavage of its V5-epitope/6xHis tag which has been observed previously.[143,208]

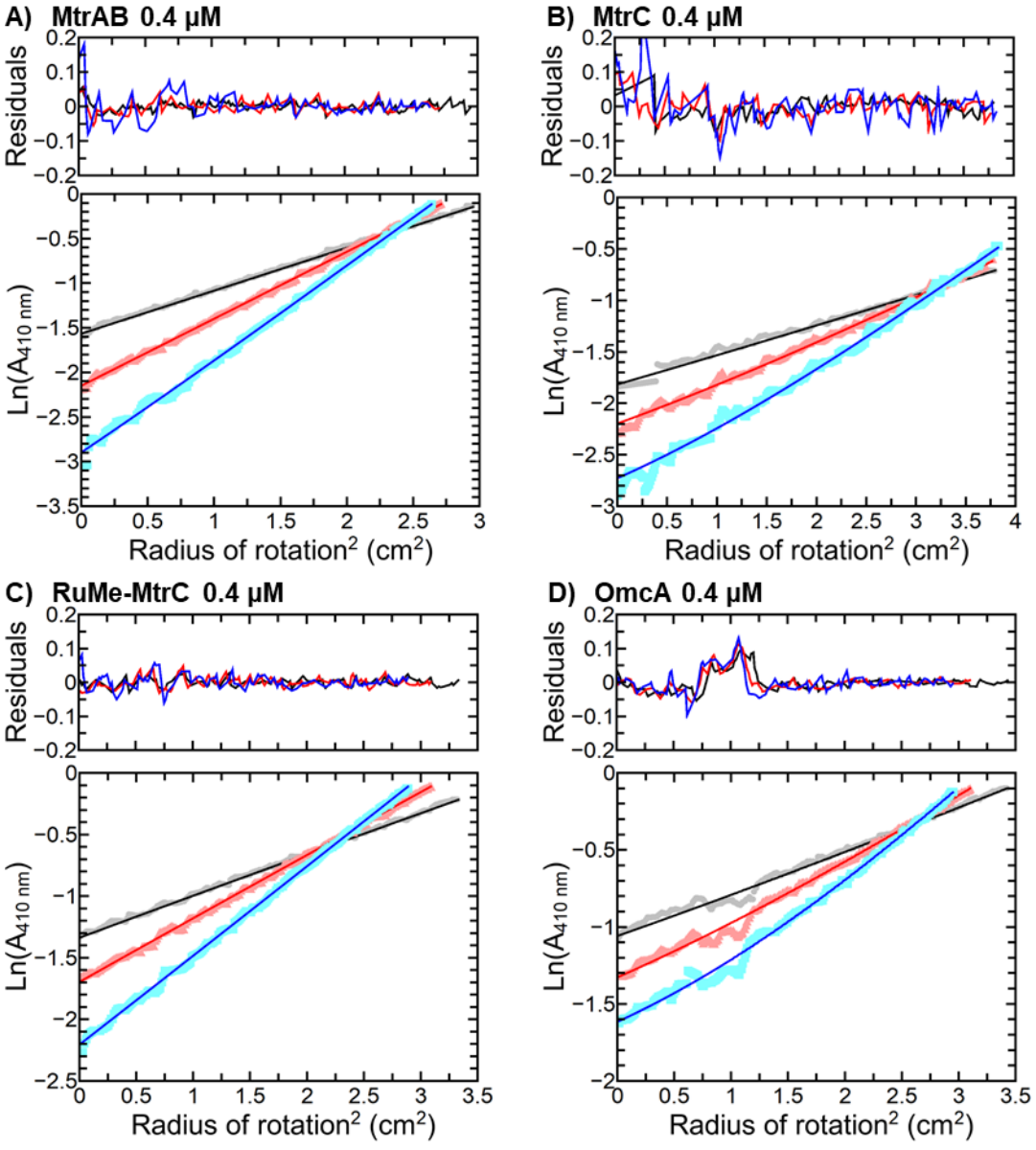

Figure 4.2.2 Sedimentation equilibrium data for 0.4 µM samples of: MtrAB (A), MtrC (B), RuMe-MtrC (C) and OmcA (D). Data was collected at three speeds: 8 kRPM (Black/circles), 10 kRPM (Red/triangles) and 12 kRPM (Blue/squares) and one scan at each speed is shown. Lower panels show the natural log of absorbance at 410 nm against the square of the radius of rotation. Symbols represent the processed data and solid lines show the fit generated by Ultrascan II. Upper panels show the residuals when subtracting the processed data from the fitted data. Samples in PNTx Buffer

Table 4.2.2 Biophysical parameters from SE analysis of Mtr proteins at 0.4 μM

Sample components	$\bar{\nu}$ ($cm^3\ g^{-1}$)	M_W predicted from sequence (kDa)	M_w derived from AUC (kDa)	% difference (derived/predicted)
MtrAB	0.716	114	119.6	+5
MtrC	0.722	76.3	79.4	+4
RuMe-MtrC	0.721	76.8	82.4	+7
OmcA	0.720	85.6	80.0	-7

MtrAB was combined with each of the outer membrane multiheme cytochromes at a 1:1 ratio and SE was performed under the same conditions as above. Results from these experiments are shown in Figure 4.2.3. SE data for the mixtures of RuMe-MtrC or MtrC with MtrAB were well described by a 1-component model with derived masses of 203.3 and 196.5 kDa respectively. By comparing the data from RuMe-MtrC, MtrAB, and RuMe-MtrC + MtrAB (Fig. 4.2.4) we see that the gradient of the data for the protein mixtures is greater than that for the isolated proteins. These results are consistent with the formation of 1:1 RuMe-MtrC:MtrAB and MtrC:MtrAB complexes and the derived masses are within 7% of the masses calculated from the protein sequences (Table 4.2.3).

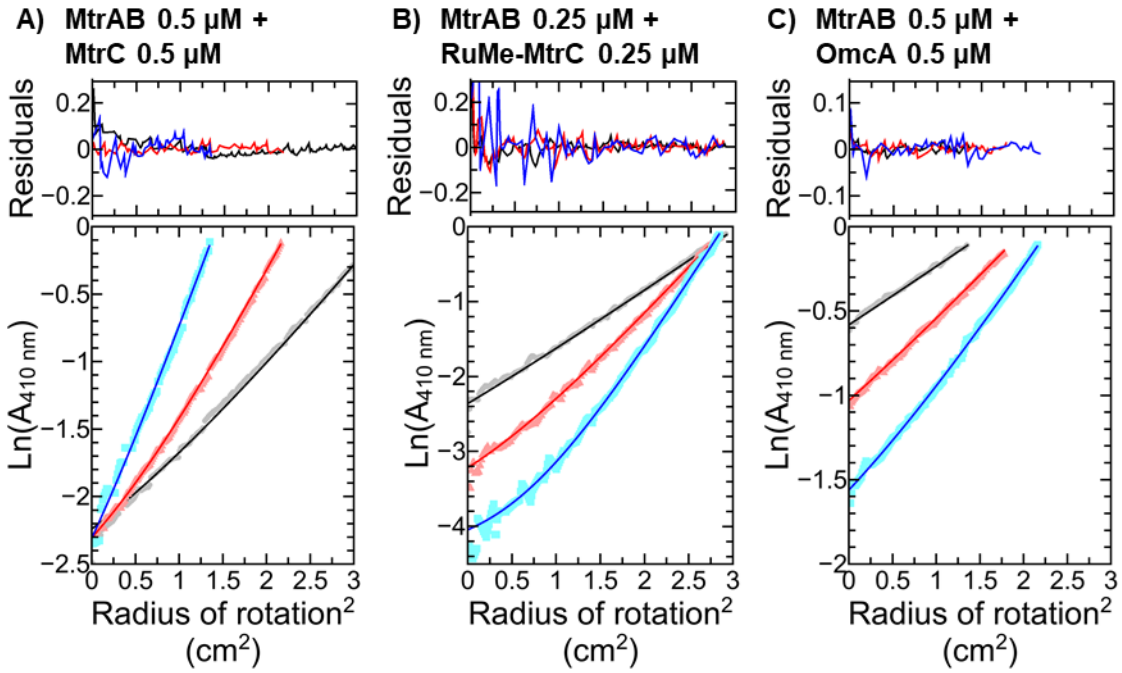

Figure 4.2.3 Sedimentation equilibrium data for samples of: MtrAB + MtrC (A), MtrAB + RuMe-MtrC (B) and MtrAB + OmcA (C). Data was collected at three speeds: 8 kRPM (Black/circles), 10 kRPM (Red/triangles) and 12 kRPM (Blue/squares) and one scan at each speed is shown. Lower panels show the natural log of absorbance at 410 nm against the square of the radius of rotation. Symbols represent the processed data and solid lines show the fit generated by Ultrascan II. Upper panels show the residuals when subtracting the processed data from the fitted data. Samples in PNTx Buffer

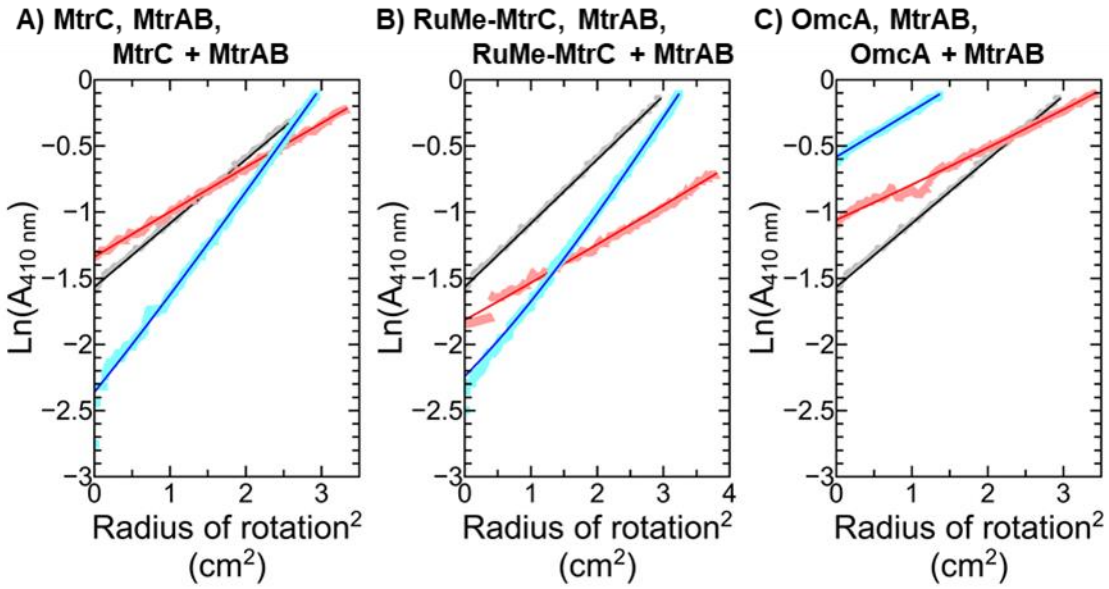

Figure 4.2.4 Sedimentation equilibrium data for samples of MtrAB (Black/circles), Outer membrane cytochromes (Red/triangles) MtrC (A), RuMe-MtrC (B) and OmcA (C) and mixtures of MtrAB with these outer-membrane cytochromes (Blue/squares). Only data collected at 8 kRPM is shown. Panels show the natural log of absorbance at 410 nm against the square of the radius of rotation. Symbols represent the processed data and solid lines show the fit generated by Ultrascan II. Samples in PNTx Buffer

Table 4.2.3 Biophysical parameters from SE analysis of mixtures of Mtr proteins.

Sample components	Number of components in model	$\bar{\nu}$ ($cm^3\ g^{-1}$)	M_W predicted from sequence (kDa)	M_w derived from AUC (kDa)	% difference (derived/ predicted
MtrAB + MtrC	1	0.718	190.3	196.5	+3
MtrAB + RuMe-MtrC	1	0.718	190.9	203.3	+7
MtrAB + OmcA	1	0.717	199.6	89.9	-55
MtrAB + OmcA	2	0.716	114	119.3	+5
		0.720	86.5	79.7	-8

Analysis of the SE data from the mixture of OmcA and MtrAB using the 1-component gave a good fit, though it predicted a mass of 89.9 kDa which represents an average of the masses of OmcA and MtrAB. A more sensible result was obtained using a 2-component non-interacting model which gave derived masses of 79.7 and 119.3 kDa which reflect the masses obtained for the two components in isolation (Table 4.2.2). These data suggest that OmcA does not form a complex with MtrAB and reinforces that the MtrC:MtrAB complexes observed here are specific.

These results corroborate the interpretation of the gel filtration analysis, that the putative complex observed in gel filtration studies is in fact a RuMe-MtrC:MtrAB complex. The

protein concentrations in these experiments are also around 2 orders of magnitude lower than in the gel filtration experiments; even at these more dilute concentrations the MtrC:MtrAB complexes show no signs of being in an equilibrium which implies a low K_d. The lack of interaction between OmcA and MtrAB is also encouraging as it suggests that the MtrC:MtrAB and RuMe-MtrC:MtrAB complexes have some specificity and thus may be more likely to resemble WT MtrCAB complexes.

4.3 - Structural characterisation of the RuMe-MtrC:MtrAB complex by SANS

Having formed MtrC:MtrAB complexes *in vitro* and purified them using gel filtration as described in Section 4.2.1, more descriptive structural information was sought to establish whether these complexes truly reflect the structure of WT MtrCAB formed *in vivo*. Structural biology of large protein complexes is already a challenging task, and when the proteins in question are membrane-associated the task becomes even more difficult. Colleagues have attempted, over a number of years, to obtain X-ray diffraction quality crystals of MtrCAB from MR-1 but the conditions required to achieve this have eluded them. As such, an alternative approach was pursued to structurally characterise the RuMe-MtrC:MtrAB complex.

Fortunately, there are other techniques besides X-ray diffraction available to gather structural information on macromolecules. Small angle scattering techniques determine the interatomic distances of all pairs of atoms in a species; from this, models of the "molecular envelope" can be generated which give the overall shape of the species. While small angle X-ray scattering (SAXS) is commonly used for the study of soluble proteins, the micelles in detergent solutions strongly scatter X-rays making this technique unsuitable for experimentation on membrane-associated proteins. To overcome this, small angle neutron scattering (SANS) (see Section 2.6.2) was used instead. The most valuable feature of this technique, which makes it useful for studying membrane proteins, is that at different concentrations of D_2O certain components of the sample can be made effectively invisible. These concentrations are known as match points and, by carefully applying this principle, detergent micelles can be subtracted away from the scattering data revealing just the membrane proteins. SANS has been employed previously to gain structural information about MtrCAB and MtrAB from MR-1 using Fos-choline 12 as a detergent.[157]

4.3.1 - SANS Data collection and validation

As described in Section 2.6.2.2, samples of MtrC:MtrAB, RuMe-MtrC:MtrAB and WT MtrCAB were prepared in 20 mM HEPES, 100 mM NaCl, 2.8 mM Fos-Choline 12, pH 7.8, 13% D_2O Buffer (HNFD Buffer). Scattering curves for the protein samples and HNFD Buffer were obtained at three detector distances. Initial data processing was carried out to produce scattering curves for each protein complex covering Q = 0.006 to 0.5 $Å^{-1}$. Data from previous experiments collected under comparable conditions,[157] here termed WT MtrCAB MJE and MtrAB MJE, were kindly provided by Dr. M.J. Edwards for comparison.

The scattering curve for WT MtrCAB collected for this work overlays well with that obtained previously meaning that this work can be confidently compared to the findings of Edwards et al.[157] The scattering curve for RuMe-MtrC:MtrAB also overlays well with WT MtrCAB whereas the curve for MtrC:MtrAB does not. The latter has lower relative scattering intensity at low Q indicating a smaller species (see Fig. 2.6.3). The curve for MtrAB is clearly distinct from the others, as expected for the smaller complex.

The scattering curves shown in Figure 4.3.1A were loaded into ATSAS 3.0.1 software where Guinier plots were generated by plotting the natural log of the scattering intensity against Q^2 (Fig 4.3.1B). Scattering curves in this form should be linear at low values of Q^2. The gradient of these lines can be used to approximate the radius of gyration (R_g) of the species which is the root-mean-square distance to the centre of mass for all atoms in the species. The Guinier approximation equation is shown below:

$$I = I_0 e^{\left(\frac{Q^2 R_g^2}{-3}\right)}$$

where I is the intensity at a given scattering distance; I_0 is the extrapolated scattering intensity at a hypothetical Q of 0 $Å^{-1}$; Q is the momentum transfer in $Å^{-1}$ and R_g is the radius of gyration in Å.

The approximation can be rearranged to give R_g in terms of the gradient of the Guinier plot.

$$R_g = \sqrt{-3\left(\frac{Ln(I)-Ln(I_0)}{Q^2}\right)} = \sqrt{-3(slope)}$$

The Guinier approximation is valid for $Q < \frac{1.3}{R_g}$.[209] Using this equation and the linear fits presented in Figure 4.3.1B, values of R_g were approximated for the five protein complexes. These values are presented in Table 4.3.1.

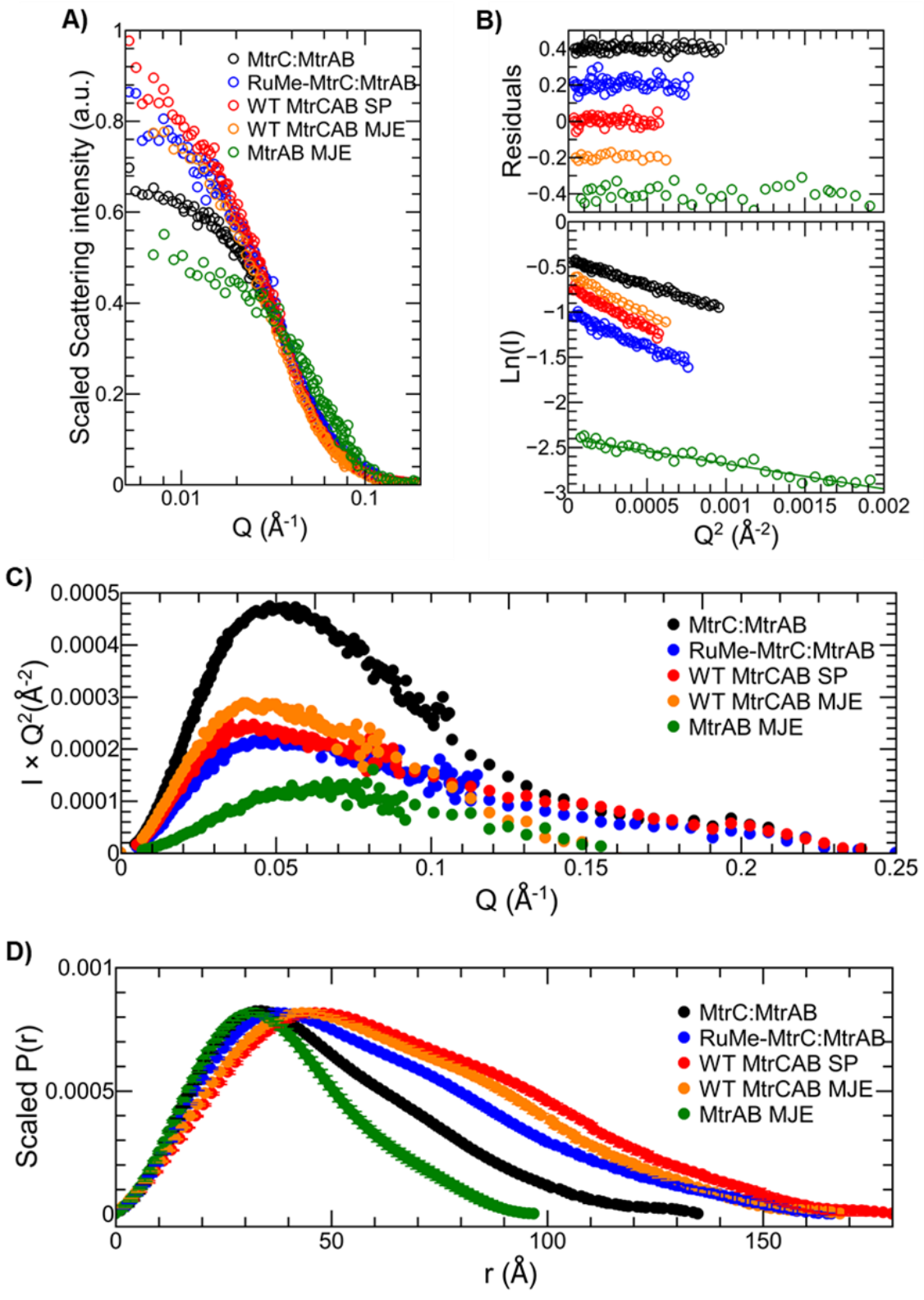

Figure 4.3.1 SANS curves of Mtr protein complexes: MtrC:MtrAB (black); RuMe-MtrC:MtrAB (blue); WT MtrCAB measured in this work (Red); WT MtrCAB (orange) and MtrAB (green) measured on a previous occasion and reported in Edwards et al.[157] **A)** Scattering curves produced by merging Scattering data from different detector distances, data has been scaled to be equal at Q=0.03 Å^{-1}; **B)** Guinier region of the scattering curves are shown in the lower panel, lines are linear fits to the data and residuals are shown in the upper panel where they have been staggered by 0.2 to aid distinction; **C)** Kratky plots of the scattering curves; **D)** P(r) curves produced from the scattering curves, curves have been scaled linearly to have equal maxima.

Continuing in ATSAS, Kratky plots were produced for the five complexes (Fig. 4.3.1C). Plotting the curves in this way allows the global flexibility of the protein structures to be assessed. Globular proteins with minimal flexibility show a bell-shaped peak in a Kratky plot and the curve will smoothly converge to the x-axis. This is seen for the previously studied MtrAB and MtrCAB.[157] The protein complexes used in this study converge to the x-axis at higher Q, indicative of structures with multiple protein domains. The reason for this difference is unclear and may be a result of slight differences in buffer subtraction. Crucially the Kratky plots of all five protein complexes converge to the x-axis. A Kratky plot that does not converge in this way indicates a partially unfolded protein or a structure with a flexible linkage.

Finally, P(r) distributions were generated in GNOM software (Fig. 4.3.1D). These curves represent the proportional distribution of interatomic distances in the complexes. From these distributions we can derive the maximum dimensions of the complex (D_{max}) and re-determine R_g which were found to be similar to the approximated values from the Guinier analysis. These findings suggest that WT MtrCAB and RuMe-MtrC:MtrAB have similar overall dimensions whereas the MtrC:MtrAB sample has a significantly lower D_{max} and R_g values.

Table 4.3.1 Biophysical parameters for Mtr protein complexes derived from Guinier approximations and P(r) curves. Entries labelled MJE were obtained from Edwards et al.[157]

Protein complex	R_g (Å) (from Guinier approx.)	R_g (Å) (from P(r))	D_{max} (Å)
MtrC:MtrAB	40.7 ± 0.3	42.0	135
RuMe-MtrC:MtrAB	47.0 ± 0.6	47.8	166
WT MtrCAB	53.1 ± 0.6	49.8	168
WT MtrCAB MJE	51.8 ± 0.5	50.7	170
MtrAB MJE	29.0 ± 0.6	29.9	97

These initial results provided from simple data analyses support the hypothesis that RuMe-MtrC:MtrAB resembles WT MtrCAB in its global structure. Given this, it is unusual that MtrC:MtrAB appears to have different structural properties.

Theoretically the sample of MtrC:MtrAB could have degraded before the SANS experiments were run, or a contaminant could have been present which altered the scattering curve of MtrC:MtrAB. To investigate these possibilities the samples of RuMe-MtrC:MtrAB and MtrC:MtrAB were analysed by SV AUC after the SANS experiments had been completed. This technique is related to the SE AUC discussed previously (Section 4.2.2) and details can be found in Section 2.6.1. Briefly, instead of allowing a

sample to come to equilibrium in a low speed centrifugal field, the sample is instead centrifuged at a high speed and the sedimentation process is monitored over time. SV AUC allows for identification of heterogeneity in a sample as different species will sediment at different rates in a centrifugal field. Using SEDFIT software the sedimentation profiles can be fitted to the Lamm equation and a sedimentation coefficient for each species can be extracted. These sedimentation coefficients can then be used to derive the M_W of each species.

Results for SV AUC analysis of RuMe-MtrC:MtrAB and MtrC:MtrAB are shown in Figure 4.3.2A. These plots show that in both samples the majority of the proteins are of the correct M_W to be MtrC:MtrAB complexes (≈190 kDa). The peaks at this M_W are symmetrical, suggesting that the proteins have not degraded; this would have resulted a wider distribution on the lower M_W side of the peak. The key difference between the two protein samples is the presence of a species at ≈120 kDa in the distribution for MtrC:MtrAB. This species is likely MtrAB which was carried through from the gel filtration purification. Given that MtrAB has only 10 hemes to the 20 hemes of MtrCAB, this small feature represents a larger proportion of the sample than might otherwise be assumed.

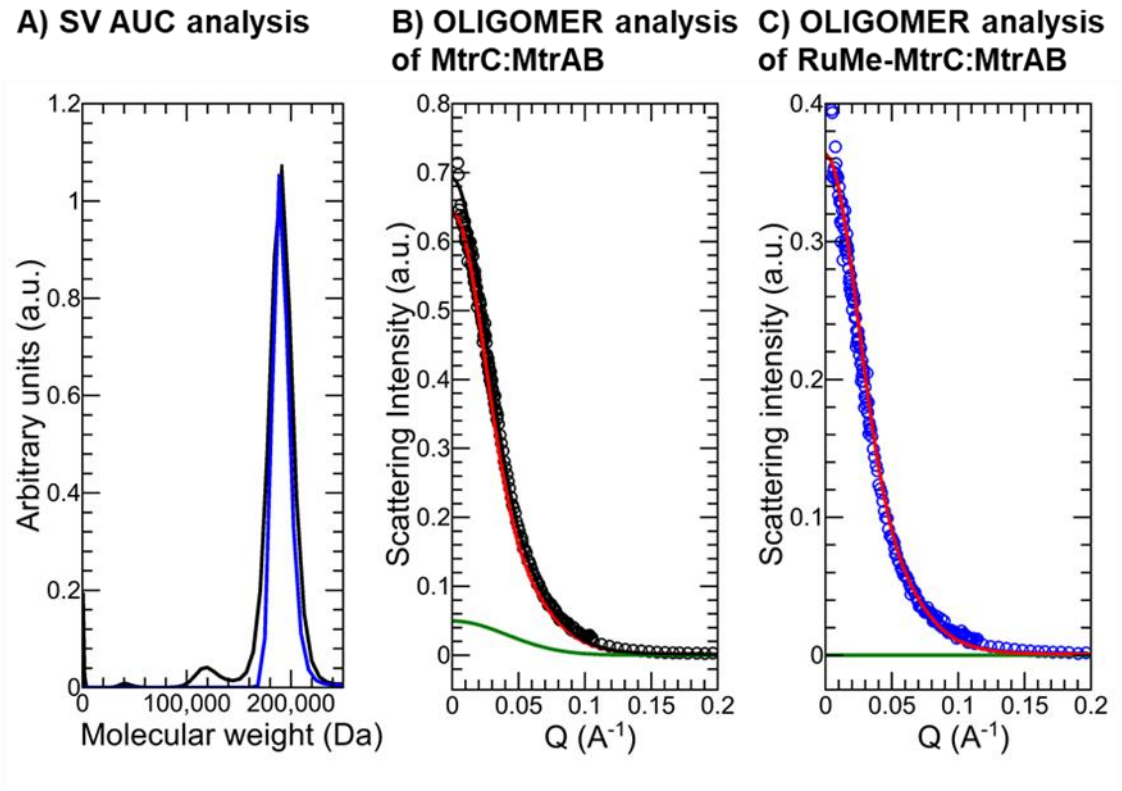

Figure 4.3.2 Analysis of heterogeneity in RuMe-MtrC:MtrAB and MtrC:MtrAB samples. **A)** M_W distribution of MtrC:MtrAB (black) and RuMe-MtrC:MtrAB (blue) derived from SEDFIT analysis of SV AUC data; **B+C)** Fitting of SANS scattering curves for MtrC:MtrAB (Black) and RuMe-MtrC:MtrAB (Blue) using OLIGOMER, Scattering curves shown as circles, fitted data shown as lines, Contributions from MtrAB (Green) and MtrCAB (Red) also shown.

The presence of MtrAB in the MtrC:MtrAB sample could explain the different scattering curve that was obtained. To examine this further, OLIGOMER software[210] was used to estimate the relative proportions of different species contributing to the SANS scattering curves. The scattering curves for RuMe-MtrC:MtrAB and MtrC:MtrAB were imported into OLIGOMER along with the structures of MtrAB and the homology model of MtrCAB from MR-1 built by Dr. Edwards (Fig. 1.6.2).[134] For MtrC:MtrAB the software assigned 83% of the contribution to this model of MtrCAB and 17% to MtrAB indicating that the fit to the scattering curve could be improved by addition of MtrAB. The fit to the scattering curve for RuMe-MtrC:MtrAB on the other hand could not be improved in this way and the software assigned the MtrCAB model 100% of the contribution.

These results taken together provide strong evidence that the MtrC:MtrAB sample was contaminated with a small amount of MtrAB. Unfortunately, this limits the usefulness of the data collected for this sample and further analysis on the scattering curves for MtrC:MtrAB will not be carried out. In future, SV AUC analysis would be a good choice for quality control of samples before SANS is carried out.

4.3.2 - *Ab initio* structural modelling

In order to further test whether the RuMe-MtrC:MtrAB complex resembles the WT MtrCAB complex, models of the possible protein structure of the four remaining samples were produced using DAMMIN software[211] as part of the ATSAS Online suite of tools. This software takes a P(r) distribution and creates a bead model that fits to both the described distribution and the scattering curves. The models produced by DAMMIN (Fig. 4.3.3) suggest a similar structure among all the MtrCAB complexes with comparable overall dimensions and shape. The fits of these models to the scattering data are presented in Figure 4.3.4 and χ^2 values describing goodness-of-fit are given in Table 4.3.2.

It should be noted that the models created by DAMMIN are by no means definitive representations of the complexes. For any P(r) distribution or scattering curve there are many possible structures that could explain the data. The models presented here represent a likely solution to the P(r) distribution and scattering data based on comparison of many such structures. Their good alignment to the structure of MtrCAB is, however, encouraging.

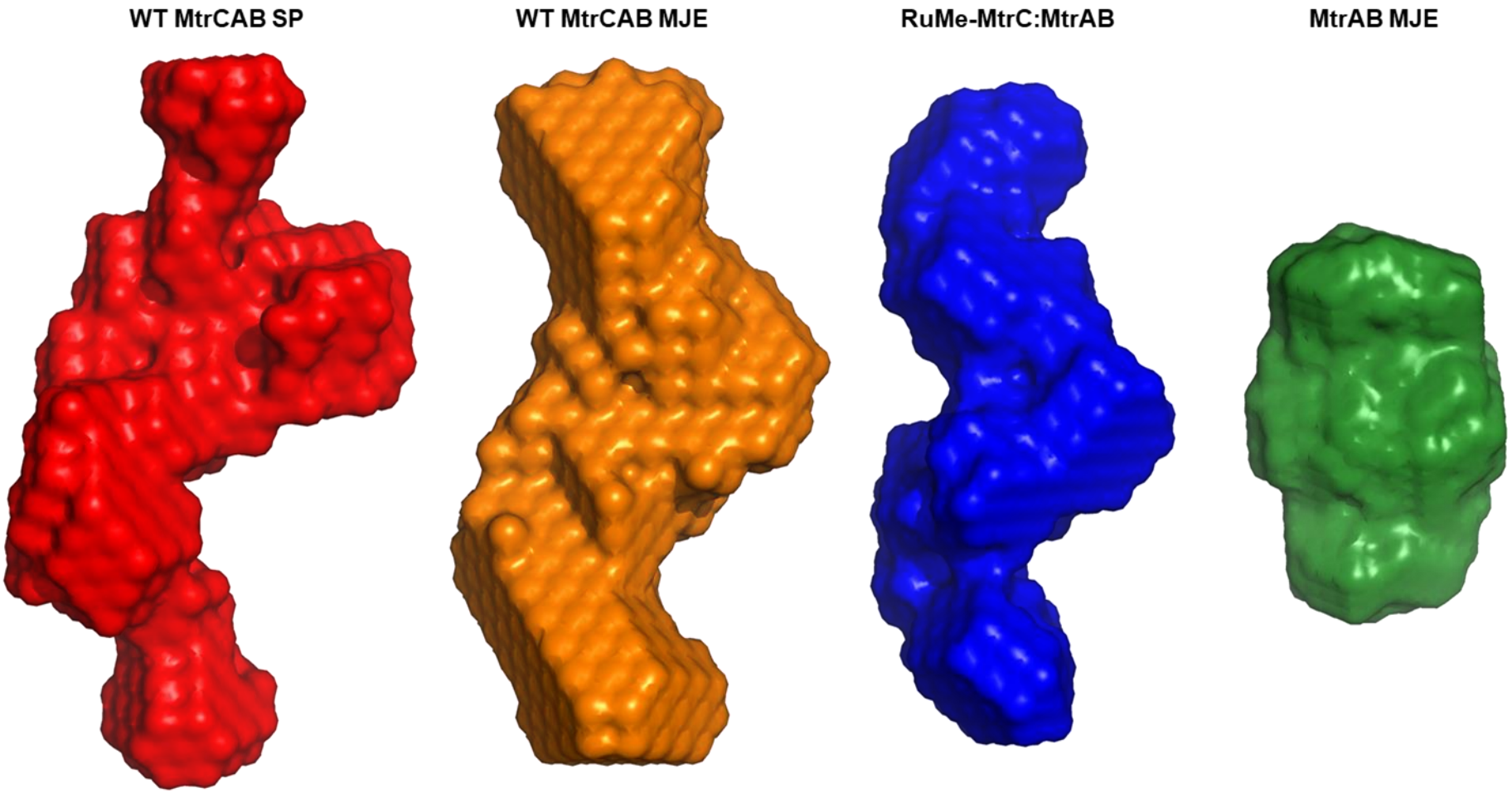

Figure 4.3.3 DAMMIN envelopes produced from P(r) distributions shown in Figure 4.3.1D for Mtr protein complexes: WT MtrCAB SP (red); WT MtrCAB MJE (orange); RuMe-MtrC:MtrAB (blue); and MtrAB MJE (green). Models rendered in Pymol software.

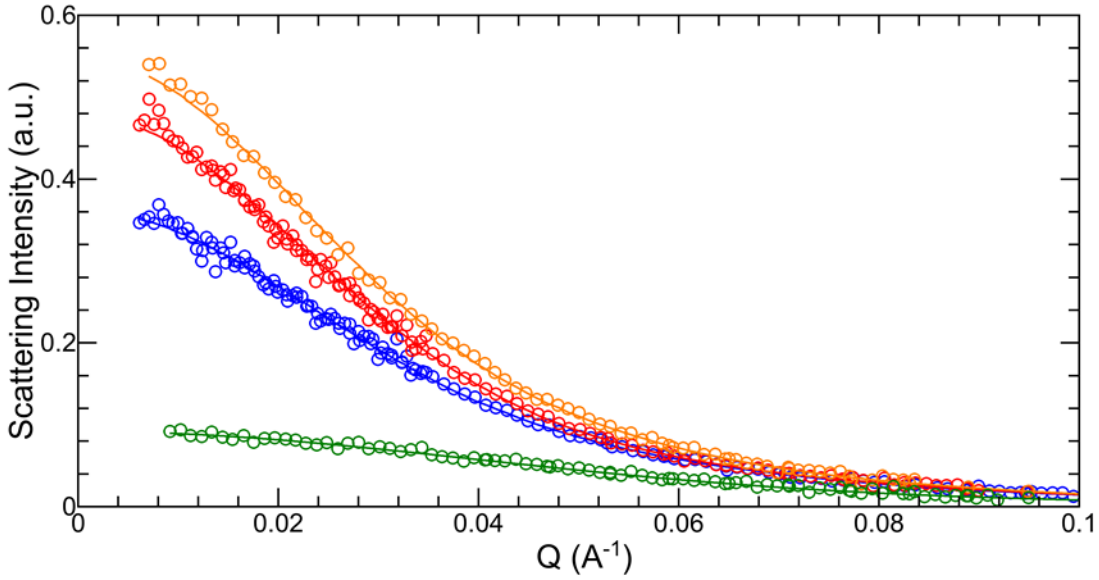

Figure 4.3.4 Fits of DAMMIN models to experimental scattering data for WT MtrCAB SP (red), WT MtrCAB MJE (orange), RuMe-MtrC:MtrAB (blue), and MtrAB MJE (green). Experimental data is shown as empty circles, fits are shown as solid lines.

Table 4.3.2 Goodness-of-fit parameters for DAMMIN modelling and subsequent SUPCOMB alignment to the structure of Mtr(C)AB

Protein complex	χ^2 of DAMMIN fit	NSD of SUPCOMB alignment
RuMe-MtrC:MtrAB	4.7	2.14
WT MtrCAB	1.9	2.61
WT MtrCAB MJE	3.0	2.97
MtrAB MJE	1.8	1.51

The models produced in DAMMIN were then aligned to the homology model of WT MtrCAB or MtrAB, using SUPCOMB software[212] as part of the ATSAS package. The aligned structures (Fig. 4.3.5) show that the DAMMIN models of RuMe-MtrC:MtrAB and WT MtrCAB fit well with the MtrCAB structure, having similar dimensions and good overlap. Normalised spatial discrepancies (NSDs) for these alignments are also provided in Table 4.3.2.

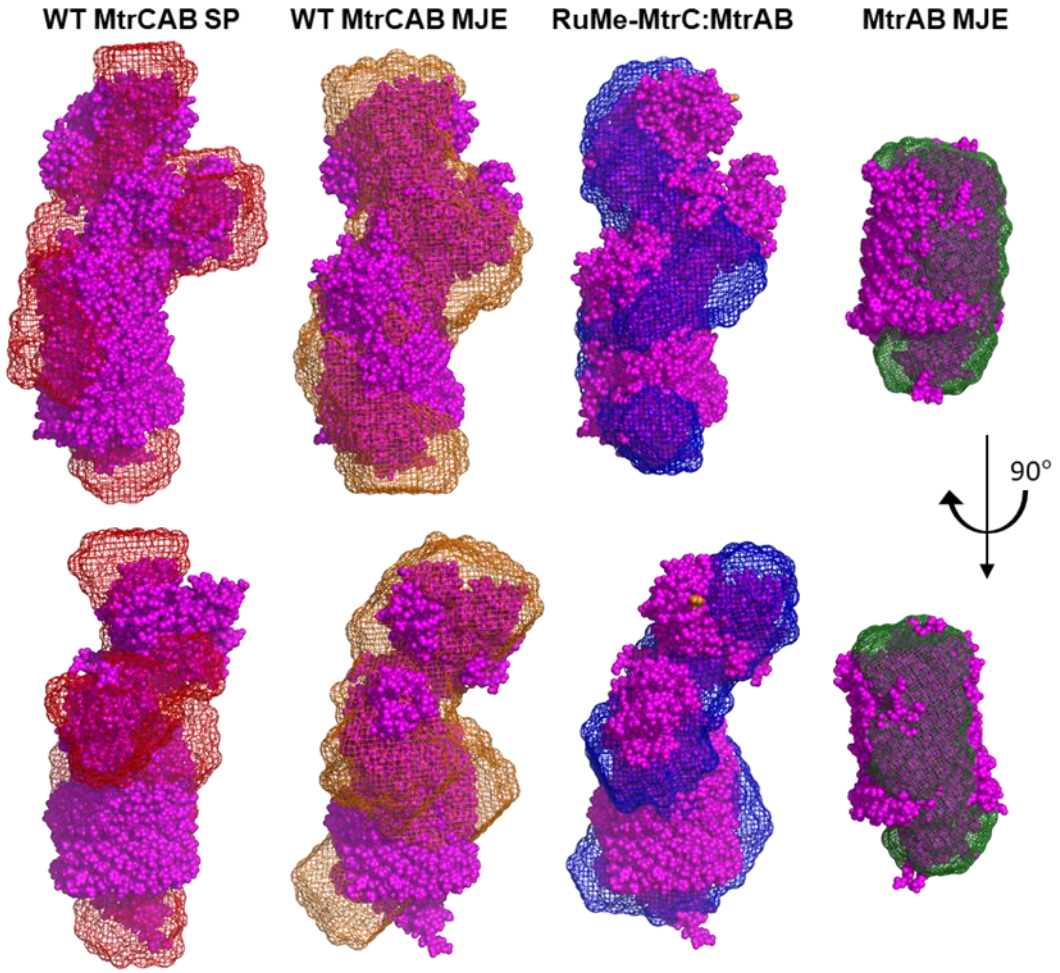

Figure 4.3.5 DAMMIN envelopes (Fig. 4.3.4) shown as surface mesh and aligned to the structure of MtrCAB or MtrAB using SUPCOMB. Mtr(C)AB is shown as purple spheres. Residue 657 of MtrC shown in orange for RuMe-MtrC:MtrAB. DAMMIN models are coloured as previously. The aligned structures are shown in two orientations as indicated by the arrow. Models rendered in Pymol software.

4.3.3 - Rigid-body modelling of scattering data based on pre-existing structures

To further validate the results presented above, a second round of modelling was carried out using SASREF-CV,[213] another part of the ATSAS Online suite of tools. This software takes pre-existing protein structures and attempts to dock them to each other in various orientations to create a structure that matches a given scattering curve. In this case the structures of MtrC and MtrAB were fed into the software along with the scattering curves obtained for RuMe-MtrC:MtrAB. The model produced by SASREF is shown in Figures 4.3.6A&C where it has been aligned to the structure of MtrCAB using SUPCOMB as described above. Goodness-of-fit parameters for this simulation are presented in Table 4.3.3. χ^2 values are reported for how well the SASREF model accounts for the

experimental scattering data and RMSD describes how well the SASREF model aligns with the structure of MtrCAB.

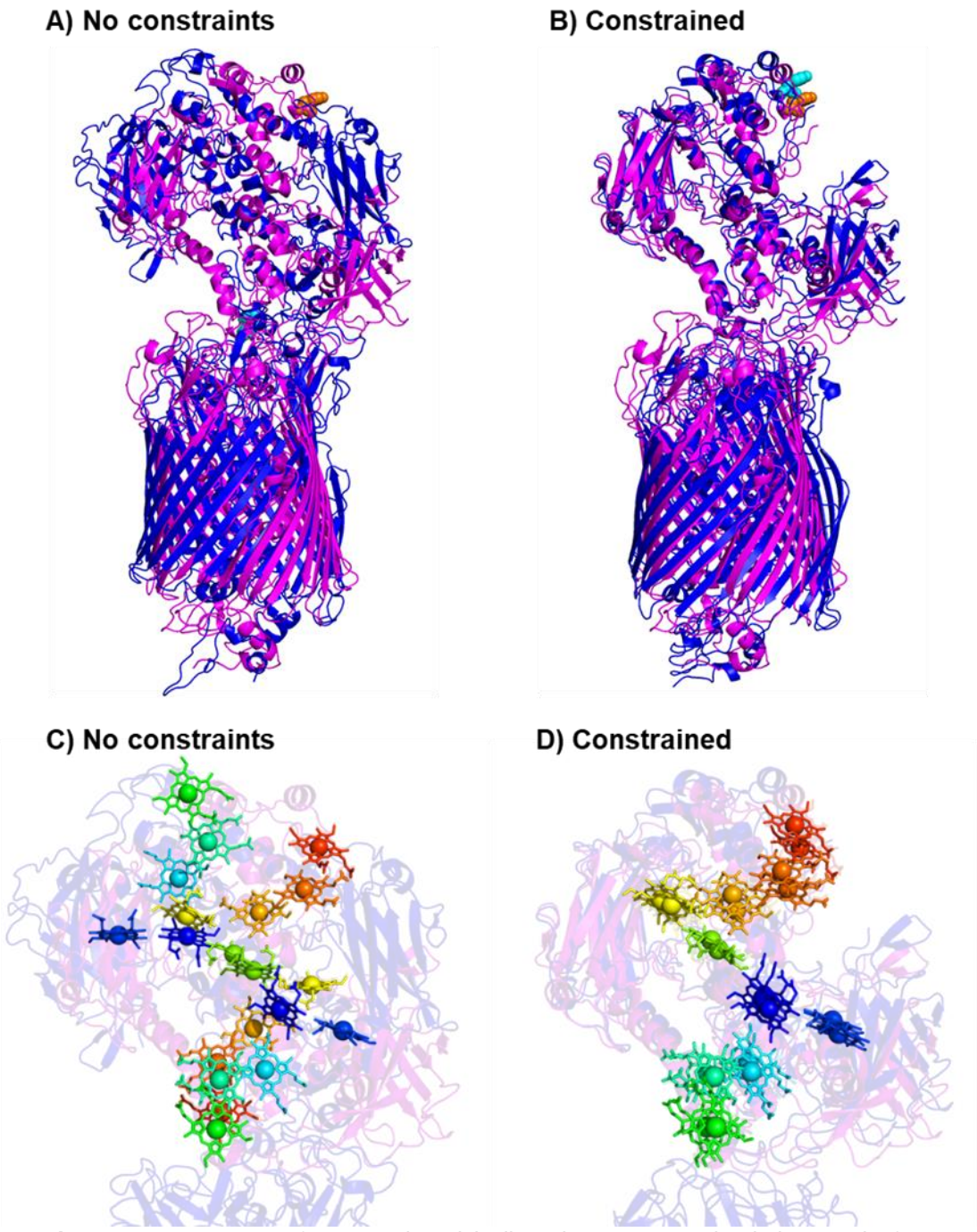

Figure 4.3.6 Structure of MtrCAB (purple) aligned to SASREF simulation results for RuMe-MtrC:MtrAB (blue) with no constraints made upon the simulations (A) or after constraining $MtrA_{H253}$ + $MtrC_{I307}$, $MtrA_{G265}$ + $MtrC_{G98}$ to be within 10 Å (B); MtrC residue 657 is shown as spheres in either orange (for Structure of MtrCAB) or cyan (for model of RuMe-MtrC:MtrAB) **C+D)** as A+B with focus on the heme wires of MtrC which are coloured as a spectrum from heme 10 in red to heme 1 in blue, iron atoms shown as spheres. Models rendered in Pymol software.

Table 4.3.3 Goodness-of-fit parameters for fitting of the scattering curve for RuMe-MtrC:MtrAB using SASREF-CV and subsequent alignment to the structure of MtrCAB

Distance constraints	χ^2 from SASREF-CV fitting	RMSD of SUPCOMB alignment (Å)
None	3.3	27.2
$MtrA_{H253}$ + $MtrC_{I307}$, $MtrA_{G265}$ + $MtrC_{G98}$ (<10 Å)	3.5	9.7

The SASREF model for RuMe-MtrC:MtrAB fits to the scattering data (low χ^2) however the fitting to the structure of MtrCAB is poor. In the SASREF model domain IV of MtrC is interacting with MtrAB whereas in the MtrCAB crystal structure it is domain II of MtrC that forms this connection. This is more clearly seen in Figure 4.3.6C where the focus is on the MtrC portion of the aligned structures and the hemes are brought into focus and coloured according to number.

MtrC is relatively symmetrical in its global structure, meaning that distinguishing which orientation MtrC is in would be difficult for the SASREF software. To account for this, a further SASREF simulation was run with the added constraints that specific pairs of residues at the "true" MtrA-MtrC interface should be within 10 Å of each other ($MtrA_{H253}$ + $MtrC_{I307}$, $MtrA_{G265}$ + $MtrC_{G98}$). The resulting SASREF model (Figs 4.3.6B&D) much better resembles the MtrCAB structure (lower RMSD) whilst providing a similarly good fit to the experimental data (Table 4.3.3).

To further validate this constraint, the PL of RuMe-MtrC was investigated as described in Section 2.5.4 in the absence and presence of MtrAB. If domain IV of RuMe-MtrC were interacting with MtrAB, as in the structure depicted in Figures 4.3.6A&C, we might expect the PL intensity or spectral distribution of the RuMe label to be affected due to interactions with MtrAB. This effect has been observed previously with a RuMe-labelled STC variant where the emission of the RuMe label was blue-shifted relative to the typical emission of this photosensitiser.[132] Additionally, proximity of RuMe to the hemes of MtrA might introduce another quenching pathway, further decreasing the PL intensity.

The PL emission spectrum of 1 μM RuMe-MtrC was measured in anaerobic PNL Buffer (Fig. 4.3.7). The intensity of the emission was very low, however it was felt to be important that the concentration was close to that used in the SE experiments discussed above where complex formation was demonstrated. To this solution was added MtrAB in anaerobic PNL buffer to final concentrations of 0.5, 1 or 2 μM. PL emission spectra obtained after these additions showed minimal changes in profile or intensity. Emission spectra were obtained again after 5 h and no changes were observed (data not shown).

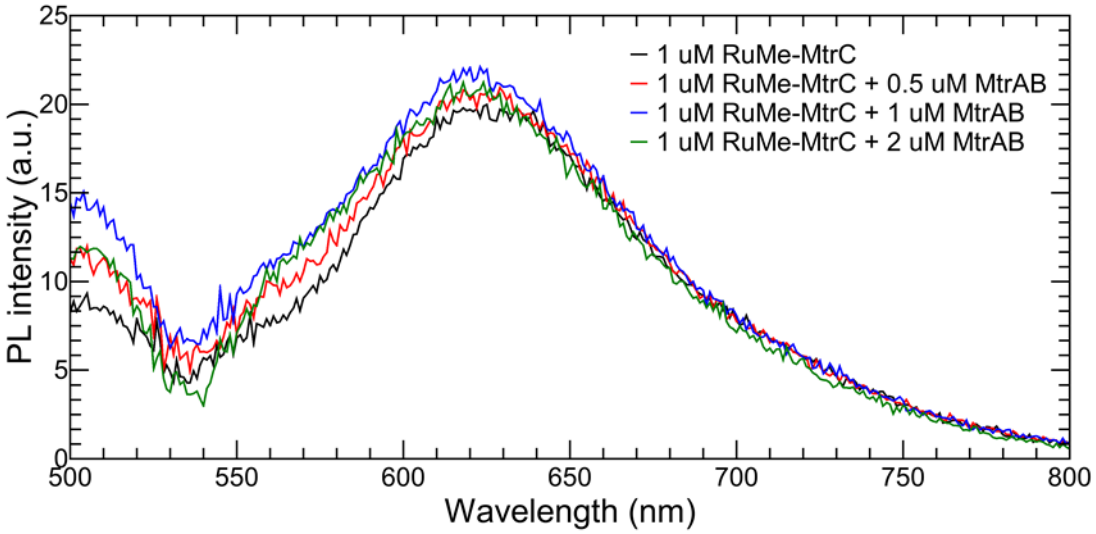

Figure 4.3.7 Photoluminescence emission spectra (excitation wavelength = 455 nm) of 1 μM RuMe-MtrC in isolation (black) and with MtrAB at 0.5 μM (red), 1 μM (blue) and 2 μM (green) under conditions where a complex would be expected to form. Samples in PNL Buffer.

The results presented in this section are valuable in a number of ways. Firstly they support the hypothesis that RuMe-MtrC:MtrAB resembles WT MtrCAB in structure which is important for building the light-driven transmembrane conduit discussed in Section 1.6. Secondly, they provide the first evidence that the solution and crystal structures of MtrCAB are comparable and that the forces acting on the protein in the crystallisation process appear not to have distorted the global protein structure.

4.4 - Photoreduction of RuMe-MtrC:MtrAB

Given that the complex formed by RuMe-MtrC and MtrAB likely resembles WT MtrCAB, electron transfer from the former to the latter should be possible. Whilst electron transfer in this direction is against the physiological direction of electron transport, MtrCAB has been shown to be capable of bidirectional electron transport in a number of different cell and liposomal studies[160,171,214,215] To test whether RuMe-MtrC can pass electrons to MtrAB, the RuMe-MtrC:MtrAB complex was irradiated in the presence of EDTA as a SED as described in Section 2.5.3 using anaerobic 50 mM Tris:HCl, 10 mM KCl, 0.2% (v/v) TX100, pH 8.5 Buffer (TKTx Buffer) + 100 mM EDTA. TX100 was used as a buffer here as LDAO was found to prevent electron accumulation in RuMe-MtrC:MtrAB.

As shown in Figure 4.4.1, RuMe-MtrC:MtrAB was able to be photoreduced to almost 80% within 90 minutes and would likely have reached a more reduced state if irradiated further. The hemes of RuMe-MtrC and MtrA are, unfortunately, challenging to distinguish from one another so we have no way to definitively assign the photogenerated electrons

to one protein or the other in these experiments. We can however say that, as the complex becomes more than 50% reduced, some of the electrons have transferred to the hemes of MtrA.

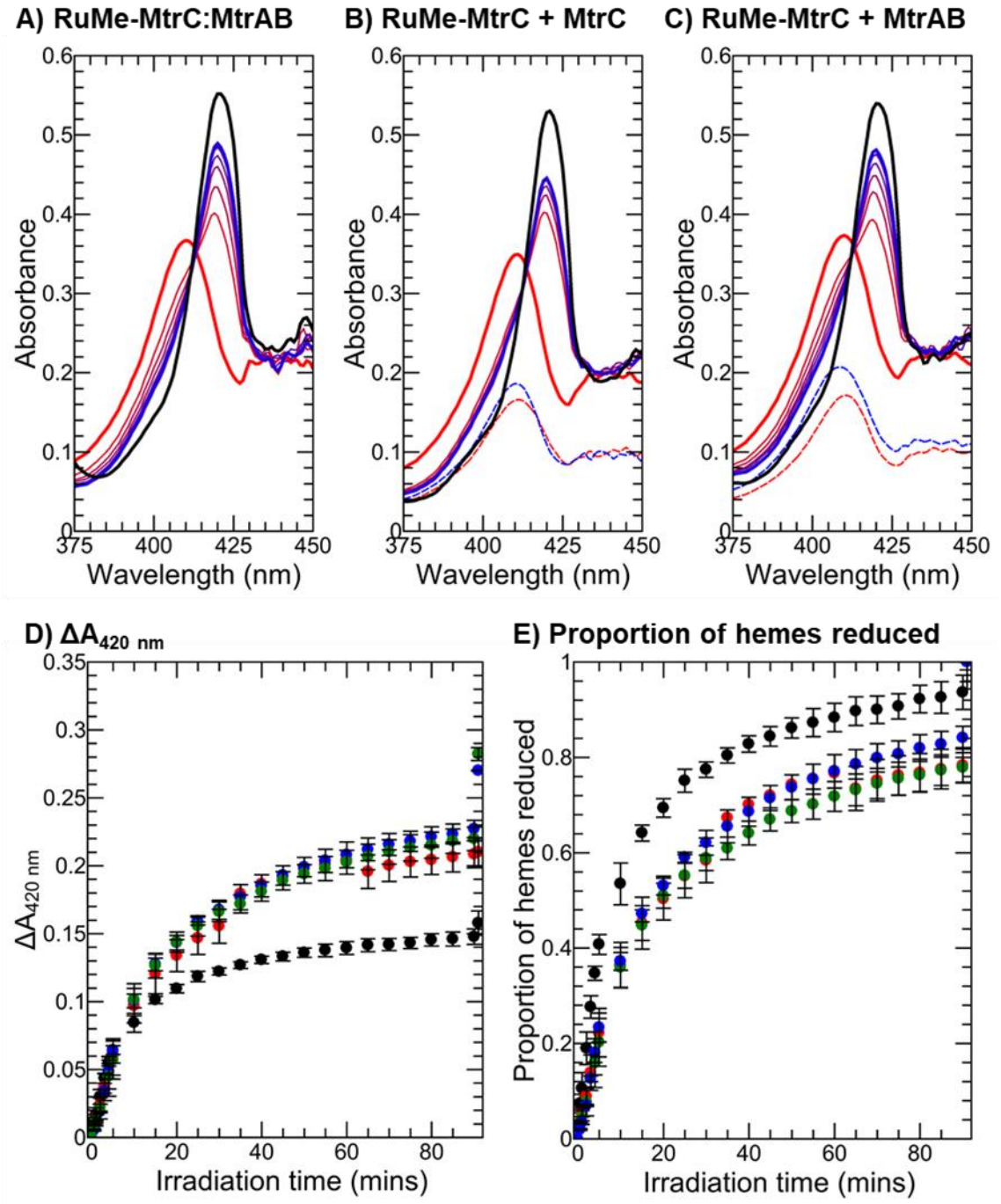

Figure 4.4.1 Photoreduction of RuMe-MtrC:MtrAB and ≈1:1 mixtures of RuMe-MtrC with MtrC or MtrAB. **A-C)** Example spectra of indicated protein systems at t=0 (red) and at 15 minute intervals of irradiation up to 90 mins (blue) and after addition of DT (black). For 1:1 mixtures the component spectra from RuMe-MtrC (Red) and MtrC/MtrAB (Blue) are shown as dashed lines. **D+E)** Timecourses following the photoreduction of the different protein systems: 0.12 μM RuMe-MtrC (Black), 0.14 μM RuMe-MtrC:MtrAB (Red), 0.13 μM RuMe-MtrC + 0.14 μM MtrC (Blue), 0.14 μM RuMe-MtrC + 0.17 μM MtrAB (Green). Error bars represent the data range from n=2 replicates. Samples in TKTx Buffer + 100 mM EDTA.

In order to shed some light on the rate determining step for electron transfer in this system and help to inform mechanistic interpretations, RuMe-MtrC was also mixed with MtrC or MtrAB under the same conditions. RuMe-MtrC and MtrC are not expected to form a stable complex, therefore electron transfer between these proteins should be due to transient encounters. Example spectra and timecourses for these experiments are shown in Figures 4.4.1B-E.

These results show clearly that the presence of additional cytochromes increases the overall electron accumulation rate under photoreducing conditions. The timecourses for RuMe-MtrC:MtrAB, RuMe-MtrC+MtrC and RuMe-MtrC+MtrAB show that these systems generate more reduced heme after just 10 mins of irradiation than the timecourse for RuMe-MtrC alone (Fig. 4.4.1D). Interestingly, MtrAB and MtrC appear able to accept electrons from RuMe-MtrC with similar efficacy and the preformation of the RuMe-MtrC:MtrAB complex also does not enhance the electron accumulation. The red, blue and green timecourses in Figures 4.4.1D&E overlay very well indicating that the nature of the encounter between RuMe-MtrC and the other protein does not impact the rate determining step. This was to be expected considering the orders of magnitude difference between typical rates of interheme electron transfer ($>10^3$ s^{-1})[178,204] vs the rate of electron production by RuMe-MtrC (<1 min^{-1}). An experiment with much lower concentrations of RuMe-MtrC and MtrC might allow interprotein electron transfer due to transient encounters to become rate limiting, however this would likely require concentrations so low that the sample would have negligible absorbance and not be able to be monitored.

By adding MtrAB or MtrC to RuMe-MtrC the effective electron capacity of the system is increased, and any electrons produced are distributed over a larger population. This means that heme 10 of RuMe-MtrC will more likely be in an oxidised state at any time, allowing more productive photochemistry to occur. This effect is akin to that observed previously in Section 3.4 where addition of a SEA to RuMe-MtrC allowed for steady state production of electrons.

4.5 - General discussion

This chapter has examined the formation and photochemistry of the reconstituted RuMe-MtrC:MtrAB complex. The RuMe-MtrC:MtrAB complex forms the core of the photocatalytic systems proposed Section 1.6. It is therefore of significant importance to study the formation of this complex and its photochemical properties.

It has been confirmed here by a variety of methods that RuMe-MtrC and MtrAB form a complex under several different conditions. Gel filtration (Section 4.2.1) identified that a higher molecular weight species was generated when RuMe-MtrC and MtrAB were combined in PNL Buffer. This species contained both RuMe-MtrC and MtrAB as confirmed by SDS-PAGE and analysis of absorbance ratios in the chromatograms supported a 1:1 ratio of these subunits. Further study of this complex by AUC in PNTx Buffer (Section 4.2.2) confirmed the stoichiometry of the complex and demonstrates that it forms with some specificity under sub-μM conditions.

Further investigations into the structure of RuMe-MtrC:MtrAB by SANS (Section 4.3) suggested that this complex has a similar shape to WT MtrCAB. Models produced from the scattering data of RuMe-MtrC:MtrAB closely align to the structure of WT MtrCAB. Collectively, all these data support the hypothesis that RuMe-MtrC and MtrAB form a tight complex in a variety of detergent solutions which structurally resembles WT MtrCAB.

It should be noted that the experiments in this chapter were carried out using a variety of different buffer conditions, in particular there were three different detergents used. When it comes to detergents, there is not a universal option which is suitable for all experiments and each detergent was used due to its particular properties. TX100, for example, is a good choice of detergent for AUC because of its high $\bar{v}$ which diminishes its effect on protein sedimentation. It was not, however, a good choice for gel filtration experiments due to its large size[135] and strong absorbance at $A_{280\ nm}$. For gel filtration, LDAO was used as it has no significant UV-Vis absorbance and has a small micelle size (≤21.5 kDa).[205–207]

Fos-Choline-12 was used for SANS experiments because the match point of this detergent has been well characterised on the same instrument being used for data collection and it was used in the previous study of Mtr proteins,[157] allowing for direct comparison between the data. Determining suitable conditions for SANS data collection can be time consuming, requiring lengthy data collection and analysis at different D_2O concentrations to identify match points. The beamtime allotted at ILL was limited and it was not sufficient to attempt data collection using reported match points for TX100 (16.8% D_2O) or LDAO (5.5% D_2O).[156] Fos-choline-12 is significantly more expensive than LDAO or TX100 making it impractical for use in other experiments.

Having established the structural reconstitution of RuMe-MtrC and MtrAB, the functional aspect of this complex then needed to be investigated. In order to fulfil the role of a light-driven transmembrane electron conduit, RuMe-MtrC must pass electrons to MtrAB. Solution studies RuMe-MtrCAB show that not only can this electron transfer occur, but

the overall rate of electron generation by RuMe-MtrC was increased when it had a partner upon which to unload its electrons. The rationale for this is consistent with previous experiments investigating RuMe-MtrC in combination with azo dyes: when RuMe-MtrC has a larger pool of redox centres to reduce, the bottleneck effects that slow down electron generation take longer to kick in. TX100 was used in these photoreduction experiments as LDAO was found to inhibit photoreduction of cytochromes.

An important caveat to these photoreduction experiments is that we cannot be certain that RuMe-MtrC passes electrons to MtrAB via the physiological MtrC:MtrA interface. The comparatively slow electron accumulation observed for RuMe-MtrC will likely be rate limiting under all but the most dilute conditions. It is entirely possible, therefore, that RuMe-MtrC reduces MtrAB by transient encounters in solution. If RuMe-MtrC were able to generate electrons more quickly, intra and inter-complex electron transfer might be able to be distinguished more easily. The ability of RuMe-MtrCAB to transfer electrons across a lipid bilayer would also provide strong evidence for intracomplex electron transfer. Experiments to investigate this are described in Chapter 6.

In summary, work described in this chapter has established the formation of RuMe-MtrCAB complexes and findings are consistent with electron transfer between the two cytochrome subunits. This supports the formation of the nanoreactors depicted in Figure 1.6.2. In the following chapter the enzyme cargo of these nanoreactors will be considered.

CHAPTER 5

NITROUS OXIDE REDUCTASE AS AN ENCAPSULATED REDOX CATALYST

Chapter 5 - Nitrous oxide reductase as encapsulated redox catalyst

5.1 - Properties of the proposed encapsulated redox catalyst: Nitrous oxide reductase

One of the core components of any photocatalytic system is, of course, the catalyst. In the nanoreactor design depicted in Figure 1.6.2 the chosen catalyst is the enzyme nitrous oxide reductase which reduces N_2O to N_2, the final step in the denitrification pathway. The primary reason for selecting this enzyme was that both N_2O and N_2 are gases meaning they should permeate freely through the liposome lipid bilayer. Specialised importers/exporters are therefore not required to maintain concentrations of substrate within the liposome. Using of this enzyme provides a greatly simplified system for establishing a proof-of-principle nanoreactor using RuMe-MtrCAB as a transmembrane electron conduit.

Though there are advantages to using nitrous oxide reductase, the activity of this enzyme is known to be complex, with requirements for *in vitro* activation. Furthermore, there will be a need to establish a method to encapsulate active enzyme in liposomes and ensure a means of moving electrons from MtrCAB to the enzyme. This chapter begins with a review of the enzyme's structure and previous reports of its catalytic properties. Experiments probing catalytic properties of the enzyme relevant to the aims of this thesis are then described. Finally, a method for successful encapsulation of active NosZ in liposomes is presented.

5.1.1 - Structure and function of Nitrous oxide reductase: NosZ

The most common known nitrous oxide reductase enzyme is named NosZ. This enzyme has been purified from different species of bacteria and crystal structures have been obtained of the enzyme in different forms.[216–219] NosZ from *Paracoccus denitrificans* is a soluble periplasmic protein containing copper-based cofactors.[217] It exists as a functional dimer stabilised by calcium ions with each monomer containing two copper centres (Fig. 5.1.1 - Left).[219]

The first copper centre is named Cu_A and consists of two copper atoms ligated by sulfur atoms from two cysteines, one methionine, two histidines, and a carbonyl from the protein backbone (Fig. 5.1.1 - Right).[217,220,221] This centre is also found in other enzymes

such as cytochrome *c* oxidase[222–224] where it acts as an electron transport relay. The second copper centre is the active site and is named Cu_Z, it contains four copper atoms and is unique to NosZ. Crystal structures for NosZ agree that Cu_Z contains four copper atoms in a distorted tetrahedron coordinated by seven histidine residues and with a bridging sulfur atom (Fig. 5.1.1 - Right).[216,217,221,225] The copper atoms of Cu_Z are designated $Cu_{I\text{-}IV}$ and each is coordinated by two histidine residues apart from Cu_{IV} which is only coordinated by one histidine. The NosZ dimer forms in a head-to-toe arrangement to allow electron transfer from Cu_A of one monomer to Cu_Z of the other monomer during catalysis, these sites are only 10 Å apart. The distance between Cu_A and Cu_Z in a single monomer is 40 Å which precludes facile electron transfer.

The remaining ligand of Cu_{IV} has been the subject of some debate and appears to depend on the presence or absence of oxygen in the protein purification/crystallisation. The earlier structural analyses[216,217,221] of NosZ were carried out on aerobically purified protein and, under these conditions, Cu_{IV} was determined to be ligated by water, hydroxyl or simply an oxygen atom bridging between Cu_{IV} and Cu_I[216,217,221] giving a [4Cu:1S-1O] cluster. When purified anaerobically, a second sulfur atom bridged between Cu_{IV} and Cu_I.[218] This site is proposed to be where N_2O interacts with Cu_Z which suggests this ligand is related to the enzyme function. The [4Cu:1S-1O] cluster has since been termed Cu_Z^* while the [4Cu:2S] cluster is called Cu_Z.

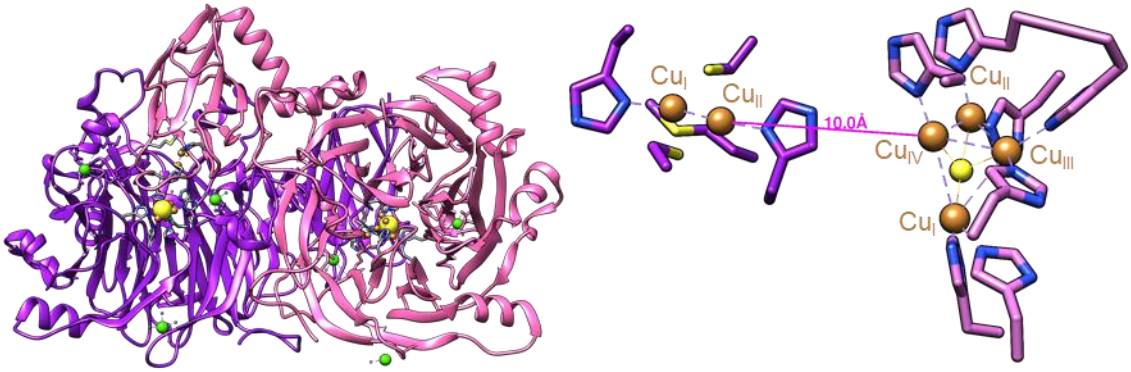

Figure 5.1.1 X-ray crystal structure of NosZ from *Paracoccus denitrificans* (1FWX).[217] **Left)** Full dimer structure with monomers coloured pink and purple, and copper cofactor binding residues shown, cofactors shown as spheres: copper-bronze, sulfur-yellow, calcium-green. **Right)** focus on copper clusters showing distance between Cu_A from one monomer (left cluster) and Cu_Z from the other monomer (right cluster). Distance measurement and image rendering in Chimera.

NosZ with a [4Cu:2S] cluster is difficult to isolate due to its oxygen sensitivity and has not been studied so thoroughly. Crystal structures have been obtained of this form of the enzyme with N_2O bound[218] however the role of the second sulfur is not yet conclusively understood and NosZ in this form is observed to react very slowly with N_2O.[226] The Cu_Z^*

form of the aerobically purified enzyme is much simpler to obtain and was used in this work.

It is well established that Cu_Z^* has a complex catalytic cycle which is outlined in Fig. 5.1.2.[227–229] Aerobically purified protein typically contains Cu_Z^* in an off-cycle state, [$3Cu^+$-$1Cu^{2+}$:1S-1O], that must be reductively activated to the [$4Cu^+$:1S] state, here termed Cu_Z^{*-} before catalysis can begin. *In vivo* this activation is thought to be catalysed by the membrane bound flavoprotein NosR.[230–232]

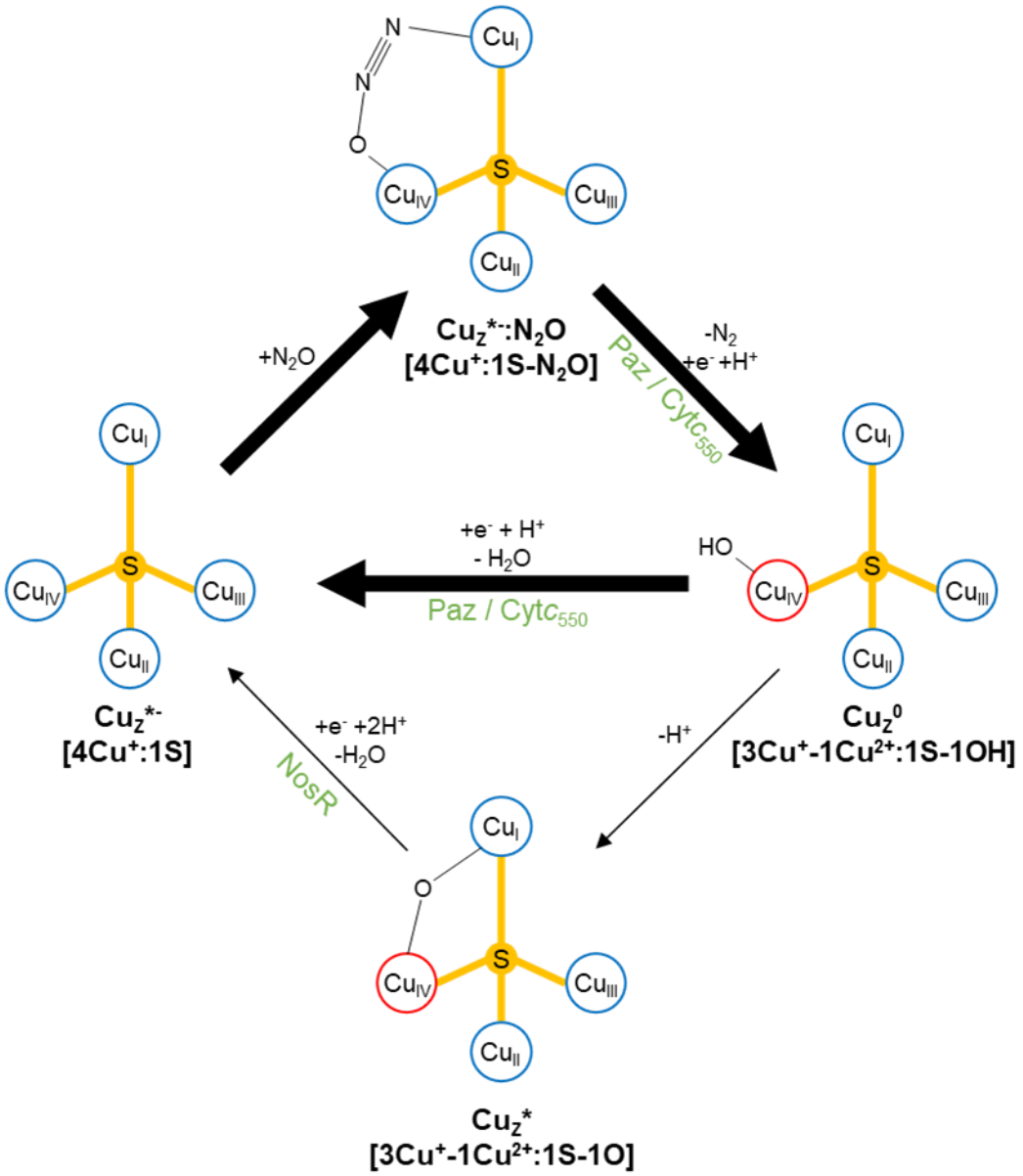

Figure 5.1.2 Proposed catalytic cycle for aerobically purified NosZ. Only the Cu_Z^* site is shown, with copper atoms displayed as either reduced (blue) or oxidised (red). Thick arrows show the catalytic cycle and thin arrows show the off-cycle activation and deactivation. Proposed *in vivo* redox partners for the reductions are shown in green. Adapted from Johnston et al.[227]

In vivo, the physiological redox donors to NosZ have been identified as pseudoazurin (Paz) (E^0 = +230 mV vs SHE) and cytochrome c_{550} (Cytc_{550}) (E^0 = +260 mV vs SHE)[233] and the two are functionally redundant.[234–236] These soluble periplasmic redox proteins accept electrons from the inner membrane associated cytochrome bc_1 and are able to donate them to a variety of enzymes including NosZ and the nitrite and nitric oxide reductases.[234] *In vitro*, the widely used redox mediator methyl viologen (MV) is often used as a redox partner for NosZ. In its oxidised state (MV^{2+}) this compound is colourless, however the singly reduced state ($MV^{\bullet+}$) (E^0 = -446 mV)[237] has a strong blue colour with absorbance features in the visible and near-UV regions of the spectrum (Fig. 2.4.1) which allow for spectroscopic monitoring. $MV^{\bullet+}$ is also known to be able to carry out reductive activation of the Cu_Z^* state to Cu_Z^{*-}.[238,239]

This chapter describes work that aimed to study NosZ with a view to using this enzyme in the light-driven biohybrid nanoreactors depicted in Figure 1.6.2. To this end experiments described below consider the activity of the enzyme with two redox partners: Paz and MV. Conditions supporting high and sustained catalytic rates were sought to maximise the possibility of detecting activity from small amounts of enzyme that would be encapsulated in liposomes. Methods to effectively encapsulate NosZ in such liposomes alongside these redox partners were also explored.

5.2 - MV as a redox partner for NosZ

For *in vitro* studies of NosZ activity many research groups have turned to the viologen mediators, MV in particular, to support catalysis. The strong colour of the reduced viologens make them useful for spectroscopic monitoring of redox reactions. They are also small molecules and have kinetically facile redox chemistry,[237] both of which aid in transferring electrons to enzymes. $MV^{\bullet+}$ is also reported to activate the Cu_Z^* site of NosZ, generating the active Cu_Z^{*-} cluster[229,239] though the concentration dependence of this activation has not been previously explored. In addition, MV is known to accept electrons from MtrCAB[214,215,240] suggesting it would be able to mediate the flow of electrons from MtrCAB to NosZ in the nanoreactors depicted in Figure 1.6.2.

5.2.1 - Reductive activation of Cu_Z* by $MV^{\bullet+}$

The ability of $MV^{\bullet+}$ to activate and support catalysis by NosZ was confirmed by spectrophotometric assays using two different methods (see Section 2.4.1), one with an activation period (Method 1) and one without (Method 2). With a 5 minute activation

period in 60 μM $MV^{\bullet+}$ the TOF ($\frac{\text{moles } N_2O \text{ consumed } s^{-1}}{\text{moles NosZ}}$) of the enzyme was determined to be 40 s^{-1} (Fig. 5.2.1 – Red line). Without this activation the enzyme activity was significantly lower with a TOF of ≈ 9 s^{-1} (Fig. 5.2.1 - Black Line).

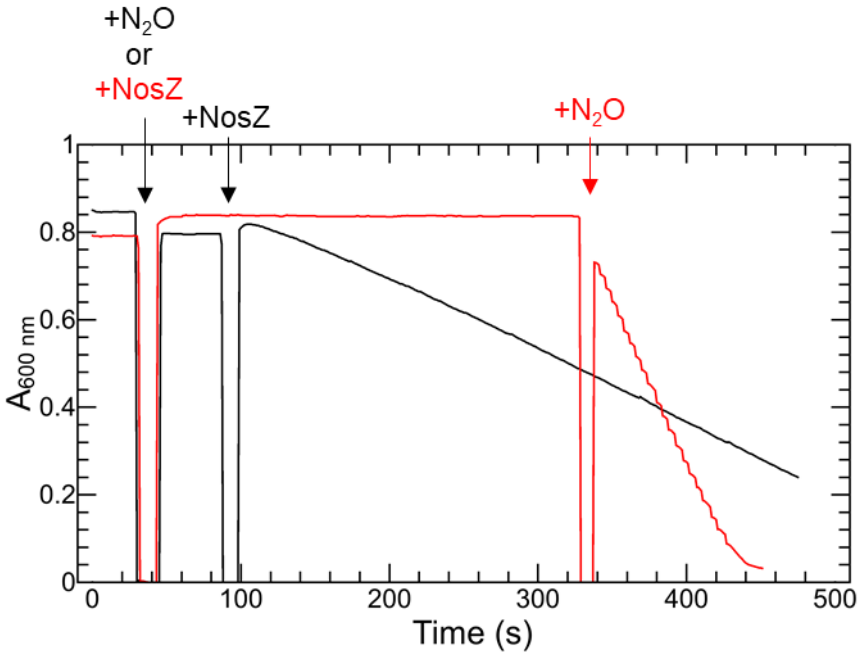

Figure 5.2.1 Spectrophotometric assay to assess activity of NosZ with (Method 1 - Red) or without (Method 2 - Black) a 5 minute incubation period in $MV^{\bullet+}$ to allow for enzyme activation. Initial [$MV^{\bullet+}$] ≈ 60 μM, [NosZ] = 7 nM, [N_2O] ≈ 750 μM.

In order to determine the TOF_{max} of the enzyme the entire sample needed to be activated, however previous studies of activation by $MV^{\bullet+}$ suggest relatively slow kinetics for this process.[229,239] The concentration dependence of this activation was explored by incubating the enzyme in solutions of defined [$MV^{\bullet+}$] and taking aliquots at set time intervals. Spectrophotometric assays, without further activation (i.e. by Method 2), were carried out on the aliquots and the activity was quantified as previously. The activity of the enzyme was found to increase with both incubation time (Fig. 5.2.2A) and with [$MV^{\bullet+}$] (Fig. 5.2.2B).

Plots of TOF against activation time were fitted to single exponential saturation curves ($TOF_t = TOF_{max} \times (1-e^{-k_{obs}t})$) which gave a TOF_{max} of 150 s^{-1} (Fig. 5.2.2B). The values of k_{obs} obtained from these fits scaled linearly with $MV^{\bullet+}$ (Fig. 5.2.2C). These data suggest that activation is first-order with respect to both Cu_Z* and $MV^{\bullet+}$ with a second-order rate constant k_{activ} of 1.12 M^{-1} s^{-1}.

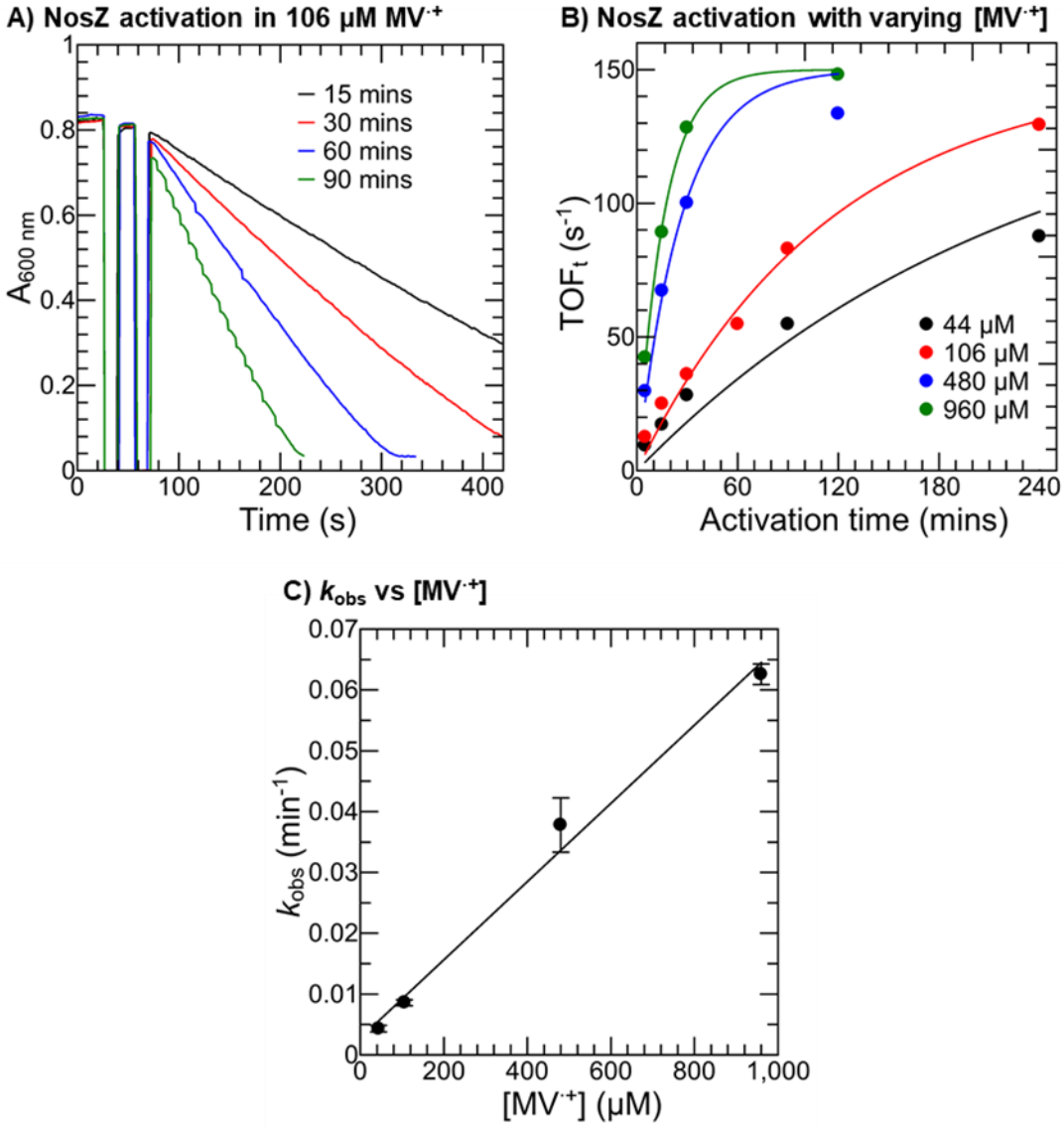

Figure 5.2.2 $MV^{\bullet+}$ concentration dependence of NosZ activation. **A)** MV assay timecourses for aliquots taken from 106 µM $MV^{\bullet+}$ incubation sample after indicated time periods; **B)** TOF_t, determined from slope of MV assays, as a function of time and [$MV^{\bullet+}$], fits to single exponential saturation curves are shown as lines; **C)** Plot of k_{obs} against [$MV^{\bullet+}$] with linear fit, error bars show error from exponential fitting.

5.2.2 - K_M and K_{cat} for N_2O reduction by activated NosZ

Having established conditions for accessing maximal activation of NosZ, experiments were performed to define K_m and K_{cat}. From a concentrated stock solution of N_2O, a series of dilutions into TK buffer were prepared in 3 mL Exetainer vials which were then allowed to equilibrate. GC was used, as described in Section 2.4.2, to quantify the N_2O concentration in these dilutions. Spectrophotometric assays were carried out using Method 2 (see Section 2.4.1). The N_2O dilutions were used to give assay [N_2O] concentrations ranging from 0.5 µM to 375 µM and fully activated NosZ (1.4 nM) was added to initiate the reaction. The initial rate and overall extent of the reaction were found

to increase with N_2O concentration (Fig. 5.2.3 - Left). Fitting of the initial rates to the Michaelis-Menten equation ($TOF = \frac{K_{cat} \times [N_2O]}{K_M + [N_2O]}$) gave a K_{cat} of 166±9 s^{-1} and K_M of 9±1.5 μM (Fig. 5.2.3 - Right) which are consistent with literature values[228,241].

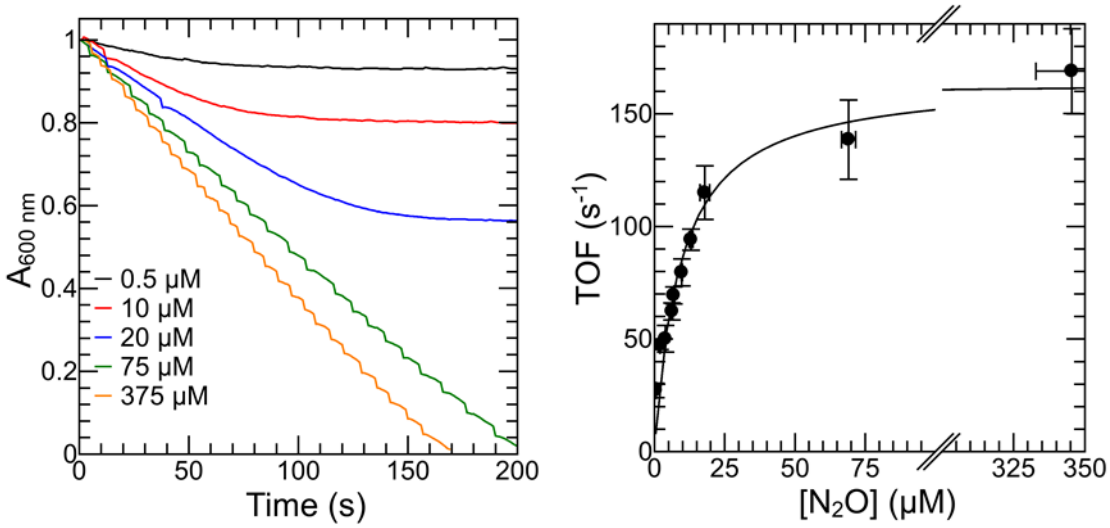

Figure 5.2.3 Determination of K_M for N_2O. **Left)** Timecourses showing $MV^{\bullet+}$ oxidation by 1.4 nM NosZ at different [N_2O], Initial [$MV^{\bullet+}$] = 75 μM in anaerobic TK buffer; **Right)** Michaelis-Menten plot of initial rate against [N_2O] (as determined by GC), data points are the average of n≥3 MV assays or n=3 GC measurements, error bars show standard deviation.

5.2.3 - NosZ deactivation during prolonged catalysis

While $MV^{\bullet+}$ is clearly able to activate NosZ, the catalytic cycle presented in Figure 5.1.2 would suggest that, during continuous catalysis, enzyme deactivation can occur from the Cu_Z^0 state back to the off-cycle Cu_Z* state. This process is in competition with reduction of Cu_Z^0 to the Cu_Z^{*-} state which is predicted to be very fast when $MV^{\bullet+}$ is used as a redox partner. The assays described thus far are complete in a matter of minutes and, as the $MV^{\bullet+}$ oxidation timecourses are effectively linear, enzyme deactivation does not appear to play a significant role. The planned experiments with NosZ encapsulated in liposomes may take place over much longer time scales. It is therefore important to understand this process of deactivation. For NosZ from *Marinobacter hydrocarbonclasticus* (renamed from *Pseudomonas nautica*) Dell'Acqua et al.[228] found this deactivation to follow pH dependent, first-order kinetics with a rate constant $k_{deactiv} = 1.3 \times 10^{-3}$ s^{-1} at pH 8.5.

Spectrophotometric assays were carried out using fully activated NosZ at sub nM concentrations such that catalysis was detectable over >1 h. The assays were carried out following Method 2 in sealed cuvettes to prevent loss of N_2O and $A_{600\ nm}$ was monitored over 90 mins (Fig. 5.2.4). The initial concentrations of $MV^{\bullet+}$ and N_2O were 75 μM and 750 μM respectively. The results show that the activity of NosZ decreased over time, and eventually reached a semi-steady state with a TOF of around 5 s^{-1}. In this state, it is hypothesised, the vast majority of the enzyme is in the off cycle Cu_Z* state but activation by $MV^{\bullet+}$ and deactivation are occurring at the same rate.

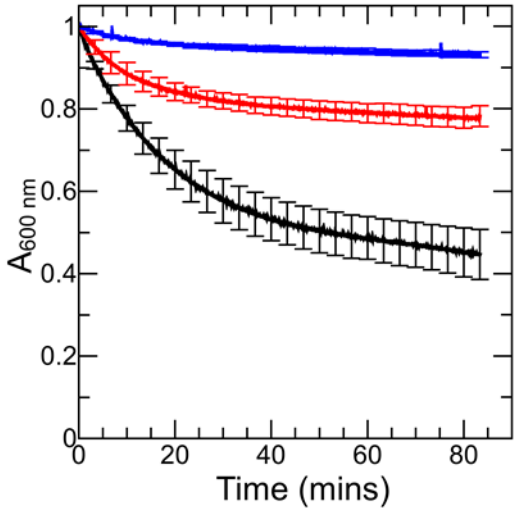

Figure 5.2.4 Long-term activity assays of NosZ. MV assay timecourse after addition of 140 pM (Black), 70 pM (Red) or 35 pM (Blue) NosZ to 75 μM $MV^{\bullet+}$, 750 μM N_2O in anaerobic TK Buffer. Data are the average of n≥2 normalised data sets and error bars show standard deviation.

For the timecourse obtained with 140 pM NosZ the steady state is reached at a [$MV^{\bullet+}$] of ≈ 40 μM. Using the rate constant for activation determined in Section 5.2.1 (k_{activ} = 1.12 M^{-1} s^{-1}), the pseudo-first-order rate constant for activation at 40 μM $MV^{\bullet+}$ would be 4.5 × 10^{-5} s^{-1}. This is significantly slower than the reported first-order rate constant for deactivation ($k_{deactiv}$ = 1.3 × 10^{-3} s^{-1})[228] although this was obtained with NosZ from a different species in a different buffer system so direct comparison is difficult at this time.

The results presented in this section demonstrate two properties of the *Paracoccus denitrificans* NosZ enzyme: first, that without high concentrations of $MV^{\bullet+}$, the fully activated state is not maintainable over long periods of time; but second, the presence of even low concentrations of $MV^{\bullet+}$ allows the enzyme to continue operating indefinitely.

5.2.4 - Compatibility of NosZ with reagents for photoreduction and liposome experiments

When working in the proposed liposome environment, other reagents may be required; TX100 and EDTA will be of particular use, the former for lysing the liposomes such that the internal cargo can be assessed and the latter as a SED for photocatalysis. It must, therefore, be established whether these reagents affect the results of the spectrophotometric assay. Assays were carried out using fully activated NosZ following a variation of Method 1 (see Section 2.4.1). In these experiments a 10 min incubation step was used, and the buffer was either:

TK Buffer (as a control)

TK Buffer + EDTA at 5, 25 or 100 mM

TKTx Buffer

Timecourses of $A_{600\ nm}$ are shown in Figure 5.2.5 where t=0 corresponds to the addition of N_2O to 750 µM.

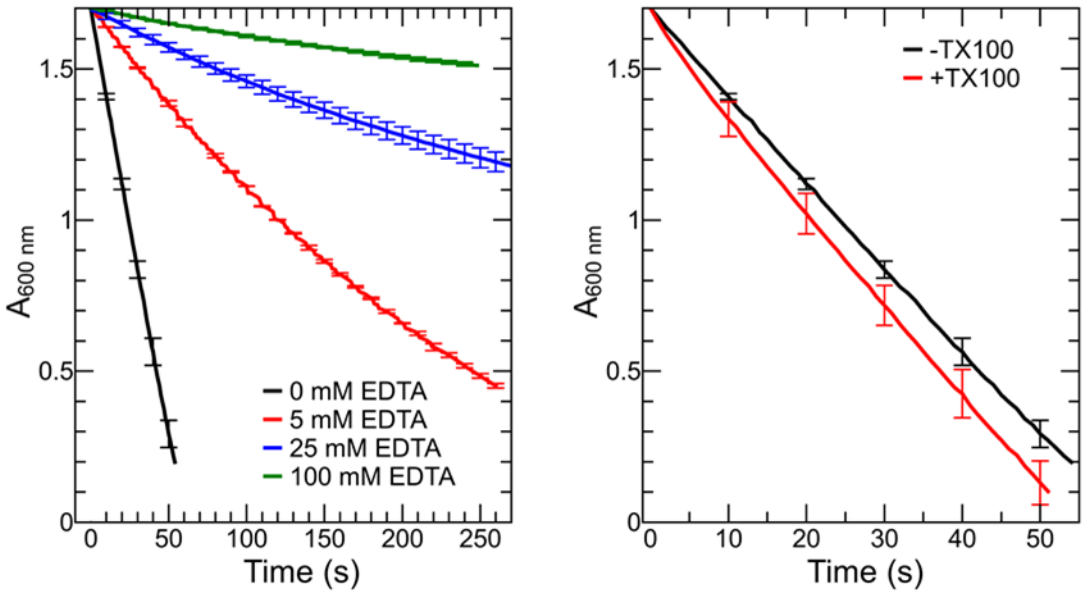

Figure 5.2.5 Spectrophotometric assays to determine NosZ compatibility with EDTA (Left) or TX100 (Right). **Left)** $A_{600\ nm}$ timecourses obtained for fully activated NosZ (7.5 nM) incubated for 10 mins in anaerobic TK Buffer + ≈120 µM $MV^{\bullet+}$ (Black) + 5 mM (Red), 25 mM (Blue) or 100 mM (Green) EDTA; **Right)** $A_{600\ nm}$ timecourses obtained for NosZ (7.5 nM) incubated for 10 mins in TK Buffer + ≈120 µM $MV^{\bullet+}$ (Black) or TKTx Buffer + 120 µM $MV^{\bullet+}$ (Red). t = 0 s corresponds to addition of ≈750 µM N_2O. Data are the average of n=3 normalised data sets and error bars show standard deviation.

These results suggest that TX100, at 0.2% (v/v), does not affect the activity of NosZ. Exposure to EDTA, however, significantly decreases the activity of NosZ in a

concentration dependent manner. NosZ exists as a functional dimer where the Cu_A site of one unit provides the electron relay to the Cu_Z site of the other unit. This dimer is stabilised by calcium ions[219] (Fig. 5.1.1 - Left) which may be abstracted by EDTA which has strong affinity for calcium ($K_d \approx 2.5 \times 10^{-11}$ M).[182] Destabilisation of the cofactor binding domains of NosZ may also allow for abstraction of the copper from the cofactors for which EDTA has even higher affinity ($K_d \approx 1.6 \times 10^{-19}$ M, for Cu^{2+}).[182] Addition of EDTA to a solution of concentrated NosZ with visible absorbance bands from Cu_A and Cu_Z[231] may inform on which, if any, of the copper clusters are abstracted from the enzyme. This would likely, however, irreversibly destroy the enzyme and was not deemed necessary.

These findings are important for the study of encapsulated NosZ. They suggest that the results of spectrophotometric assays on liposomes lysed by addition of TX100 to 0.2% (v/v) can be trusted. They also demonstrate that contact between NosZ and EDTA will lead to loss of activity. In the nanoreactors depicted in Figure 1.6.2, EDTA is present in the extraliposomal solution as a SED for the photosensitiser. Since EDTA, in its deprotonated state, is highly charged it should not readily cross the liposome bilayer and therefore NosZ should not come into contact with EDTA in our planned experiments.

5.2.5 - Conclusions regarding MV as a redox partner for encapsulated NosZ

In the sections above, MV has been demonstrated to support activity of NosZ both as an electron donor during the catalytic cycle, and as an activator to generate the active form of the enzyme. Given the propensity of aerobically purified NosZ to deactivate during prolonged catalysis (Fig. 5.2.4), both of these functions seem necessary to allow for sustained activity of encapsulated NosZ. From this perspective, MV is a strong candidate for use in the nanoreactors depicted in Figure 1.6.2. MV does, however, have some capacity to permeate lipid bilayers[128,242–244], particularly in the $MV^{\bullet+}$ state where the positive charge is delocalised over the MV structure. It is therefore prudent to consider other redox partners for NosZ which may be more suitable for liposome experiments.

5.3 - Paz as a redox partner for NosZ

NosZ can accept electrons from redox shuttle proteins, Paz and Cytc_{550}.[235,245] Encapsulating one of these proteins alongside NosZ could provide an elegant means to electrically connect MtrCAB and NosZ. These small, soluble proteins can be purified in large quantities and are highly unlikely to cross an intact lipid bilayer. While either partner would likely have filled this role Cytc_{550}, as a heme-containing protein, has absorbance features similar to those of MtrCAB which may have complicated spectral interpretations downstream. Paz, as a copper-containing protein with distinct absorbance bands, was therefore selected for experimentation. An expression system for Paz from *Paracoccus pantotrophus* was kindly provided by Dr. Nick Watmough. This protein shares 95% sequence identify with Paz from *Paracoccus denitrificans*, differing in just six amino acids (Fig. 5.3.1 - Pink residues). These differences are not located at the copper-binding face of the protein. They are, therefore, not expected to affect the interaction of Paz with its redox partners. A Strep-tagII was also introduced at the C-terminal of Paz (Fig. 5.3.1 - Red terminus) (producing PazSII) which simplified the purification process. Details of purification of PazSII and its spectral features can be found in Section 2.3.4.

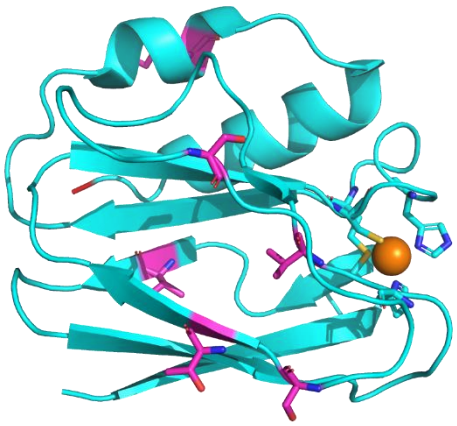

Figure 5.3.1 Structure of Paz from *Paracoccus pantotrophus* (3ERX) with copper binding residues shown and copper atoms shown as a bronze sphere. Residues that differ between Paz from *Paracoccus denitrificans* are shown in pink, C-terminal coloured red. Protein rendered in Pymol.

5.3.1 - Confirming PazSII can support catalysis by NosZ

PazSII was first confirmed to act as an electron shuttle for purified NosZ. Spectrophotometric assays were performed following a variation of Method 2 described above. To a solution of blue oxidised (Cu^{2+}) PazSII was added an excess of DT, producing the colourless reduced (Cu^{+}) form. This was followed by addition of N_2O to ≈750 μM from a saturated stock solution (see Section 2.4.1). Addition of as-purified NosZ

initiated oxidation of the excess DT (decrease at $A_{315\ nm}$) and, once the DT had been depleted, the oxidation of PazSII (Fig. 5.3.2). The reappearance of the absorbance features from oxidised Paz confirm that NosZ is able to accept electrons from this protein. The rate of decrease in $A_{315\ nm}$ was used to determine the activity of the enzyme which was found to be much lower than when $MV^{\bullet+}$ was used as a redox shuttle with a TOF of ≈1.3 s^{-1} (vs ≈9 s^{-1} with $MV^{\bullet+}$ under similar conditions).

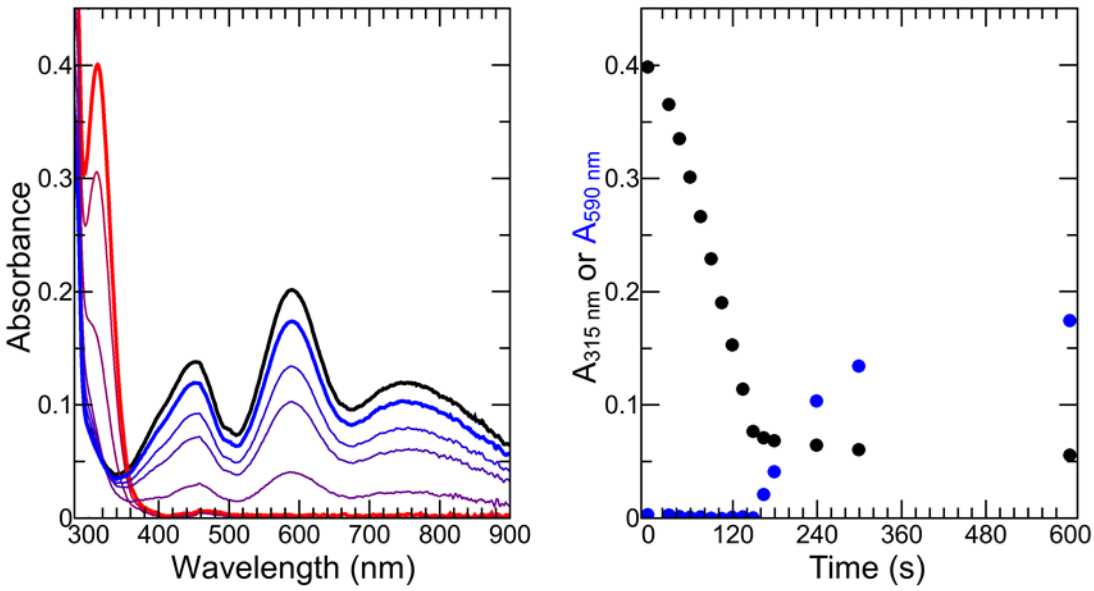

Figure 5.3.2 PazSII as a redox partner for NosZ. **Left)** Spectra obtained of 150 µM Paz (Black), after addition of 120 µM DT (Red), and over 10 mins after addition of 750 µM N_2O and 250 nM NosZ (Red to blue); **Right)** Timecourses following consumption of DT ($A_{315\ nm}$) and oxidation state of Paz ($A_{590\ nm}$). Samples in TK Buffer.

Similar experiments were also carried out with lower concentrations of NosZ and with different concentrations of PazSII. As was observed with MV, the rate of N_2O reduction slowed down over time (Fig. 5.3.3). In contrast to the experiments with $MV^{\bullet+}$ (Fig. 5.2.4), a steady state was not reached, and activity continued to decrease. Increasing the concentration of PazSII increased the initial rate of DT oxidation and the overall amount of DT oxidised after 20 mins. The rate of deactivation, however, appeared similar across this concentration range with ≈10% of initial activity remaining after 20 mins.

These observations suggest that a small population of NosZ started in the active Cu_Z^{*-} state and during continuous catalysis the reaction rate was limited by electron transfer from PazSII to NosZ. Increasing [PazSII] beyond 60 µM appeared not to provide any additional benefit suggesting this may be the maximum output that can be expected from the system under these conditions. Gradual deactivation of Cu_Z^0 to Cu_Z^* led to loss of activity.

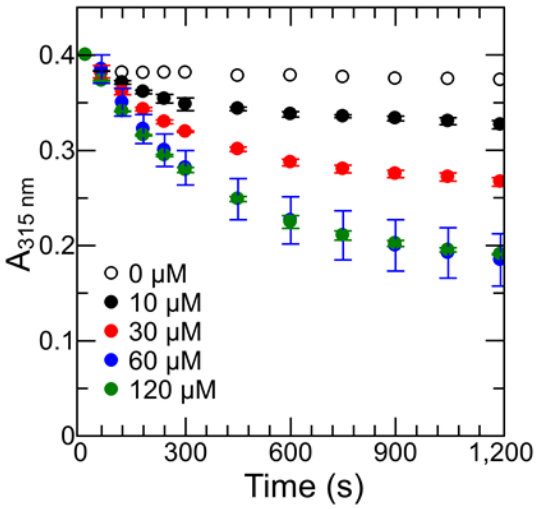

Figure 5.3.3 DT consumption timecourses obtained after addition of NosZ (50 nM) to anaerobic TK Buffer (Black-hollow), + PazSII (concentrations indicated) + 750 μM N_2O + DT. Data are the average of n=2 normalised data sets and error bars show data range.

5.3.2 - Can PazSII activate NosZ?

The results presented in Figure 5.3.3 suggest that PazSII cannot activate the Cu_Z* site to the active Cu_Z*$^-$ state. If it could, we would expect to have reached a steady-state level of DT oxidation as was seen for similar experiments with MV (Fig. 5.2.2). This was confirmed by carrying out a spectrophotometric assay using a variation of Method 1 (see Section 2.4.1). NosZ was added to a solution of 50 μM reduced PazSII in an excess of DT and incubated for 0 mins, 10 mins or 30 mins (Fig. 5.3.4). Incubation time had minimal effect on the enzyme activity or rate of deactivation. By comparison, after just 5 minutes incubation with a similar concentration of $MV^{\bullet+}$ the enzyme activity increased ≈5 fold.

Whilst an interesting choice for an encapsulated redox partner, PazSII appears not to possess all the qualities required to support long term activity of this form of NosZ. The deactivation rate of NosZ when using PazSII as an electron source and the inability of PazSII to reactivate NosZ would likely result in liposomes with limited activity. The rate of activity that PazSII can support is also significantly lower than MV is able to. This is consistent with reports of similar systems.[228,241,245]

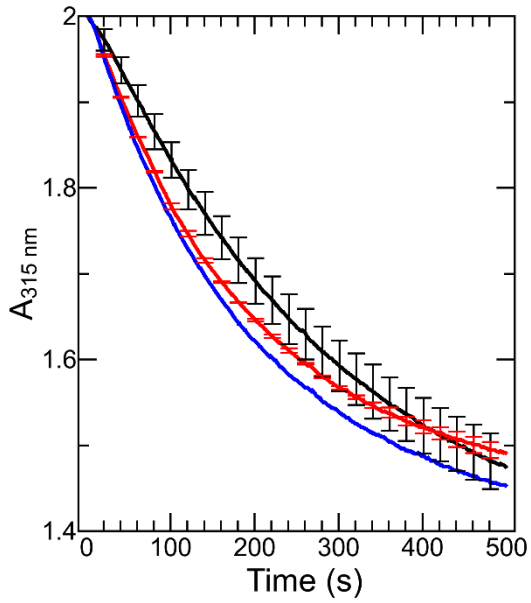

Figure 5.3.4 DT consumption timecourses after adding 750 μM N_2O to 50 μM PazSII, + 250 μM DT + 100 μM NosZ which had been incubating for 0 mins (Black), 10 mins (Red), or 30 mins (Blue). Data for 0 mins and 10 mins incubation are the average of n=2 normalised data sets and error bars show standard deviation, for 30 mins incubation n=1.

5.4 - Encapsulation of NosZ and redox partners in liposomes

Another aspect that must be considered when designing and assembling the nanoreactors described in Figure 1.6.2 is whether the components can be successfully coassembled in a liposome. Previous work has established that incorporating MtrCAB into liposomes during liposome formation allows for high loading.[160,214,215] This is achieved by solublisation of a mixture of lipid and MtrCAB using OG as a detergent. OG has a critical micelle concentration of ≈20 mM which is relatively high among detergents.[246] Dilution of the solution below this concentration results in spontaneous liposome formation with MtrCAB incorporated into the lipid bilayer. Any soluble species in the solution are encapsulated as the liposomes form. This method is termed the dilution method and has previously been used successfully to encapsulate the azo dye RR120 inside liposomes with MtrCAB in the liposome bilayer.[160]

The dilution method allows for high incorporation efficiencies of MtrCAB[160] however encapsulation efficiency of cargo species is low. The lipid:detergent solution is typically diluted into 50 mL of cargo-containing buffer, however it is estimated that <100 μL of this is actually encapsulated (see Section 2.7.4) meaning over 99% of the material remains outside the liposomes and is subsequently washed away. This is less of an issue for cargos like azo dyes[160] which can be procured inexpensively. Enzymes, including NosZ, are far more challenging to obtain and wasting them following the dilution method is not

desirable. A new method was, therefore, developed which lowered the OG concentration by sequestration in place of dilution. Biobeads, small microporous polystyrene beads, are able to adsorb hydrophobic organics from aqueous media and were used to sequester OG.

The experiments described below were performed in parallel with the previous studies when it was not clear whether PazSII or MV would be selected as the preferred redox partner for NosZ.

5.4.1 - Encapsulation of NosZ and PazSII in liposomes by Biobead-mediated detergent sequestration

Liposomes were formed with NosZ and PazSII in the liposome interior and with, or without, MtrAB incorporated into the liposome bilayer. These liposomes are termed MtrAB:PLE-[NosZ+PazSII] and PLE-[NosZ+PazSII] (Fig. 5.4.1). MtrCAB was not used at this point as MtrC and NosZ can be challenging to discriminate by SDS-PAGE which was the primary method for detecting NosZ in the final liposomes. Liposomes were prepared as described in Section 2.7.2.2 with 5 nMol MtrAB or an equivalent volume of PNL buffer, 25 nMol PazSII and 2.5 nMol pre-activated NosZ. All sample handling was carried out in an anaerobic chamber and DT was used throughout the preparation procedure to maintain anaerobicity. The strict anaerobicity was maintained in order to prevent the oxidation of NosZ back to the inactive Cu_Z* state. Successive rounds of incubation with biobeads sequestered the OG before the resulting liposome suspension was washed by 3 cycles of spin washing. After the final wash the liposomes were resuspended to 1 mL in anaerobic TK buffer + 100 µM DT to produce a stock suspension.

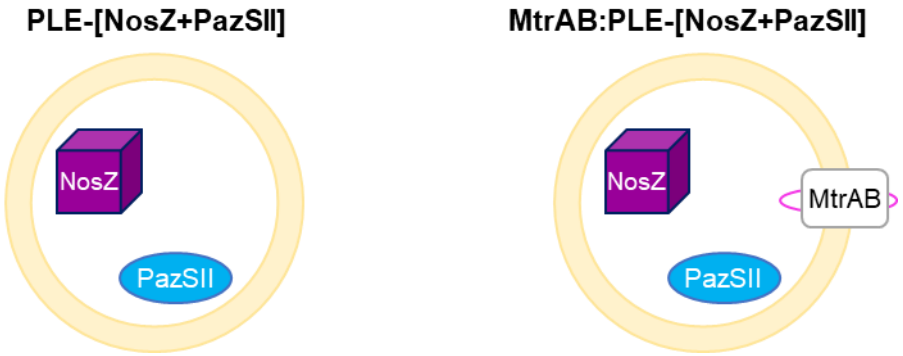

Figure 5.4.1 Schematics of PLE-[NosZ+PazSII] and MtrAB:PLE-[NosZ+PazSII] liposomes.

The liposomes were analysed by DLS which showed them to have similar size distributions with average diameters of ≈250 nm (Fig. 5.4.2B). Based on this size the

liposome concentration in the final 1 mL stock suspension was estimated as 50 nM. Absorbance spectra of a 2.5 nM solution of MtrAB:PLE-[NosZ+PazSII] liposomes in TK buffer + 100 μM DT show a clear feature at 419 nm attributable to ferrous heme which is not present in PLE-[NosZ+PazSII] (Fig. 5.2.4A). This absorbance, and $\varepsilon_{419\ nm}$ = 1944000 M^{-1} cm^{-1} (see Section 2.2.5), was used to quantify [MtrAB] in the stock liposome suspension at 2.2 μM, meaning ≈48% of the added MtrAB was retained in the final suspension and each liposome contained, on average, 45 MtrAB complexes. SDS-PAGE analysis revealed that both types of liposome contained the correct proteins (Fig. 5.4.2C). This gel, and a Bradford assay, also confirmed that the extraliposomal space was clear of protein at any detectable concentration.

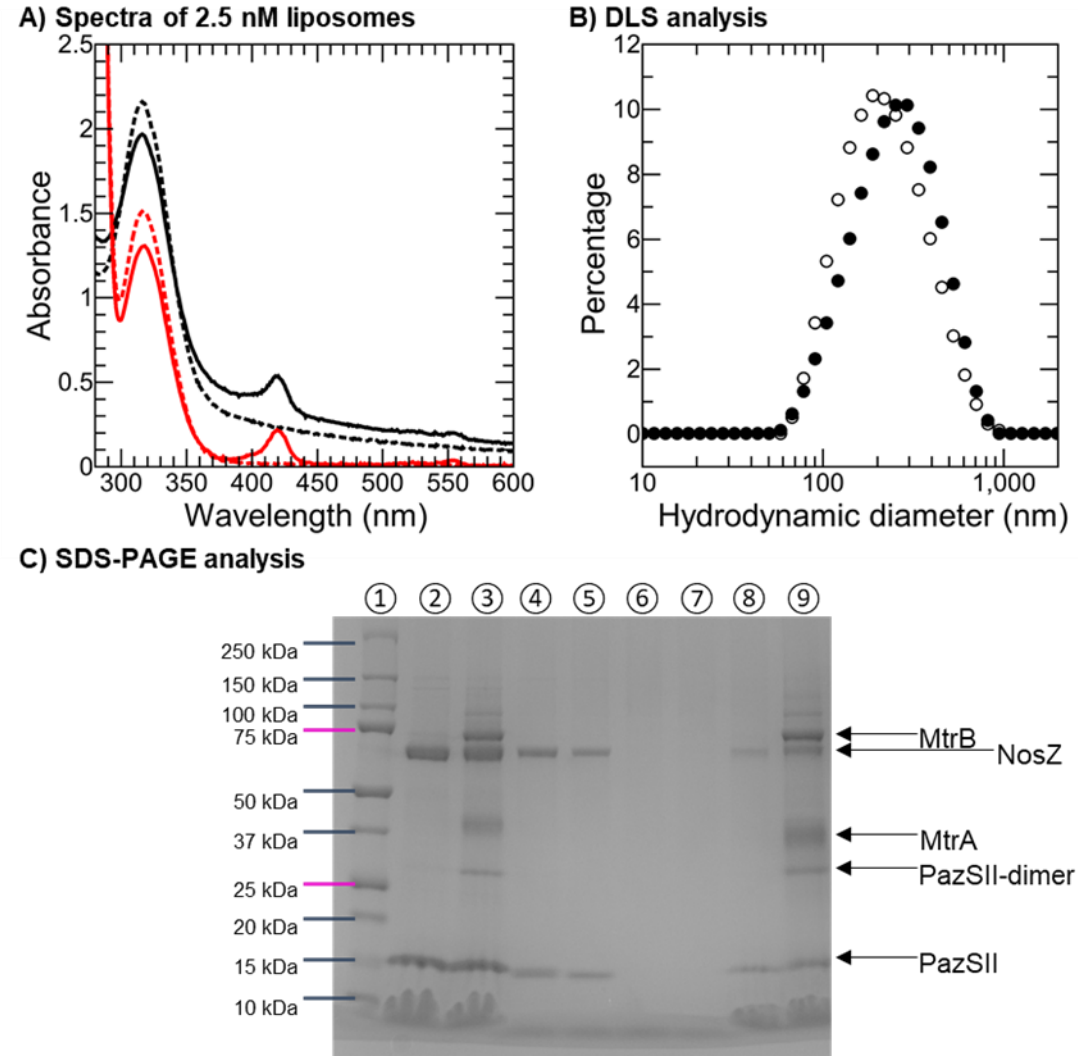

Figure 5.4.2 Characterisation of liposomes. **A)** Spectra of MtrAB:PLE-[NosZ+PazSII] (Solid) and PLE-[NosZ+PazSII] (Dashed) diluted to 2.5 nM in TK Buffer + 100 μM DT (Black), and after addition of TX100 to 0.2% (v/v) (Red); **B)** DLS analysis of MtrAB:PLE-[NosZ+PazSII] (Filled) and PLE-[NosZ+PazSII] (Hollow); **C)** SDS-PAGE analysis of liposomes throughout preparation procedure: ① - Precision Plus Dual Colour, ② - PLE-[NosZ+PazSII] before spin-washing, ③ - MtrAB:PLE-[NosZ+PazSII] before spin-washing, ④ - supernatant from first spin wash of PLE-[NosZ+PazSII], ⑤ - supernatant from first spin wash of MtrAB:PLE-[NosZ+PazSII], ⑥ - supernatant from third spin wash of PLE-[NosZ+PazSII], ⑦ - supernatant from third spin wash of MtrAB:PLE-[NosZ+PazSII], ⑧ - Final PLE-[NosZ+PazSII], ⑨ - Final MtrAB:PLE-[NosZ+PazSII].

MtrAB:PLE-[NosZ+PazSII] and PLE-[NosZ+PazSII liposomes were tested for transmembrane electron transfer using DT as an electron source. Addition of MtrAB:PLE-[NosZ+PazSII] liposomes to a solution of 275 μM DT and 750 μM N_2O led to some DT oxidation (decrease at $A_{315\ nm}$) though this was short-lived, with all activity ceasing after only 5 mins (Fig. 5.4.3A). A similar response was observed with the PLE-[NosZ+PazSII] liposomes but to a lesser extent. If the liposomes were lysed with TX100 prior to exposure to DT and N_2O, the two types of liposome behaved almost identically (Fig. 5.4.3B), but consumed less overall DT than when they were intact.

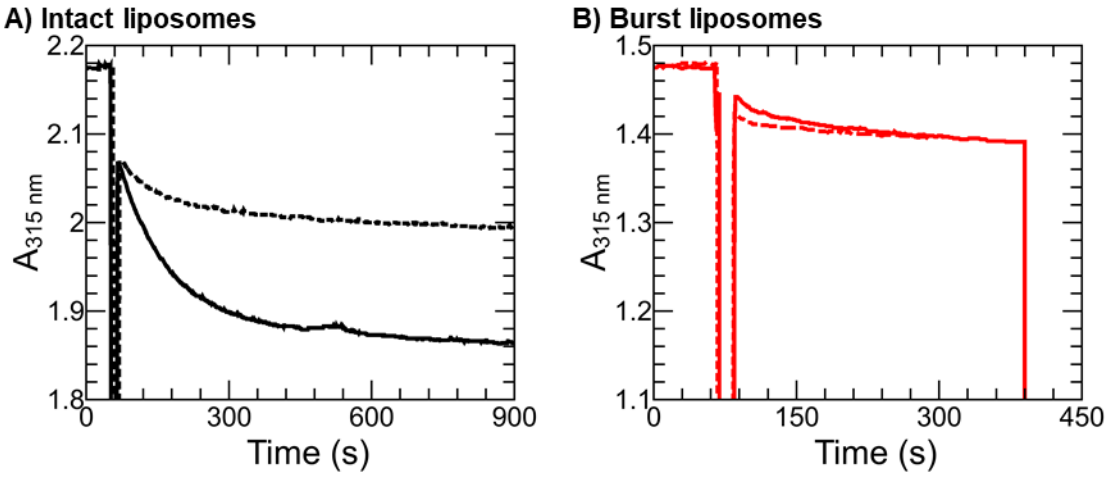

Figure 5.4.3 DT reduction timecourses obtained by addition of MtrAB:PLE-[NosZ+PazSII] (Solid) or PLE-[NosZ+PazSII] (Dashed) to: **A)** 250 μM DT + ≈ 750 μM N_2O in anaerobic TK Buffer; **B)** 180 μM DT + ≈ 750 μM + 0.2% (v/v) TX100 in anaerobic TK Buffer.

These results suggest that MtrAB is able to transfer electrons to PazSII inside a liposome environment. Reduced PazSII can then, briefly, be used to support catalysis by NosZ. The results also highlight that the higher local concentration of PazSII inside the intact liposomes allows for greater enzyme activity. After lysis the effective concentration of PazSII is predicted to be 100× lower. These experiments demonstrate that, whilst encapsulation of PazSII alongside NosZ is relatively simple, and can be achieved without excessive wastage of enzyme, PazSII simply cannot support long-term activity of NosZ. Based on these findings, PazSII had to be ruled out as an option for an electron transfer partner for NosZ for use in liposomes.

5.4.2 - Attempted encapsulation of NosZ and $MV^{\bullet+}$ in liposomes by Biobead-mediated detergent sequestration

A comparable experiment to that described in Section 5.4.1 was carried out to attempt to coencapsulate NosZ and $MV^{\bullet+}$ however even after 5 rounds of Biobead-mediated sequestration of OG there was no evidence of liposome formation. Instead, the samples appeared to lose their blue colour over time, indicating that the $MV^{\bullet+}$ was being sequestered in place of the OG. The decision had to be made, therefore, to use an adaptation of the dilution method reported in Stikane et al[160] which would require a large commitment of NosZ. These experiments are described in the following chapter.

5.5 - General discussion

The results presented in this chapter underpin the choice of the encapsulated components of the nanoreactors depicted in Figure 1.6.2. From studies of $MV^{\bullet+}$ and PazSII it seems that only $MV^{\bullet+}$ is able to fulfil all the roles required of a redox partner for NosZ. It is able to supply electrons to NosZ quickly during catalysis and can reductively activate the active site from the off-cycle Cu_Z* state to the active Cu_Z*$^{-}$ state. At assay concentrations of $MV^{\bullet+}$ (<100 μM) this activation is slow and deactivation gradually returns the enzyme to the Cu_Z* state until a steady state is reached (Fig. 5.2.4). The presence of even low concentrations of $MV^{\bullet+}$ means that activity can likely continue over several hours. PazSII appears unable to activate NosZ, resulting in complete depletion of activity from the enzyme.

The results presented in Section 5.2 also add to the understanding of the catalytic cycle of NosZ and are consistent with more recently published mechanisms.[227] The rate constant for activation by $MV^{\bullet+}$ (1.12 M^{-1} s^{-1}) has not been previously published and highlights a possible explanation for discrepancies in NosZ activity between results from different research groups. Whilst it is well accepted that incubation with $MV^{\bullet+}$ is required to activate NosZ, the use of different concentrations of $MV^{\bullet+}$ and different activation times would be expected to have significant effects on enzyme activity.

The long-term assays presented in Figure 5.2.4 present an interesting way to study the various components of the NosZ catalytic cycle under different conditions such as pH or [$MV^{\bullet+}$]. It may be more time-effective, however, to begin with fully deactivated enzyme and monitor the increasing activity and steady state processes. Such experiments would give much of the same information in a much shorter time period. A full kinetic description of the catalytic cycle of NosZ with MV as a redox partner should be achievable and would help to unite some of the disparate literature.

$MV^{\bullet+}$ is an excellent choice for a redox partner as it can play 2 vital roles in supporting NosZ activity: it can provide electrons for catalysis which allows N_2O to be reduced, and it can also activate the off-cycle state of the enzyme enabling continuous activity. PazSII on the other hand appears to be capable of only the former function. The reduction potential of Paz is +230 mV vs SHE[233] which is far more positive than $MV^{\bullet+}$ (-446 mV vs SHE)[237]. It may be the case that a more negative reduction potential is required to activate the Cu_Z* state and *in vivo* this is provided by the flavoprotein NosR. This is supported by the observations that deletion of the *nosR* gene produced a strain incapable of *in vivo* N_2O reduction, however NosZ purified from this strain could be activated by $MV^{\bullet+}$ and showed no difference from WT enzyme.[230] NosX is a small periplasmic protein that is proposed to play a role in flavinylation of NosR and the same phenotype was observed for Δ*nosX* mutants.[232] the redox chemistry of NosR and NosX have not yet been studied.

The findings regarding the inability of PazSII to activate NosZ are unfortunate as NosZ and PazSII can be effectively co-encapsulated in liposomes using Biobead-mediated detergent sequestration. This method improves on the dilution method published by Stikane et al.[160] by lessening the requirement for large quantities of cargo, the vast majority of which is wasted. Co-encapsulation of NosZ and $MV^{\bullet+}$ using this method was unsuccessful and this was attributed to $MV^{\bullet+}$ binding preferentially to the Biobeads and preventing OG sequestration. In addition, $MV^{\bullet+}$ is known to have some propensity to cross lipid bilayers and it can be used to drive enzyme activity in intact cells.[128,242–244] It is therefore possible that MV will leak out of liposomes, this will be explored further in Chapter 6.

In summary, MV is the appropriate choice for encapsulation as a redox partner for NosZ. It is already established that MV can accept electrons from MtrCAB in liposomes[214,215] and this chapter has established that MV can activate and support catalysis by NosZ. The behaviour of nanoreactors containing MV and NosZ is described in Chapter 6.

CHAPTER 6

LIGHT-DRIVEN TRANSMEMBRANE ELECTRON TRANSFER THROUGH RuMe-MtrCAB TO ENCAPSULATED CARGOS

Chapter 6 - Light-driven transmembrane electron transfer through RuMe-MtrCAB to encapsulated cargos

6.1 - MtrCAB as a transmembrane electron conduit

Whilst MtrCAB naturally acts as a route for outward electron transfer from MR-1, the reduction profiles of the isolated cytochromes suggest that bidirectional electron transfer through the complex should be feasible.[171] Indeed, this has been observed and utilised to achieve biological electrosynthesis on a cathodic electrode in MR-1.[247,248] Addition of the electron acceptor fumarate to MR-1 adhered on a graphite electrode poised at -360 mV (vs SHE) yielded a catalytic cathodic current which was severely diminished in mutant strains lacking MtrB or MtrA demonstrating the important role of these proteins in electron uptake.[247] Similar experiments showed that deletions of MtrC and OmcA diminished the ability of MR-1 to couple cathodic electrons to oxygen reduction by over 80%, again indicating that MtrCAB can transport electrons into MR-1.[248]

The model bacterium *E. coli* is not able to carry out extracellular electron transport as was discussed briefly in Section 1.5.3.3. Heterologous expression of MtrCAB conferred on *E. coli* the ability to reduce insoluble α-Fe_2O_3[249] and carbon anodes[250] using electrons derived from lactate respiration. Fumarate dependent cathodic current was observed for *E. coli* expressing MtrCAB, indicating that the heterologously expressed complex is also capable of bidirectional electron transport.[251] Developments in this area could allow for the coupling of electricity to the wide enzymatic capabilities of *E. coli*, giving rise to a new platform for electrosynthetic biology.

In addition to its *in vivo* functionality, MtrCAB is an effective electron conduit *in vitro* when used in liposome studies. MtrCAB has been incorporated into liposomes containing a number of different redox active cargos including small molecules and proteins. When incorporated into preformed, phosphatidylcholine-derived liposomes, encapsulated colourless methyl viologen (MV^{2+}) was able to be reduced to its blue, one-electron reduced state ($MV^{\bullet+}$) by addition of extraliposomal DT.[215] Subsequent addition of external ferric citrate led to near instant reoxidation of $MV^{\bullet+}$ to MV^{2+}, again demonstrating facile, bidirectional electron transport through MtrCAB (Fig. 6.1.1). Comparable liposomes without MtrCAB showed no evidence of MV^{2+} reduction. Some leakage of $MV^{\bullet+}$ into the extraliposomal space was observed, however this was minimised by addition of valinomycin, an ionophore capable of transporting potassium ions across membranes.[240]

This addition was hypothesised to dissipate the charge imbalance generated when MV^{2+} was reduced and thus it stabilised the membrane.[214]

Transfer of electrons from encapsulated $MV^{\bullet+}$ through liposomal MtrCAB to external iron oxide minerals has also been observed (Fig. 6.1.1).[215] Kinetic analysis of the transmembrane electron transport properties in that study revealed that each MtrCAB could transfer between 1130 and 8500 $e^- s^{-1}$ with rates dependant on the identity of the mineral acceptor. Liposomes incorporating only MtrAB were capable of reducing 16% of encapsulated MV^{2+} when treated with DT. These stored electrons could subsequently be used to reduce external ferric citrate but transfer to iron oxide minerals was not possible, suggesting the importance of MtrC as the interface for mineral reduction.[215] These results demonstrate that when incorporating MtrCAB into preformed liposomes, the complex is oriented with MtrC on the external face.[215] This makes logical sense, as the hydrophobic barrel of MtrB is more likely to insert into the membrane. For the complex to insert in the opposite orientation, the entirety of MtrC would first have to pass across the membrane which is unlikely.

Electron transfer through MtrCAB to encapsulated proteins was demonstrated using STC from MR-1 (Fig. 6.1.1).[157] This small 13.5 kDa protein contains four His/His coordinated *c*-type hemes (-50 to -200 mV vs SHE) and is part of the periplasmic cytochrome pool of MR-1, implicated in shuttling electrons from CymA to MtrCAB (see Fig. 1.6.1). Reduction of encapsulated STC was only possible when MtrCAB was present in the liposome bilayer. Electron transfer rates were however, significantly lower than in previous studies with MV, with transfer rates of around 10 $e^- s^{-1}$ $MtrCAB^{-1}$.[157] This process is likely limited by MtrCAB-to-STC or STC-to-STC electron transfer, the latter was found to have rates lower than 100 s^{-1} by NMR studies.[252]

In collaboration with the group of Prof. Lars Jeuken (University of Leeds) an alternate strategy for preparing MtrCAB liposomes was developed.[160] Here MtrCAB was incorporated during liposome formation by dilution of a mixture of lipid, MtrCAB and cargo in an OG suspension. This produced liposomes with greater amounts of MtrCAB incorporated than could be achieved by previous methods. Of the 500 pMol MtrCAB added during liposome formation, over 200 pMol was incorporated into just 5 mg of lipid.[160] By comparison, in Hartshorne et al. only ≈30 of the 200 pMol of MtrCAB added to liposomes was incorporated into 10 mg lipid.[171] This new method thus presents a means to incorporate greater amounts of MtrCAB with higher efficiency. It should be noted that this new method uses PLE whereas previous works used phosphatidyl choline.[157,214,215] It is also not known what orientations of MtrCAB this method yields.

MtrCAB incorporated into liposomes prepared by the “dilution” method was capable of transmembrane electron transfer. Using the azo dye RR120 (see Fig. 3.4.1) as a spectroscopic indicator, the electron transfer through MtrCAB was investigated using DT or nanoparticle photosensitisers as sources of electrons (Fig. 6.1.1). The design of such experiments formed much of the foundation for the work presented in this chapter.

In this chapter the RuMe-MtrCAB complex, discussed in detail in Chapter 4, is first evaluated against WT MtrCAB as a transmembrane electron transfer conduit. This was accomplished using liposomes with encapsulated RR120 as in Stikane et al.[160] Electrons were generated in the extraliposomal space either chemically, using DT, or photochemically using photosensitisers and SEDs. These techniques were then applied to liposomes with encapsulated NosZ, explored as a redox catalyst in Chapter 5, culminating in an operational light-driven nanoreactor shown schematically in Figure 1.6.2.

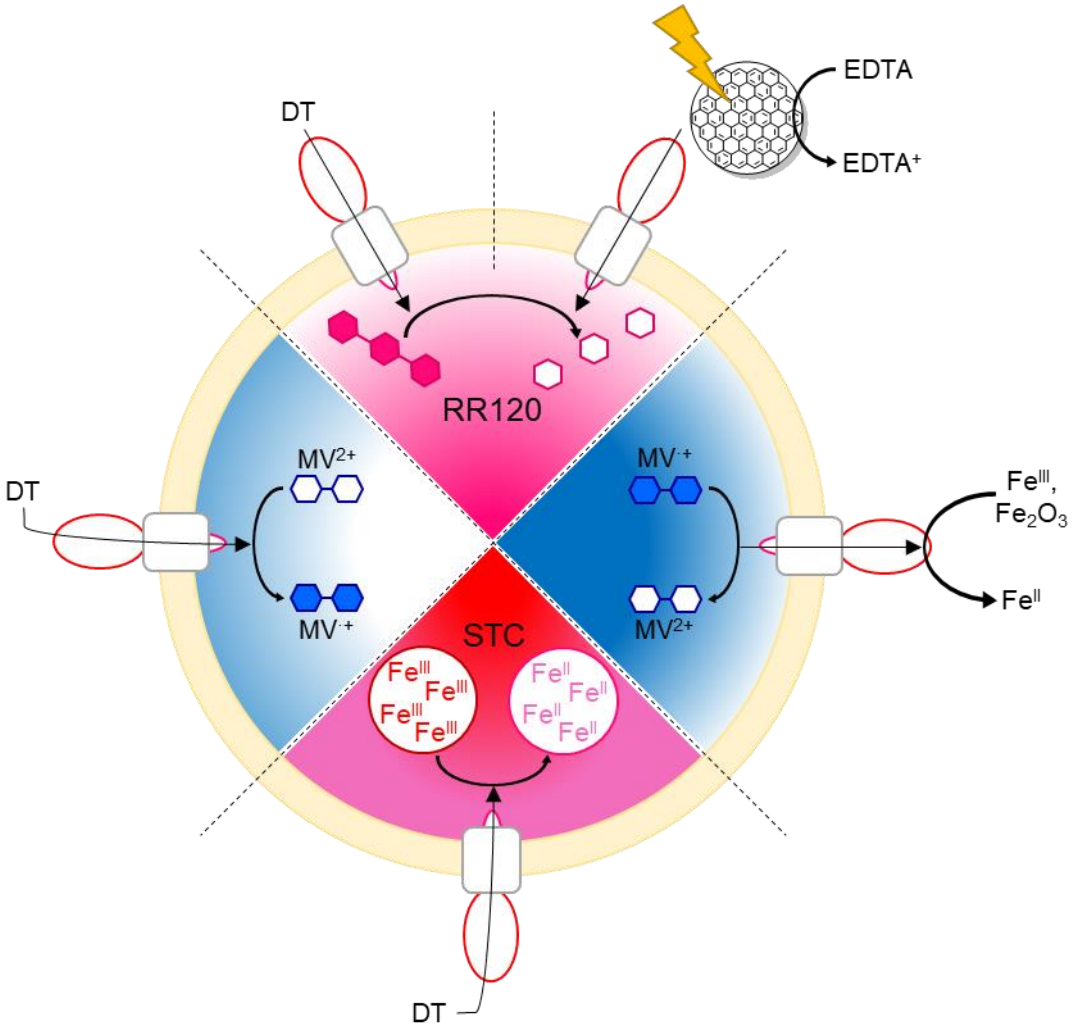

Figure 6.1.1 Examples of liposomal studies of transmembrane electron transfer through the MtrCAB complex. **Top)** DT-driven or light-driven reduction of encapsulated RR120 (see Fig. 3.4.1 for structure) leading to dye bleaching[160]; **Left)** DT-driven reduction of encapsulated MV^{2+} to $MV^{\bullet+}$[214,215]; **Right)** using the encapsulated $MV^{\bullet+}$ as a source of electrons to reduce extraliposomal Fe^{III}(citrate) or insoluble metal oxides[214,215]; **Bottom)** DT-driven reduction of encapsulated STC, a native redox partner of MtrAB[157].

6.2 - Transmembrane electron transfer to encapsulated redox dyes

Work presented in Stikane et al. demonstrated that MtrCAB could be used to facilitate electron transfer across a liposome membrane as evidenced by reduction of encapsulated RR120 (Fig. 6.1.1).[160] This reduction could be achieved either by using DT as a reductant or by using nanoparticle photosensitisers: RuP-TiO_2, amorphous carbon dots or g-N-CDs. In the following sections the experimental design employed in Stikane et al. will be used to compare the reconstituted RuMe-MtrCAB complex (see Chapter 4) to WT MtrCAB, and the parameter space of light-driven transmembrane electron transport using nanoparticle photosensitisers will be explored.

6.2.1 - Evaluation of different azo dyes as internal cargos for studying transmembrane electron transfer

The liposomes prepared in Stikane et al. contained RR120 as a reporter for transmembrane electron transfer.[160] Given the results presented in Section 3.4, where RB5 was found to be a better acceptor of electrons from MtrC than RR120, a comparison was made between RR120 and RB5 (see Fig. 3.4.1 for structures) as redox active cargos. The rationale being that the more facile reduction of RB5 might allow for greater electron flux through MtrCAB.

Liposomes were prepared by the dilution method as described in Section 2.7.2.1 using either RR120 or RB5 as the internal cargo and incorporating RuMe-MtrCAB into the liposome wall or having no protein present (Fig. 6.2.1). These liposomes were examined by DLS (see Section 2.7.3) and found to have similar size distributions with mean diameters of 60-100 nm (Fig. 6.2.2A). Using the procedure described in Section 2.7.4 the concentration of liposomes in the final 1 mL stock liposome suspensions was estimated at 0.3 μM. SDS-PAGE analysis (Fig. 6.2.2C) of the liposomes demonstrated the presence of the RuMe-MtrCAB proteins in RuMe-MtrCAB:PLE-[RR120] and RuMe-MtrCAB:PLE-[RB5] whereas PLE-[RR120] and PLE-[RB5] contained no protein, as expected.

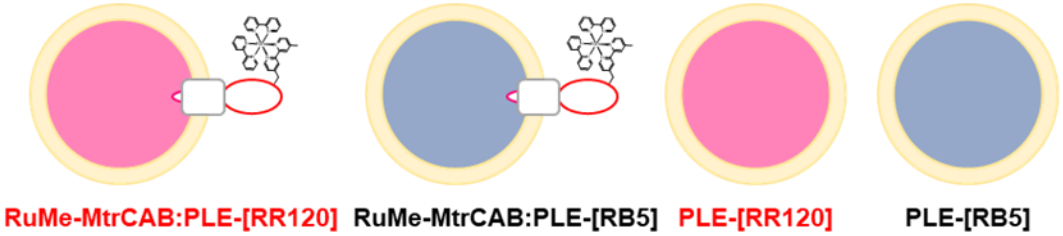

Figure 6.2.1 Schematics and nomenclature of liposomes under consideration in Section 6.2.1. RuMe-MtrCAB orientation is assumed. Dyes RR120 (pink) and RB5 (Blue) shown as coloured liposome interiors.

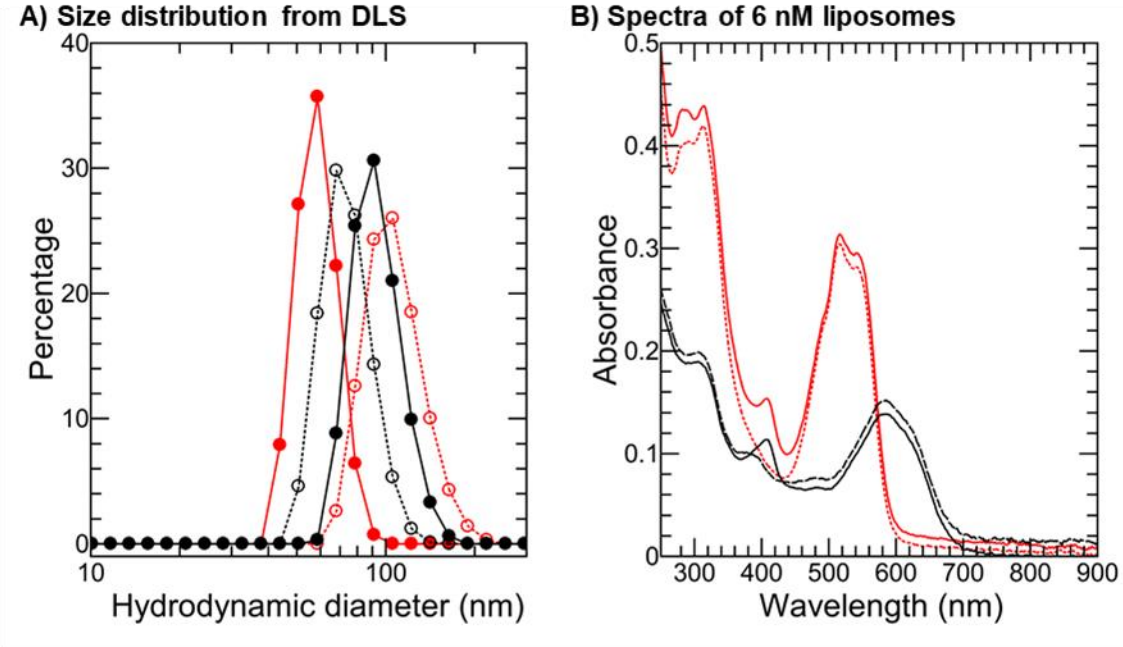

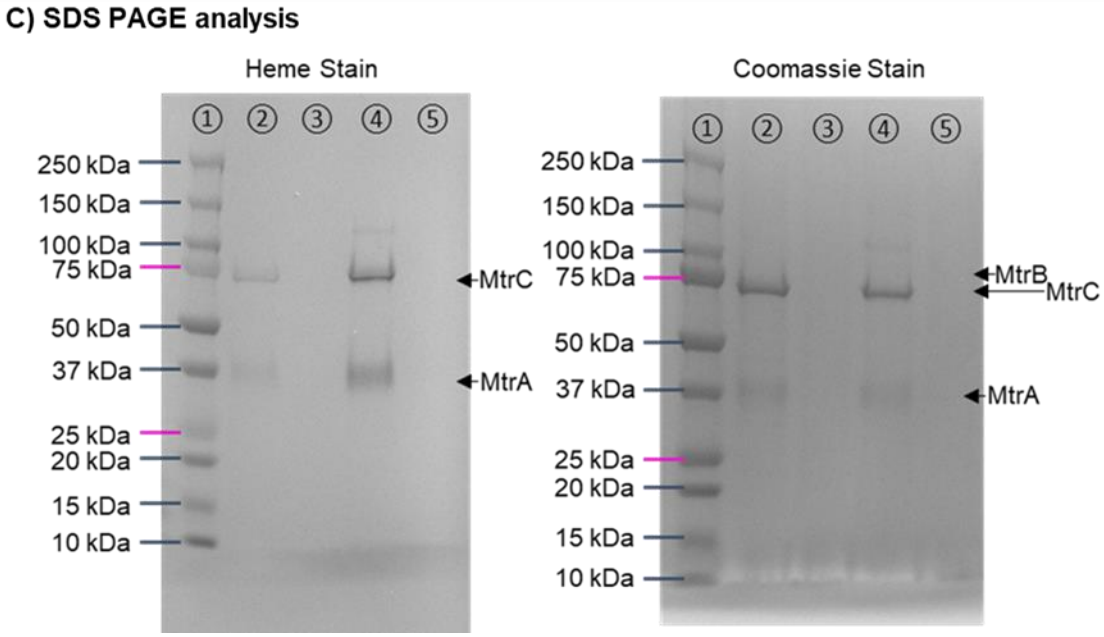

Figure 6.2.2 Characterisation of liposomes. **A+B)** Size distributions obtained by DLS (A) and UV-Vis absorbance spectra of 6 nM liposomes (B) in TK Buffer for RuMe-MtrCAB:PLE-[RR120] (Red-solid), PLE-[RR120] (Red-hollow/dashed), RuMe-MtrCAB:PLE-[RB5] (Black-solid) and PLE-[RB5] (Black-hollow/dashed) liposomes; **C)** SDS PAGE analysis of liposomes with staining and identified proteins indicated: ① - Precision Plus Dual Colour, ② - RuMe-MtrCAB:PLE-[RR120], ③ - PLE-[RR120], ④ - RuMe-MtrCAB:PLE-[RB5], ⑤ - PLE-[RB5].

A 6 nM sample of these liposomes was lysed by addition of TX100 to 0.2% (v/v) which produced an absorbance spectrum without the scattering contribution indicative of intact liposomes (Fig. 6.2.3). Using $\varepsilon_{539\ nm}$ = 32300 $M^{-1}\,cm^{-1}$ for RR120[160] and $\varepsilon_{600\ nm}$ = 23000 $M^{-1}\,cm^{-1}$ for RB5[e], dye concentrations in the liposome stock suspensions were determined to be 460 μM and ≈180 μM respectively (Table 6.2.1). Based on an estimated total internal liposome volume of 73 μL (see Section 2.7.4) the intraliposomal dye concentrations were therefore 6.3 mM for RR120 and ≈2.5 mM for RB5.

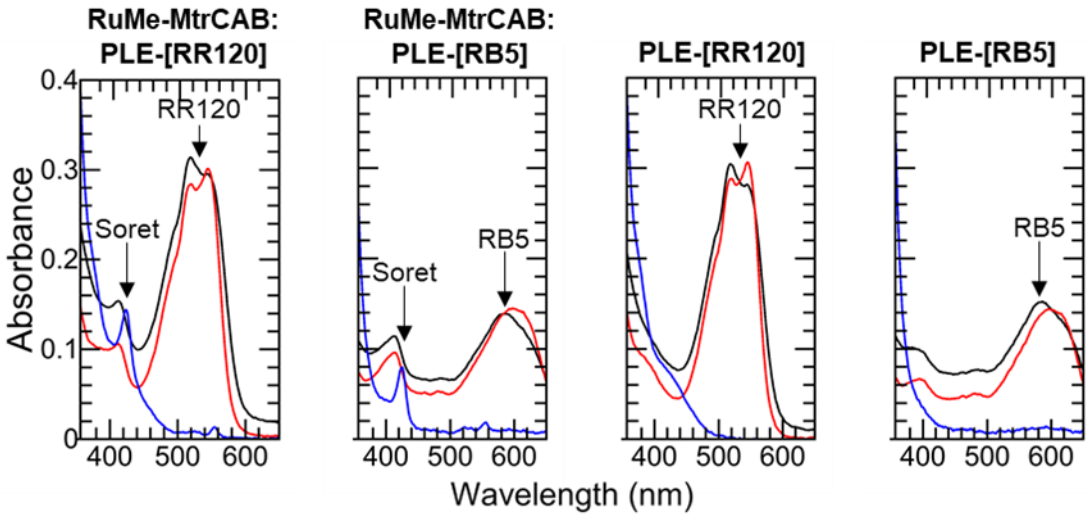

Figure 6.2.3 Spectra of indicated liposomes at 6 nM in TK Buffer (Black), after addition of TX100 to 0.2% (v/v) (Red) and subsequent addition of 100 μM DT (Blue).

Table 6.2.1 Spectroscopically determined liposome composition in stock liposome suspensions

Liposomes	[Dye] (μM)	[RuMe-MtrCAB] (μM)	RuMe-MtrCAB: Liposome ratio
RuMe-MtrCAB:PLE-[RR120]	460	0.9	3.0
RuMe-MtrCAB:PLE-[RB5]	180	0.8	2.7
PLE-[RR120]	460	-	-
PLE-[RB5]	190	-	-

In addition to the features from the dyes, spectra of RuMe-MtrCAB:PLE-[RR120] and RuMe-MtrCAB:PLE-[RB5] also show a clear feature at 410 nm indicative of oxidised heme. The extinction coefficient $\varepsilon_{410\ nm}$ = 2660000 $M^{-1}\,cm^{-1}$ (see Section 2.3.2) was used to determine the RuMe-MtrCAB concentration in the stock liposome suspensions (≈ 1 μM). This would suggest RuMe-MtrCAB:liposome ratios of around 3:1. It would, therefore, be expected that the vast majority of liposomes contain at least one RuMe-MtrCAB complex.

[e] Determined from 10 μM solution in TK buffer

To evaluate the two different dyes as reporters for transmembrane electron transfer, aliquots of the liposomes were diluted into TK buffer to give a concentration of 6 nM and DT was added to 100 μM. Spectra were then obtained over 40 minutes (Fig. 6.2.4). These spectra show that, upon addition of DT, the hemes, where present, were immediately reduced as evidenced by the shift in the Soret band maximum from 410 nm to 420 nm. Also evident is that the dye in liposomes containing RuMe-MtrCAB was reduced much more quickly than in liposomes without protein, confirming the integrity and insulating properties of the liposome bilayer. A decrease in absorbance at $A_{315\ nm}$ was also observed which corresponds to oxidation of DT.

The progress of the dye reduction was following using $A_{539\ nm}$ for RR120 and $A_{600\ nm}$ for RB5 and timecourses for these reductions are shown in Figure 6.2.4E. RR120 reduction in RuMe-MtrCAB:PLE-[RR120] could be fitted well with a single exponential decay function:

$$y = Ae^{-kt} + y_0$$

where A is the overall change in concentration, k is the rate constant and y_0 is the remaining concentration at t=∞.

RB5 reduction in RuMe-MtrCAB:PLE-[RB5], on the other hand, required a biexponential decay function:

$$y = A_1e^{-k_1t} + A_2e^{-k_2t} + y_0$$

to be effectively fitted (Table 6.2.2). This behaviour is, perhaps unsurprisingly, similar to the biphasic photoreduction of RB5 presented in Section 3.4 and is likewise thought to stem from the different properties of the two azo bonds in RB5. The initial rates of dye reduction were determined from the initial gradients of the timecourses and used to calculate the electron flux through RuMe-MtrCAB (Table 6.2.2). It is clear from these that reduction of RB5 proceeds much faster than RR120.

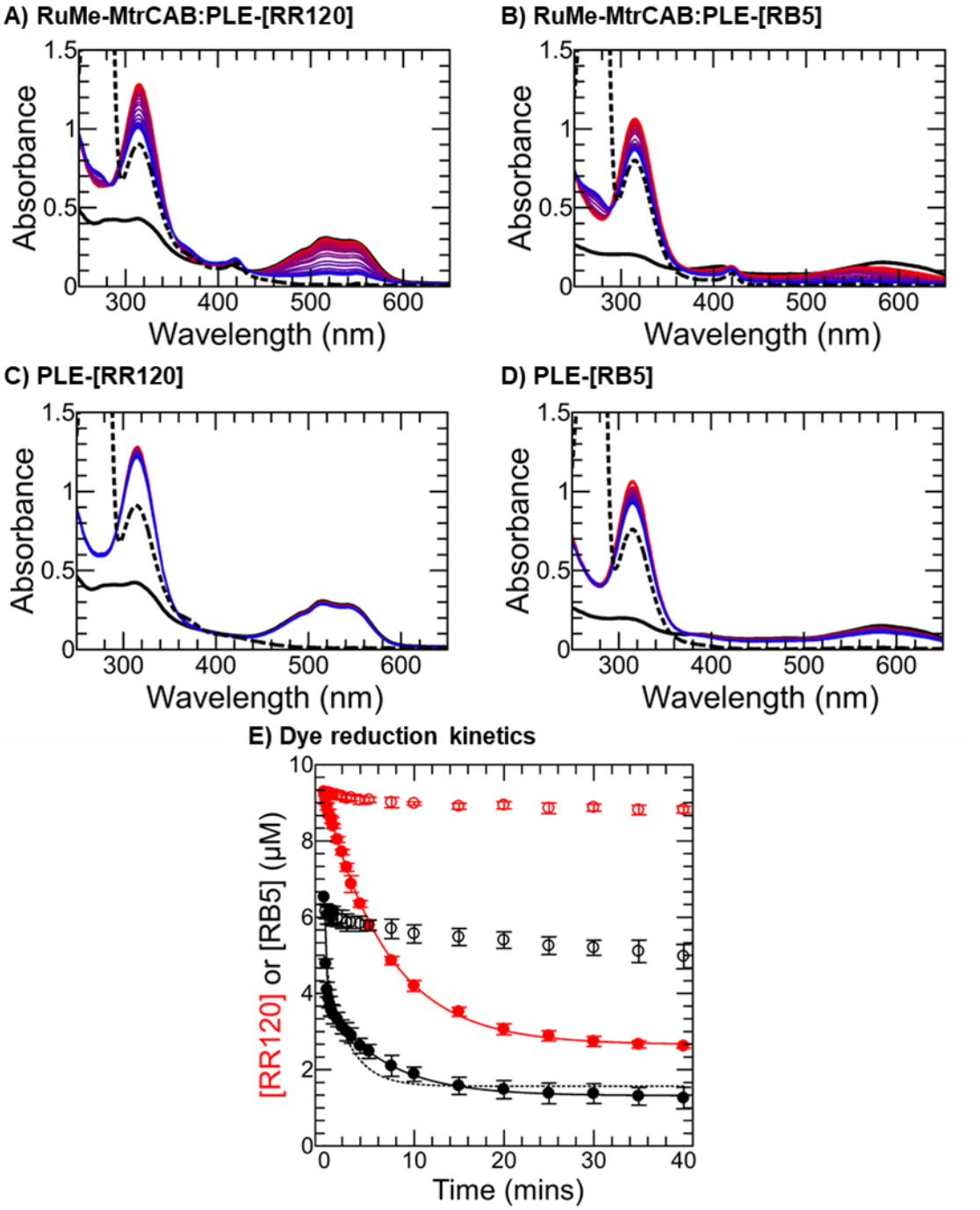

Figure 6.2.4 DT-driven reduction of encapsulated azo dyes in indicated liposomes at 6 nM in TK Buffer. **A-D)** spectra obtained before addition of DT (Black-solid), over 40 minutes following addition of 100 μM DT (Red-to-blue) and after addition of TX100 to 0.2% (v/v) (Black-dashed); **E)** Reduction timecourses obtained at $A_{539\ nm}$ for RR120 (Red) or $A_{600\ nm}$ for RB5 (Black) with +RuMe-MtrCAB liposomes (Solid) or -RuMe-MtrCAB liposomes (Hollow). Kinetic fits are shown as lines: data for RuMe-MtrCAB:PLE-[RR120] fits to a single exponential decay (Red solid), data for RuMe-MtrCAB:PLE-[RB5] fits poorly to a single exponential decay (Black-dashed) but well to a biexponential decay (Black-solid). Data are the average of n=3 normalised data sets and error bars show standard deviation.

Table 6.2.2 Encapsulated azo dye reduction kinetics using single exponential (1-exp) or biexponential (2-exp) fitting

	[RuMe-MtrCAB] (μM)	A (μM Dye)	k × 10^3 (s^{-1})	y_0 (μM Dye)	Initial rate (e^- s^{-1} RuMe-MtrCAB^{-1})
RuMe-MtrCAB RR120 1-exp	0.018	6.6 ± 0.03	2.4 ± 0.04	2.7 ± 0.03	5.7
RuMe-MtrCAB RB5 1-exp	0.016	3.4 ± 0.3	6.7 ± 1.6	1.6 ± 0.18	87
RuMe-MtrCAB RB5 2-exp		2.5 ± 0.03	2.6 ± 0.08	1.3 ± 0.02	
		2.7 ± 0.04	94 ± 3.5		

It is evident from these results that, particularly in RuMe-MtrCAB:PLE-[RR120] liposomes, the reduction of the dye does not proceed to completion. This is likely due in part to pseudoabsorbance caused by scattering from the liposomes. It may also be a result of a small population of liposomes containing no RuMe-MtrCAB. A scattering background can be reasonably estimated using the equation:

$$I_\lambda = A + \frac{B}{\lambda^4}$$

Where I_λ is the pseudoabsorbance due to scattering at wavelength λ, and A and B are variables that are varied in order to produce a suitable curve. Subtraction of such curves from the spectra depicted in Figures 6.2.4A-D and other such spectra reported in this chapter can be used to isolate the absorbances of the proteins and cargo.

To assess the robustness of the liposomes and the RuMe-MtrCAB complex, these experiments were repeated on the liposomes on the day after their preparation and after 1 week of storage in an anaerobic chamber at room temperature (Fig. 6.2.5). The lack of any significant change in the results for PLE-[RR120] and PLE-[RB5] suggests that the liposomes remained intact and impermeable to dye over this time period. The slight decrease in the rate of dye reduction when RuMe-MtrCAB was present in the liposomes, suggests the complex lost a little of its original ET capability over this time period.

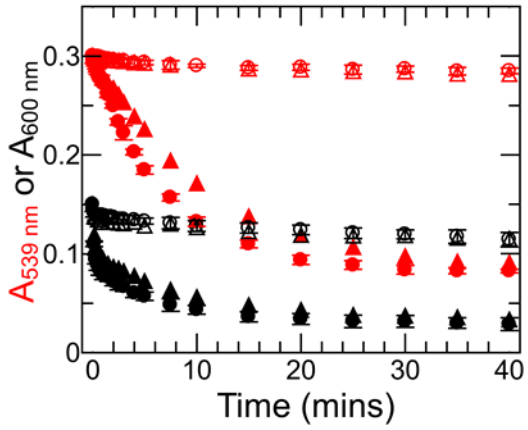

Figure 6.2.5 DT-driven reduction timecourses obtained at $A_{539\ nm}$ for RR120 (Red) or $A_{600\ nm}$ for RB5 (Black) with +RuMe-MtrCAB liposomes (Solid) or -RuMe-MtrCAB liposomes (hollow) at a concentration of 6 nM in TK Buffer on Day 1 following preparation (Circles) or 8 days later (Triangles). For Day 1 data are the average of n=3 normalised data sets and error bars show standard deviation, for Day 8 n=1.

Both dyes have advantages and disadvantages. RB5 is reduced very quickly, which may allow for the study of more rapid electron flux through RuMe-MtrCAB, however the biphasic nature of the dye reduction makes kinetic analyses more challenging. The simplified, monophasic reduction kinetics of RR120 provides a simpler platform for kinetic interpretations. Also, RR120 was used in our previous study of transmembrane electron transfer by WT MtrCAB.[160] By using RR120 here the data can be more readily compared to the previous study. RR120 will therefore be used as the transmembrane electron transfer reporter in the following sections.

6.2.2 - MtrCAB vs MtrAB vs RuMe-MtrCAB as transmembrane electron conduits

A factor that has not yet been determined is whether the reconstituted RuMe-MtrCAB complex resembles WT MtrCAB as a transmembrane electron conduit. To determine this, liposomes were prepared as described in Section 2.7.2.1 using 10 mM RR120 and either MtrCAB (MtrCAB:PLE-[RR120]), RuMe-MtrCAB (RuMe-MtrCAB:PLE-[RR120]), MtrAB (MtrAB:PLE-[RR120]) or no proteins (PLE-[RR120]) (Fig. 6.2.6). These liposomes were examined by DLS (see Section 2.7.3) and were found to have a size distribution centred on 100 nm in diameter (Fig. 6.2.7A). As previously, the final stock liposome suspensions are estimated to have a liposome concentration of 0.3 μM.

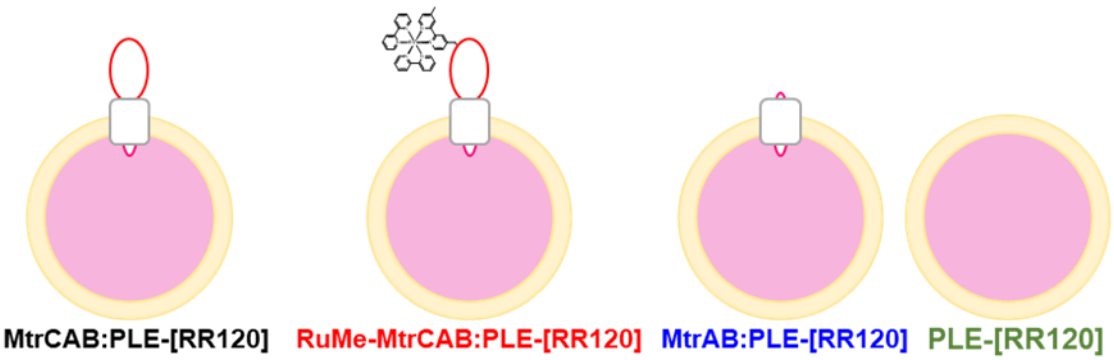

Figure 6.2.6 Schematics and nomenclature of liposomes under consideration in Section 6.2.2. Mtr protein orientation is assumed.

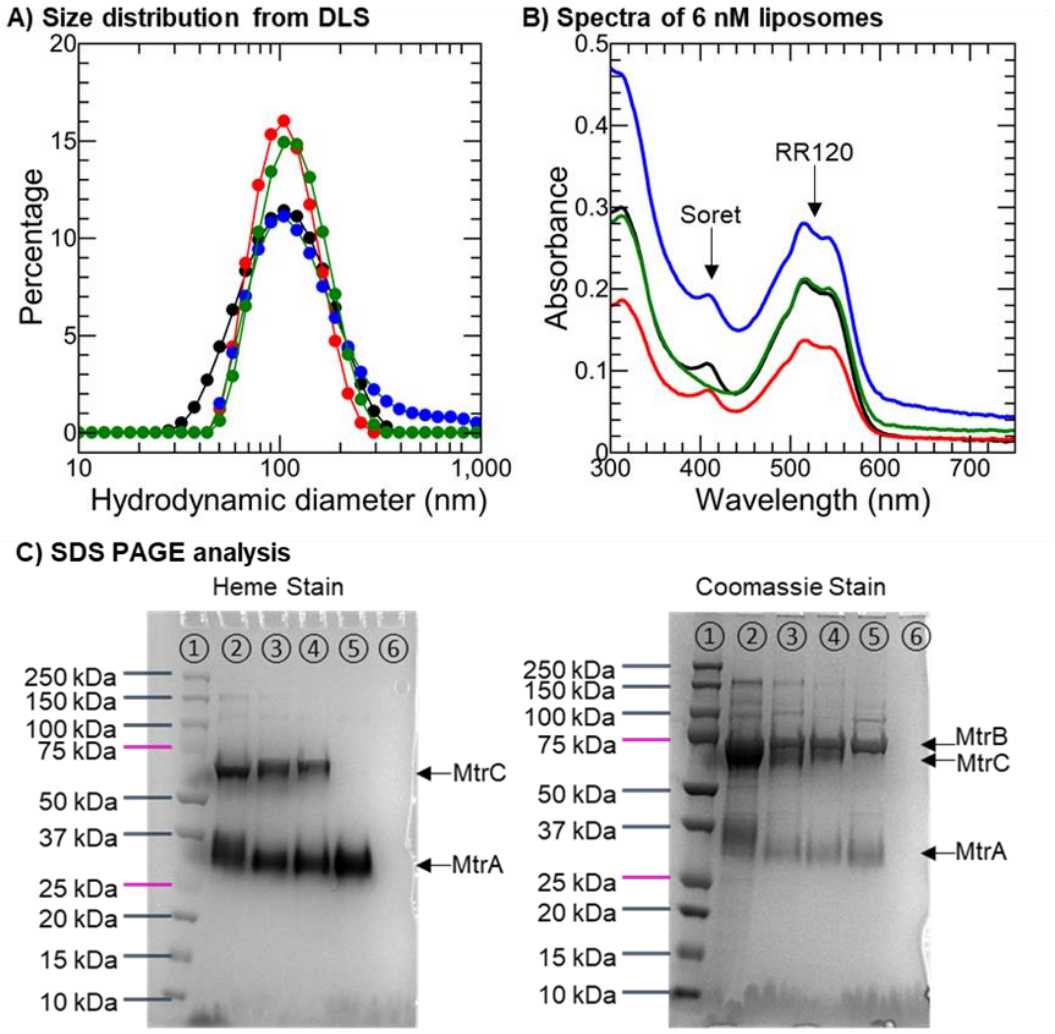

Figure 6.2.7 Characterisation of liposomes. **A+B**) Size distributions obtained by DLS (A) and UV-Vis absorbance spectra of 6 nM liposomes (B) in TK Buffer for MtrCAB:PLE-[RR120] (Black), RuMe-MtrCAB:PLE-[RR120] (Red), MtrAB:PLE-[RR120] (Blue) and PLE-[RR120] (Green) liposomes; **C)** SDS PAGE analysis of liposomes with staining and identified proteins indicated: ① Precision Plus Dual Colour, ② MtrCAB, ③ MtrCAB:PLE-[RR120], ④ RuMe-MtrCAB:PLE-[RR120], ⑤ MtrAB:PLE-[RR120], ⑥ PLE-[RR120].

SDS-PAGE confirmed that the proteins added during the liposome formation were retained in the final liposomes (Fig. 6.2.7C). UV-Vis absorbance spectra of 6 nM liposomes in TK Buffer (Fig. 6.2.7B) show a feature at 410 nm in liposomes which contain protein indicating the presence of oxidised heme. As previously: $A_{410\ nm}$ was used to determine the quantity of proteins in the liposome stocks; and $A_{539\ nm}$ was used to determine the RR120 concentration (Table 6.2.3).

Table 6.2.3 Spectroscopically determined liposome compositions in stock liposome suspensions

Liposomes	[RR120] (μM)	[Conduit] (μM)	Conduit:Liposome ratio
MtrCAB:PLE-[RR120]	270	0.50	1.7
RuMe-MtrCAB:PLE-[RR120]	170	0.45	1.5
MtrAB:PLE-[RR120]	340	1.0	3.3
PLE-[RR120]	270	-	-

Spectra obtained after addition of 2.5 mM DT to a 6 nM solution of liposomes led to immediate reduction of any hemes present, (shift of the Soret band from 410 to 420 nm), and onset of RR120 reduction (decrease of $A_{539\ nm}$). Examples of these spectra and timecourses of $A_{539\ nm}$ along with fitting to single or biexponential fits[f] are presented in Figure 6.2.8. Kinetic parameters from fitting are shown in Table 6.2.4.

[f] Single exponential function: $y = Ae^{-kt} + y_0$, biexponential function: $y = A_1e^{-k_1t} + A_2e^{-k_2t} + y_0$

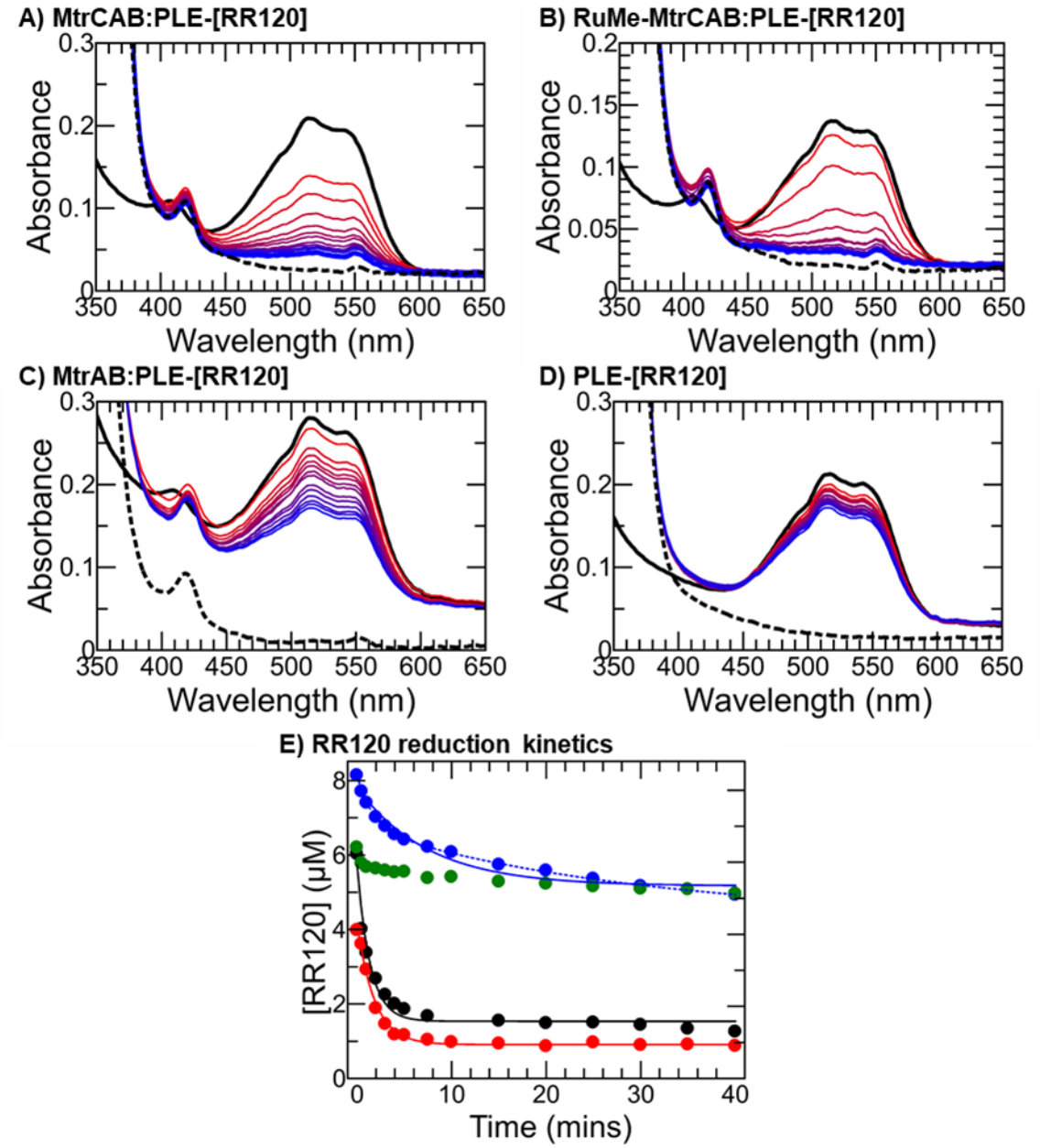

Figure 6.2.8 DT-driven reduction of encapsulated azo dyes in indicated liposomes at 6 nM in TK Buffer. **A-D)** Spectra obtained before addition of DT (Black-solid), over 40 minutes following addition of 2.5 mM DT (Red-to-blue), and after addition of TX100 to 0.2% (v/v) (Black-dashed); **E)** timecourses of [RR120] for MtrCAB:PLE-[RR120] (Black), RuMe-MtrCAB:PLE-[RR120] (Red), MtrAB:PLE-[RR120] (Blue) or PLE-[RR120] (Green). Single exponential (solid) and biexponential (dashed) fits shown as lines.

Table 6.2.4 Encapsulated RR120 reduction kinetics using single exponential (1-exp) or biexponential (2-exp) fitting

	[Conduit] (nM)	A (μM RR120)	$k \times 10^3$ (s^{-1})	y_0 (μM RR120)	k /[Conduit] (s^{-1} nM^{-1})	Initial rate (e^- s^{-1} $Conduit^{-1}$)
MtrCAB 1-exp	10	4.2 ± 0.2	12 ± 1.5	1.5 ± 0.09	1200 ± 0.15	20
RuMe-MtrCAB 1-exp	9	3.2 ± 0.1	9.0 ± 0.6	0.9 ± 0.04	1000 ± 0.07	16
MtrAB 1-exp	20	2.6 ± 0.1	2.2 ± 0.3	3.2 ± 0.1	110 ± 0.02	3.6
MtrAB 2-exp		1.4 ± 0.1	10 ± 0.8	4.3 ± 0.2	510 ± 0.04	
		2.4 ± 0.1	0.57 ± 0.08		28 ± 0.004	

As previously, when Mtr proteins were not present, reduction of RR120 was minimal (Fig. 6.2.8D). RR120 reduction in MtrCAB:PLE-[RR120] and RuMe-MtrCAB:PLE-[RR120] proceeded to near completion and followed monoexponential kinetics. When accounting for the difference in protein concentration between the two liposomes, the rate constants are within error of one another (Table 6.2.4). These data suggest that RuMe-MtrCAB is equivalent to MtrCAB as an electron transfer conduit. This finding is of critical importance to the development of the nanoreactors envisaged here.

RR120 reduction in MtrAB:PLE-[RR120], on the other hand, appears to be biphasic, and only ≈ 40% of the encapsulated dye is predicted to be reduced at t=∞. This is consistent with previous studies where MtrAB in liposomes was only capable of reducing a portion of encapsulated MV.[215]

The reason for the difference in behaviour between MtrCAB and MtrAB might be explained by protein orientation. It is possible that, without the bulk provided by MtrC, MtrAB is able to incorporate into the liposome bilayer in both orientations. Presumably the “correct” orientation, where the periplasmic face of MtrAB is in the liposome interior, is responsible for the faster phase and the “inside-out” orientation has slower kinetics of RR120 reduction. Heme 10 of MtrA, which sits closest to the MtrC interaction site, has less solution exposure than hemes 1&2 on the periplasmic face (Fig. 6.2.9). It is therefore expected that RR120 reduction by the extracellular face of MtrAB might be slower. Experiments attempting to reconstitute RuMe-MtrCAB by combining RuMe-MtrC with MtrAB:PLE-[-] liposomes have seen little success, further supporting the hypothesis that MtrAB inserts into the liposomes at random or, potentially, with a preference for the

inside-out orientation. The reason that dye reduction in MtrAB:PLE-[RR120] does not go to completion is still unknown.

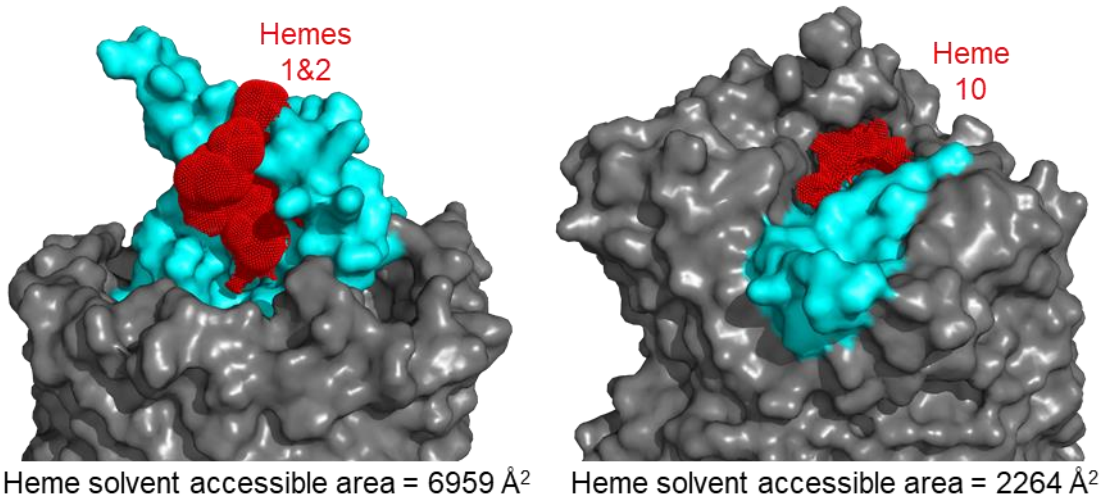

Figure 6.2.9 Depiction of the solution exposure of the hemes at the periplasmic face (Left) and extracellular face (Right) of MtrAB. Peptide surface coloured grey for MtrB and cyan for MtrA. Solution exposed heme was determined and quantified using Pymol and is depicted as red dots. Structure is the homology model of MtrAB from MR-1 which is based on the structure of MtrCAB from *Shewanella baltica* (6R2Q).[134] Proteins rendered in Pymol.

Controlling membrane protein orientation in liposomes is not trivial and can be affected by many factors including formation method, buffer composition, lipid formulation and detergent.[253,254] Incorporation by the dilution method used here, where liposome formation and protein incorporation occur simultaneously, is likely to lead to more randomised insertion than is seen when proteins are incorporated into preformed liposomes. Regardless, RuMe-MtrCAB and WT MtrCAB appear to be effective transmembrane electron conduits when incorporated using the dilution method. This bodes well for the development of the nanoreactors envisaged at the start of this work and illustrated in Figure 1.6.2.

6.2.3 - Attempted light-driven transmembrane electron transfer to an encapsulated redox dye using attached RuMe photosensitiser

The RuMe-MtrCAB:PLE-[RR120/RB5] liposomes discussed in Section 6.2.1 were studied to assess whether the covalently attached RuMe photosensitiser could be used to drive transmembrane electron transfer to the encapsulated redox dye. The liposomes were diluted into TK Buffer + 100 mM EDTA and irradiated with blue light for 5h with spectra obtained periodically (Fig. 6.2.10) in a manner similar to that described for photoreduction of RuMe-MtrC (Sections 2.5.3, 3.2, 3.3).

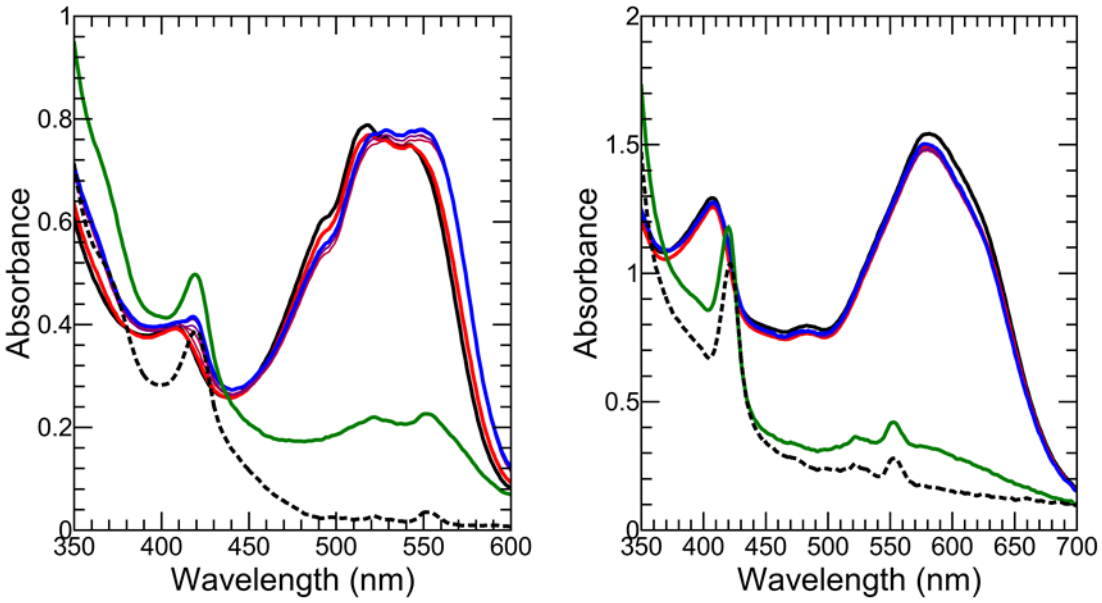

Figure 6.2.10 Attempt to drive photoreduction of encapsulated azo dyes using RuMe-MtrCAB. Spectra of 15 nM RuMe-MtrCAB:PLE-[RR120] (Left) or 60 nM RuMe-MtrCAB:PLE-[RB5] (Right) in TK Buffer (Black solid), after addition of 100 mM EDTA (Red) and irradiated over 5h (Red to Blue), after addition of DT (Green) and addition of TX100 to 0.04% (v/v) (Black dashed).

Unfortunately, the dyes were not observed to reduce over this time period. Heme reduction in RuMe-MtrCAB:PLE-[RR120] liposomes was evident in the shift of the Soret peak maximum from 410 to 420 nm, however this was sluggish compared to the behaviour seen for RuMe-MtrCAB in detergent solution (Fig. 4.4.1). Heme reduction was not observed for RuMe-MtrCAB:PLE-[RB5] liposomes. RB5 has been found to have more favourable reduction kinetics than RR120 (Sections 6.2.1 & 3.4), it is therefore possible that the steady-state level of reduced heme is too low to be detectable. Based on the concentrations of RuMe-MtrCAB in these experiments and electron production rates determined for RuMe-MtrC in Section 3.4 (≈ 1 min^{-1} at 100 mM EDTA) the theoretical rate of dye reduction and the corresponding absorbance change can be calculated (Table 6.2.5) assuming 8e^- per dye and ε values given in Section 6.2.1.

Table 6.2.5 Predicted results for RuMe-MtrCAB driven photoreduction of encapsulated azo dyes.

Liposomes	[RuMe-MtrCAB] (nM)	Electron production rate (nM min^{-1})	Rate of dye reduction (nM dye min^{-1})	Rate of absorbance change (min^{-1}) (λ)	Total absorbance change over 5h (λ)
RuMe-MtrCAB: PLE-[RR120]	45	45	5.6	0.00018 (539 nm)	0.054 (539 nm)
RuMe-MtrCAB: PLE-[RB5]	160	160	20	0.00046 (600 nm)	0.14 (600 nm)

The expected changes in absorbance are low. Even after 5 h irradiation the absorbance would be expected to decrease by less than 10% relative to the starting point. It seems evident that the photochemistry of RuMe-MtrCAB will need to be optimised to produce greater electron fluxes before an experiment such as these can be seen to work. The possibilities for engineering of RuMe-MtrC to increase electron supply are discussed in Chapter 7.

6.3 - Light-driven transmembrane electron transfer using carbon-based photosensitisers

Given the results of the previous section a different strategy was pursued in an attempt to demonstrate light-driven transmembrane electron transfer through RuMe-MtrCAB to RR120 and thereby provide proof-of-principle for the nanoreactors described in Figure 1.6.2. Dr Carla Casadevall from the group of Prof. Reisner (University of Cambridge) kindly provided carbon dots (CDs) to use as photosensitisers. These materials are an increasingly popular class of photosensitiser due to their wide spectral coverage, water solubility, excellent photochemical properties and their versatility towards chemical modification. They are also a sustainable choice of photosensitiser, able to be prepared from simple organic molecules such as citric acid or amino acids.[150,255] In Stikane et al. similar materials were shown to support light-driven transmembrane electron transfer through WT MtrCAB to drive RR120 reduction (Fig. 6.1.1).[160]

6.3.1 - Establishing the use of CDs as photosensitisers for driving transmembrane electron transfer through MtrCAB

Two types of CDs were provided: graphitic carbon dots (g-CDs) and graphitic nitrogen-doped carbon dots (g-N-CDs). These are formed by high-temperature pyrolysis of citric acid or aspartic acid respectively (Fig. 6.3.1), and their structural, spectroscopic and electrochemical properties were found to be consistent with those reported by Martindale et al. (Table 6.3.1)[150].

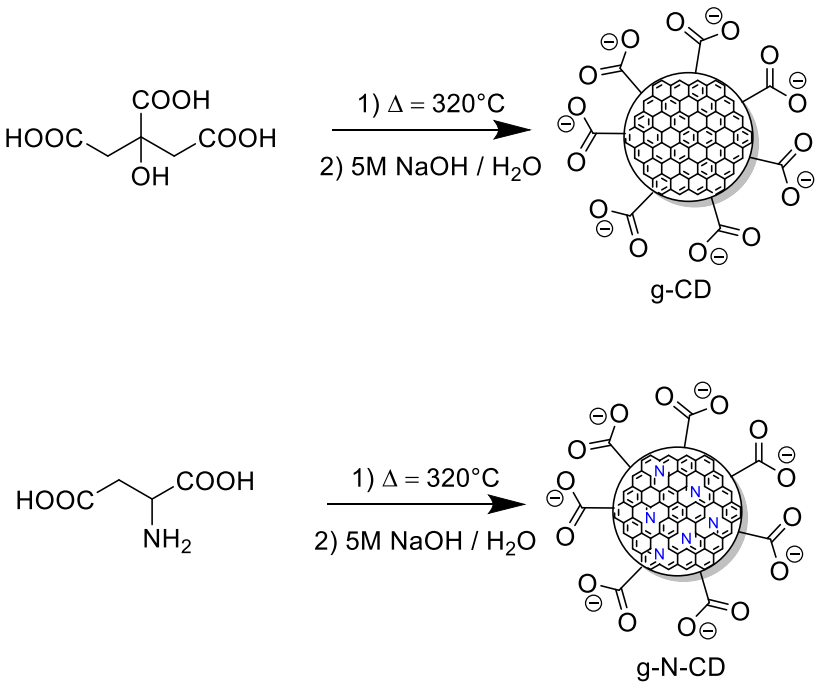

Figure 6.3.1 Syntheses of g-CDs and g-N-CDs

Table 6.3.1 Sizes and MW of g-CDs and g-N-CDs determined using TEM and assuming density is equal to graphite (2.266 g cm^{-3})

CD	Size (nm)	MW (kDa)
g-CD	3.6 ± 1.1	33
g-N-CD	3.1 ± 1.1	21

Both g-N-CDs and g-CDs were trialled as photosensitisers to drive transmembrane electron transfer through RuMe-MtrCAB to RR120. For standard experiments, CDs were diluted from a 1 mg/mL stock in TK Buffer to 10 µg/mL. RuMe-MtrCAB:PLE-[RR120] or PLE-[RR120] liposomes, as prepared in section 6.2.1, were then added to a concentration of 6 nM. Then, 25 mM EDTA was added as a SED and the samples were irradiated for 30 mins with a Krüss cold light source at maximum power (2.5 kW m^{-2}) which has a broad spectral range (see Section 2.5.1). Spectra of the CDs and the spectral distribution of this light source can be found in Section 2.5.1. After the irradiation period was complete, 100 µM DT was added to the samples and a spectrum was obtained after 5 mins. Finally, TX100 was added to 0.2% (v/v) to lyse the liposomes and allow any remaining RR120 to be reduced by DT. Examples of the spectra obtained throughout this process with and timecourses of $A_{539\ nm}$ and $A_{420\ nm}$ are shown in Figure 6.3.2.

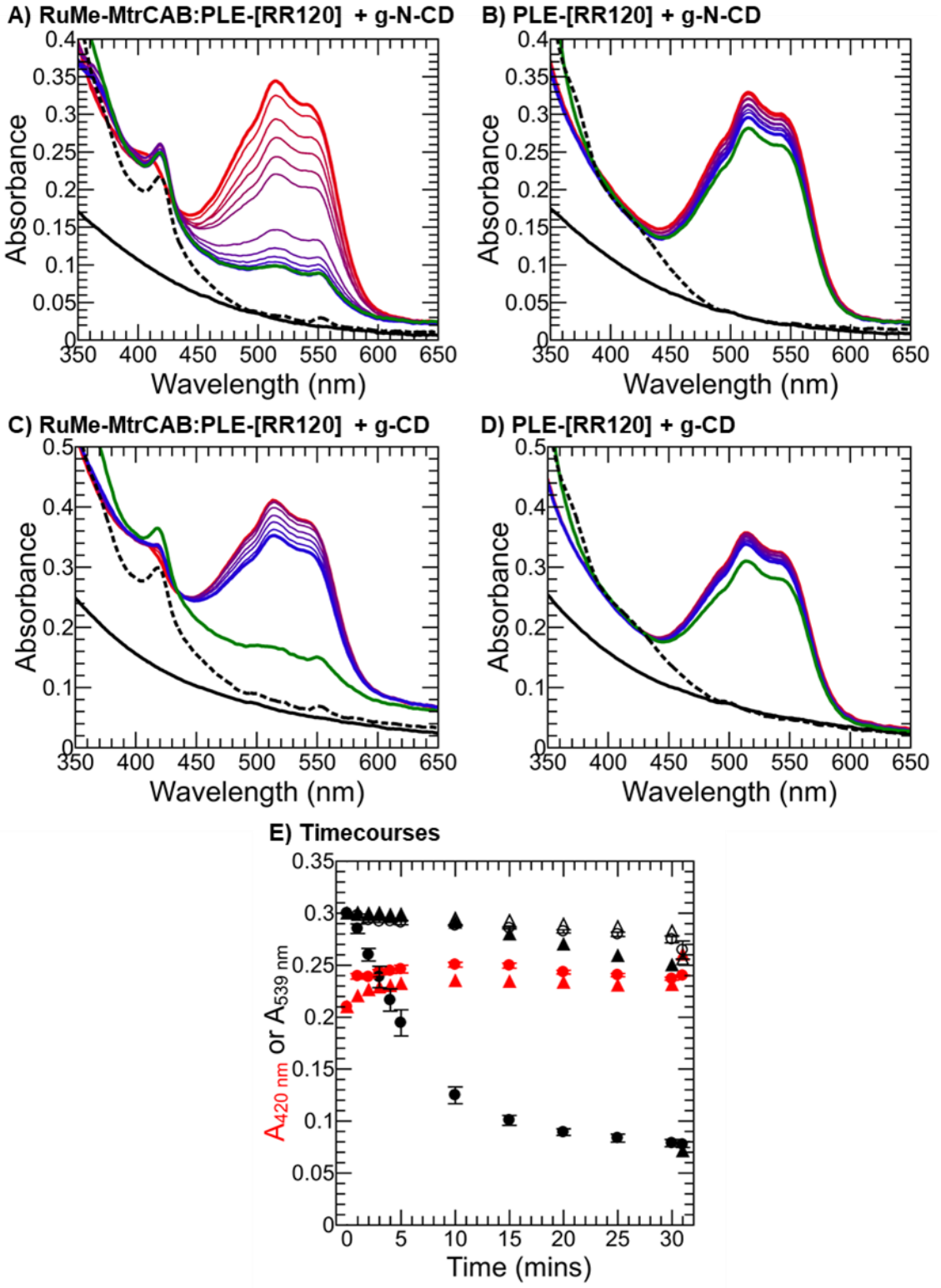

Figure 6.3.2 Spectra showing CD driven photoreduction of RR120 in indicated liposomes with indicated CDs in anaerobic TK buffer. **A-D)** Spectrum of 10 μg/mL CDs (Solid-black), after adding 6 nM liposomes and 25 mM EDTA (Red), over 30 mins irradiation (Red-to-blue), after addition of 100 μM DT (Green) and subsequent addition of TX100 to 0.2% (v/v) (Black-dashed); **E)** Timecourses extracted from the spectra of RuMe-MtrCAB:PLE-[RR120] (Filled) and PLE-[RR120] (Hollow) at $A_{539\ nm}$ (Black) to show reduction of RR120 and at $A_{420\ nm}$ (Red) to show reduction of RuMe-MtrCAB using g-N-CDs (Circles) and g-CDs (Triangles). For g-N-CDs data are the average of n=3 normalised data sets and error bars show standard deviation, for g-CD data n=1.

By extracting $A_{420\ nm}$ and $A_{539\ nm}$ we can observe and compare reduction of the various components of the system (Fig. 6.3.2E). It is immediately clear from the more rapid decrease at $A_{539\ nm}$ that the g-N-CDs were able to drive transmembrane electron transfer more effectively than the g-CDs at this concentration. The hemes of RuMe-MtrCAB were fully reduced by g-N-CDs in the first 5 mins of irradiation, as evidenced by the shift of the Soret to 420 nm. In contrast the g-CDs appeared unable to completely reduce the hemes at the concentration used here. It is likely that a steady state population of reduced heme was reached where heme reduction by CDs was in competition with oxidation by RR120. The presence of nitrogen atoms in g-N-CDs has been proposed to lead to rapid hole quenching in the graphitic core of the CD allowing for longer-lived CSSs compared to the all-carbon analogues.[255]

Based on these results, g-N-CDs were selected for further experimentation. The goal of the following sections was to identify parameters that affect the rate of electron production and transfer through MtrCAB to RR120. Knowing what can be changed to increase or decrease the electron production rate is important for designing experiments with encapsulated enzymes. The parameters of EDTA concentration, g-N-CD concentration, and light intensity were explored. The parameters used in the experiments shown in Fig. 6.3.2 (10 μg/mL g-N-CDs, 25 mM EDTA, 2.5 kW m^{-2} light intensity) were selected as the “core” conditions and each parameter was varied individually from there.

6.3.2 - Identifying parameters that affect light-driven transmembrane electron transfer through RuMe-MtrCAB

Photoreduction of RR120 in RuMe-MtrCAB:PLE-[RR120] using 10 μg/mL g-N-CDs at light intensity of 2.5 kW m^{-2} was investigated using EDTA concentrations from 0 to 50 mM (Fig. 6.3.3) and it was observed that 25 mM EDTA provided the maximum rate of RR120 reduction. Using 50 mM EDTA appeared not to provide any further increase in the rate of reduction of RR120. The effect of changing g-N-CD concentrations from 0 to 50 μg/mL while keeping [EDTA] fixed at 25 mM was explored and the results are presented in Figure 6.3.4.

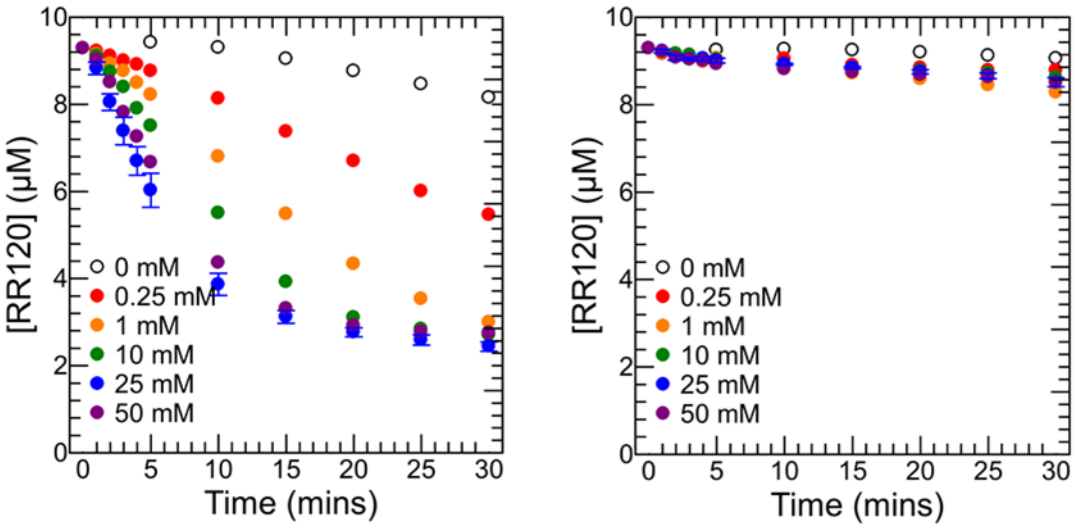

Figure 6.3.3 [EDTA] dependence of RR120 photoreduction in RuMe-MtrCAB:PLE-[RR120] (Left) and PLE-[RR120] (Right) using 10 μg/mL g-N-CDs in TK Buffer. For 25 mM EDTA data are the average of n=3 normalised data sets and error bars show standard deviation. For other concentrations n=1.

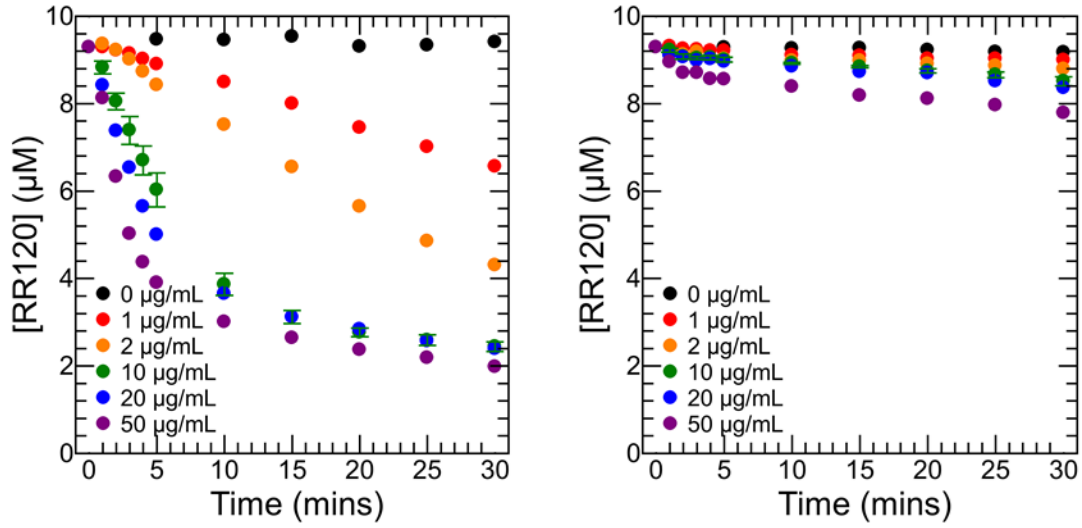

Figure 6.3.4 [g-N-CD] dependence of RR120 photoreduction in RuMe-MtrCAB:PLE-[RR120] (Left) and PLE-[RR120] (Right) using 25 mM EDTA in TK Buffer. For 10 μg/mL g-N-CD data are the average of n=3 normalised data sets and error bars show standard deviation. For other concentrations n=1.

It is clear from this data that RR120 photoreduction in RuMe-MtrCAB:PLE-[RR120] liposomes is dependent on [g-N-CD]. In fact, the timecourses obtained at 25 and 50 μg/mL g-N-CDs suggest faster dye reduction than when DT was used as an electron donor (Fig. 6.2.4); however, at these concentrations of g-N-CDs a significant level of dye reduction was observed in PLE-[RR120] liposomes suggesting some limited ability for the carbon dots to directly reduce encapsulated dye. This may be due to slight perturbation of the membranes leading to low levels of dye leakage.

The data presented in Figure 6.3.4[g] were fitted to single exponential decay functions[h] (Fig. 6.3.5) to try to gain a picture of the kinetic regime in play here. The values of *k* were plotted against [g-N-CD]; fitting of this plot to the Michaelis-Menten equation gave a k_{max} of $8 \times 10^{-3} \pm 3 \times 10^{-4}$ s^{-1} and a K_m of 27 ± 2.4 µg/mL. These results demonstrate that increasing the g-N-CD concentration is an effective way to increase the rate of electron production. If the Michaelis-Menten fitting is an appropriate model for this process, then the "core conditions" (10 µg/mL g-N-CDs) are reaching only ≈25% of the theoretical maximum rate.

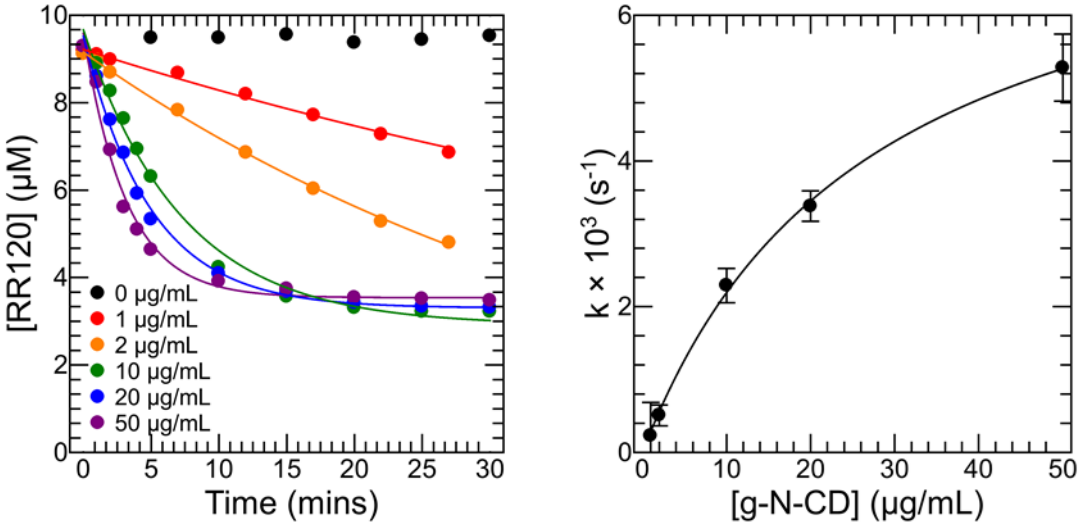

Figure 6.3.5 [g-N-CD] dependence of RR120 photoreduction with 25 mM EDTA in TK Buffer. Left) Timecourses of RR120 photoreduction at indicated [g-N-CD] after subtraction of non-specific reduction and normalisation at t=0. Monoexponential fits shown as lines. For 10 µg/mL g-N-CD data are the average of n=3 normalised data sets and error bars show standard deviation, for other concentrations n=1. Right) RR120 photoreduction rate vs [g-N-CD] with fitting to the Michaelis-Menten equation, error bars represent errors from monoexponential fitting.

Light intensity was modified by reducing the output of light source from the maximum at 2.5 kW m^{-2} to 1.6 and 0.6 kW m^{-2}. The rate of RR120 reduction decreased with light intensity (Fig. 6.3.6) indicating that the system was externally limited. Rates of RR120 reduction at lower light intensity could be enhanced somewhat by using greater concentrations of g-N-CDs and EDTA.

---

[g] Change in [RR120] for PLE-[RR120] under same conditions were subtracted from data for RuMe-MtrCAB:PLE-[RR120] before fitting. For 1 and 2 µg/mL g-N-CD t=3 mins was considered to be the start point to account for the lag observed with these concentrations.

[h] $y=Ae^{-kt}+y_0$ where A = overall change in RR120 concentration, k = rate constant, y_0 = remaining concentration of RR120 at t=∞.

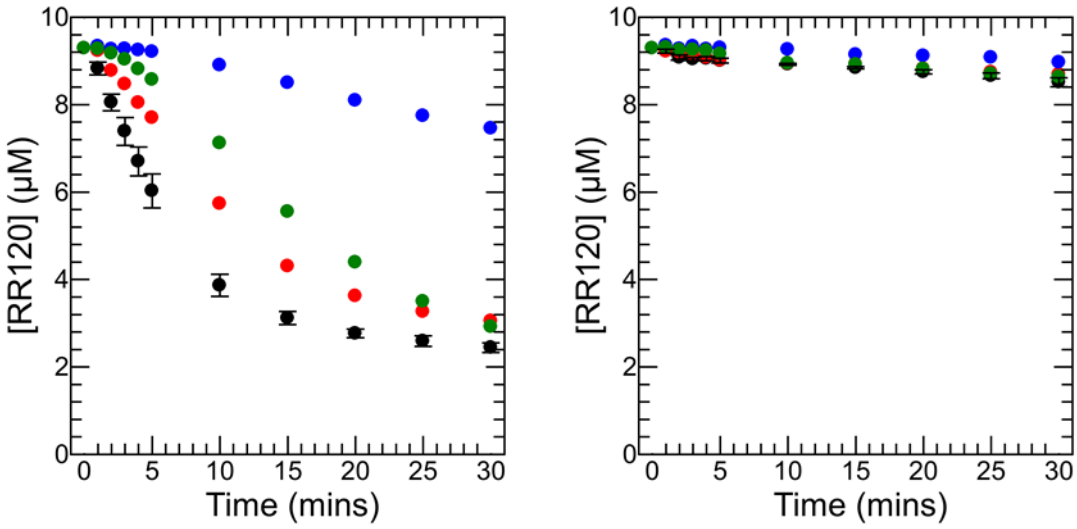

Figure 6.3.6 Light intensity dependence of RR120 photoreduction in RuMe-MtrCAB:PLE-[RR120] (Left) and PLE-[RR120] (Right) using either 10 μg/mL g-N-CDs and 25 mM EDTA at light intensity of 2.5 (Black), 1.6 (Red) or 0.6 (Blue) kW m^{-2} or 50 μg/mL g-N-CDs and 50 mM EDTA (Green) in anaerobic TK Buffer. For maximum light intensity data are the average of n=3 normalised data sets and error bars show standard deviation. For other light intensities n=1.

These results suggest that further increases in light intensity would lead to even greater rates of RR120 reduction. The intensity of the light source at maximum power is, however, approximately 20 times higher than the average intensity of sunlight in Southern UK.[256]

6.3.3 - Conclusions on CD driven transmembrane electron transfer through MtrCAB

As demonstrated in the preceding sections, g-N-CDs are effective photosensitisers for driving transmembrane electron transfer through MtrCAB. [g-N-CD], [EDTA] and light intensity can all be used as handles for controlling the rate of electron production and, in turn, the rate of transmembrane electron transfer. The present results suggest the system is limited both on the external face of liposome (generation of electrons by CDs and transfer to RuMe-MtrCAB) and on the internal face (reduction of RR120 by RuMe-MtrCAB). A more detailed consideration of these aspects, however, was beyond the scope of this study. The results presented here serve to inform the conditions used to explore proof-of-principle nanoreactors as described in the next section.

Whilst the RuMe-MtrCAB complex was used for the experiments in Section 6.3, the RuMe photosensitiser is not expected to contribute to the observed photoreduction of RR120 to any significant level. The Krüss light source used for photoreduction with CDs

does not emit strongly at 450 nm where the RuMe absorbs (Fig. 2.5.1). A control experiment where the liposomes were irradiated with white light in the absence of g-N-CDs showed no evidence of dye reduction over 30 mins.

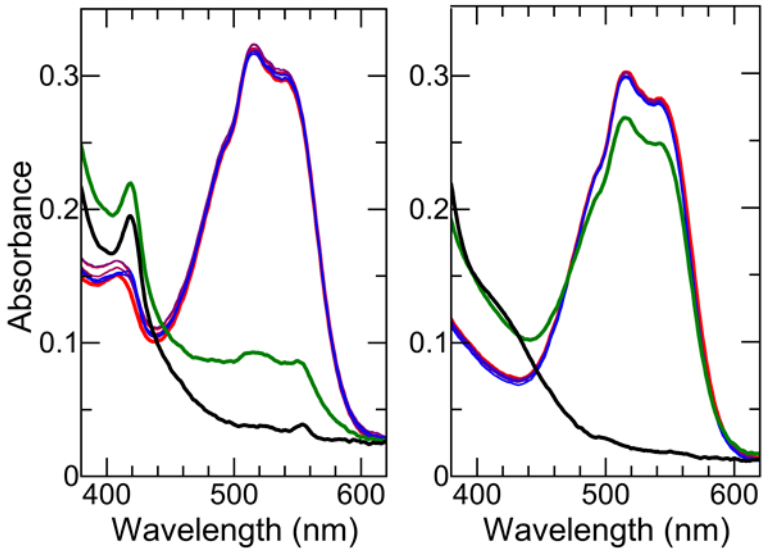

Figure 6.3.7 Spectra obtained during white-light irradiation of RuMe-MtrCAB:PLE-RR120] (Left) or PLE-[RR120] (Right) in absence of g-N-CD. Initial liposomes (Red), over 30 mins irradiation (Red-to-Blue), after addition of DT (Green) and after subsequent addition of TX100 to 0.2% (v/v) (Black). Samples in 50 mM Tris:HCl, 10 mM KCl, 25 mM EDTA, pH 8.5 buffer.

6.4 - Transmembrane electron transfer to an encapsulated redox enzyme

In the previous section it was established that transmembrane electron transfer through RuMe-MtrCAB can be accomplished either chemically, using DT, or photochemically, using g-N-CDs. In this section, the coupling of such transmembrane electron transfer to enzyme catalysis to create nanoreactors is explored. Liposomes were formed containing the redox enzyme NosZ from *Paracoccus denitrificans* which has been explored in Chapter 5. Both N_2O, the substrate, and N_2, the product, are gases, making them membrane permeable and ideal for these liposome studies. The aim is, therefore, to use DT or g-N-CDs to drive transmembrane electron transfer via RuMe-MtrCAB to encapsulated NosZ and reduce N_2O.

In Chapter 5 it was identified that Paz, while able to support catalysis as a redox shuttle, is not able to activate the Cu_Z* site of NosZ leading to rapid enzyme deactivation in the presence of N_2O. Sustained *in vitro* NosZ activity is entirely dependent on the presence of $MV^{\bullet+}$ which can both activate the enzyme and support catalysis. It was decided, therefore, that some quantity of $MV^{\bullet+}$ must be included in the preparation of the

liposomes. DT was also present throughout much of the procedure as a means of maintaining anaerobicity when the solutions had to be removed from the anaerobic chamber for centrifugation.

6.4.1 - Preparation of RuMe-MtrCAB:PLE-[NosZ] liposomes

As discussed in Section 5.4, the Biobead-mediated detergent sequestration method (see Section 2.7.2.2) for liposome formation was found to be incompatible with the presence of $MV^{\bullet+}$. Liposomes (Fig. 6.4.1) were therefore prepared by the dilution method as described in Section 2.7.2.1. Briefly: 20 mg aliquots of PLE were suspended in anaerobic TK Buffer and solublised by addition of OG; either RuMe-MtrCAB (2.5 nMol) in PNL Buffer or an equivalent volume of PNL buffer were then added; the sample was reduced with an excess of DT and MV was added to a concentration of 150 μM. Finally, preactivated NosZ (6 nMol) was added (Fig. 6.4.2 - Left). To trigger liposome formation, these solutions were then gradually diluted to 50 mL in TK buffer containing 100 μM $MV^{\bullet+}$ and an excess of DT.

The liposomes were washed by centrifugation twice and finally resuspended in 1 mL of TK Buffer containing 0.5 mM DT. Spectra of liposome suspensions at 0.3 μM are shown in Figure 6.4.2 - Right. From these spectra it is clear that little, if any, of the $MV^{\bullet+}$ added during the preparation stages was retained. $MV^{\bullet+}$ is known to be membrane permeable and is used for redox enzyme assays on whole cells.[128,242–244] It is therefore, perhaps, unsurprising that the washing steps removed the $MV^{\bullet+}$ from the liposomes.

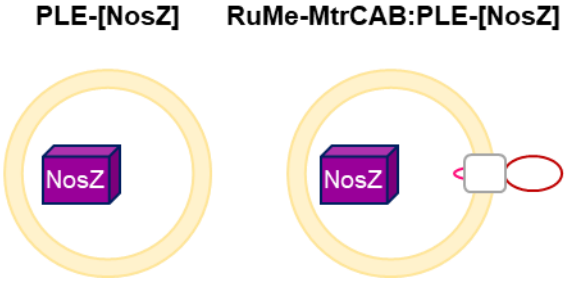

Figure 6.4.1 Schematics and nomenclature of liposomes under consideration in Section 6.4. For simplicity the RuMe photosensitiser is not shown and protein orientation is assumed.

DLS showed that the sizes of the liposomes are distributed around 100 nm (Fig. 4.6.3B), similar to those described in Section 6.2 & 6.3. The concentration of liposomes in the stock suspensions were, as previously, estimated at 0.3 μM. Aliquots of the liposomes were allowed to oxidise in air and were diluted to 7.5 nM in TK Buffer. Spectra of these solutions (Fig. 6.4.3A) were used to quantify the RuMe-MtrCAB concentration in the liposome stock suspension of RuMe-MtrCAB:PLE-[NosZ] as 1.3 μM. This suggests that around 50% of the RuMe-MtrCAB added during preparation was successfully

incorporated and that each liposome contained an average of ≈4 RuMe-MtrCAB. SDS-PAGE analysis (Fig. 6.4.3C) also indicated the presence of the RuMe-MtrCAB proteins and NosZ in appropriate liposomes, though bands for NosZ did not stain strongly.

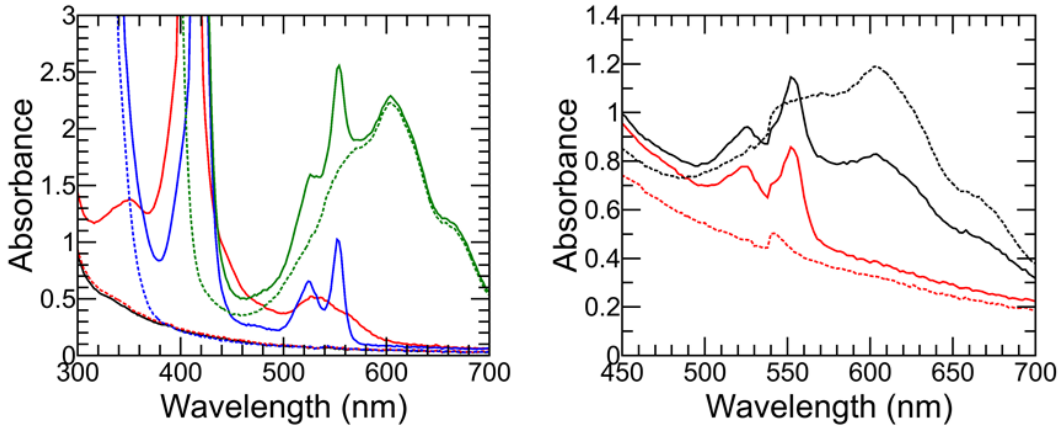

Figure 6.4.2 Spectra obtained during preparation of RuMe-MtrCAB:PLE-[NosZ] (Solid lines) and PLE-[NosZ] liposomes (Dashed lines). **Left)** Solublised lipid (Black), after addition of RuMe-MtrCAB or PNL buffer (Red), after addition of DT (Blue) and after addition of MV and NosZ (Green); **Right)** Spectra of liposomes after first (Black) and second (Red) spin-wash and resuspension in 1 mL TK Buffer.

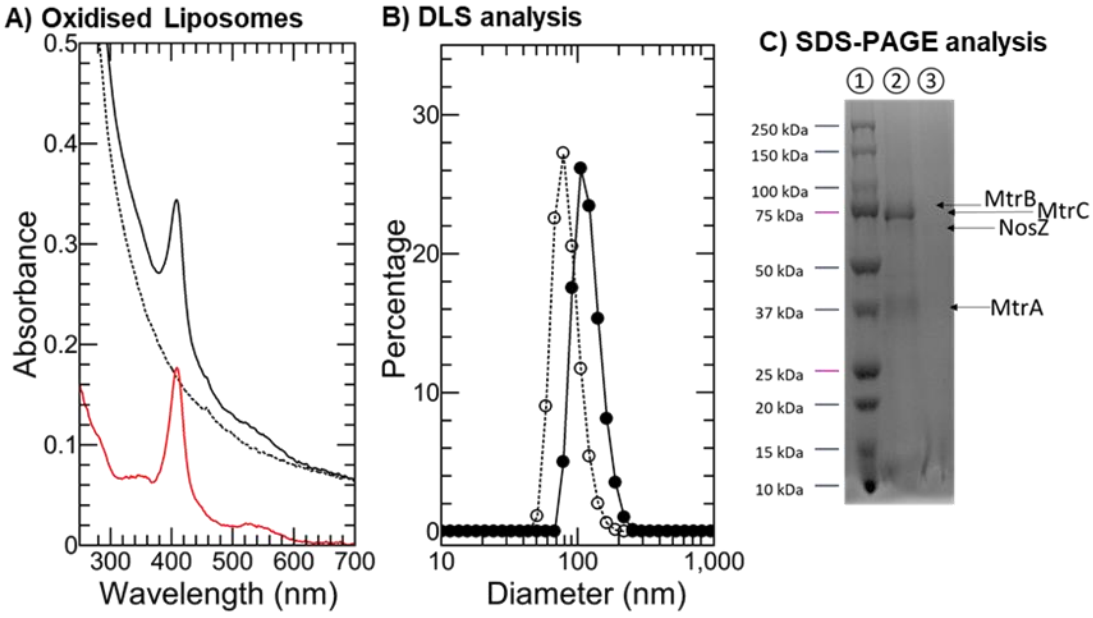

Figure 6.4.3 A) Spectra of oxidised RuMe-MtrCAB:PLE-[NosZ] (Solid) and PLE-[NosZ] (Dashed) liposomes allowed to oxidise in air and diluted to 7.5 nM in TK buffer, difference spectrum shown in red; **B)** size distribution of RuMe-MtrCAB:PLE-[NosZ] (Filled/solid) and PLE-[NosZ] (Dashed/hollow) liposomes from DLS analysis; **C)** SDS-PAGE analysis with Coomassie stain: ① - Precision Plus Dual Colour, ② - RuMe-MtrCAB:PLE-[NosZ], ③ - PLE-[NosZ].

To quantify the NosZ concentration in the liposomes, MV assays were carried out (see Section 2.4.1) with TX100 added to lyse the liposomes. Liposomes were diluted from the stock suspension to 3 nM in anaerobic TKTx Buffer + ≈60 μM $MV^{\bullet+}$. After 5 mins, to allow all liposomes to lyse, N_2O was added to ≈750 μM and the decrease at $A_{600\ nm}$ was used

to quantify activity. Examples of these assays are shown in Figure 6.4.4, both types of liposome have similar activity. By assuming the NosZ was fully activated (TOF = 160 s^{-1}), these assays were used to calculate the minimum concentration of NosZ in the assay to be around 1 nM (Table 6.4.1). Based on this, the NosZ concentration in the liposome stock suspensions was determined to be ≈0.1 μM (Table 6.4.2).

The total internal volume of the liposomes is estimated at 73 μL (see Section 2.7.4), meaning the NosZ concentration inside the liposomes is around 1.4 μM. Also shown in Figure 6.4.4 are the same assays run after storing the liposomes overnight at room temperature under anaerobic conditions. A small decrease in activity was observed, as evidenced by slightly slower loss of $A_{600\ nm}$; This may be due to enzyme deactivation or general protein degradation. All experiments on intact liposomes described below were carried out on Day 1.

Table 6.4.1 Determination of [NosZ] in liposomes using results from MV assays and a TOF of 160 s^{-1}. Results are the average of n=3 replicates and errors represent standard deviation.

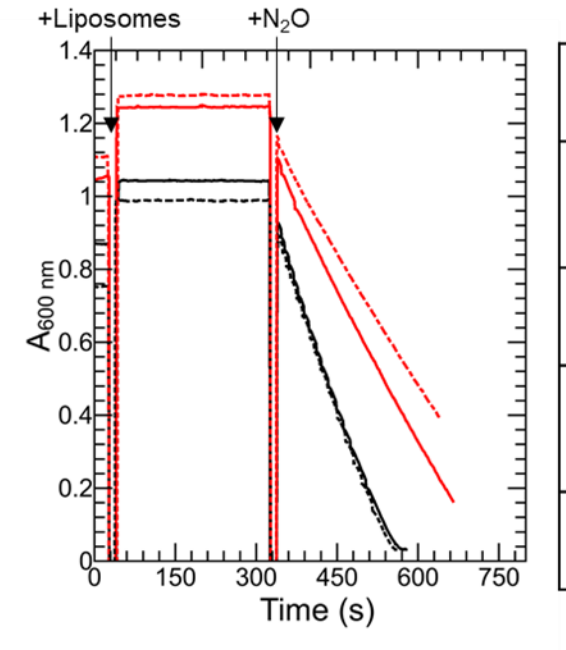

	$\Delta A_{600\ nm}$ × 10^3 s^{-1}	pMol N_2O s^{-1}	[NosZ] (nM)
RuMe-MtrCAB:PLE-[NosZ] Day 0	4.9 ± 0.3	180 ± 12	1.1 ± 0.08
PLE-[NosZ] Day 0	4.4 ± 0.2	160 ± 16	1 ± 0.04
RuMe-MtrCAB:PLE-[NosZ] Day 1	3.4 ± 0.1	125 ± 4	-
PLE-[NosZ] Day 1	2.0 ± 0.6	76 ± 22	-

Figure 6.4.4 MV assays of lysed RuMe-MtrCAB:PLE-[NosZ] (Solid) and PLE-[NosZ] (Dashed) liposomes on day of preparation (Day 0 - Black) and after 16 hours (Day 1 - Red), assays carried out in TKTx buffer.

Table 6.4.2 Protein concentrations in liposome stock suspensions

Liposomes	[RuMe-MtrCAB] (μM)	Encapsulation efficiency	[NosZ] (μM)	Encapsulation efficiency
RuMe-MtrCAB:PLE-[NosZ]	1.3	52%	0.11	2%
PLE-[NosZ]	-	-	0.1	2%

6.4.2 - Chemically driven transmembrane electron transfer to an encapsulated redox enzyme

To establish whether transmembrane electron transfer through RuMe-MtrCAB to NosZ would be possible, DT was used as a reductant. An equilibrated solution of N_2O was prepared containing 4 mL of anaerobic TK Buffer and 1 mL of headspace ($[N_2O]_{sol}$ = 240 µM, $[N_2O]_{HS}$ = 400 µM, total N_2O = 1.4 µMol) and to this was added DT to 200 µM and RuMe-MtrCAB:PLE-[NosZ] liposomes to 4 nM. The progress of the reaction was followed by monitoring the absorbance of DT at 315 nm, however unfortunately in this case DT oxidation was not detected over 20 mins. This reason for this is most likely that there was insufficient MV remaining inside the liposomes to allow for any turnover of N_2O and therefore oxidation of DT was not observed.

To remedy this, the decision was made to supplement the reaction with $MV^{\bullet+}$ in the hope that it would cross the lipid bilayer and initiate N_2O activity. Experiments were set up as previously, but with the addition of 10 µM $MV^{\bullet+}$ before the liposomes were added. Addition of liposomes to 7.5 nM caused the DT to immediately begin oxidising (decrease in $A_{315\ nm}$ - Fig. 6.4.5C) while the $MV^{\bullet+}$ remained mostly reduced (minimal change in $A_{397\ nm}$ - Fig. 6.4.5D). Upon complete oxidation of the DT the $MV^{\bullet+}$ was also oxidised back to the colourless MV^{2+} (decrease in $A_{397\ nm}$). The hemes of RuMe-MtrCAB appeared to remain reduced throughout the experiment (Soret band at 420 nm). GC measurements confirmed the loss of some N_2O from the headspace (Fig. 6.4.5E). In contrast, PLE-[NosZ] liposomes in a parallel experiment showed minimal oxidation of DT (Fig. 6.4.5C), rapid oxidation of the majority of the $MV^{\bullet+}$ present in the solution (Fig. 6.4.5D) and no overall loss of N_2O from the headspace (Fig. 6.4.5E).

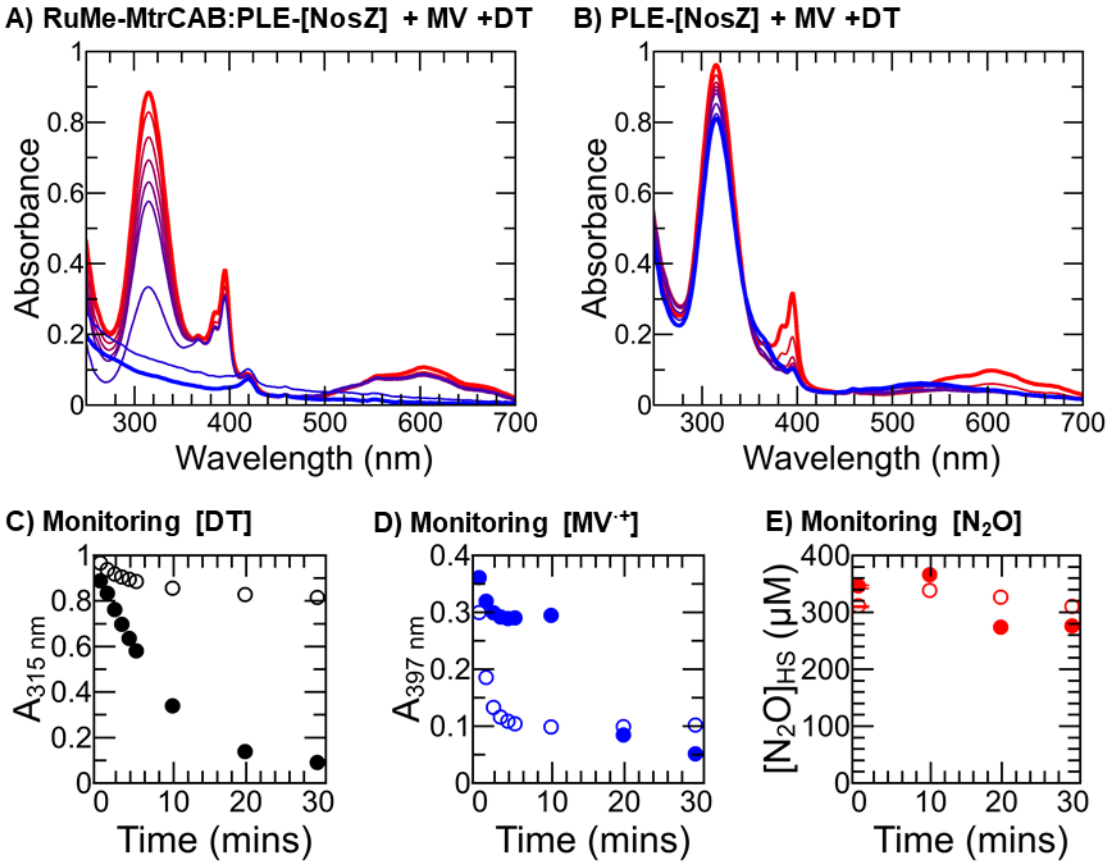

Figure 6.4.5 DT-driven reduction of N_2O by encapsulated NosZ. **A+B)** spectra of RuMe-MtrCAB:PLE-[NosZ] (A) or PLE-[NosZ] (B) liposomes diluted 40X into TK Buffer containing 10 μM $MV^{\bullet+}$ + 100 μM DT + ≈200 μM N_2O (Red) and monitored over 30 mins (Red to Blue); **C-E)** Timecourses of $A_{315\ nm}$ (for monitoring [DT]), $A_{397\ nm}$ (for monitoring [$MV^{\bullet+}$]), and Headspace (HS) [N_2O] measured by GC, for RuMe-MtrCAB:PLE-[NosZ] (Filled) and PLE-[NosZ] (Hollow).

When taken together, the data presented in Figure 6.4.5 are consistent with a role for RuMe-MtrCAB in delivering electrons from external DT to support N2O reduction by internal NosZ. Given that for RuMe-MtrCAB:PLE-[NosZ] liposomes the $MV^{\bullet+}$ and hemes remained mostly reduced while DT was present (Figs. 6.4.5C&D) it can be assumed that the rate limiting step in this system is at the NosZ end. Based on estimated concentrations of RuMe-MtrCAB and NosZ in these liposomes we can use the DT oxidation rate to calculate rates of electron transfer through RuMe-MtrCAB and the TOF of NosZ.

$$\text{DT oxidation rate} = \frac{\frac{dA_{315\ nm}}{dt}}{\varepsilon_{315\ nm}} \times \text{assay volume} = 520\ \text{pMol}\ s^{-1}$$

$$\text{Rate of transmembrane electron transfer} = \frac{\text{DT oxidation rate} \times 2}{\text{Mol of RuMe-MtrCAB}} = \frac{1.04\ \text{nMol}\ s^{-1}}{132\ \text{pMol}} \approx 8\ s^{-1}$$

$$\text{NosZ TOF} = \frac{\text{DT oxidation rate}}{\text{Mol of NosZ}} = \frac{520\ \text{pMol}\ s^{-1}}{10\ \text{pMol}} = 52\ s^{-1}$$

The TOF for NosZ determined in this way is significantly lower than for fully activated NosZ (TOF = 160 s^{-1}). Mass transport of the gases through the liposome membrane may be causing this limitation. N_2O, like other small gases, is membrane permeable but it is possible that it is unable to cross the membrane fast enough to allow NosZ to operate at its V_{max}. It is also possible that the activity of NosZ has simply decreased over time due to protein degradation or alteration of the active site.

Another interesting observation is that with PLE-[NosZ] liposomes, after bleaching of the blue colour from $MV^{\bullet+}$ the solution gradually turned purple and absorbance bands around 362 nm, 530 nm and >750 nm were seen to grow in (Fig. 6.4.5B). These bands are characteristic of $MV^{\bullet+}$ dimers, also known as pimers due to their π-interactions, which can form when MV•+ is present in high local concentrations; K_d values ranging from 125 μM to 2.6 mM have been reported.[257–260]

Control experiments were carried out where the liposomes were exposed to DT and $MV^{\bullet+}$ without any N_2O present (Fig. 6.4.6). In both experiments a slow oxidation of DT was observed while the $MV^{\bullet+}$ concentration remained constant. Addition of N_2O initiated rapid DT oxidation (Fig. 6.4.6C) with RuMe-MtrCAB:PLE-[NosZ] liposomes whereas the DT continued to oxidise at around the same slow rate with PLE-[NosZ] liposomes but the $MV^{\bullet+}$ was completely oxidised in just 2-3 minutes (Fig. 6.4.6D). The N_2O concentrations were not allowed to come to equilibrium meaning they could not be accurately followed by GC.

Schematics illustrating proposed mechanisms for the experiments of Figure 6.4.5&6 are shown in Figure 6.4.7. At the outset of the experiment all of the MV present was in the singly reduced $MV^{\bullet+}$ redox state and was able to diffuse with relative ease into the liposomal interior. Once NosZ began reducing N_2O the $MV^{\bullet+}$ was oxidised to MV^{2+} which is far less membrane permeable due to its higher charge and therefore became trapped in the liposome interior. The presence of RuMe-MtrCAB allowed for the coupling of extraliposomal oxidation of DT to internal reduction of the trapped MV^{2+} back to $MV^{\bullet+}$ such that it could go on to support further activity by NosZ. In the absence of RuMe-MtrCAB, extraliposomal $MV^{\bullet+}$ also diffused into the liposomes and was oxidised to MV^{2+} by NosZ. However, in this case the encapsulated MV^{2+} has no means to be reduced back to $MV^{\bullet+}$. Within 5 mins, all of the $MV^{\bullet+}$ became encapsulated and, thus, isolated from the extraliposomal DT.

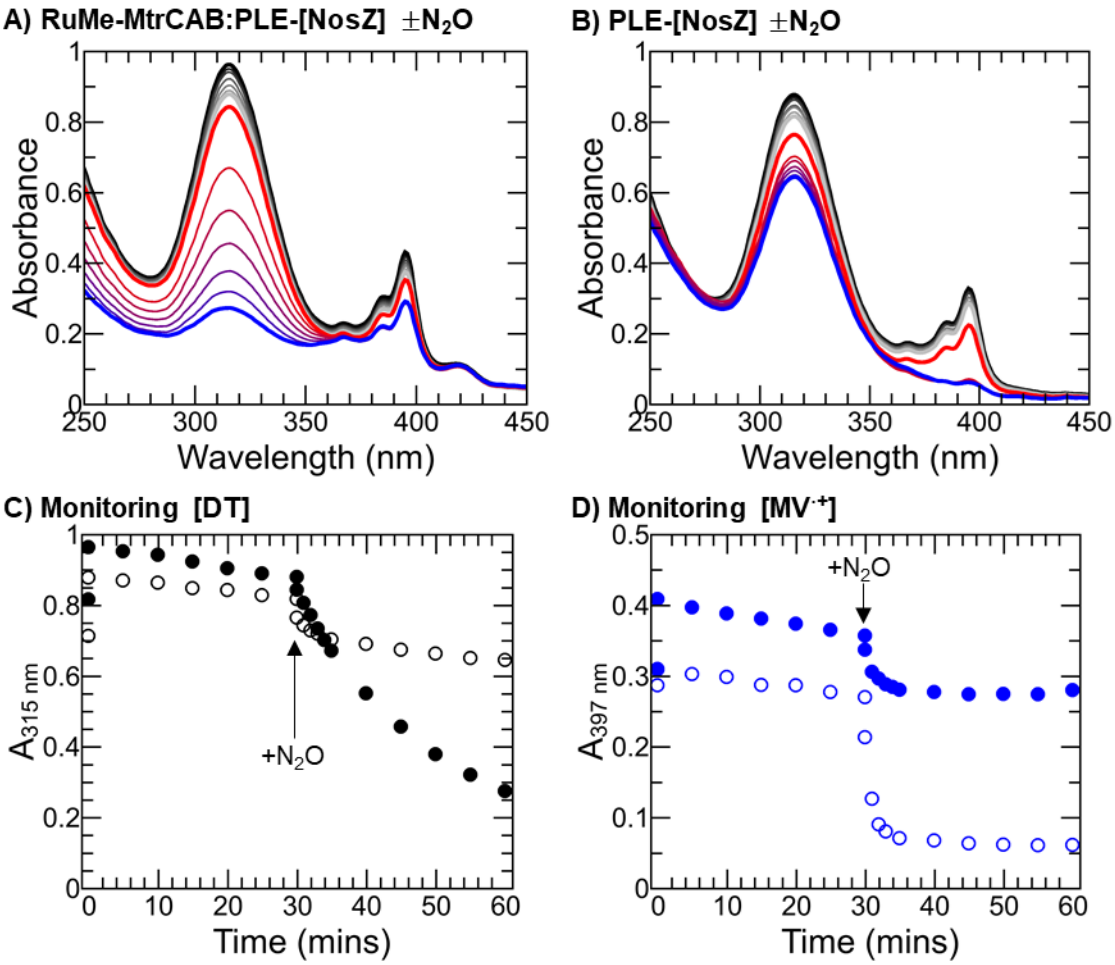

Figure 6.4.6 A-B) Spectra of RuMe-MtrCAB:PLE-[NosZ] (Left) or PLE-[NosZ] (right) liposomes diluted to 7.5 nM in anaerobic TK buffer + 10 μM $MV^{\bullet+}$ + 100 μM DT (Black) and over the subsequent 30 mins (Black to grey). To these were then added N_2O and spectra were monitored over a further 30 mins (Red to Blue); **C+D)** Timecourses of $A_{315\ nm}$ (for monitoring [DT]) (C) and $A_{397\ nm}$ (for monitoring [$MV^{\bullet+}$]) (D) for RuMe-MtrCAB:PLE-[NosZ] (Filled) and PLE-[NosZ] (Hollow), Liposomes were added to $MV^{\bullet+}$ and DT at t=0, arrows indicate addition of N_2O at t=30 mins.

The appearance of $MV^{\bullet+}$ dimers after prolonged exposure of PLE-[NosZ] liposomes to MV, DT and N_2O is indicative of a concentrating effect. The internal liposome volume in these experiments is likely only ≈3 μL of the total 4 mL reaction solution (see Section 2.7.4). The 10 μM MV added at the outset of the reaction could potentially be concentrated up to 13 mM if it were all trapped in the liposomes; this is above all reported K_d values for dimerization.[257–260] It was found in Section 6.2 that these lipid bilayers are not completely impermeable to DT so some low levels of MV^{2+} reduction would be expected even in the absence of an MtrCAB conduit. Whilst the global concentration of $MV^{\bullet+}$ may be low, the local concentration inside the liposomes is likely enough to initiate dimerization. It is also possible that the lipid membrane has some effect on stabilising the dimer.

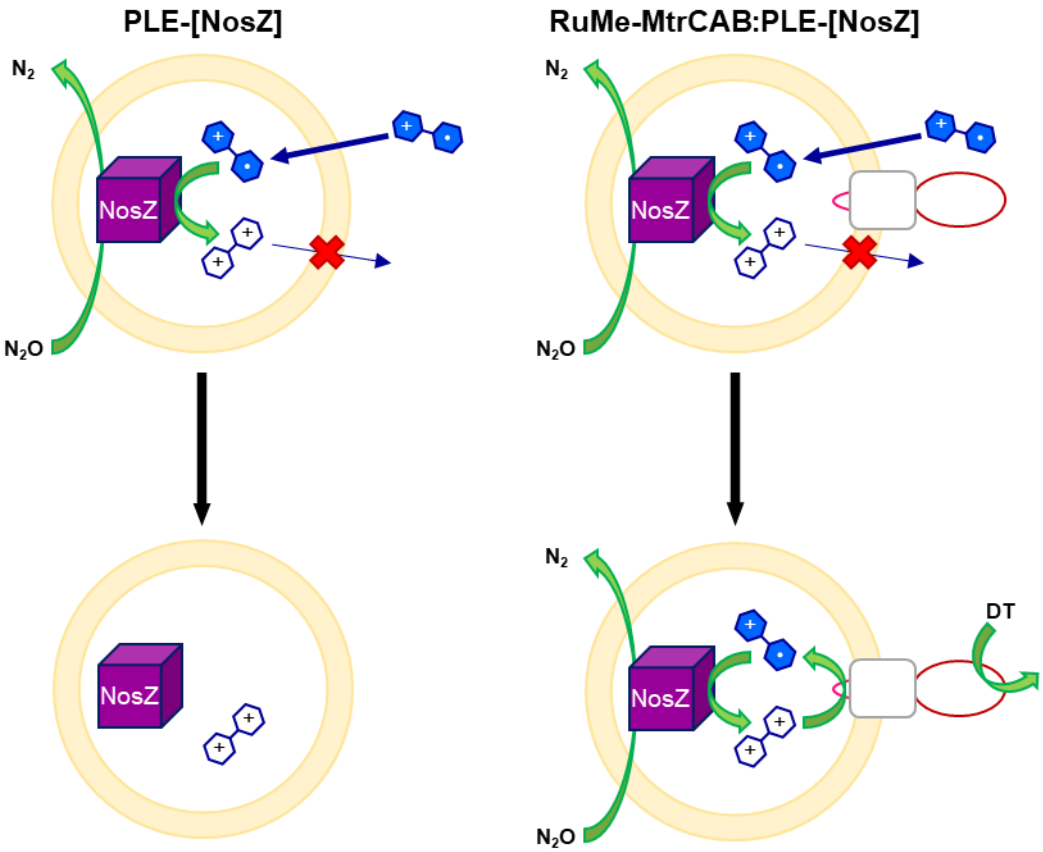

Figure 6.4.7 Proposed mechanisms that explain results obtained by addition of DT, MV and N_2O to PLE-[NosZ] (Left) or RuMe-MtrCAB:PLE-[NosZ] (Right). MV shown as blue hexagons either in oxidised (Hollow) or reduced (Filled) state with charges shown. In the top panels, MV has been reduced by DT though this is not shown. For simplicity, RuMe-MtrCAB is shown in only one orientation and the RuMe- label is omitted.

While the mechanisms presented require closer investigation for confirmation, the stark difference between PLE-[NosZ] and RuMe-MtrCAB:PLE-[NosZ] is undeniable. The RuMe-MtrCAB complex enables the coupling of external reductants to encapsulated MV which can support redox catalysis by NosZ. The following section builds on these results to use irradiated g-N-CDs, in place of DT, as the source of electrons.

6.4.3 - Light-driven transmembrane electron transfer to an encapsulated redox enzyme

The experiments discussed in the previous section provided evidence that RuMe-MtrCAB can be used to transfer electrons across a liposome membrane at a rate sufficient to support enzymatic redox catalysis. Here the electrons will be supplied photochemically to create a biohybrid nanoreactor as described in Section 1.6. Given the results of Section 6.2.3 the decision was made not to attempt to drive transmembrane electron transfer to NosZ using the inherent RuMe photosensitiser. The low electron production rate of this system would not be able to keep up with the activity of NosZ and, this would likely cause the enzyme to rapidly deactivate (see Fig. 5.1.2). g-N-CDs showed great promise as photosensitisers in Section 6.3 and were chosen to drive transmembrane electron transfer here.

Experiments were set up similarly to those above; a sealed and equilibrated solution of N_2O in TK Buffer + 10 μM MV^{2+} was prepared and the headspace N_2O concentration was measured by GC. To this were added g-N-CDs to 12.5 μg/mL and EDTA to 25 mM. Liposomes were then added to 7.5 nM, and the solution was irradiated by the Krüss cold light source at an intensity of 2.5 kW m^{-2}. Spectra and headspace GC measurements were then obtained over 30 minutes to monitor concentrations of $MV^{\bullet+}$ and N_2O. The results are presented in Figure 6.4.8.

In both experiments the increase of $A_{397\ nm}$ at t=0 (Fig. 6.4.8C) is due to an initial spike of $MV^{\bullet+}$ generated by the DT present in the liposome stock suspension. This $MV^{\bullet+}$ was rapidly oxidised in both liposomes as evidenced by the drop in $A_{397\ nm}$. For PLE-[NosZ] liposomes the spectra then remained constant, neither reduction of MV^{2+} nor formation of $MV^{\bullet+}$ dimers were observed. For RuMe-MtrCAB:PLE-[NosZ] liposomes, however, $MV^{\bullet+}$ began to be formed after around 4 minutes and after 10 minutes the MV^{2+} had been completely reduced to $MV^{\bullet+}$. Headspace N_2O concentrations remained constant for PLE-[NosZ] liposomes whereas for RuMe-MtrCAB:PLE-[NosZ] liposomes the N_2O had been heavily depleted after 20 minutes (Fig. 6.4.8D). Is also possible that this depletion was complete in a shorter timeframe, but the headspace had not yet equilibrated and therefore the initial concentrations were still observed. These results demonstrate the formation and operation of light-driven nanoreactors similar to those described in Section 1.6.2, the only difference being the identity of the photosensitiser.

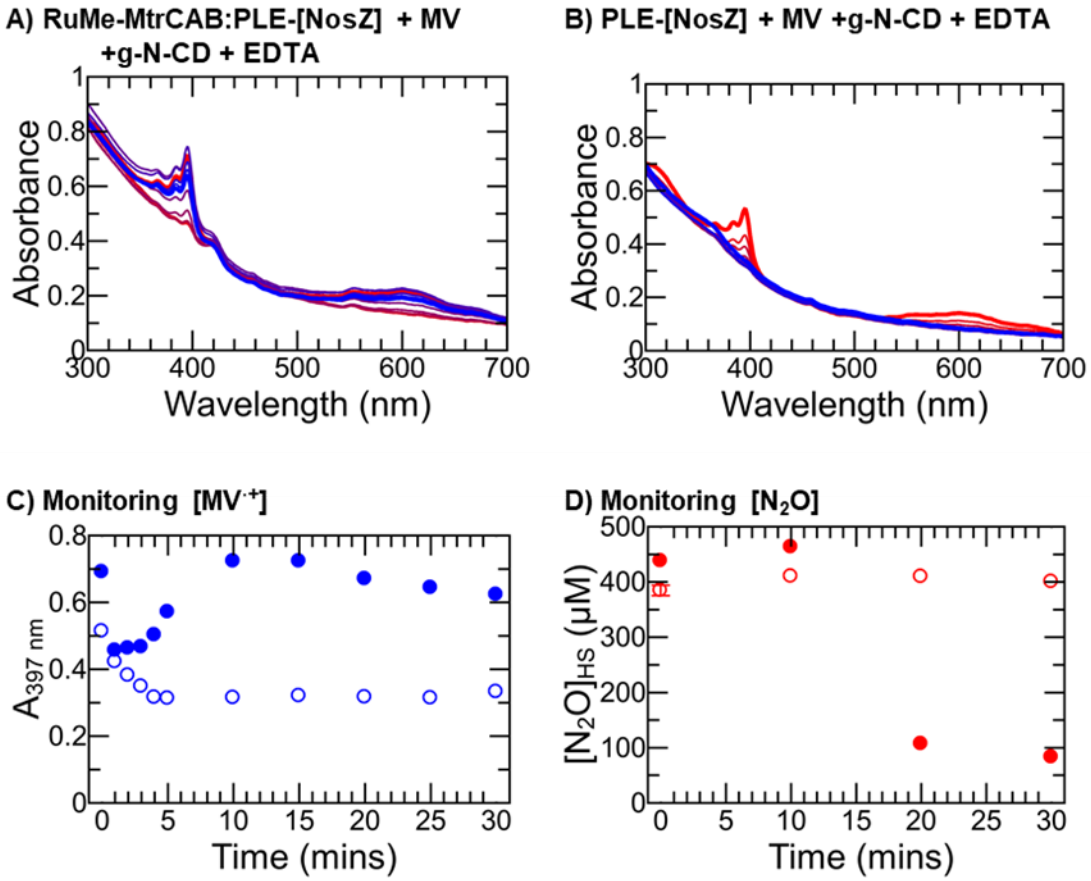

Figure 6.4.8 Light-driven reduction of N_2O by encapsulated NosZ. **A+B)** spectra of RuMe-MtrCAB:PLE-[NosZ] (A) or PLE-[NosZ] (B) liposomes diluted to 7.5 nM in anaerobic TK Buffer containing 10 μM $MV^{\bullet+}$ + 12.5 μg/mL g-N-CD + 25 mM EDTA + ≈240 μM N_2O (Red) and over 30 mins irradiation (Red to Blue); **C+D)** Timecourses of $A_{397\,nm}$ (for monitoring [$MV^{\bullet+}$] (C) and Headspace [N_2O] (D) for RuMe-MtrCAB:PLE-[NosZ] (Filled) and PLE-[NosZ] (Hollow).

The mechanisms presented in Figure 6.4.7 to explain the behaviour with DT as the electron source can be adapted to rationalise the results obtained with the g-N-CDs (Fig. 6.4.9). For PLE-[NosZ] liposomes the mechanism remains largely the same: MV^{2+} is reduced to $MV^{\bullet+}$ either by the DT from the liposome stock or by the g-N-CDs. After diffusing into the liposome interior, the $MV^{\bullet+}$ becomes oxidised and thus trapped. The liposome membranes are less "leaky" when g-N-CDs are used compared to DT, this may explain why we see no evidence of $MV^{\bullet+}$ dimers in these experiments. The same steps occur in RuMe-MtrCAB:PLE-[NosZ] liposomes however the trapped MV^{2+} can be reduced by RuMe-MtrCAB which itself is photoreduced by the g-N-CDs. This allows for sustained activity of NosZ.

The low overall $MV^{\bullet+}$ concentration from t=0 to t=3 mins indicates that light-driven transmembrane electron transfer was not able to keep up with the activity of NosZ. The K_M of NosZ for N_2O was previously determined to be 9±1.5 μM (Fig. 5.2.3 - Right),[228,241] therefore as the solution N_2O concentration dropped, particularly below 100 μM, the

enzyme would no longer have been operating at V_{max} and therefore the electron demand would also have decreased. This is likely what occurred between t=4 and t=10 mins. After this point the $MV^{\bullet+}$ likely diffused out of the liposomes where it may have been reduced further by g-N-CDs to the colourless MV^0. This would provide a rationale for why $A_{397\ nm}$ decreased after t=15 mins (Fig. 6.4.8C). Experiments with g-N-CDs and MV outside of the liposome environment confirm that g-N-CDs have the thermodynamic potential to photoreduce MV^{2+} to $MV^{\bullet+}$ and to MV^0 (Fig. 6.4.10).

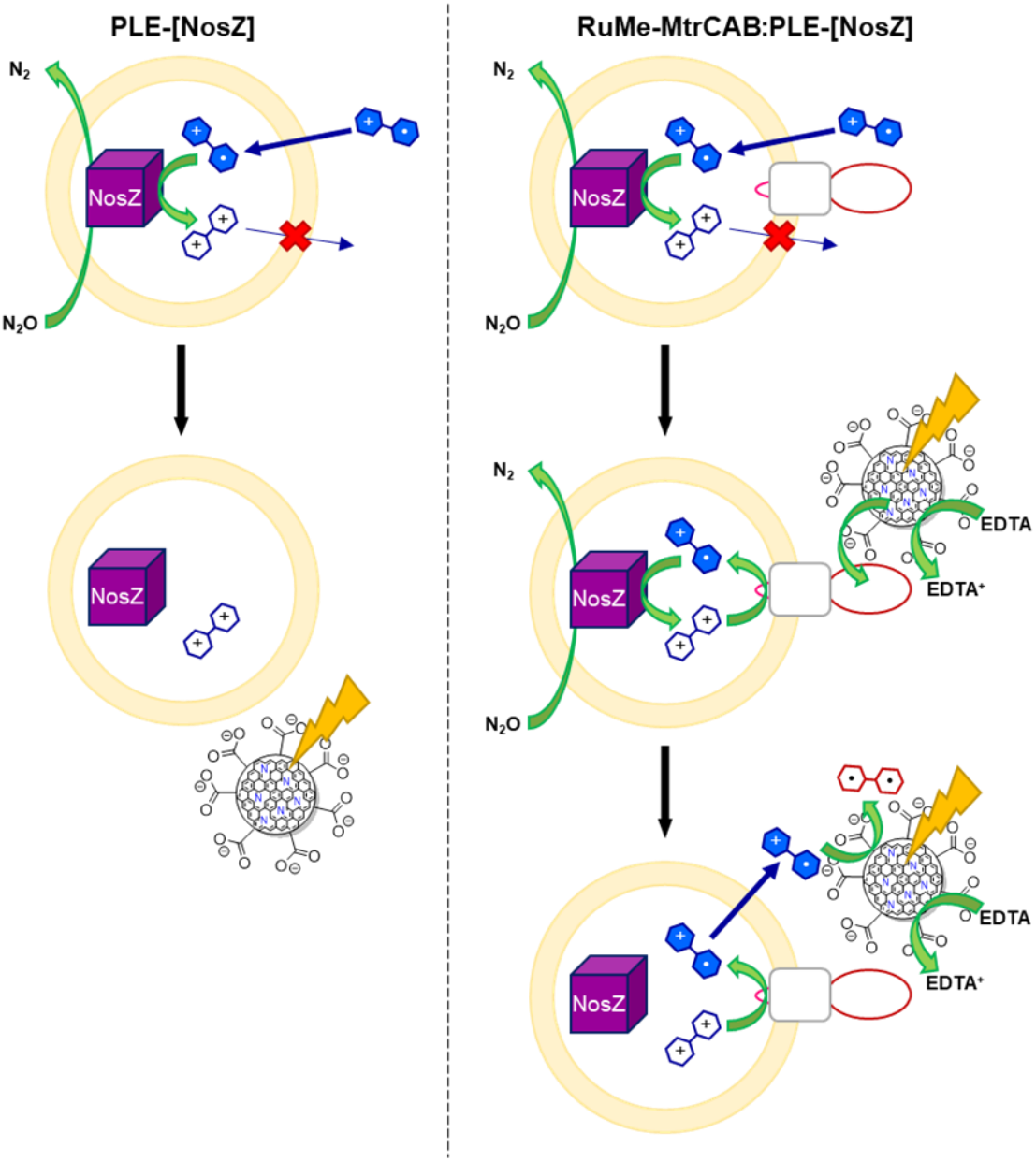

Figure 6.4.9 Proposed mechanisms to explain results observed when irradiating mixture of PLE-[NosZ] (Left) or RuMe-MtrCAB:PLE-[NosZ] (Right) liposomes, g-N-CDs, MV and EDTA. MV is shown as hexagons in either oxidised (Blue-hollow), singly reduced (Blue-filled), or doubly reduced (Red-hollow) states with charges shown. g-N-CDs are depicted as in Figure 6.3.1, and irradiation is shown as a lightning bolt. In the top panels, MV has been reduced by DT though this is not shown. For simplicity: g-N-CDs are not shown in the top panels though they are present and RuMe-label is not shown.

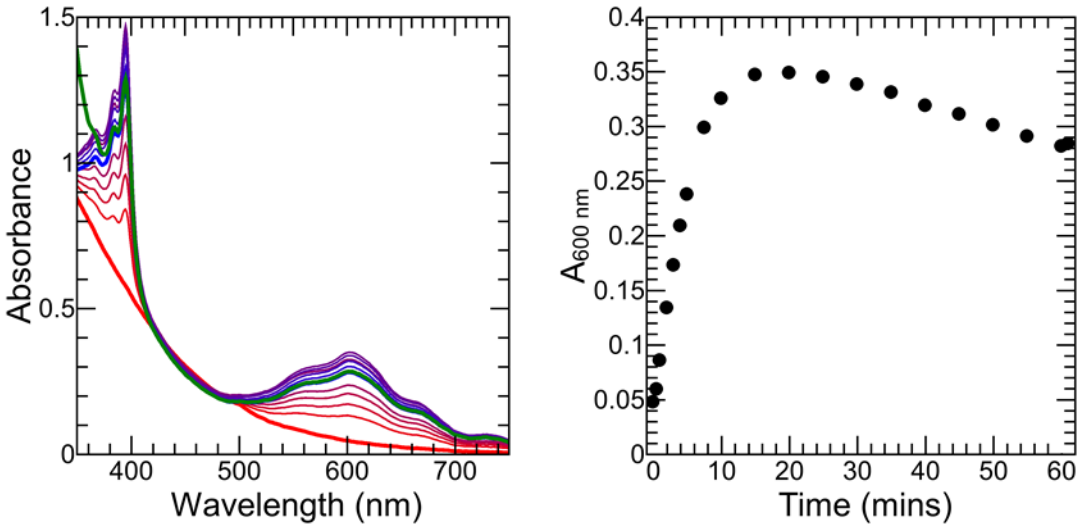

Figure 6.4.10 Photoreduction of MV by g-N-CDs. **Left)** Spectra of 50 µg/mL g-N-CDs + 25 µM MV^{2+} + 25 mM EDTA in TK Buffer (Red) and over 1h irradiation with Krüss cold light source (Red-to-Blue) and finally after addition of 100 µM DT (Green); **Right)** Timecourse following $A_{600\ nm}$ to monitor concentration of $MV^{\bullet+}$.

Given the low temporal resolution of GC measurements it is challenging to quantify the rate of N_2O reduction and, by extension, the rate of transmembrane electron transfer. Based on Figure 6.4.8D we can say that within 20 mins the headspace concentration of N_2O dropped by ≈350 µM. Assuming equilibrium conditions, this means the aqueous concentration dropped by ≈210 µM (see Section 2.4.2) meaning a total of ≈1.2 µMoles of N_2O were consumed. The reaction contained 130 pMoles of RuMe-MtrCAB allowing a flux of ≈15 electrons s^{-1} RuMe-MtrCAB^{-1} to be determined:

$$\text{Electron flux} = \frac{\text{mol } N_2O \times 2}{\text{mol RuMe-MtrCAB} \times \text{time}} = \frac{2.4\mu\text{Mol}}{130\ \text{pMol} \times 1200\ \text{s}} = 15.4\ s^{-1}$$

This represents a lower-limit estimate as it is likely this quantity of N_2O was consumed in a shorter time frame, but this could not be monitored by GC. This estimate is, however, around double the rate obtained when using DT as an electron source under similar conditions (see Section 6.4.2). The excited state of g-N-CDs is confirmed to have a more negative reduction potential than DT (≈ -660 mV vs SHE[149]) as it able to generate the doubly reduced neutral MV^0 (E^0 ≈ -760 mV vs SHE[261]) (Fig. 6.4.10) which DT is unable to form.[149] It is possible, therefore that this difference in rate is attributable to the larger driving force provided by g-N-CDs.

6.5 - General discussion

In this chapter the RuMe-MtrCAB complex has been used to support transmembrane electron transfer from chemical reductants or photosensitisers to azo dyes or enzymes. This complex was found to be almost indistinguishable from WT MtrCAB in its ability to translocate chemically derived electrons which validates MtrC+MtrAB reconstitution as a viable method for constructing modified transmembrane electron conduits. Unfortunately, the RuMe photosensitiser was unable to be used to drive productive transmembrane electron transfer. The results of Chapter 3 established that RuMe-MtrC could produce a maximum of 1 e^- min^{-1} which, when the concentration of RuMe-MtrC is in the nM range, is a very slow supply rate. This coupled with the relatively small extinction coefficients of the azo dyes used here and the requirement for 8 equivalents of electrons per equivalent of dye makes observing any change in absorbance a real challenge.

Efforts are underway to improve the photochemistry of RuMe-MtrC, which will be outlined in Chapter 7. Greater rates of electron production should allow RuMe-MtrC driven photoreduction of encapsulated redox dyes to show visible dye reduction on a reasonable time frame. Until these modifications are realised the CD based photosensitisers have been used to great success for driving transmembrane electron transfer. These results represent the first example, of which we are aware, of *in vitro* light-driven transmembrane electron transfer coupled to enzyme catalysis. The results presented provide a proof-of-principle for designing biohybrid nanoreactors, both liposomal and whole-cell (Fig. 1.6.1), however the story is by no means complete. Further studies are required, both to confirm the results observed here and to expand upon them.

Other factors that have not yet been considered are the consequences of electron flux in these liposomes. Continuous transfer of electrons across the lipid bilayer should lead to the development of an electrochemical gradient that may eventually hinder electron flux. The use of the ionophore valinomycin, which carries potassium ions to cross lipid bilayers could be used to investigate this further.

Also, the reduction of azo dyes or N_2O requires protons in addition to electrons. The continued reduction of substrates in the liposome interior may lead to a pH change that the encapsulated buffer cannot fully compensate for. Some researchers propose that MtrCAB complexes can also transfer protons across membranes[262] and the recently reported structure of MtrCAB from *Shewanella baltica* includes what may be a solvent channel that could allow for proton translocation.[134] The ionophore nigericin or a pH

sensitive dye could be used to investigate the capacity of MtrCAB to transport protons across membranes during catalysis.

Future studies will be aided by the finding that $MV^{\bullet+}$ can, and must, be added to liposomes after they are formed. This removes the requirement to include it in the liposome preparation. Future liposome preparations could therefore make use of the Biobead-mediated detergent sequestration method to form liposomes containing only NosZ without requiring large quantities of enzyme to go to waste. This alteration would greatly increase the cost-effectiveness and viability of these nanoreactors. Further experiments could also investigate:

- lowering the concentration of MV added to the liposomes as the concentration used here was likely far greater than necessary after becoming concentrated inside the liposomes,
- effect of ionophores such as valinomycin or nigericin on rates of N_2O consumption,
- using greater initial concentrations of N_2O which might allow for longer assays and thus greater resolution of N_2O consumption by GC.

In addition, other enzymes could also be studied in a similar way such as the O_2 tolerant [NiFeSe] hydrogenase from *Desulfomicrobium baculatum*.[94,95] The use of this enzyme would have some advantages: this system would produce hydrogen which, as a fuel, would have value; hydrogen production is the most common target of artificial photosynthesis allowing such systems to be more readily evaluated against the literature; hydrogen concentrations can be monitored accurately by several different methods including GC and *in situ* electrochemical detection[128]; monitoring the formation of a product is generally preferable to monitoring loss of a reactant and the theoretical amount of hydrogen that could be produced would be limited only by the availability of protons, not the amount of N_2O added to the assay.

To conclude, the results presented here demonstrate a proof-of-principle that MtrCAB can be used as a light-driven transmembrane electron conduit to supply photogenerated electrons to a redox catalyst as envisaged at the outset of this work. While preliminary and in need of further investigation, the experiments provide a basis for new lines of inquiry. Some future perspectives will be explored in Chapter 7.

CHAPTER 7

SUMMARY AND FUTURE PERSPECTIVES

Chapter 7 - Summary and Future Perspectives

7.1 - Summary

The results presented in this thesis have been oriented towards the design, construction and testing of biohybrid nanoreactors which use MtrCAB to couple photochemistry and enzyme catalysis on either side of a membrane. Such nanoreactors provide proof-of-principle for whole-cell photocatalysis using electroactive organisms (Fig. 1.6.1). Aspects of the original design of the nanoreactors (Fig. 1.6.2) were considered in turn: the photochemistry of RuMe-MtrC (Chapter 3); the formation of the transmembrane electron conduit RuMe-MtrCAB (Chapter 4); identification of suitable catalytic machinery, NosZ and MV, (Chapter 5); and finally the assembly and functionality of the complete photocatalytic system (Chapter 6). Unfortunately, the photochemistry of RuMe-MtrC was unable to generate sufficient electron flux to drive detectable catalysis in liposomes. As a result, the design of the nanoreactors required some modifications to the photoactive components in order to operate. The final nanoreactor design is presented in Figure 7.1.1. The results presented in Section 6.4.3 demonstrate that this nanoreactor is capable of catalytic N_2O reduction upon irradiation.

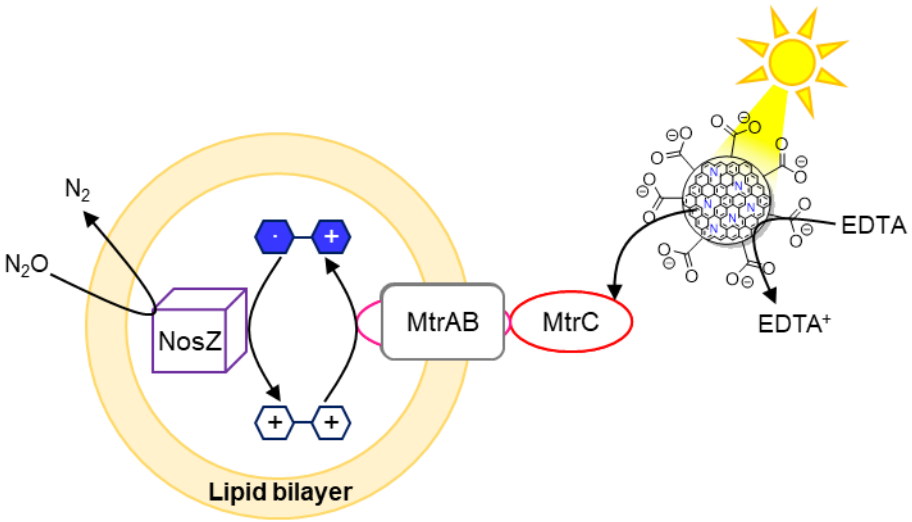

Figure 7.1.1 Schematic of the final, operational nanoreactor developed in this work. Electrons are photogenerated by g-N-CD using EDTA as a SED. These are used to reduce RuMe-MtrCAB (RuMe label not shown) in a liposome membrane. Inside the liposome MV^{2+} (hollow hexagons) is reduced to $MV^{\bullet+}$ (blue hexagons) which goes on to supply electrons to NosZ. NosZ is then able to reduce N_2O to N_2.

At present, this system is challenging to place in the broader context of solar fuels synthesis, not least because no fuel is being produced. We are also unable to accurately quantify the rate of transmembrane electron transfer to NosZ as GC does not have sufficient time resolution. From the results presented in Section 6.4.3, it is estimated that

RuMe-MtrCAB was able to support electron flux of at least 15 s^{-1} RuMe-MtrCAB^{-1}. It is unclear where the rate determining step lies in this system however if this same flux were coupled to hydrogen production it would represent a $TOF_{RuMe\text{-}MtrCAB}$ of 27000 h^{-1} which compares relatively well with other biohybrid systems (see Section 1.5). Given the preliminary nature of this work there is still significant room for optimisation and improvement. It is possible, if not likely, that this TOF can be greatly improved.

With this proof-of-principle system in place, there are several different paths which could be explored. In the following sections some of these will be explored.

7.2 - Optimisation of RuMe-MtrCAB

In Chapters 3 & 4 the assembly and photochemistry of RuMe-MtrCAB was explored. It was found that RuMe-MtrC is able to be photoreduced to completion using EDTA as a SED. The kinetics of photoreduction was found to depend on a number of factors, namely the concentration of EDTA, the light intensity and an internal negative feedback loop. These findings, together with the results from extensive time-resolved spectroscopy of RuMe-MtrC, were used to construct a kinetic model of RuMe-MtrC photoreduction.

RuMe-MtrC was found to act as a photocatalyst for reduction of RB5, a widely used azo dye and pollutant. This dye was used to test the long-term photoactivity and photostability of RuMe-MtrC which were found to be good, with at most 30% of activity being lost after 9h continuous photocatalysis. On the other hand, the absolute rate of electron supply by RuMe-MtrC was found to be quite low, at ≈1 e^- min^{-1} using 100 mM EDTA. In terms of solar-fuels synthesis this would correspond to a maximum $TOF_{RuMe\text{-}MtrC}$ for H_2 of only 30 h^{-1} which is significantly lower than other reported biohybrid systems. The poor electron supply stems from two main factors:

non-optimal kinetics of charge recombination vs SED oxidation

too few photons being absorbed

Tackling these issues presents a fascinating project with many possible avenues, some of which are already being explored.

To optimise the photocycle kinetics of RuMe-MtrC the key will be to extend the lifetime of the CSS such that the SED has more of a chance of reacting with Ru^{III} before charge recombination occurs. The adaptability of proteins provides many different ways of achieving this. Firstly, the site of RuMe attachment can be varied. The $Y_{657}C$ site was selected because it is very close to heme 10. With current understanding this was likely a poor choice for an attachment site as this leads to very fast kinetics of charge

recombination and, thus, poor photochemical efficiency. Other attachment sites are currently being explored. These include sites slightly further from Heme 10 and near other Hemes such as 5 or 7.

A second strategy is to alter the redox landscape of the hemes of MtrC to extend the CSS. This strategy takes some inspiration from the carefully tuned redox centres in natural photosystems. The redox landscape of the hemes of MtrC has been computationally derived by two different groups[178,204]. There are some differences between the results of the calculations but both agree that the microscopic reduction potential of Heme 8 is more negative than Hemes 10 and 9. Electron transfer from Heme 9 to Heme 8 is predicted to be slow and this, according to the models presented in Section 3.5, has a strong effect on the photoreduction of RuMe-MtrC.

The ligation of Heme 8 has been changed from His/His to His/Met, producing RuMe-MtrC$_{H/M}$. This mutation raises the potential of Heme 8 to ≈+200 mV vs. SHE. In this variant, instead of acting as a hurdle for electron transfer, Heme 8 now acts as an electron "trap" which holds onto electrons. TAS of RuMe-MtrC$_{His/Met}$ variant shows that it has a CSS two orders of magnitude longer than the His/His protein. The effect of this mutation on the photoreduction of the protein has not yet been fully characterised, however it expected to be much more efficient. This strategy could be continued, and the first and second coordination spheres of several hemes could be modified to extend the lifetime of the CSS further.

Perfecting the internal kinetic and redox landscapes of RuMe-MtrC presents only one side of the equation. The other being the incorporation of better photosensitisers. The advantage of Ru-diimine photosensitisers is that their photochemistry is well understood, this simplifies kinetic measurements and analyses. There are, however, several disadvantages. The low extinction coefficient ($\varepsilon_{452\ nm}$ = 14600 M^{-1} cm^{-1}) and relatively narrow spectral coverage (see Fig. 2.5.1 - Left) of Ru-diimines leads to low amounts of light being absorbed. Even with the powerful monochromatic light source used in this work each RuMe absorbs ≈1 photon per second. If the photocatalytic system had a perfect quantum yield, the TOF$_{RuMe}$ for H_2 generation would have a maximum of 1800 h^{-1} which is not high in comparison to other reported biohybrid systems (see Section 1.5). Other, more productive systems either use antennas of chromophores to increase the effective photon flux at a photosensitiser[93] (e.g. natural photosystems) or use nanoparticle photosensitisers[114–117] which tend to be larger and have greater extinction coefficients. Either of these strategies could be adopted for use here:

- the staggered-cross structure of MtrC could be used as the foundation of an array of photosensitisers, each connecting to a different heme. These could all be the

same type of photosensitiser (e.g. all RuMe bound to cysteines) or they could be different photosensitisers absorbing photons of different wavelengths. The latter would require orthogonal labelling strategies such as click-chemistry with UAAs[263–265], or disulfide specific chemistry[266,267] (Fig. 7.2.1).

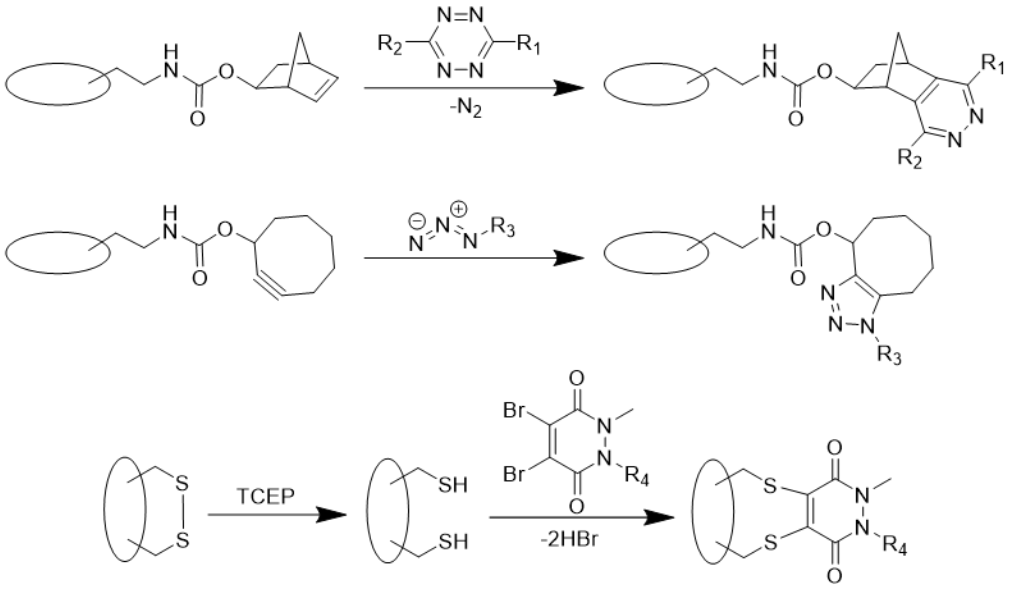

Figure 7.2.1 Alternate labelling strategies that could be used to selectively attach different photosensitisers to MtrC, R groups could include conventional molecular photosensitisers. **Top)** Genetically encoded norbornene UAA reacting with tetrazine[263]; **Middle)** Genetically encoded cyclooctyne UAA reacting with azide[264,265]; **Bottom)** Disulfide is first reduced with TCEP then reacted with dibromopyridazinedione[266,267].

nanoparticle photosensitisers often have high extinction coefficients owing to their relatively large size. Some, such as the CDs used in Chapter 6, also have broad spectral coverage and can prepared from cheap, organic materials. As a result, a single nanoparticle could likely replace several molecular photosensitisers. The problem is how to couple them to MtrC or MtrCAB as their large size can complicate selective bond formation. Our collaborators in the groups of Prof. Erwin Reisner at the University of Cambridge and Prof. Lars Jeuken at the University of Leeds are currently tackling this problem.

Of course, all of these modifications would have to be carefully designed such that the interaction between MtrC and MtrAB is not impacted. Chapter 4 presents a variety of methods for confirming complexation. These could be readily adapted for the study of new constructs. Some techniques, such as AUC or gel filtration, require only small commitments of material and could be used to trial new systems relatively easily. SANS, however, requires beamtime and cannot be carried out routinely. The best way to demonstrate the functional reconstitution of new MtrC:MtrAB complexes might be

through their function in liposomes. Efforts are also under way to attach photosensitisers to “WT” MtrCAB with cysteine mutations which would avoid the need for reconstitution and could potentially be performed on the surface of living MR-1.

In conclusion, MtrC presents a platform for near infinite modification. A large diversity of possible photosensitisers could be attached at different sites and mutations to the chain of hemes could make it a more effective electron relay. Reconstitution of MtrC with MtrAB appears robust and specific and presents a route to preparing improved photocatalytic nanoreactors or driving photocatalysis in whole cells.

7.3 - Optimisation of nanoreactor catalyst

The catalyst employed in this work was NosZ from *Paracoccus denitrificans*. This enzyme has a complex catalytic cycle and the roles of different forms of the active are not yet fully understood. Its gaseous substrate and product, however, make it a useful choice for an encapsulated redox catalyst in a proof-of-principle nanoreactor.

The dependence of NosZ on $MV^{\bullet+}$ for *in vitro* activity was troublesome as $MV^{\bullet+}$ is able to cross lipid membranes with relative ease. $MV^{\bullet+}$ also prohibits the use of the Biobead-mediated detergent sequestration method (see Section 2.7.2.2). A strategy could be used where Biobeads are used to form liposomes containing NosZ without MV. This would take advantage of the superior encapsulation efficiency of the Biobead method. MV could then be added after the liposomes are formed. Alternatively, a solution would be to use an enzyme that is not dependant on MV and requires only a redox shuttle protein to support catalysis. This could be NosZ from a different bacterium that does not undergo deactivation so easily and where Paz could be used as a redox partner.

A drawback of the experiments presented in Section 6.4 is the low temporal resolution of N_2O concentration. Measurement by GC simply took too long, under the conditions used, to accurately quantify rates of N_2O consumption. Also, the gaseous N_2O concentration can only be related to the aqueous concentration under equilibrium conditions which are near impossible to achieve during an assay where N_2O concentrations are changing. Future experiments should consider using an *in situ* system such as a N_2O detecting electrode.[268,269] This would allow the aqueous N_2O concentration to be measured directly with high resolution.

Alternatively, a different enzyme could be used. Hydrogenases reduce protons to H_2 meaning that only the substrate would require importing into the liposome interior. Many methods are available for translocating protons across a membrane such as the ionophore nigericin.[270] It is also hypothesised that MtrCAB can translocate protons[134,262]

which, if true, would mean that an ionophore may not be necessary. The [NiFeSe] hydrogenase from *Desulfmicrobium baculatum* may make a good choice due to its reported oxygen tolerance[111]. By adapting the systems presented here for H_2 production they could be better compared to the systems explored in Chapter 1.

7.4 - Whole-cell photocatalysis

The nanoreactors produced in this thesis serve as proof-of principle for the development of whole-cell photocatalytic systems in MR-1. Where the enzymes of MR-1[128] are the recipients of photogenerated electrons. The assembly of RuMe-MtrCAB complexes (or new photosensitiser-MtrCAB complexes) *in vivo* are currently being pursued by different routes. Cysteine labelling sites have been introduced to MtrCAB both in the native gene and on a plasmid over-expression system. Successful expression of such proteins could allow for *in situ* labelling of MtrCAB. Alternatively, MtrCAB complexes could be reconstituted on the surface of cells expressing MtrAB by addition of MtrC to a cell suspension. The latter strategy would have the advantage that the process of labelling MtrC could take place in the absence of cells, allowing more extreme conditions to be used. It would likely, however, require more input on behalf of the researchers.

Assembling a whole-cell photocatalytic system would likely require alternate SEDs to be found as EDTA is known to be antimicrobial.[271] This could be cysteine which has already been demonstrated to act as a SED for RuMe-MtrC and has been used as a SED for other whole-cell photocatalytic systems.[122,125] Cysteine can be regenerated from its oxidised form (cystine) by several methods both chemical and photochemical, such as TiO_2 nanoparticles doped with manganese phthalocyanine.[125] The latter can use water as a SED which presents opportunities for clean photocatalytic systems.

Once a route is established for producing photosensitised MtrCAB in whole cells it may be possible to transfer this conduit to other bacteria, *E. coli* for instance. Some success has already been seen for expressing MtrCAB in *E. coli* and conferring electroactivity on this otherwise insulating bacterium. Many interesting enzymes can be expressed in *E. coli* which could potentially be powered photochemically using photosensitised MtrCAB.

Having demonstrated the operation of the nanoreactors envisaged at the start of this work, the opportunities to develop the system for novel biotechnology are clear. Photosensitised MtrCAB is likely to provide a robust and adaptable platform for coupling transmembrane redox chemistry in a range of environments, both abiotic (liposomes) and biotic (living cells). A wide range of redox chemistry may be able to be catalysed through coupling to various enzymes or synthetic materials.

References

1. Ritchie, H. & Roser, M. Energy. *Our World Data* (2014).
2. *NIST Chemistry WebBook, NIST Standard Reference Database Number 69*. (National Institute of Standards and Technology). doi:10.18434/T4D303.
3. Benson, E. E., Kubiak, C. P., Sathrum, A. J. & Smieja, J. M. Electrocatalytic and homogeneous approaches to conversion of CO_2 to liquid fuels. *Chem. Soc. Rev.* **38**, 89–99 (2009).
4. Mustafa, A., Lougou, B. G., Shuai, Y., Wang, Z. & Tan, H. Current technology development for CO_2 utilization into solar fuels and chemicals: A review. *J. Energy Chem.* **49**, 96–123 (2020).
5. Gust, D., Moore, T. A. & Moore, A. L. Solar fuels via artificial photosynthesis. *Acc. Chem. Res.* **42**, 1890–1898 (2009).
6. Montoya, J. H. *et al.* Materials for solar fuels and chemicals. *Nat. Mater.* **16**, 70–81 (2016).
7. Nocera, D. G. Solar fuels and solar chemicals industry. *Acc. Chem. Res.* **50**, 616–619 (2017).
8. Centi, G. & Perathoner, S. Towards solar fuels from water and CO_2. *ChemSusChem* **3**, 195–208 (2010).
9. Schulman, S. G. *Fluorescence and Phosphorescence Spectroscopy*. (Elsevier, 1977). doi:10.1016/C2013-0-02750-8.
10. Pellegrin, Y. & Odobel, F. Sacrificial electron donor reagents for solar fuel production. *Comptes Rendus Chim.* **20**, 283–295 (2017).
11. Gust, D. *et al.* Photodriven electron transfer in triad molecules: a two-step charge-recombination reaction. *J. Am. Chem. Soc.* **108**, 8028–8031 (1986).
12. Gust, D. *et al.* Charge separation in carotenoporphyrin-quinone triads: synthetic, conformational, and fluorescence lifetime studies. *J. Am. Chem. Soc.* **109**, 846–856 (1987).
13. Gust, D. *et al.* Photoinitiated charge separation in a carotenoid-porphyrin-diquinone tetrad: enhanced quantum yields via multistep electron transfers. *J. Am. Chem. Soc.* **110**, 321–323 (1988).
14. Gust, D. *et al.* A carotenoid-diporphyrin-quinone model for photosynthetic multistep electron and energy transfer. *J. Am. Chem. Soc.* **110**, 7567–7569 (1988).
15. Gust, D. *et al.* Efficient multistep photoinitiated electron transfer in a molecular pentad. *Science* **248**, 199–201 (1990).
16. Gust, D. *et al.* Long-lived Photoinitiated Charge Separation In Carotene Diporphyrin Triad Molecules. *J. Am. Chem. Soc.* **113**, 3638–3649 (1991).
17. Whang, D. R. & Apaydin, D. H. Artificial Photosynthesis: Learning from Nature. *ChemPhotoChem* **2**, 148–160 (2018).
18. Dokić, M. & Soo, H. Sen. Artificial photosynthesis by light absorption, charge separation, and multielectron catalysis. *Chem. Commun.* **54**, 6554–6572 (2018).
19. De Lacey, A. L., Fernández, V. M., Rousset, M. & Cammack, R. Activation and inactivation of hydrogenase function and the catalytic cycle: Spectroelectrochemical studies. *Chem. Rev.* **107**, 4304–4330 (2007).

20. Wakerley, D. W., Gross, M. A. & Reisner, E. Proton reduction by molecular catalysts in water under demanding atmospheres. *Chem. Commun.* **50**, 15995–15998 (2014).

21. Wakerley, D. W. & Reisner, E. Oxygen-tolerant proton reduction catalysis: Much O_2 about nothing? *Energy Environ. Sci.* **8**, 2283–2295 (2015).

22. Lubner, C. E., Grimme, R., Bryant, D. A. & Golbeck, J. H. Wiring photosystem I for direct solar hydrogen production. *Biochemistry* **49**, 404–414 (2010).

23. Ferreira, K. N., Iverson, T. M., Maghlaoui, K., Barber, J. & Iwata, S. Architecture of the photosynthetic oxygen-evolving center. *Science* **303**, 1831–8 (2004).

24. Cardona, T., Sedoud, A., Cox, N. & Rutherford, A. W. Charge separation in Photosystem II: A comparative and evolutionary overview. *Biochim. Biophys. Acta - Bioenerg.* **1817**, 26–43 (2012).

25. Brettel, K. & Leibl, W. Electron transfer in photosystem I. *Biochim. Biophys. Acta - Bioenerg.* **1507**, 100–114 (2001).

26. Peter, G. F. & Thornber, J. P. Biochemical composition and organization of higher plant photosystem II light -harvesting pigment-proteins. *J. Biol. Chem.* **266**, 16745–16754 (1991).

27. Rasmussen, M. & Minteer, S. D. Photobioelectrochemistry: Solar Energy Conversion and Biofuel Production with Photosynthetic Catalysts. *J. Electrochem. Soc.* **161**, H647–H655 (2014).

28. Kern, J. & Renger, G. Photosystem II: Structure and mechanism of the water:plastoquinone oxidoreductase. *Photosynth. Res.* **94**, 183–202 (2007).

29. Gorka, M., Schartner, J., Van Der Est, A., Rögner, M. & Golbeck, J. H. Light-mediated hydrogen generation in photosystem I: Attachment of a naphthoquinone-molecular wire-Pt nanoparticle to the A_{1A} and A_{1B} sites. *Biochemistry* **53**, 2295–2306 (2014).

30. Taniguchi, M. & Lindsey, J. S. Database of Absorption and Fluorescence Spectra of >300 Common Compounds for use in PhotochemCAD. *Photochem. Photobiol.* **94**, 290–327 (2018).

31. Gueymard, C. A., Myers, D. & Emery, K. Proposed reference irradiance spectra for solar energy systems testing. *Sol. Energy* **73**, 443–467 (2002).

32. Mieghem, F. J. E. Van, Searle, G. F. W., R, A. W. & Schaafsma, T. J. The influence of the double reduction of OA on the fluorescence decay kinetics of Photosystem II. *Biochim. Biophys. Acta* **1100**, 198–206 (1992).

33. Telfer, A., He, W. & Barber, J. Spectral resolution of more than one chlorophyll electron donor in the isolated Photosystem II reaction centre complex. *Biochim. Biophys. Acta - Bioenerg.* **1017**, 143–151 (1990).

34. Mattoo, A. K., Hoffman-Falk, H., Marder, J. B. & Edelman, M. Regulation of protein metabolism: Coupling of photosynthetic electron transport to in vivo degradation of the rapidly metabolized 32-kilodalton protein of the chloroplast membranes. *Proc. Natl. Acad. Sci.* **81**, 1380–1384 (1984).

35. Zhu, X.-G., Long, S. P. & Ort, D. R. Improving Photosynthetic Efficiency for Greater Yield. *Annu. Rev. Plant Biol.* **61**, 235–261 (2010).

36. McCalmont, J. P. *et al.* Environmental costs and benefits of growing Miscanthus for bioenergy in the UK. *GCB Bioenergy* **9**, 489–507 (2017).

37. Chen, M. & Blankenship, R. E. Expanding the solar spectrum used by

photosynthesis. *Trends Plant Sci.* **16**, 427–431 (2011).

38. Lewandowski, I. *et al.* Progress on optimizing miscanthus biomass production for the european bioeconomy: Results of the EU FP7 project OPTIMISC. *Front. Plant Sci.* **7**, 1–23 (2016).

39. Pade, N. & Hagemann, M. Salt acclimation of cyanobacteria and their application in biotechnology. *Life* **5**, 25–49 (2015).

40. Singh, J. S., Kumar, A., Rai, A. N. & Singh, D. P. Cyanobacteria: A precious bio-resource in agriculture, ecosystem, and environmental sustainability. *Front. Microbiol.* **7**, 1–19 (2016).

41. Lan, E. I. & Liao, J. C. Metabolic engineering of cyanobacteria for 1-butanol production from carbon dioxide. *Metab. Eng.* **13**, 353–363 (2011).

42. Rillema, D. P., Allen, G., Meyer, T. J. & Conrad, D. Redox properties of ruthenium(II) tris chelate complexes containing the ligands 2,2'-bipyrazine, 2,2'-bipyridine, and 2,2'-bipyrimidine. *Inorg. Chem.* **22**, 1617–1622 (1983).

43. Millett, F., Havens, J., Rajagukguk, S. & Durham, B. Design and use of photoactive ruthenium complexes to study electron transfer within cytochrome bc_1 and from cytochrome bc_1 to cytochrome *c*. *Biochim. Biophys. Acta - Bioenerg.* **1827**, 1309–1319 (2013).

44. Losse, S., Vos, J. G. & Rau, S. Catalytic hydrogen production at cobalt centres. *Coord. Chem. Rev.* **254**, 2492–2504 (2010).

45. Fihri, A. *et al.* Cobaloxime-based photocatalytic devices for hydrogen production. *Angew. Chemie - Int. Ed.* **47**, 564–567 (2008).

46. Fihri, A., Artero, V., Pereira, A. & Fontecave, M. Efficient H_2-producing photocatalytic systems based on cyclometalated iridium- and tricarbonylrhenium-diimine photosensitizers and cobaloxime catalysts. *Dalton Trans.* 5567–9 (2008) doi:10.1039/b812605b.

47. Cropek, D. M. *et al.* A novel ruthenium(II)-cobaloxime supramolecular complex for photocatalytic H_2 evolution: Synthesis, characterisation and mechanistic studies. *Dalt. Trans.* **41**, 13060–13073 (2012).

48. Li, C. *et al.* Photochemical hydrogen production catalyzed by polypyridyl ruthenium-cobaloxime heterobinuclear complexes with different bridges. *J. Organomet. Chem.* **694**, 2814–2819 (2009).

49. Mulfort, K. L. & Tiede, D. M. Supramolecular cobaloxime assemblies for H_2 photocatalysis: An initial solution state structure-function analysis. *J. Phys. Chem. B* **114**, 14572–14581 (2010).

50. Zhang, P. *et al.* Photochemical H_2 production with noble-metal-free molecular devices comprising a porphyrin photosensitizer and a cobaloxime catalyst. *Chem. Commun.* **46**, 8806–8808 (2010).

51. McCormick, T. M. *et al.* Impact of ligand exchange in hydrogen production from cobaloxime-containing photocatalytic systems. *Inorg. Chem.* **50**, 10660–10666 (2011).

52. Veldkamp, B. S. *et al.* Photoinitiated multi-step charge separation and ultrafast charge transfer induced dissociation in a pyridyl-linked photosensitizer-cobaloxime assembly. *Energy Environ. Sci.* **6**, 1917–1928 (2013).

53. Kaeffer, N., Chavarot-Kerlidou, M. & Artero, V. Hydrogen evolution catalyzed by cobalt diimine-dioxime complexes. *Acc. Chem. Res.* **48**, 1286–1295 (2015).

54. Kaeffer, N. *et al.* Covalent Design for Dye-Sensitized H_2-Evolving Photocathodes Based on a Cobalt Diimine-Dioxime Catalyst. *J. Am. Chem. Soc.* **138**, 12308–12311 (2016).

55. Pati, P. B. *et al.* Insights into the Mechanism of a Covalently Linked Organic Dye–Cobaloxime Catalyst System for Dye-Sensitized Solar Fuel Devices. *ChemSusChem* **10**, 2480–2495 (2017).

56. Queyriaux, N. *et al.* CuAAC-based assembly and characterization of a ruthenium-copper dyad containing a diimine-dioxime ligand framework. *Faraday Discuss.* **198**, 251–261 (2017).

57. Bae, E. & Choi, W. Effect of the anchoring group (carboxylate vs phosphonate) in Ru-complex-sensitized TiO_2 on hydrogen production under visible light. *J. Phys. Chem. B* **110**, 14792–14799 (2006).

58. Lakadamyali, F. & Reisner, E. Photocatalytic H_2 evolution from neutral water with a molecular cobalt catalyst on a dye-sensitised TiO_2 nanoparticle. *Chem. Commun.* **47**, 1695–1697 (2011).

59. Lakadamyali, F., Reynal, A., Kato, M., Durrant, J. R. & Reisner, E. Electron Transfer in Dye-Sensitised Semiconductors Modified with Molecular Cobalt Catalysts: Photoreduction of Aqueous Protons. *Chem. - A Eur. J.* **18**, 15464–15475 (2012).

60. Willkomm, J., Muresan, N. M. & Reisner, E. Enhancing H_2 evolution performance of an immobilised cobalt catalyst by rational ligand design. *Chem. Sci.* **6**, 2727–2736 (2015).

61. Gross, M. A., Reynal, A., Durrant, J. R. & Reisner, E. Versatile photocatalytic systems for H_2 generation in water based on an efficient DuBois-type nickel catalyst. *J. Am. Chem. Soc.* **136**, 356–366 (2014).

62. Soltau, S. R. *et al.* Aqueous light driven hydrogen production by a Ru-ferredoxin-Co biohybrid. *Chem. Commun.* **51**, 10628–10631 (2015).

63. Soltau, S. R. *et al.* Ru-protein-Co biohybrids designed for solar hydrogen production: understanding electron transfer pathways related to photocatalytic function. *Chem. Sci.* **7**, 7068–7078 (2016).

64. Soltau, S. R. *et al.* Charge Separation Related to Photocatalytic H_2 Production from a Ru-Apoflavodoxin-Ni Biohybrid. *ACS Energy Lett.* **2**, 230–237 (2017).

65. Brahmachari, U. *et al.* Interprotein electron transfer biohybrid system for photocatalytic H_2 production. *Photosynth. Res.* **143**, 183–192 (2020).

66. Utschig, L. M. *et al.* Photocatalytic hydrogen production from noncovalent biohybrid Photosystem I/Pt nanoparticle complexes. *J. Phys. Chem. Lett.* **2**, 236–241 (2011).

67. Antonkine, M. L. *et al.* Chemical rescue of a site-modified ligand to a [4Fe-4S] cluster in PsaC, a bacterial-like dicluster ferredoxin bound to Photosystem I. *Biochim. Biophys. Acta - Bioenerg.* **1767**, 712–724 (2007).

68. Grimme, R. A., Lubner, C. E., Bryant, D. A. & Golbeck, J. H. Photosystem I/molecular wire/metal nanoparticle bioconjugates for the photocatalytic production of H_2. *J. Am. Chem. Soc.* **130**, 6308–6309 (2008).

69. Grimme, R. A., Lubner, C. E. & Golbeck, J. H. Maximizing H_2 production in Photosystem I/dithiol molecular wire/platinum nanoparticle bioconjugates. *Dalton Trans.* 10106–13 (2009) doi:10.1039/b909137h.

70. Walters, K. A. & Golbeck, J. H. Designing a modified clostridial 2[4Fe–4S]

ferredoxin as a redox coupler to directly link photosystem I with a Pt nanoparticle. *Photosynth. Res.* **143**, 165–181 (2020).

71. Johnson, T. W. *et al.* Recruitment of a foreign quinone into the A_1 site of photosystem I: In vivo replacement of plastoquinone-9 by media-supplemented naphthoquinones in phylloquinone biosynthetic pathway mutants of *Synechocystis* sp. PCC 6803. *J. Biol. Chem.* **276**, 39512–39521 (2001).

72. Gorka, M. *et al.* Electron transfer from the A_{1A} and A_{1B} sites to a tethered Pt nanoparticle requires the FeS clusters for suppression of the recombination channel. *J. Photochem. Photobiol. B Biol.* **152**, 325–334 (2015).

73. Utschig, L. M., Silver, S. C., Mulfort, K. L. & Tiede, D. M. Nature-driven photochemistry for catalytic solar hydrogen production: A Photosystem I-transition metal catalyst hybrid. *J. Am. Chem. Soc.* **133**, 16334–16337 (2011).

74. Utschig, L. M., Soltau, S. R., Mulfort, K. L., Niklas, J. & Poluektov, O. G. Z-scheme solar water splitting: Via self-assembly of photosystem I-catalyst hybrids in thylakoid membranes. *Chem. Sci.* **9**, 8504–8512 (2018).

75. Silver, S. C. *et al.* Protein delivery of a Ni catalyst to photosystem I for light-driven hydrogen production. *J. Am. Chem. Soc.* **135**, 13246–13249 (2013).

76. Tsao, M., Summerer, D., Ryu, Y. & Schultz, P. G. The Genetic Incorporation of a Distance Probe into Proteins in *Escherichia coli*. *J. Am. Chem. Soc.* **128**, 4572–4573 (2006).

77. Liu, X. *et al.* Genetic Incorporation of a Metal-Chelating Amino Acid as a Probe for Protein Electron Transfer. *Angew. Chemie Int. Ed.* **51**, 10261–10265 (2012).

78. Liu, X. *et al.* Significant Expansion of the Fluorescent Protein Chromophore through the Genetic Incorporation of a Metal-Chelating Unnatural Amino Acid. *Angew. Chemie Int. Ed.* **52**, 4805–4809 (2013).

79. Lv, X. *et al.* Ultrafast Photoinduced Electron Transfer in Green Fluorescent Protein Bearing a Genetically Encoded Electron Acceptor. *J. Am. Chem. Soc.* **137**, 7270–7273 (2015).

80. Liu, X. *et al.* A genetically encoded photosensitizer protein facilitates the rational design of a miniature photocatalytic CO_2-reducing enzyme. *Nat. Chem.* **10**, 1201–1206 (2018).

81. Chitnis, P. R. Photosystem I. *Plant Physiol.* **111**, 661–669 (1996).

82. Zimmer, M. Green fluorescent protein (GFP): Applications, structure, and related photophysical behavior. *Chem. Rev.* **102**, 759–781 (2002).

83. Prasher, D. C., Eckenrode, V. K., Ward, W. W., Prendergast, F. G. & Cormier, M. J. Primary structure of the *Aequorea victoria* green-fluorescent protein. *Gene* **111**, 229–233 (1992).

84. Pakhomov, A. A. & Martynov, V. I. GFP Family: Structural Insights into Spectral Tuning. *Chem. Biol.* **15**, 755–764 (2008).

85. Noren, C. J., Anthony-Cahill, S. J., Griffith, M. C. & Schultz, P. G. A general method for site-specific incorporation of unnatural amino acids into proteins. *Science* **244**, 182–8 (1989).

86. Zhang, W. H., Otting, G. & Jackson, C. J. Protein engineering with unnatural amino acids. *Curr. Opin. Struct. Biol.* **23**, 581–587 (2013).

87. Wals, K. & Ovaa, H. Unnatural amino acid incorporation in *E. coli*: current and future applications in the design of therapeutic proteins. *Front. Chem.* **2**, 1301

(2014).

88. Kuehnel, M. F., Orchard, K. L., Dalle, K. E. & Reisner, E. Selective Photocatalytic CO_2 Reduction in Water through Anchoring of a Molecular Ni Catalyst on CdS Nanocrystals. *J. Am. Chem. Soc.* **139**, 7217–7223 (2017).

89. Ihara, M. *et al.* Light-driven Hydrogen Production by a Hybrid Complex of a [NiFe]-Hydrogenase and the Cyanobacterial Photosystem I. *Photochem. Photobiol.* **82**, 676 (2006).

90. Yacoby, I. *et al.* Photosynthetic electron partitioning between [FeFe]-hydrogenase and ferredoxin:$NADP^+$-oxidoreductase (FNR) enzymes in vitro. *Proc. Natl. Acad. Sci.* **108**, 9396–9401 (2011).

91. Gorka, M. & Golbeck, J. H. Generating dihydrogen by tethering an [FeFe]hydrogenase via a molecular wire to the A_{1A}/A_{1B} sites of photosystem I. *Photosynth. Res.* **143**, 155–163 (2020).

92. Lubner, C. E. *et al.* Wiring an [FeFe]-hydrogenase with Photosystem I for light-induced hydrogen production. *Biochemistry* **49**, 10264–10266 (2010).

93. Lubner, C. E. *et al.* Solar hydrogen-producing bionanodevice outperforms natural photosynthesis. *Proc. Natl. Acad. Sci. U. S. A.* **108**, 20988–20991 (2011).

94. Reisner, E., Powell, D. J., Cavazza, C., Fontecilla-Camps, J. C. & Armstrong, F. A. Visible light-driven H_2 production by hydrogenases attached to dye-sensitized TiO_2 nanoparticles. *J. Am. Chem. Soc.* **131**, 18457–18466 (2009).

95. Reisner, E., Fontecilla-Camps, J. C. & Armstrong, F. A. Catalytic electrochemistry of a [NiFeSe]-hydrogenase on TiO_2 and demonstration of its suitability for visible-light driven H_2 production. *Chem. Commun. (Camb).* 550–2 (2009) doi:10.1039/b817371k.

96. Tran, N. H. *et al.* Light-initiated hydroxylation of lauric acid using hybrid P450 BM3 enzymes. *Chem. Commun.* **47**, 11936–11938 (2011).

97. Tran, N. H. *et al.* A series of hybrid P450 BM3 enzymes with different catalytic activity in the light-initiated hydroxylation of lauric acid. *J. Inorg. Biochem.* **115**, 50–56 (2012).

98. Tran, N. H. *et al.* An efficient light-driven P450 BM3 biocatalyst. *J. Am. Chem. Soc.* **135**, 14484–14487 (2013).

99. Kato, M. *et al.* Regio- and stereoselective hydroxylation of 10-undecenoic acid with a light-driven P450 BM3 biocatalyst yielding a valuable synthon for natural product synthesis. *Bioorganic Med. Chem.* **22**, 5687–5691 (2014).

100. Institute for Industrial productivty. Industrial Efficiency Technology Database: Ammonia. http://www.iipinetwork.org/wp-content/Ietd/content/ammonia.html.

101. Burgess, B. K. & Lowe, D. J. Mechanism of molybdenum nitrogenase. *Chem. Rev.* **96**, 2983–3011 (1996).

102. Howard, J. B. & Rees, D. C. Structural basis of biological nitrogen fixation. *Chem. Rev.* **96**, 2965–2982 (1996).

103. Roth, L. E., Nguyen, J. C. & Tezcan, F. A. ATP- and Iron−Protein-Independent Activation of Nitrogenase Catalysis by Light. *J. Am. Chem. Soc.* **132**, 13672–13674 (2010).

104. Roth, L. E. & Tezcan, F. A. ATP-Uncoupled, Six-Electron Photoreduction of Hydrogen Cyanide to Methane by the Molybdenum–Iron Protein. *J. Am. Chem.*

Soc. **134**, 8416–8419 (2012).

105. Seefeldt, L. C., Hoffman, B. M. & Dean, D. R. Mechanism of Mo-Dependent Nitrogenase. *Annu. Rev. Biochem.* **78**, 701–722 (2009).

106. Okura, I. & Kim-Thuan, N. Comparison of ruthenium complexes for photoinduced methyl viologen reduction and hydrogen evolution form water by hydrogenase. *Chem. Lett.* **9**, 1511–1512 (1980).

107. Zadvornyy, O. A. *et al.* Photo-induced H_2 production by [NiFe]-hydrogenase from *T. roseopersicina* covalently linked to a Ru(II) photosensitizer. *J. Inorg. Biochem.* **106**, 151–155 (2012).

108. Teixeira, M. *et al.* Nickel-[iron-sulfur]-selenium-containing hydrogenases from *Desulfovibrio baculatus* (DSM 1743). Redox centers and catalytic properties. *Eur. J. Biochem.* **167**, 47–58 (1987).

109. Garcin, E. *et al.* The crystal structure of a reduced [NiFeSe] hydrogenase provides an image of the activated catalytic center. *Structure* **7**, 557–566 (1999).

110. Medina, M., Hatchikian, E. C. & Cammack, R. Studies of light-induced nickel EPR signals in hydrogenase: Comparison of enzymes with and without selenium. *Biochim. Biophys. Acta - Bioenerg.* **1275**, 227–236 (1996).

111. Parkin, A., Goldet, G., Cavazza, C., Fontecilla-Camps, J. C. & Armstrong, F. A. The Difference a Se Makes? Oxygen-Tolerant Hydrogen Production by the [NiFeSe]-Hydrogenase from *Desulfomicrobium baculatum*. *J. Am. Chem. Soc.* **130**, 13410–13416 (2008).

112. Rhee, J. H., Chung, C.-C. & Diau, E. W.-G. A perspective of mesoscopic solar cells based on metal chalcogenide quantum dots and organometal-halide perovskites. *NPG Asia Mater.* **5**, e68–e68 (2013).

113. Brown, K. A., Dayal, S., Ai, X., Rumbles, G. & King, P. W. Controlled assembly of hydrogenase-CdTe nanocrystal hybrids for solar hydrogen production. *J. Am. Chem. Soc.* **132**, 9672–9680 (2010).

114. Brown, K. A., Wilker, M. B., Boehm, M., Dukovic, G. & King, P. W. Characterization of photochemical processes for H_2 production by CdS nanorod-[FeFe] hydrogenase complexes. *J. Am. Chem. Soc.* **134**, 5627–5636 (2012).

115. Utterback, J. K. *et al.* Competition between electron transfer, trapping, and recombination in Cds nanorod-hydrogenase complexes. *Phys. Chem. Chem. Phys.* **17**, 5538–5542 (2015).

116. Utterback, J. K. *et al.* Quantum Efficiency of Charge Transfer Competing against Nonexponential Processes: The Case of Electron Transfer from CdS Nanorods to Hydrogenase. *J. Phys. Chem. C* **123**, 886–896 (2019).

117. Wilker, M. B. *et al.* Role of Surface-Capping Ligands in Photoexcited Electron Transfer between CdS Nanorods and [FeFe] Hydrogenase and the Subsequent H_2 Generation. *J. Phys. Chem. C* **122**, 741–750 (2018).

118. Wang, X., Feng, Y., Dong, P. & Huang, J. A Mini Review on Carbon Quantum Dots: Preparation, Properties, and Electrocatalytic Application. *Front. Chem.* **7**, 1–9 (2019).

119. Hutton, G. A. M. *et al.* Carbon Dots as Versatile Photosensitizers for Solar-Driven Catalysis with Redox Enzymes. *J. Am. Chem. Soc.* **138**, 16722–16730 (2016).

120. Cunningham, D. P. & Lundie, L. L. Precipitation of cadmium by Clostridium thermoaceticum. *Appl. Environ. Microbiol.* **59**, 7–14 (1993).

121. Can, M., Armstrong, F. A. & Ragsdale, S. W. Structure, function, and mechanism of the nickel metalloenzymes, CO dehydrogenase, and acetyl-CoA synthase. *Chem. Rev.* **114**, 4149–4174 (2014).

122. Sakimoto, K. K., Wong, A. B. & Yang, P. Self-photosensitization of nonphotosynthetic bacteria for solar-to-chemical production. *Science* **351**, 74–7 (2016).

123. Honda, Y., Hagiwara, H., Ida, S. & Ishihara, T. Application to Photocatalytic H_2 Production of a Whole-Cell Reaction by Recombinant *Escherichia coli* Cells Expressing [FeFe]-Hydrogenase and Maturases Genes. *Angew. Chemie - Int. Ed.* **55**, 8045–8048 (2016).

124. Wei, W. *et al.* A surface-display biohybrid approach to light-driven hydrogen production in air. *Sci. Adv.* **4**, 1–7 (2018).

125. Sakimoto, K. K., Zhang, S. J. & Yang, P. Cysteine–Cystine Photoregeneration for Oxygenic Photosynthesis of Acetic Acid from CO_2 by a Tandem Inorganic–Biological Hybrid System. *Nano Lett.* **16**, 5883–5887 (2016).

126. Yu, Y. *et al.* Identification of a highly luminescent $Au_{22}(SG)_{18}$ nanocluster. *J. Am. Chem. Soc.* **136**, 1246–1249 (2014).

127. Gai, P. *et al.* Solar-Powered Organic Semiconductor–Bacteria Biohybrids for CO_2 Reduction into Acetic Acid. *Angew. Chemie - Int. Ed.* **59**, 7224–7229 (2020).

128. Rowe, S. F. *et al.* Light-Driven H_2 Evolution and C═C or C═O Bond Hydrogenation by *Shewanella oneidensis* : A Versatile Strategy for Photocatalysis by Nonphotosynthetic Microorganisms. *ACS Catal.* **7**, 7558–7566 (2017).

129. Wang, B., Jiang, Z., Yu, J. C., Wang, J. & Wong, P. K. Enhanced CO_2 reduction and valuable C2+ chemical production by a CdS-photosynthetic hybrid system. *Nanoscale* **11**, 9296–9301 (2019).

130. Guo, J. *et al.* Light-driven fine chemical production in yeast biohybrids. *Science* **362**, 813–816 (2018).

131. van Wonderen, J. H. *et al.* Ultrafast Light-Driven Electron Transfer in a Ru(II)tris(bipyridine)-Labeled Multiheme Cytochrome. *J. Am. Chem. Soc.* **141**, 15190–15200 (2019).

132. van Wonderen, J. H. *et al.* Photosensitised Multiheme Cytochromes as Light-Driven Molecular Wires and Resistors. *ChemBioChem* **19**, 2206–2215 (2018).

133. Myhre, G. *et al.* Anthropogenic and Natural Radiative Forcing. in *Climate Change 2013 - The Physical Science Basis* (ed. Intergovernmental Panel on Climate Change) 659–740 (Cambridge University Press, 2013). doi:10.1017/CBO9781107415324.018.

134. Edwards, M. J., White, G. F., Butt, J. N., Richardson, D. J. & Clarke, T. A. The Crystal Structure of a Biological Insulated Transmembrane Molecular Wire. *Cell* **181**, 665–673 (2020).

135. Paradies, H. H. Shape and size of a nonionic surfactant micelle. Triton X-100 in aqueous solution. *J. Phys. Chem.* **84**, 599–607 (1980).

136. Sybirna, K. *et al. Shewanella oneidensis*: A new and efficient System for Expression and Maturation of heterologous [Fe-Fe] Hydrogenase from *Chlamydomonas reinhardtii*. *BMC Biotechnol.* **8**, 1–8 (2008).

137. Vishniac, W. & Santer, M. The Thiobacilli. *Bacteriol. Rev.* **21**, 195–213 (1957).

138. Blair, D. & Diehl, H. Bathophenanthrolinedisulphonic acid and bathocuproinedisulphonic acid, water soluble reagents for iron and copper. *Talanta* **7**, 163–174 (1961).

139. Barr, I. & Guo, F. Pyridine Hemochromagen Assay for Determining the Concentration of Heme in Purified Protein Solutions. *Bio-protocol* **5**, 1–8 (2015).

140. Thorndycroft, F. H., Butland, G., Richardson, D. J. & Watmough, N. J. A new assay for nitric oxide reductase reveals two conserved glutamate residues form the entrance to a proton-conducting channel in the bacterial enzyme. *Biochem. J.* **401**, 111–119 (2007).

141. Leung, Y. C. *et al.* The pseudoazurin gene from *Thiosphaera pantotropha*: Analysis of upstream putative regulatory sequences and overexpression in *Escherichia coli*. *Biochem. J.* **321**, 699–705 (1997).

142. Shi, L. *et al.* Direct involvement of type II secretion system in extracellular translocation of *Shewanella oneidensis* outer membrane cytochromes MtrC and OmcA. *J. Bacteriol.* **190**, 5512–5516 (2008).

143. Lockwood, C. W. J. *et al.* Membrane-spanning electron transfer proteins from electrogenic bacteria: Production and investigation. in *Methods in Enzymology* vol. 613 257–275 (Academic Press, 2018).

144. Filip, C., Fletcher, G., Wulff, J. L. & Earhart, C. F. Solubilization of the cytoplasmic membrane of *Escherichia coli* by the ionic detergent sodium lauryl sarcosinate. *J. Bacteriol.* **115**, 717–722 (1973).

145. Bennett, S. P. *et al.* NosL is a dedicated copper chaperone for assembly of the Cu Z center of nitrous oxide reductase. *Chem. Sci.* **10**, 4985–4993 (2019).

146. Dixon, M. The acceptor specificity of flavins and flavoproteins. *BBA - Bioenerg.* **226**, 269–284 (1971).

147. Watanabe, T. & Honda, K. Measurement of the extinction coefficient of the methyl viologen cation radical and the efficiency of its formation by semiconductor photocatalysis. *J. Phys. Chem.* **86**, 2617–2619 (1982).

148. Sander, R. Compilation of Henry's law constants (version 4.0) for water as solvent. *Atmos. Chem. Phys.* **15**, 4399–4981 (2015).

149. MAYHEW, S. G. The Redox Potential of Dithionite and SO^{-}_{2} from Equilibrium Reactions with Flavodoxins, Methyl Viologen and Hydrogen plus Hydrogenase. *Eur. J. Biochem.* **85**, 535–547 (1978).

150. Martindale, B. C. M. *et al.* Enhancing Light Absorption and Charge Transfer Efficiency in Carbon Dots through Graphitization and Core Nitrogen Doping. *Angew. Chemie - Int. Ed.* **56**, 6459–6463 (2017).

151. Hatchard, C. G. & Parker, C. A. A new sensitive chemical actinometer - II. Potassium ferrioxalate as a standard chemical actinometer. *Proc. R. Soc. London. Ser. A. Math. Phys. Sci.* **235**, 518–536 (1956).

152. Pitre, S. P. *et al.* Visible-Light Actinometry and Intermittent Illumination as Convenient Tools to Study $Ru(bpy)_3Cl_2$ Mediated Photoredox Transformations. *Sci. Rep.* **5**, 16397 (2015).

153. Vistica, J. *et al.* Sedimentation equilibrium analysis of protein interactions with global implicit mass conservation constraints and systematic noise decomposition. *Anal. Biochem.* **326**, 234–256 (2004).

154. Brautigam, C. A. Using Lamm-Equation modeling of sedimentation velocity data to determine the kinetic and thermodynamic properties of macromolecular

interactions. *Methods* **54**, 4–15 (2011).

155. Zaccai, G. & Jacrot, B. Small Angle Neutron Scattering. *Annu. Rev. Biophys. Bioeng.* **12**, 139–157 (1983).

156. Svergun, D. I., Koch, M. H. J., Timmins, P. A. & May, R. P. *Small Angle X-Ray and Neutron Scattering from Solutions of Biological Macromolecules*. (Oxford University Press, 2013). doi:10.1093/acprof:oso/9780199639533.001.0001.

157. Edwards, M. J. *et al.* Structural modeling of an outer membrane electron conduit from a metal-reducing bacterium suggests electron transfer via periplasmic redox partners. *J. Biol. Chem.* **293**, 8103–8112 (2018).

158. Breyton, C. *et al.* Small angle neutron scattering for the study of solubilised membrane proteins. *Eur. Phys. J. E. Soft Matter* **36**, 71 (2013).

159. Compton, E. L. R., Karinou, E., Naismith, J. H., Gabel, F. & Javelle, A. Low resolution structure of a bacterial SLC26 transporter reveals dimeric stoichiometry and mobile intracellular domains. *J. Biol. Chem.* **286**, 27058–27067 (2011).

160. Stikane, A. *et al.* Towards compartmentalized photocatalysis: multihaem proteins as transmembrane molecular electron conduits. *Faraday Discuss.* **215**, 26–38 (2019).

161. Stetefeld, J., McKenna, S. A. & Patel, T. R. Dynamic light scattering: a practical guide and applications in biomedical sciences. *Biophys. Rev.* **8**, 409–427 (2016).

162. Malloy, A. & Carr, B. NanoParticle Tracking Analysis - The Halo™ System. *Part. Part. Syst. Charact.* **23**, 197–204 (2006).

163. Avanti Polar lipids Inc. E. coli Extract Polar. https://avantilipids.com/product/100600.

164. Avanti Polar lipids Inc. E. coli PE. https://avantilipids.com/product/840027.

165. Avanti Polar lipids Inc. E. coli PG. https://avantilipids.com/product/841188.

166. Avanti Polar lipids Inc. E. coli CA. https://avantilipids.com/product/841199.

167. Nagle, J. F. & Tristram-Nagle, S. Structure of lipid bilayers. *Biochim. Biophys. Acta - Rev. Biomembr.* **1469**, 159–195 (2000).

168. Ross, D. E. *et al.* Characterization of protein-protein interactions involved in iron reduction by *Shewanella oneidensis* MR-1. *Appl. Environ. Microbiol.* **73**, 5797–5808 (2007).

169. Baiden, N. *et al.* Exploring the biochemistry at the extracellular redox frontier of bacterial mineral Fe(III) respiration. *Biochem. Soc. Trans.* **40**, 493–500 (2012).

170. Shi, L. *et al.* Molecular underpinnings of Fe(III) oxide reduction by *Shewanella oneidensis* MR-1. *Front. Microbiol.* **3**, 1–10 (2012).

171. Hartshorne, R. S. *et al.* Characterization of an electron conduit between bacteria and the extracellular environment. *Proc. Natl. Acad. Sci.* **106**, 22169–22174 (2009).

172. Pitts, K. E. *et al.* Characterization of the *Shewanella oneidensis* MR-1 decaheme cytochrome MtrA: Expression in *Escherichia coli* confers the ability to reduce soluble Fe(III) chelates. *J. Biol. Chem.* **278**, 27758–27765 (2003).

173. Willie, A., Durham, B., Millett, F., Stayton, P. S. & Sligar, S. G. Genetic Engineering of Redox Donor Sites : Measurement of Intracomplex Electron Transfer between Ruthenium-65-Cytochrome b_5 and Cytochrome *c*.

Biochemistry **31**, 7237–7242 (1992).

174. Seung, H., Bill, D. & Francis, M. Photoinduced Electron Transfer Between Cytochrome *c* Peroxidase and Horse Cytochrome *c* Labeled at Specific Lysines with (Dicarboxybipyridine)(bisbipyridine)ruthenium(II). *Biochemistry* **31**, 3472–3477 (1992).

175. Geren, L., Hahm, S., Durham, B. & Millett, F. Photoinduced electron transfer between Cytochrome *c* peroxidase and yeast cytochrome *c* labeled at Cys 102 with (4-bromomethyl-4'-methylbipyridine)[bis(bipyridine)]ruthenium^{2+}. *Biochemistry* **30**, 9450–9457 (1991).

176. Kokhan, O. *et al.* Bidirectional Photoinduced Electron Transfer in Ruthenium(II)-Tris-bipyridyl-Modified PpcA, a Multi-heme c -Type Cytochrome from *Geobacter sulfurreducens*. *J. Phys. Chem. B* **119**, 7612–7624 (2015).

177. Millett, F. & Durham, B. Design of Photoactive Ruthenium Complexes To Study Interprotein Electron Transfer †. *Biochemistry* **41**, 11315–11324 (2002).

178. Barrozo, A., El-Naggar, M. Y. & Krylov, A. I. Distinct Electron Conductance Regimes in Bacterial Decaheme Cytochromes. *Angew. Chemie - Int. Ed.* **57**, 6805–6809 (2018).

179. Geren, L., Durham, B. & Millett, F. Use of ruthenium photoreduction techniques to study electron transfer in cytochrome oxidase. in *Methods in Enzymology* vol. 456 507–520 (Elsevier Inc., 2009).

180. Sano, Y., Onoda, A. & Hayashi, T. Photocatalytic hydrogen evolution by a diiron hydrogenase model based on a peptide fragment of cytochrome c_{556} with an attached diiron carbonyl cluster and an attached ruthenium photosensitizer. *J. Inorg. Biochem.* **108**, 159–162 (2012).

181. Kennelly, T., Strekas, T. C. & Gafney, H. D. Evidence for the formation of a photoactive tris(2,2'-bipyridine)ruthenium(II)-ethylenediaminetetraacetic acid ion pair. *J. Phys. Chem.* **90**, 5338–5339 (1986).

182. Harris, D. C. & Lucy, C. A. *Quantitative chemical analysis, 9th ed.* (W.H.Freeman & Co Ltd, 2015).

183. Mulazzani, Q. G., Venturi, M. & Hoffman, M. Z. Radiolytically induced one-electron reduction of methylviologen in aqueous solution. Reactivity of EDTA radicals toward methylviologen. *J. Phys. Chem.* **89**, 722–728 (1985).

184. Bafana, A., Devi, S. S. & Chakrabarti, T. Azo dyes: Past, present and the future. *Environ. Rev.* **19**, 350–370 (2011).

185. Clarke, E. A. & Anliker, R. Organic Dyes and Pigments. in *Anthropogenic Compounds* (eds. Anliker, R. et al.) 181–215 (Springer Berlin Heidelberg, 1980). doi:10.1007/978-3-540-38522-6_7.

186. Singh, R. L., Singh, P. K. & Singh, R. P. Enzymatic decolorization and degradation of azo dyes - A review. *Int. Biodeterior. Biodegrad.* **104**, 21–31 (2015).

187. Pandey, A., Singh, P. & Iyengar, L. Bacterial decolorization and degradation of azo dyes. *Int. Biodeterior. Biodegrad.* **59**, 73–84 (2007).

188. Maier, J., Kandelbauer, A., Erlacher, A., Cavaco-Paulo, A. & Gübitz, G. M. A New Alkali-Thermostable Azoreductase from *Bacillus* sp. Strain SF. *Appl. Environ. Microbiol.* **70**, 837–844 (2004).

189. Chen, H., Hopper, S. L. & Cerniglia, C. E. Biochemical and molecular characterization of an azoreductase from *Staphylococcus aureus*, a tetrameric

NADPH-dependent flavoprotein. *Microbiology* **151**, 1433–1441 (2005).

190. Nakanishi, M., Yatome, C., Ishida, N. & Kitade, Y. Putative ACP Phosphodiesterase Gene (*acpD*) Encodes an Azoreductase. *J. Biol. Chem.* **276**, 46394–46399 (2001).

191. Bin, Y. *et al.* Expression and characteristics of the gene encoding azoreductase from *Rhodobacter sphaeroides* AS1.1737. *FEMS Microbiol. Lett.* **236**, 129–136 (2004).

192. Chivukula, M. & Renganathan, V. Phenolic azo dye oxidation by laccase from *Pyricularia oryzae*. *Appl. Environ. Microbiol.* **61**, 4374–4377 (1995).

193. Peralta-Zamora, P. *et al.* Decolorization of reactive dyes by immobilized laccase. *Appl. Catal. B Environ.* **42**, 131–144 (2003).

194. Shrivastava, R., Christian, V. & Vyas, B. R. M. Enzymatic decolorization of sulfonphthalein dyes. *Enzyme Microb. Technol.* **36**, 333–337 (2005).

195. Goszczynski, S., Paszczynski, A., Pasti-Grigsby, M. B., Crawford, R. L. & Crawford, D. L. New pathway for degradation of sulfonated azo dyes by microbial peroxidases of *Phanerochaete chrysosporium* and *Streptomyces chromofuscus*. *J. Bacteriol.* **176**, 1339–1347 (1994).

196. Jadhav, U. U., Dawkar, V. V., Jadhav, M. U. & Govindwar, S. P. Decolorization of the Textile Dyes Using Purified Banana Pulp Polyphenol Oxidase. *Int. J. Phytoremediation* **13**, 357–372 (2011).

197. Hong, Y. G. & Gu, J. D. Physiology and biochemistry of reduction of azo compounds by Shewanella strains relevant to electron transport chain. *Appl. Microbiol. Biotechnol.* **88**, 637–643 (2010).

198. Brigé, A. *et al.* Bacterial decolorization of textile dyes is an extracellular process requiring a multicomponent electron transfer pathway. *Microb. Biotechnol.* **1**, 40–52 (2008).

199. Rauf, M. A., Hisaindee, S. & Saleh, N. Spectroscopic studies of keto-enol tautomeric equilibrium of azo dyes. *RSC Adv.* **5**, 18097–18110 (2015).

200. Hsueh, C. C., Chen, B. Y. & Yen, C. Y. Understanding effects of chemical structure on azo dye decolorization characteristics by Aeromonas hydrophila. *J. Hazard. Mater.* **167**, 995–1001 (2009).

201. Supaka, N., Juntongjin, K., Damronglerd, S., Delia, M. L. & Strehaiano, P. Microbial decolorization of reactive azo dyes in a sequential anaerobic-aerobic system. *Chem. Eng. J.* **99**, 169–176 (2004).

202. ISS. Lifetime Data of Selected Fluorophores. http://www.iss.com/resources/reference/data_tables/LifetimeDataFluorophores.html.

203. Kuzmič, P. Program DYNAFIT for the Analysis of Enzyme Kinetic Data: Application to HIV Proteinase. *Anal. Biochem.* **237**, 260–273 (1996).

204. Jiang, X. *et al.* Kinetics of trifurcated electron flow in the decaheme bacterial proteins MtrC and MtrF. *Proc. Natl. Acad. Sci. U. S. A.* **116**, 3425–3430 (2019).

205. Strop, P. & Brunger, A. T. Refractive index-based determination of detergent concentration and its application to the study of membrane proteins. *Protein Sci.* **14**, 2207–2211 (2005).

206. Herrmann, K. W. Non-ionic-cationic micellar properties of dimethyldodecylamine oxide. *J. Phys. Chem.* **66**, 295–300 (1962).

207. Timmins, P. A., Leonhard, M., Weltzien, H. U., Wacker, T. & Welte, W. A physical characterization of some detergents of potential use for membrane protein crystallization. *FEBS Lett.* **238**, 361–368 (1988).

208. Edwards, M. J. *et al.* The X-ray crystal structure of *Shewanella oneidensis* OmcA reveals new insight at the microbe-mineral interface. *FEBS Lett.* **588**, 1886–1890 (2014).

209. Putnam, C. D. Guinier peak analysis for visual and automated inspection of small-Angle X-ray scattering data. *J. Appl. Crystallogr.* **49**, 1412–1419 (2016).

210. Konarev, P. V., Volkov, V. V., Sokolova, A. V., Koch, M. H. J. & Svergun, D. I. PRIMUS : a Windows PC-based system for small-angle scattering data analysis. *J. Appl. Crystallogr.* **36**, 1277–1282 (2003).

211. Svergun, D. I. Restoring low resolution structure of biological macromolecules from solution scattering using simulated annealing. *Biophys. J.* **76**, 2879–2886 (1999).

212. Kozin, M. B. & Svergun, D. I. Automated matching of high- and low-resolution structural models. *J. Appl. Crystallogr.* **34**, 33–41 (2001).

213. Petoukhov, M. V. & Svergun, D. I. Joint use of small-angle X-ray and neutron scattering to study biological macromolecules in solution. *Eur. Biophys. J.* **35**, 567–576 (2006).

214. White, G. F. *et al.* Development of a proteoliposome model to probe transmembrane electron-transfer reactions. *Biochem. Soc. Trans.* **40**, 1257–1260 (2012).

215. White, G. F. *et al.* Rapid electron exchange between surface-exposed bacterial cytochromes and Fe(III) minerals. *Proc. Natl. Acad. Sci. U. S. A.* **110**, 6346–51 (2013).

216. Paraskevopoulos, K., Antonyuk, S. V, Sawers, R. G., Eady, R. R. & Hasnain, S. S. Insight into Catalysis of Nitrous Oxide Reductase from High-resolution Structures of Resting and Inhibitor-bound Enzyme from *Achromobacter cycloclastes*. *J. Mol. Biol.* **362**, 55–65 (2006).

217. Brown, K. *et al.* Revisiting the catalytic CuZ cluster of nitrous oxide (N_2O) reductase: Evidence of a bridging inorganic sulfur. *J. Biol. Chem.* **275**, 41133–41136 (2000).

218. Pomowski, A., Zumft, W. G., Kroneck, P. M. H. & Einsle, O. N_2O binding at a [4Cu:2S] copper-sulphur cluster in nitrous oxide reductase. *Nature* **477**, 234–237 (2011).

219. Schneider, L. K. & Einsle, O. Role of Calcium in Secondary Structure Stabilization during Maturation of Nitrous Oxide Reductase. *Biochemistry* **55**, 1433–1440 (2016).

220. Prudêncio, M. *et al.* Purification, Characterization, and Preliminary Crystallographic Study of Copper-Containing Nitrous Oxide Reductase from *Pseudomonas nautica* 617 †. *Biochemistry* **39**, 3899–3907 (2000).

221. Haltia, T. *et al.* Crystal structure of nitrous oxide reductase from *Paracoccus denitrificans* at 1.6 A resolution. *Biochem. J.* **369**, 77–88 (2003).

222. Kelly, M. *et al.* Two cysteines, two histidines, and one methionine are ligands of a binuclear purple copper center. *J. Biol. Chem.* **268**, 16781–16787 (1993).

223. Iwata, S., Ostermeier, C., Ludwig, B. & Michel, H. Structure at 2.8 Å resolution of cytochrome c oxidase from *Paracoccus denitrificans*. *Nature* **376**, 660–669

(1995).

224. Tsukihara, T. *et al.* Structures of metal sites of oxidized bovine heart cytochrome c oxidase at 2.8 A. *Science* **269**, 1069–74 (1995).

225. Rasmussen, T. *et al.* The catalytic center in nitrous oxide reductase, Cu_z, is a copper-sulfide cluster. *Biochemistry* **39**, 12753–12756 (2000).

226. Johnston, E. M. *et al.* Determination of the active form of the tetranuclear copper sulfur cluster in nitrous oxide reductase. *J. Am. Chem. Soc.* **136**, 614–617 (2014).

227. Johnston, E. M. *et al.* Spectroscopic Definition of the CuZ° Intermediate in Turnover of Nitrous Oxide Reductase and Molecular Insight into the Catalytic Mechanism. *J. Am. Chem. Soc.* **139**, 4462–4476 (2017).

228. Dell'Acqua, S. *et al.* A new CuZ active form in the catalytic reduction of N_2O by nitrous oxide reductase from Pseudomonas nautica. *JBIC J. Biol. Inorg. Chem.* **15**, 967–976 (2010).

229. Ghosh, S. *et al.* Activation of N_2O Reduction by the Fully Reduced μ_4-Sulfide Bridged Tetranuclear Cu_z Cluster in Nitrous Oxide Reductase. *J. Am. Chem. Soc.* **125**, 15708–15709 (2003).

230. Wunsch, P. & Zumft, W. G. Functional domains of NosR, a novel transmembrane iron-sulfur flavoprotein necessary for nitrous oxide respiration. *J. Bacteriol.* **187**, 1992–2001 (2005).

231. Wunsch, P. *et al.* NosX function connects to nitrous oxide (N2O) reduction by affecting the CuZ center of NosZ and its activity *in vivo*. *FEBS Lett.* **579**, 4605–4609 (2005).

232. Bennett, S. P. *et al. nosX* is essential for whole-cell N_2O reduction in *Paracoccus denitrificans* but not for assembly of copper centres of nitrous oxide reductase. *Microbiology* **166**, 909–917 (2020).

233. Zajicek, R. S., Allen, J. W. A., Cartron, M. L., Richardson, D. J. & Ferguson, S. J. Paracoccus pantotrophus NapC can reductively activate cytochrome cd_1 nitrite reductase. *FEBS Lett.* **565**, 48–52 (2004).

234. Moir, J. W. B. & Ferguson, S. J. Properties of a *Paracoccus denitrificans* mutant deleted in cytochrome c_{550} indicate that a copper protein can substitute for this cytochrome in electron transport to nitrite, nitric oxide and nitrous oxide. *Microbiology* **140**, 389–397 (1994).

235. Mattila, K. & Haltia, T. How does nitrous oxide reductase interact with its electron donors? A docking study. *Proteins Struct. Funct. Genet.* **59**, 708–722 (2005).

236. Koutný, M., Kučera, I., Tesařík, R., Turánek, J. & Van Spanning, R. J. M. Pseudoazurin mediates periplasmic electron flow in a mutant strain of *Paracoccus denitrificans* lacking cytochrome c_{550}. *FEBS Lett.* **448**, 157–159 (1999).

237. Bird, C. L. & Kuhn, A. T. Electrochemistry of the viologens. *Chem. Soc. Rev.* **10**, 49–82 (1981).

238. Gorelsky, S. I., Ghosh, S. & Solomon, E. I. Mechanism of N_2O reduction by the μ_4-S tetranuclear CuZ cluster of nitrous oxide reductase. *J. Am. Chem. Soc.* **128**, 278–290 (2006).

239. Chan, J. M., Bollinger, J. A., Grewell, C. L. & Dooley, D. M. Reductively Activated Nitrous Oxide Reductase Reacts Directly with Substrate. *J. Am. Chem. Soc.* **126**, 3030–3031 (2004).

240. Mueller, P. & Rudin, D. O. Development of K^+ - Na^+ discrimination in experimental bimolecular lipid membranes by macrocyclic antibiotics. *Biochem. Biophys. Res. Commun.* **26**, 398–404 (1967).

241. Dell'Acqua, S. *et al.* Electron transfer complex between nitrous oxide reductase and cytochrome c_{552} from *Pseudomonas nautica*: Kinetic, nuclear magnetic resonance, and docking studies. *Biochemistry* **47**, 10852–10862 (2008).

242. Lacasse, M. J. *et al.* A whole-cell, high-throughput hydrogenase assay to identify factors that modulate [NiFe]-hydrogenase activity. *J. Biol. Chem.* **294**, 15373–15385 (2019).

243. Illichmanová, A., Janů, M., Sedláček, V. & Kučera, I. Nitrate reductase whole-cell assay: side effects associated with the use of benzyl viologen. *Folia Microbiol. (Praha).* **56**, 72–6 (2011).

244. Jones, R. W., Gray, T. A. & Garland, P. B. A study of the permeability of the cytoplasmic membrane of *Escherichia coli* to reduced and oxidized benzyl viologen and methyl viologen cations: complications in the use of viologens as redox mediators for membrane bound enzymes. *Biochem. Soc. Trans.* **4**, 671–673 (1976).

245. Fujita, K. *et al.* Direct electron transfer from pseudoazurin to nitrous oxide reductase in catalytic N_2O reduction. *J. Inorg. Biochem.* **115**, 163–173 (2012).

246. Lorber, B., Bishop, J. B. & DeLucas, L. J. Purification of octyl β-$_D$-glucopyranoside and re-estimation of its micellar size. *BBA - Biomembr.* **1023**, 254–265 (1990).

247. Ross, D. E., Flynn, J. M., Baron, D. B., Gralnick, J. A. & Bond, D. R. Towards electrosynthesis in *Shewanella*: energetics of reversing the Mtr pathway for reductive metabolism. *PLoS One* **6**, e16649 (2011).

248. Rowe, A. R. *et al.* Tracking electron uptake from a cathode into *Shewanella* cells: Implications for energy acquisition from solid-substrate electron donors. *MBio* **9**, 1–19 (2018).

249. Jensen, H. M. *et al.* Engineering of a synthetic electron conduit in living cells. *Proc. Natl. Acad. Sci.* **107**, 19213–19218 (2010).

250. Goldbeck, C. P. *et al.* Tuning promoter strengths for improved synthesis and function of electron conduits in Escherichia coli. *ACS Synth. Biol.* **2**, 150–159 (2013).

251. Feng, J. *et al.* Direct electron uptake from a cathode using the inward Mtr pathway in *Escherichia coli*. *Bioelectrochemistry* **134**, 107498 (2020).

252. Harada, E. *et al.* A directional electron transfer regulator based on heme-chain architecture in the small tetraheme cytochrome c from *Shewanella oneidensis*. *FEBS Lett.* **532**, 333–337 (2002).

253. Knol, J., Sjollema, K. & Poolman, B. Detergent-mediated reconstitution of membrane proteins. *Biochemistry* **37**, 16410–16415 (1998).

254. Tunuguntla, R. *et al.* Lipid bilayer composition can influence the orientation of proteorhodopsin in artificial membranes. *Biophys. J.* **105**, 1388–1396 (2013).

255. Hutton, G. A. M., Martindale, B. C. M. & Reisner, E. Carbon dots as photosensitisers for solar-driven catalysis. *Chem. Soc. Rev.* **46**, 6111–6123 (2017).

256. Burnett, D., Barbour, E. & Harrison, G. P. The UK solar energy resource and the impact of climate change. *Renew. Energy* **71**, 333–343 (2014).

257. Kosower, E. M. & Cotter, J. L. Stable Free Radicals. II. The Reduction of l-Methyl-4-cyanopyridinium Ion to Methylviologen Cation Radical. *J. Am. Chem. Soc.* **86**, 5524–5527 (1964).

258. Wadhwa, K. *et al.* Intramolecular redox-induced dimerization in a viologen dendrimer. *J. Mater. Chem. C* **1**, 2302–2307 (2013).

259. Geraskina, M. R., Dutton, A. S., Juetten, M. J., Wood, S. A. & Winter, A. H. The Viologen Cation Radical Pimer: A Case of Dispersion-Driven Bonding. *Angew. Chemie - Int. Ed.* **56**, 9435–9439 (2017).

260. Monk, P. M. S., Hodgkinson, N. M. & Ramzan, S. A. Spin pairing ('dimerisation') of the viologen radical cation: Kinetics and equilibria. *Dye. Pigment.* **43**, 207–217 (1999).

261. Xiao, L., Wildgoose, G. G. & Compton, R. G. Investigating the voltammetric reduction of methylviologen at gold and carbon based electrode materials. Evidence for a surface bound adsorption mechanism leading to electrode 'protection' using multi-walled carbon nanotubes. *New J. Chem.* **32**, 1628–1633 (2008).

262. Okamoto, A., Tokunou, Y., Kalathil, S. & Hashimoto, K. Proton Transport in the Outer-Membrane Flavocytochrome Complex Limits the Rate of Extracellular Electron Transport. *Angew. Chemie - Int. Ed.* **56**, 9082–9086 (2017).

263. Lang, K. *et al.* Genetically encoded norbornene directs site-specific cellular protein labelling via a rapid bioorthogonal reaction. *Nat. Chem.* **4**, 298–304 (2012).

264. Plass, T., Milles, S., Koehler, C., Schultz, C. & Lemke, E. A. Genetically encoded copper-free click chemistry. *Angew. Chemie - Int. Ed.* **50**, 3878–3881 (2011).

265. Plass, T. *et al.* Amino acids for diels-alder reactions in living cells. *Angew. Chemie - Int. Ed.* **51**, 4166–4170 (2012).

266. Maruani, A. *et al.* Site-selective multi-porphyrin attachment enables the formation of a next-generation antibody-based photodynamic therapeutic. *Chem. Commun.* **51**, 15304–15307 (2015).

267. Maruani, A. *et al.* A plug-and-play approach to antibody-based therapeutics via a chemoselective dual click strategy. *Nat. Commun.* **6**, 2–10 (2015).

268. Alefounder, P. R. & Ferguson, S. J. Electron transport-linked nitrous oxide synthesis and reduction by *Paracoccus denitrificans* monitored with an electrode. *Biochem. Biophys. Res. Commun.* **104**, 1149–1155 (1982).

269. Pouvreau, L. A. M., Strampraad, M. J. F., Berloo, S. Van, Kattenberg, J. H. & de Vries, S. NO, N_2O, and O_2 Reaction Kinetics: Scope and Limitations of the Clark Electrode. in *Globins and Other Nitric Oxide-Reactive Proteins, Part A* vol. 436 97–112 (Elsevier Masson SAS, 2008).

270. Pressman, B. C. Biological Applications of Ionophores. *Annu. Rev. Biochem.* **45**, 501–530 (1976).

271. Finnegan, S. & Percival, S. L. EDTA: An Antimicrobial and Antibiofilm Agent for Use in Wound Care. *Adv. Wound Care* **4**, 415–421 (2015).

APPENDIX

RuMe-MtrC PHOTOREDUCTION MODELLING

Appendix - Photoreduction kinetic modelling

A1 - Kinetic model frameworks

The RuMe-MtrC system can be split into a framework of 11 components with a total of 23 microstates: Ru can be in either the ground state (Ru), the excited state (Ru^{*}) or the oxidised state (Ru^{+}) and each heme can be oxidised or reduced.

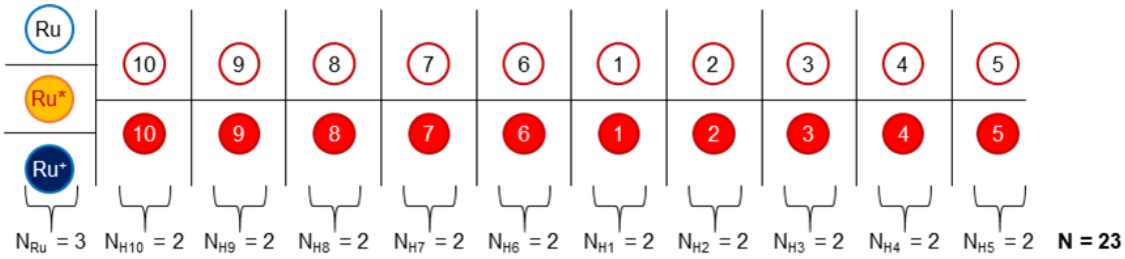

Figure A1.1 Fully dissociated RuMe-MtrC framework with 23 microstates

The RuMe-MtrC system could theoretically be considered as one component however this would require the definition of 3076 microstates.

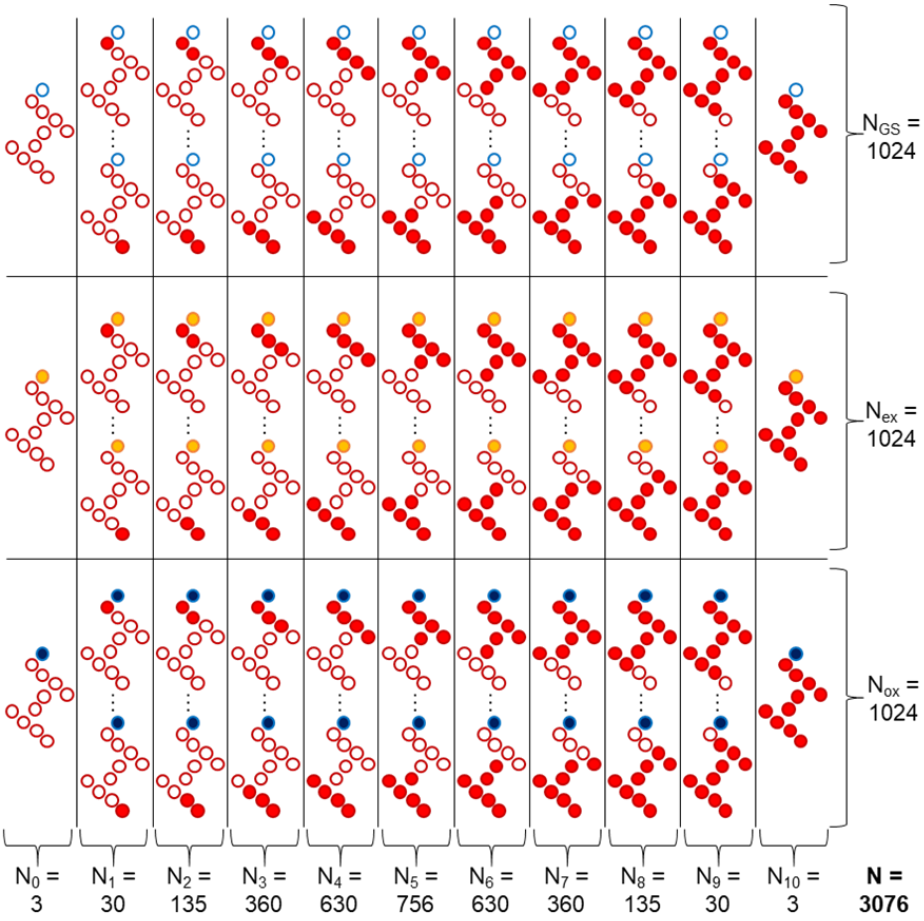

Figure A1.2 3076 microstates of a single component, fully defined RuMe-MtrC framework

To compromise, frameworks were created containing:

a fully defined component containing RuMe with either three (Ru, Ru^{*}, Ru^{+}) (Figs. A1.3&5) or four (Ru, Ru^{*}, Ru^{+}, Ru^{-}) (Figs. A1.4&6) states, and two (Figs. A1.3&4) or three (Figs. A1.5&6) hemes,

and the remaining hemes as individual components.

These frameworks were used to create Models 1-4.

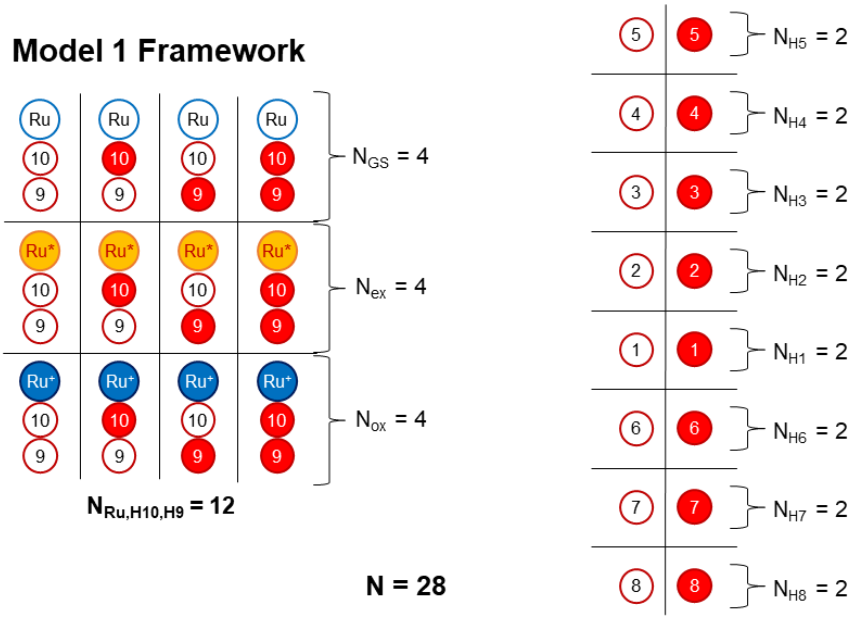

Figure A1.3 Framework used for Model 1 with 28 microstates

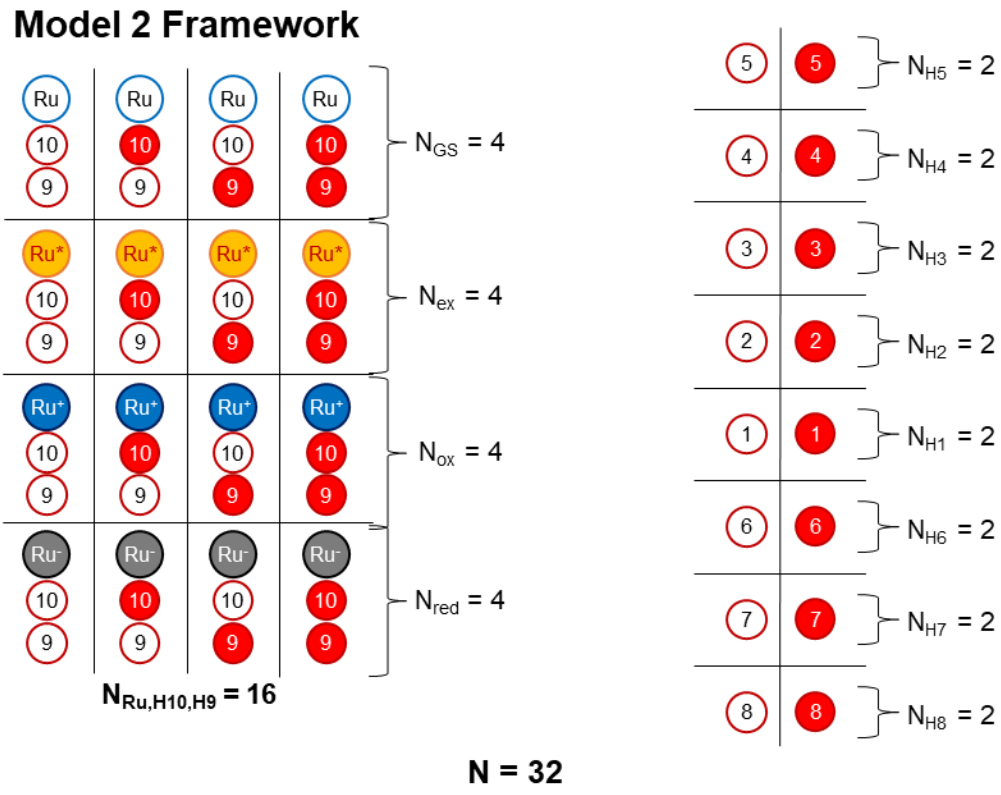

Figure A1.4 Framework used for Model 2 with 32 microstates

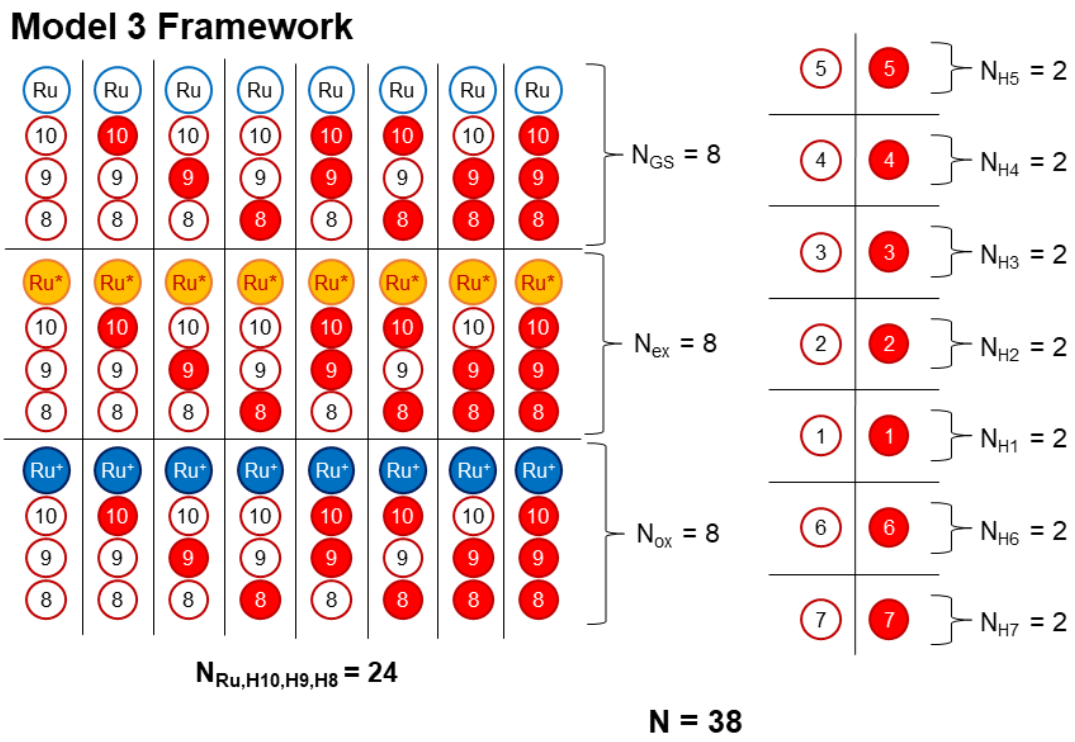

Figure A1.5 Framework used for Model 3 with 38 microstates

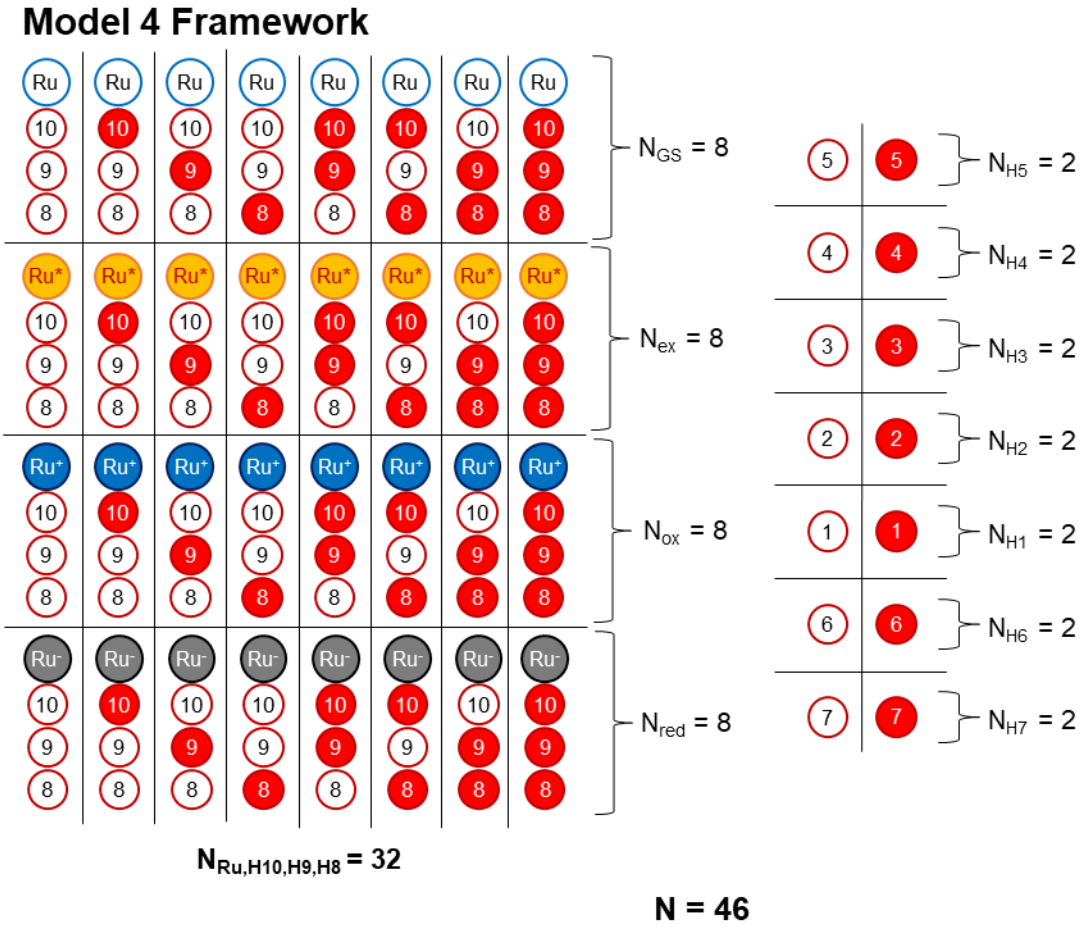

Figure A1.6 Framework used for Model 4 with 46 microstates

A2 - Interactions between microstates

All possible interactions between microstates were included in the models. This produced a complex web of interactions as shown in Figures A2.1&2 for Models 1 and 2 respectively. Models 2-4 used this same concept, producing even more complex networks.

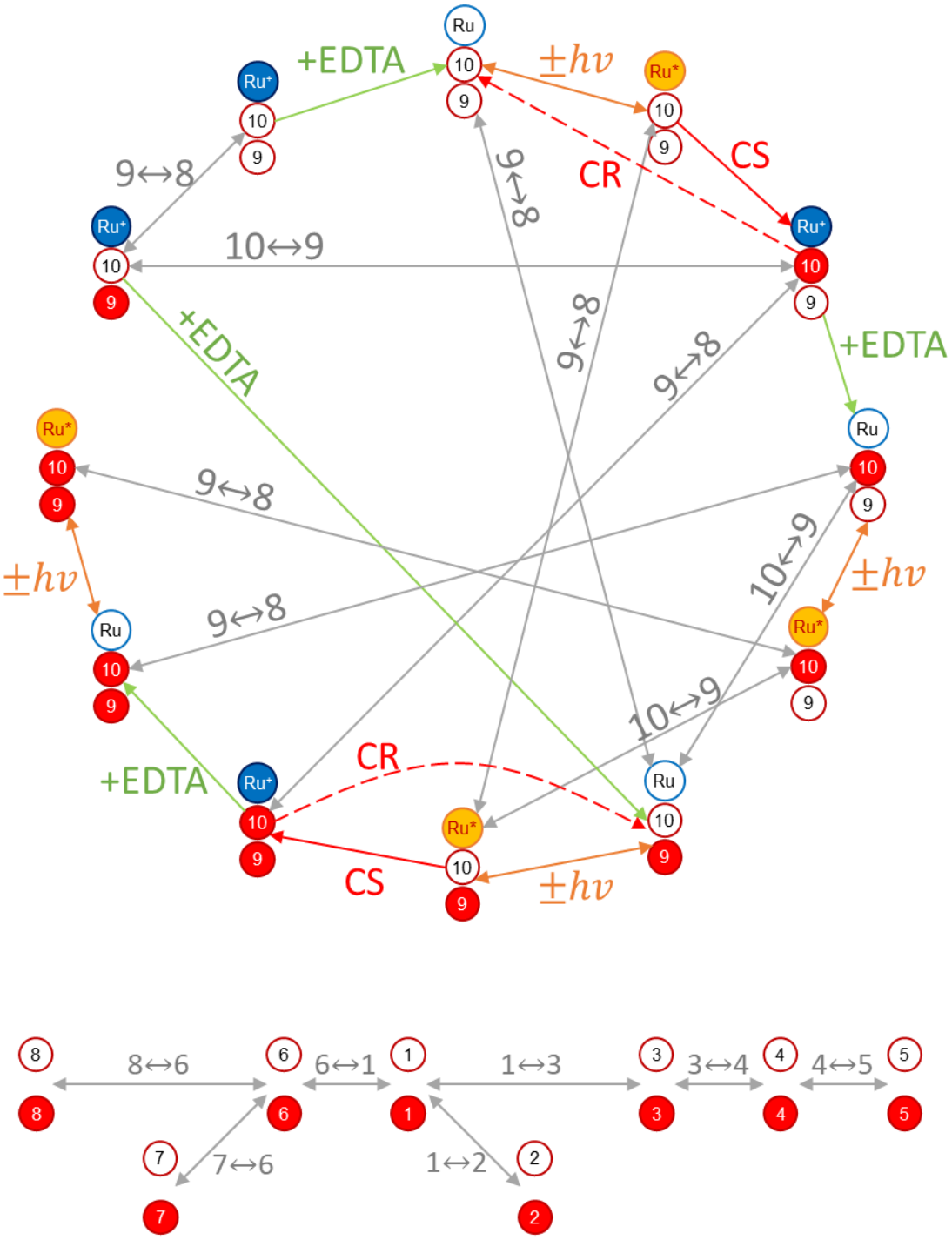

Figure A2.1 Interconversions of microstates in Model 1: excitation/relaxation ($\pm hv$) shown as orange double-headed arrow; charge separation (CS) shown as solid red arrow; charge recombination (CR) shown as dashed red arrow; charge trapping by EDTA (+EDTA) shown as green arrow; heme-heme electron transfers shown as grey double-headed arrows with specific hemes indicated.

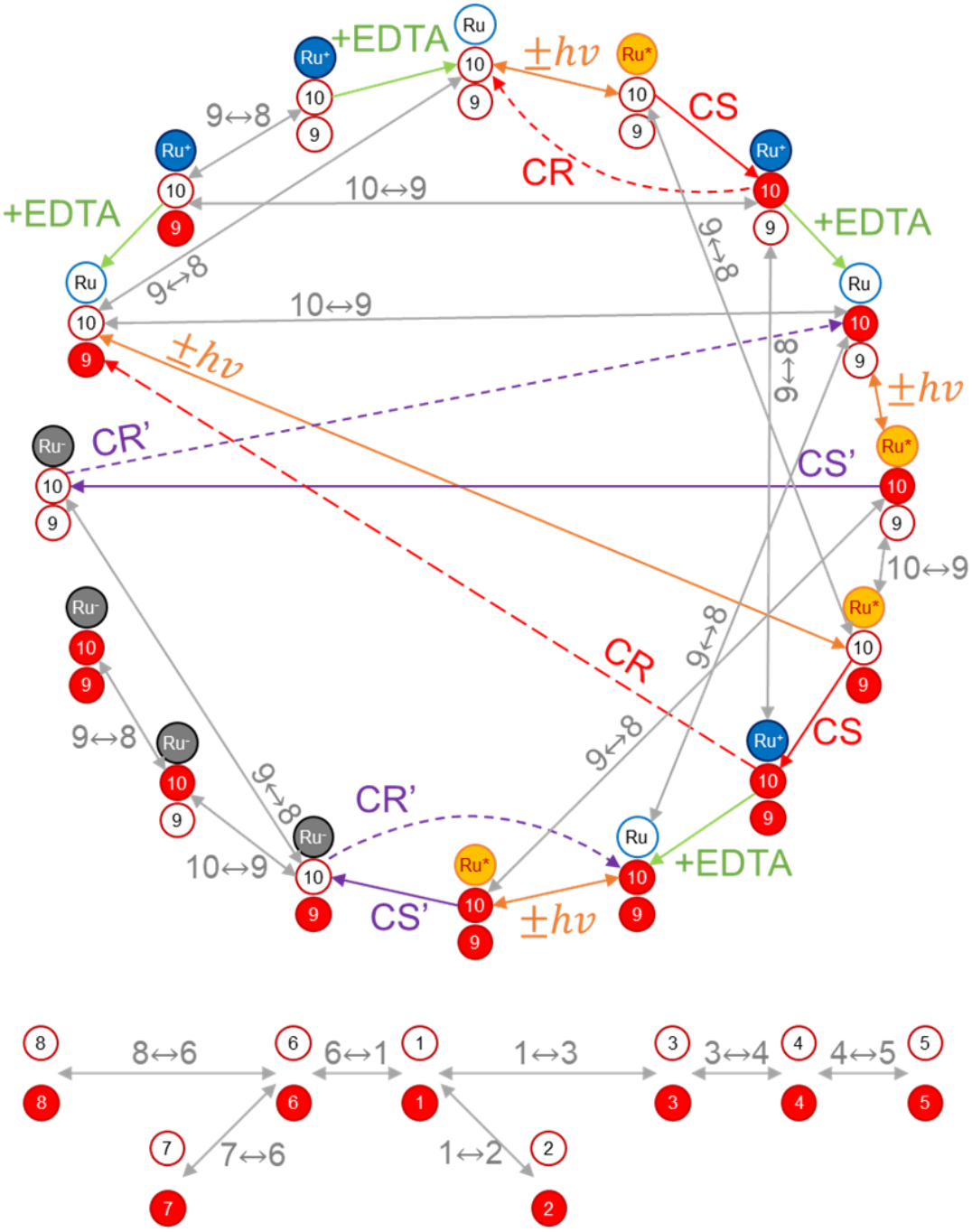

Figure A2.2 Interconversions of microstates in Model 2: excitation/relaxation ($\pm h\nu$) shown as orange double-headed arrow; charge separation by oxidative quenching (CS) shown as solid red arrow; charge recombination after oxidative quenching (CR) shown as dashed red arrow; charge separation by reductive quenching (CS') shown as solid purple arrow, charge recombination after reductive quenching (CR') shown as dashed purple arrow, charge trapping by EDTA (+EDTA) shown as green arrow; heme-heme electron transfers shown as grey double-headed arrows with specific hemes indicated.

A3 - Dynafit scripts

Model 1

```
[task]
  task = fit
  data = progress

[mechanism]
Ru.H10.H9 <===> Ruex.H10.H9 : kex krlx
Ru.H10red.H9 <===> Ruex.H10red.H9 : kex krlx
Ru.H10.H9red <===> Ruex.H10.H9red : kex krlx
Ru.H10red.H9red <===> Ruex.H10red.H9red : kex krlx

Ruex.H10.H9 ---> Ru3.H10red.H9 : kcs
Ruex.H10.H9red ---> Ru3.H10red.H9red : kcs

Ru3.H10red.H9 ---> Ru.H10.H9 : kcr
Ru3.H10red.H9red ---> Ru.H10.H9red : kcr

Ru.H10red.H9 <===> Ru.H10.H9red : k109 k910
Ruex.H10red.H9 <===> Ruex.H10.H9red : k109 k910
Ru3.H10red.H9 <===> Ru3.H10.H9red : k109 k910

Ru.H10.H9 + H8red <===> Ru.H10.H9red + H8 : k89 k98
Ru.H10red.H9 + H8red <===> Ru.H10red.H9red + H8 : k89 k98
Ruex.H10.H9 + H8red <===> Ruex.H10.H9red + H8 : k89 k98
Ruex.H10red.H9 + H8red <===> Ruex.H10red.H9red + H8 : k89 k98
Ru3.H10.H9 + H8red <===> Ru3.H10.H9red + H8 : k89 k98
Ru3.H10red.H9 + H8red <===> Ru3.H10red.H9red + H8 : k89 k98

Ru3.H10.H9 + EDTA ---> Ru.H10.H9 : ksed
Ru3.H10red.H9 + EDTA ---> Ru.H10red.H9 : ksed
Ru3.H10.H9red + EDTA ---> Ru.H10.H9red : ksed
Ru3.H10red.H9red + EDTA ---> Ru.H10red.H9red : ksed

H8red + H6 <===> H8 + H6red : k86 k68
H6red + H7 <===> H6 + H7red : k67 k76
H6red + H1 <===> H6 + H1red : k61 k16
H1red + H2 <===> H1 + H2red : k12 k21
H1red + H3 <===> H1 + H3red : k13 k31
H3red + H4 <===> H3 + H4red : k34 k43
H4red + H5 <===> H4 + H5red : k45 k54

[constants]
kex =   1.4
krlx =   2.16E6
kcs =   1.11E8
kcr =   3.33E8
ksed = 2E6 ?


k109 = 2.5E8
k910 = 1.43E7
k98 =   1E9
```

```
k89 =   1E9
k86 =   1E9
k68 =   1E9
k67 =   1E9
k76 =   1E9
k61 =   1E9
k16 =   1E9
k12 =   1E9
k21 =   1E9
k13 =   1E9
k31 =   1E9
k34 =   1E9
k43 =   1E9
k45 =   1E9
k54 =   1E9

[concentrations]
Ru.H10.H9 = 0.0000005 ;  M
H8 =    0.0000005 ; M
H7 =    0.0000005 ; M
H6 =    0.0000005 ; M
H5 =    0.0000005 ; M
H4 =    0.0000005 ; M
H3 =    0.0000005 ; M
H2 =    0.0000005 ; M
H1 =    0.0000005 ; M

[responses]
Ru.H10red.H9 = 18300
Ruex.H10red.H9 = 18300
Ru3.H10red.H9 = 18300
Ru.H10.H9red = 18300
Ruex.H10.H9red = 18300
Ru3.H10.H9red = 18300
Ru.H10red.H9red = 36600
Ruex.H10red.H9red = 36600
Ru3.H10red.H9red = 36600
H8red = 18300
H7red = 18300
H6red = 18300
H5red = 18300
H4red = 18300
H3red = 18300
H2red = 18300
H1red = 18300


[data]

mesh       from 0 to 3600 step 1

directory  ./MtrC
extension  txt

file       250mM | conc EDTA = 0.25
file       100mM | conc EDTA = 0.1
file       50mM | conc EDTA = 0.05
```

```
file       25mM | conc EDTA = 0.025
file       5mM | conc EDTA = 0.005
file       0mM | conc EDTA = 0

[output]
   directory  ./MtrC/outputs/Model_1

[end]
```

Model 2

```
[task]
   task = fit
   data = progress

[mechanism]
Ru.H10.H9 <===> Ruex.H10.H9 : kex krlx
Ru.H10red.H9 <===> Ruex.H10red.H9 : kex krlx
Ru.H10.H9red <===> Ruex.H10.H9red : kex krlx
Ru.H10red.H9red <===> Ruex.H10red.H9red : kex krlx

Ruex.H10.H9 ---> Ru3.H10red.H9 : kcs
Ruex.H10.H9red ---> Ru3.H10red.H9red : kcs

Ru3.H10red.H9 ---> Ru.H10.H9 : kcr
Ru3.H10red.H9red ---> Ru.H10.H9red : kcr

Ruex.H10red.H9 ---> Ru1.H10.H9 : kcs'
Ruex.H10red.H9red ---> Ru1.H10.H9red : kcs'

Ru1.H10.H9 ---> Ru.H10red.H9 : kcr'
Ru1.H10.H9red ---> Ru.H10red.H9red : kcr'

Ru.H10red.H9 <===> Ru.H10.H9red : k109 k910
Ruex.H10red.H9 <===> Ruex.H10.H9red : k109 k910
Ru3.H10red.H9 <===> Ru3.H10.H9red : k109 k910
Ru1.H10.H9red <===> Ru1.H10red.H9 : k109 k910

Ru.H10.H9 + H8red <===> Ru.H10.H9red + H8 : k89 k98
Ru.H10red.H9 + H8red <===> Ru.H10red.H9red + H8 : k89 k98
Ruex.H10.H9 + H8red <===> Ruex.H10.H9red + H8 : k89 k98
Ruex.H10red.H9 + H8red <===> Ruex.H10red.H9red + H8 : k89 k98
Ru3.H10.H9 + H8red <===> Ru3.H10.H9red + H8 : k89 k98
Ru3.H10red.H9 + H8red <===> Ru3.H10red.H9red + H8 : k89 k98
Ru1.H10.H9 + H8red <===> Ru1.H10.H9red + H8 : k89 k98
Ru1.H10red.H9 + H8red <===> Ru1.H10red.H9red + H8 : k89 k98

Ru3.H10.H9 + EDTA ---> Ru.H10.H9 : ksed
Ru3.H10red.H9 + EDTA ---> Ru.H10red.H9 : ksed
Ru3.H10.H9red + EDTA ---> Ru.H10.H9red : ksed
Ru3.H10red.H9red + EDTA ---> Ru.H10red.H9red : ksed

H8red + H6 <===> H8 + H6red : k86 k68
H6red + H7 <===> H6 + H7red : k67 k76
H6red + H1 <===> H6 + H1red : k61 k16
```

```
H1red + H2 <===> H1 + H2red : k12 k21
H1red + H3 <===> H1 + H3red : k13 k31
H3red + H4 <===> H3 + H4red : k34 k43
H4red + H5 <===> H4 + H5red : k45 k54

[constants]
kex =   1.4
krlx =   2.16E6
kcs =   1.11E8
kcr =   3.33E8
kcs' =   1.4E7
kcr' =   5E6 ?
ksed = 2.8E6


k109 = 2.5E8
k910 = 1.43E7
k98 =   1E9
k89 =   1E9
k86 =   1E9
k68 =   1E9
k67 =   1E9
k76 =   1E9
k61 =   1E9
k16 =   1E9
k12 =   1E9
k21 =   1E9
k13 =   1E9
k31 =   1E9
k34 =   1E9
k43 =   1E9
k45 =   1E9
k54 =   1E9

[concentrations]
Ru.H10.H9 = 0.0000005 ;  M
H8 =    0.0000005 ; M
H7 =    0.0000005 ; M
H6 =    0.0000005 ; M
H5 =    0.0000005 ; M
H4 =    0.0000005 ; M
H3 =    0.0000005 ; M
H2 =    0.0000005 ; M
H1 =    0.0000005 ; M

[responses]
Ru.H10red.H9 = 18300
Ruex.H10red.H9 = 18300
Ru3.H10red.H9 = 18300
Ru1.H10red.H9 = 18300
Ru.H10.H9red = 18300
Ruex.H10.H9red = 18300
Ru3.H10.H9red = 18300
Ru1.H10.H9red = 18300
Ru.H10red.H9red = 36600
Ruex.H10red.H9red = 36600
Ru3.H10red.H9red = 36600
```

```
Ru1.H10red.H9red = 36600

H8red = 18300
H7red = 18300
H6red = 18300
H5red = 18300
H4red = 18300
H3red = 18300
H2red = 18300
H1red = 18300


[data]

mesh       from 0 to 3600 step 1

directory  ./MtrC
extension  txt

file       250mM | conc EDTA = 0.25
file       100mM | conc EDTA = 0.1
file       50mM | conc EDTA = 0.05
file       25mM | conc EDTA = 0.025
file       5mM | conc EDTA = 0.005
file       0mM | conc EDTA = 0

[output]
   directory  ./MtrC/outputs/Model_2

[end]
```

Model 3

```
[task]
   task = fit
   data = progress

[mechanism]
Ru.H10.H9.H8 <===> Ruex.H10.H9.H8 : kex krlx
Ru.H10red.H9.H8 <===> Ruex.H10red.H9.H8 : kex krlx
Ru.H10.H9red.H8 <===> Ruex.H10.H9red.H8 : kex krlx
Ru.H10red.H9red.H8 <===> Ruex.H10red.H9red.H8 : kex krlx
Ru.H10.H9.H8red <===> Ruex.H10.H9.H8red : kex krlx
Ru.H10red.H9.H8red <===> Ruex.H10red.H9.H8red : kex krlx
Ru.H10.H9red.H8red <===> Ruex.H10.H9red.H8red : kex krlx
Ru.H10red.H9red.H8red <===> Ruex.H10red.H9red.H8red : kex krlx

Ruex.H10.H9.H8 ---> Ru3.H10red.H9.H8 : kcs
Ruex.H10.H9red.H8 ---> Ru3.H10red.H9red.H8 : kcs
Ruex.H10.H9.H8red ---> Ru3.H10red.H9.H8red : kcs
Ruex.H10.H9red.H8red ---> Ru3.H10red.H9red.H8red : kcs

Ru3.H10red.H9.H8 ---> Ru.H10.H9.H8 : kcr
Ru3.H10red.H9red.H8 ---> Ru.H10.H9red.H8 : kcr
Ru3.H10red.H9.H8red ---> Ru.H10.H9.H8red : kcr
```

Ru3.H10red.H9red.H8red ---> Ru.H10.H9red.H8red : kcr

Ru.H10red.H9.H8 <===> Ru.H10.H9red.H8 : k109 k910
Ruex.H10red.H9.H8 <===> Ruex.H10.H9red.H8 : k109 k910
Ru3.H10red.H9.H8 <===> Ru3.H10.H9red.H8 : k109 k910
Ru.H10red.H9.H8red <===> Ru.H10.H9red.H8red : k109 k910
Ruex.H10red.H9.H8red <===> Ruex.H10.H9red.H8red : k109 k910
Ru3.H10red.H9.H8red <===> Ru3.H10.H9red.H8red : k109 k910

Ru.H10.H9.H8red <===> Ru.H10.H9red.H8 : k89 k98
Ru.H10red.H9.H8red <===> Ru.H10red.H9red.H8 : k89 k98
Ruex.H10.H9.H8red <===> Ruex.H10.H9red.H8 : k89 k98
Ruex.H10red.H9.H8red <===> Ruex.H10red.H9red.H8 : k89 k98
Ru3.H10.H9.H8red <===> Ru3.H10.H9red.H8 : k89 k98
Ru3.H10red.H9.H8red <===> Ru3.H10red.H9red.H8 : k89 k98

Ru3.H10.H9.H8 + EDTA ---> Ru.H10.H9.H8 : ksed
Ru3.H10red.H9.H8 + EDTA ---> Ru.H10red.H9.H8 : ksed
Ru3.H10.H9red.H8 + EDTA ---> Ru.H10.H9red.H8 : ksed
Ru3.H10red.H9red.H8 + EDTA ---> Ru.H10red.H9red.H8 : ksed
Ru3.H10.H9.H8red + EDTA ---> Ru.H10.H9.H8red : ksed
Ru3.H10red.H9.H8red + EDTA ---> Ru.H10red.H9.H8red : ksed
Ru3.H10.H9red.H8red + EDTA ---> Ru.H10.H9red.H8red : ksed
Ru3.H10red.H9red.H8red + EDTA ---> Ru.H10red.H9red.H8red : ksed

Ru.H10.H9.H8red + H6 <===> Ru.H10.H9.H8 + H6red : k86 k68
Ruex.H10.H9.H8red + H6 <===> Ruex.H10.H9.H8 + H6red : k86 k68
Ru3.H10.H9.H8red + H6 <===> Ru3.H10.H9.H8 + H6red : k86 k68
Ru.H10red.H9.H8red + H6 <===> Ru.H10red.H9.H8 + H6red : k86 k68
Ruex.H10red.H9.H8red + H6 <===> Ruex.H10red.H9.H8 + H6red : k86 k68
Ru3.H10red.H9.H8red + H6 <===> Ru3.H10red.H9.H8 + H6red : k86 k68
Ru.H10.H9red.H8red + H6 <===> Ru.H10.H9red.H8 + H6red : k86 k68
Ruex.H10.H9red.H8red + H6 <===> Ruex.H10.H9red.H8 + H6red : k86 k68
Ru3.H10.H9red.H8red + H6 <===> Ru3.H10.H9red.H8 + H6red : k86 k68
Ru.H10red.H9red.H8red + H6 <===> Ru.H10red.H9red.H8 + H6red : k86 k68
Ruex.H10red.H9red.H8red + H6 <===> Ruex.H10red.H9red.H8 + H6red : k86 k68
Ru3.H10red.H9red.H8red + H6 <===> Ru3.H10red.H9red.H8 + H6red : k86 k68

H6red + H7 <===> H6 + H7red : k67 k76
H6red + H1 <===> H6 + H1red : k61 k16
H1red + H2 <===> H1 + H2red : k12 k21
H1red + H3 <===> H1 + H3red : k13 k31
H3red + H4 <===> H3 + H4red : k34 k43
H4red + H5 <===> H4 + H5red : k45 k54

[constants]
kex = 1.4
krlx = 2.16E6
kcs = 1.11E8
kcr = 3.33E8
ksed = 6.72E6 ?

k109 = 2.5E8
k910 = 1.43E7
k98 = 1.1E8
k89 = 1.56E9

k86 = 1E10
k68 = 1E10
k67 = 1E10
k76 = 1E10
k61 = 1E10
k16 = 1E10
k12 = 1E10
k21 = 1E10
k13 = 1E10
k31 = 1E10
k34 = 1E10
k43 = 1E10
k45 = 1E10
k54 = 1E10

[concentrations]
Ru.H10.H9.H8 = 0.0000005 ; M
H7 = 0.0000005 ; M
H6 = 0.0000005 ; M
H5 = 0.0000005 ; M
H4 = 0.0000005 ; M
H3 = 0.0000005 ; M
H2 = 0.0000005 ; M
H1 = 0.0000005 ; M

[responses]
Ru.H10red.H9.H8 = 18300
Ruex.H10red.H9.H8 = 18300
Ru3.H10red.H9.H8 = 18300
Ru.H10.H9red.H8 = 18300
Ruex.H10.H9red.H8 = 18300
Ru3.H10.H9red.H8 = 18300
Ru.H10red.H9red.H8 = 36600
Ruex.H10red.H9red.H8 = 36600
Ru3.H10red.H9red.H8 = 36600

Ru.H10red.H9.H8red = 36600
Ruex.H10red.H9.H8red = 36600
Ru3.H10red.H9.H8red = 36600
Ru.H10.H9red.H8red = 36600
Ruex.H10.H9red.H8red = 36600
Ru3.H10.H9red.H8red = 36600
Ru.H10red.H9red.H8red = 54900
Ruex.H10red.H9red.H8red = 54900
Ru3.H10red.H9red.H8red = 54900

H7red = 18300
H6red = 18300
H5red = 18300
H4red = 18300
H3red = 18300
H2red = 18300
H1red = 18300

[data]

```
mesh       from 0 to 3600 step 1

directory  ./MtrC
extension  txt

file       250mM | conc EDTA = 0.25
file       100mM | conc EDTA = 0.1
file       50mM | conc EDTA = 0.05
file       25mM | conc EDTA = 0.025
file       5mM | conc EDTA = 0.005
file       0mM | conc EDTA = 0

[output]
  directory  ./MtrC/outputs/Model_3
[end]
```

Model 4

```
[task]
  task = fit
  data = progress

[mechanism]
Ru.H10.H9.H8 <===> Ruex.H10.H9.H8 : kex krlx
Ru.H10red.H9.H8 <===> Ruex.H10red.H9.H8 : kex krlx
Ru.H10.H9red.H8 <===> Ruex.H10.H9red.H8 : kex krlx
Ru.H10red.H9red.H8 <===> Ruex.H10red.H9red.H8 : kex krlx
Ru.H10.H9.H8red <===> Ruex.H10.H9.H8red : kex krlx
Ru.H10red.H9.H8red <===> Ruex.H10red.H9.H8red : kex krlx
Ru.H10.H9red.H8red <===> Ruex.H10.H9red.H8red : kex krlx
Ru.H10red.H9red.H8red <===> Ruex.H10red.H9red.H8red : kex krlx

Ruex.H10.H9.H8 ---> Ru3.H10red.H9.H8 : kcs
Ruex.H10.H9red.H8 ---> Ru3.H10red.H9red.H8 : kcs
Ruex.H10.H9.H8red ---> Ru3.H10red.H9.H8red : kcs
Ruex.H10.H9red.H8red ---> Ru3.H10red.H9red.H8red : kcs

Ru3.H10red.H9.H8 ---> Ru.H10.H9.H8 : kcr
Ru3.H10red.H9red.H8 ---> Ru.H10.H9red.H8 : kcr
Ru3.H10red.H9.H8red ---> Ru.H10.H9.H8red : kcr
Ru3.H10red.H9red.H8red ---> Ru.H10.H9red.H8red : kcr

Ruex.H10red.H9.H8 ---> Ru1.H10.H9.H8 : kcs'
Ruex.H10red.H9red.H8 ---> Ru1.H10.H9red.H8 : kcs'
Ruex.H10red.H9.H8red ---> Ru1.H10.H9.H8red : kcs'
Ruex.H10red.H9red.H8red ---> Ru1.H10.H9red.H8red : kcs'

Ru1.H10.H9.H8 ---> Ru.H10red.H9.H8 : kcr'
Ru1.H10.H9red.H8 ---> Ru.H10red.H9red.H8 : kcr'
Ru1.H10.H9.H8red ---> Ru.H10red.H9.H8red : kcr'
Ru1.H10.H9red.H8red ---> Ru.H10red.H9red.H8red : kcr'

Ru.H10red.H9.H8 <===> Ru.H10.H9red.H8 : k109 k910
Ruex.H10red.H9.H8 <===> Ruex.H10.H9red.H8 : k109 k910
Ru3.H10red.H9.H8 <===> Ru3.H10.H9red.H8 : k109 k910
Ru1.H10red.H9.H8 <===> Ru1.H10.H9red.H8 : k109 k910
```

Ru.H10red.H9.H8red <===> Ru.H10.H9red.H8red : k109 k910
Ruex.H10red.H9.H8red <===> Ruex.H10.H9red.H8red : k109 k910
Ru3.H10red.H9.H8red <===> Ru3.H10.H9red.H8red : k109 k910
Ru1.H10red.H9.H8red <===> Ru1.H10.H9red.H8red : k109 k910

Ru.H10.H9.H8red <===> Ru.H10.H9red.H8 : k89 k98
Ru.H10red.H9.H8red <===> Ru.H10red.H9red.H8 : k89 k98
Ruex.H10.H9.H8red <===> Ruex.H10.H9red.H8 : k89 k98
Ruex.H10red.H9.H8red <===> Ruex.H10red.H9red.H8 : k89 k98
Ru3.H10.H9.H8red <===> Ru3.H10.H9red.H8 : k89 k98
Ru3.H10red.H9.H8red <===> Ru3.H10red.H9red.H8 : k89 k98
Ru1.H10.H9.H8red <===> Ru1.H10.H9red.H8 : k89 k98
Ru1.H10red.H9.H8red <===> Ru1red.H10.H9red.H8 : k89 k98

Ru3.H10.H9.H8 + EDTA ---> Ru.H10.H9.H8 : ksed
Ru3.H10red.H9.H8 + EDTA ---> Ru.H10red.H9.H8 : ksed
Ru3.H10.H9red.H8 + EDTA ---> Ru.H10.H9red.H8 : ksed
Ru3.H10red.H9red.H8 + EDTA ---> Ru.H10red.H9red.H8 : ksed
Ru3.H10.H9.H8red + EDTA ---> Ru.H10.H9.H8red : ksed
Ru3.H10red.H9.H8red + EDTA ---> Ru.H10red.H9.H8red : ksed
Ru3.H10.H9red.H8red + EDTA ---> Ru.H10.H9red.H8red : ksed
Ru3.H10red.H9red.H8red + EDTA ---> Ru.H10red.H9red.H8red : ksed

Ru.H10.H9.H8red + H6 <===> Ru.H10.H9.H8 + H6red : k86 k68
Ruex.H10.H9.H8red + H6 <===> Ruex.H10.H9.H8 + H6red : k86 k68
Ru3.H10.H9.H8red + H6 <===> Ru3.H10.H9.H8 + H6red : k86 k68
Ru1.H10.H9.H8red + H6 <===> Ru1.H10.H9.H8 + H6red : k86 k68
Ru.H10red.H9.H8red + H6 <===> Ru.H10red.H9.H8 + H6red : k86 k68
Ruex.H10red.H9.H8red + H6 <===> Ruex.H10red.H9.H8 + H6red : k86 k68
Ru3.H10red.H9.H8red + H6 <===> Ru3.H10red.H9.H8 + H6red : k86 k68
Ru1.H10red.H9.H8red + H6 <===> Ru1.H10red.H9.H8 + H6red : k86 k68
Ru.H10.H9red.H8red + H6 <===> Ru.H10.H9red.H8 + H6red : k86 k68
Ruex.H10.H9red.H8red + H6 <===> Ruex.H10.H9red.H8 + H6red : k86 k68
Ru3.H10.H9red.H8red + H6 <===> Ru3.H10.H9red.H8 + H6red : k86 k68
Ru1.H10.H9red.H8red + H6 <===> Ru1.H10.H9red.H8 + H6red : k86 k68
Ru.H10red.H9red.H8red + H6 <===> Ru.H10red.H9red.H8 + H6red : k86 k68
Ruex.H10red.H9red.H8red + H6 <===> Ruex.H10red.H9red.H8 + H6red : k86 k68
Ru3.H10red.H9red.H8red + H6 <===> Ru3.H10red.H9red.H8 + H6red : k86 k68
Ru1.H10red.H9red.H8red + H6 <===> Ru1.H10red.H9red.H8 + H6red : k86 k68

H6red + H7 <===> H6 + H7red : k67 k76
H6red + H1 <===> H6 + H1red : k61 k16
H1red + H2 <===> H1 + H2red : k12 k21
H1red + H3 <===> H1 + H3red : k13 k31
H3red + H4 <===> H3 + H4red : k34 k43
H4red + H5 <===> H4 + H5red : k45 k54

[constants]
kex = 1.4
krlx = 2.16E6
kcs = 1.11E8
kcr = 3.33E8
ksed = 6.73E6
kcs' = 1.4E7
kcr' = 5E7 ?

k109 = 2.5E8

k910 = 1.43E7
k98 = 1.1E8
k89 = 1.56E9
k86 = 1E8
k68 = 1E8
k67 = 1E8
k76 = 1E8
k61 = 1E8
k16 = 1E8
k12 = 1E8
k21 = 1E8
k13 = 1E8
k31 = 1E8
k34 = 1E8
k43 = 1E8
k45 = 1E8
k54 = 1E8

[concentrations]
Ru.H10.H9.H8 = 0.0000005 ; M
H7 = 0.0000005 ; M
H6 = 0.0000005 ; M
H5 = 0.0000005 ; M
H4 = 0.0000005 ; M
H3 = 0.0000005 ; M
H2 = 0.0000005 ; M
H1 = 0.0000005 ; M

[responses]
Ru.H10red.H9.H8 = 18300
Ruex.H10red.H9.H8 = 18300
Ru3.H10red.H9.H8 = 18300
Ru1.H10red.H9.H8 = 18300
Ru.H10.H9red.H8 = 18300
Ruex.H10.H9red.H8 = 18300
Ru3.H10.H9red.H8 = 18300
Ru1.H10.H9red.H8 = 18300
Ru.H10red.H9red.H8 = 36600
Ruex.H10red.H9red.H8 = 36600
Ru3.H10red.H9red.H8 = 36600
Ru1.H10red.H9red.H8 = 36600

Ru.H10red.H9.H8red = 36600
Ruex.H10red.H9.H8red = 36600
Ru3.H10red.H9.H8red = 36600
Ru1.H10red.H9.H8red = 36600
Ru.H10.H9red.H8red = 36600
Ruex.H10.H9red.H8red = 36600
Ru3.H10.H9red.H8red = 36600
Ru1.H10.H9red.H8red = 36600
Ru.H10red.H9red.H8red = 54900
Ruex.H10red.H9red.H8red = 54900
Ru3.H10red.H9red.H8red = 54900
Ru1.H10red.H9red.H8red = 54900

H7red = 18300
H6red = 18300

```
H5red = 18300
H4red = 18300
H3red = 18300
H2red = 18300
H1red = 18300

[data]

mesh       from 0 to 3600 step 1

directory  ./MtrC
extension  txt

file       250mM | conc EDTA = 0.25
file       100mM | conc EDTA = 0.1
file       50mM | conc EDTA = 0.05
file       25mM | conc EDTA = 0.025
file       5mM | conc EDTA = 0.005
file       0mM | conc EDTA = 0

[output]
   directory  ./MtrC/outputs/Model_4
[end]
```

Source Data

	$\Delta A_{552\ nm}$					
Irradiation time (s)	0 mM	5 mM	25 mM	50 mM	100 mM	250 mM
0	0	0	0	0	0	0
20	0.000986851	0.001409524	0.002376567	0.002283625	0.006042432	0.005314074
40	0.001230943	0.000248591	0.00374163	0.003459053	0.010013638	0.009805583
60	0.000495858	0.002106328	0.004949329	0.004549369	0.014994245	0.014944946
120	0.000308703	0.002853616	0.00885404	0.010615982	0.025490409	0.028268192
180	-0.000172576	0.003133908	0.012207766	0.016963246	0.03152895	0.037913647
240	0.000669353	0.004718139	0.014074771	0.022066711	0.03622011	0.04446479
300	0.001058476	0.004671963	0.018658523	0.02626275	0.03958863	0.051287551
450	0.001034002	0.006364888	0.024212938	0.033200018	0.047379712	0.061226328
600	0.00011681	0.009492184	0.028731485	0.038313228	0.05318764	0.067632163
900	0.000352533	0.011946285	0.035518977	0.046507801	0.060719847	0.074638068
1200	-0.000362948	0.015485733	0.041835004	0.05209349	0.065878496	0.079474662
1500	-0.000416547	0.016804207	0.045519618	0.057264784	0.069077439	0.083635261
1800	-0.000285242	0.019125219	0.050029072	0.059920689	0.072289579	0.085427404
2400	-0.000321828	0.02252146	0.054863453	0.066543007	0.075621555	0.08862418
3000	-0.000676182	0.026003856	0.059993703	0.071079325	0.078785933	0.089732116
3600	-0.000973137	0.028371663	0.063413066	0.074289855	0.080907808	0.090941021